The Mechanisms of Deep Earthquakes

Robert Myhill

Department of Earth Sciences

Magdalene College

University of Cambridge

This dissertation is submitted for the degree of

Doctor of Philosophy

July 4, 2012

This dissertation is the result of my own work and includes nothing which is the outcome of work done in collaboration except where specifically indicated in the text. It does not exceed the page limit set out by the Degree Committee for Earth Sciences and Geography, and is not substantially the same as any work that has been, or is being, submitted to any other university for any degree, diploma, or other qualification.

Robert Myhill

July 4, 2012

This is the post-viva dissertation, containing minor corrections to that submitted on May 16, 2012.
These corrections were suggested by James Jackson and Steve Roecker on June 27, 2012.

Acknowledgements

This thesis (such as it is) would not have been possible without the assistance and encouragement of many people over the last three years. A huge thank you to Dan McKenzie, for providing many fascinating conversations on diverse aspects of geology, from impact craters to pseudotachylites, earthquakes to metamorphism, the mantle to the moon. Thanks also for the awe-inspiring trip to Iceland, which gave me memories I shall never forget. Heartfelt thanks to Keith Priestley, my primary source of knowledge for all things seismological, his wisdom in finding out just what is tractable, which results are trustworthy, and for teaching me that many things are possible with good stations and arrays.

There are many academics who were never my supervisors, but who probably feel like they were at times. Thanks to Frederik Tilmann, my first forays into waveform analysis were not quite as scary. I had many discussions with both Frederik and Dietrich Lange on subduction zone deformation; they are much appreciated. Thanks also to Linda Warren at Saint Louis University, without whom I would have been unable to discover the remarkable nature of faulting in the Izu–Bonin–Marianas slab, and to Brian Emmerson for donating the beautifully described thermal modelling scripts and code from which my own were born.

I am extremely grateful to Tim Holland, who first introduced me to metamorphic petrology and Gibb's Free Energy minimisation. Despite the sketchy data and many unknowns, he attempted to construct the first upper mantle model of hydrous phases for me. In doing so, he showed me the importance of good experimental techniques, and as a result guided my plans for postdoctoral study. I owe him a great debt.

Despite a busy schedule, John Rudge has always managed to spare a moment to help me get my head around the uses and pitfalls of finite element modelling. For his patience in explaining the intricacies of FEniCS, and for several pleasant working lunches, I am very grateful.

Thank you to Nigel Woodcock, for providing me with an escape route from Cambridge to Sedbergh in 2009, 2010 and 2011, and the chance to teach my favourite course from undergrad. I also thank Arwen Deuss and Hazel Chapman for their encouragement and support. At times during both my undergrad and postgrad studies I have felt lost; they are at least partially responsible for showing me how to find my way through the thicket that is research in the Earth Sciences.

Pecuniarily, thank you to NERC and to Magdalene College. My bye-fellowship at Magdalene was both terrifying and extremely enjoyable (occasionally at the same time), and gave me a fantastic insight into how the other half lives. I am grateful to the then-President and chaplain, and to Mike Carpenter and all the other fellows who made my time with them so pleasant.

Thanks to Gill and Barbara for always being willing to go the extra mile, for keeping the Bullard functioning, and for helping make Bullard the wonderful place that it is. To Joyce, for our many conversations and for reminding me that my home town (Lowestoft) isn't all bad. To Dave Lyness for installing more and more obscure software, working on Sundays to restore access to the computer network, and for many amusing and interesting lunchtime discussions. In the Downing Site, thank you to Sarah Humbert, for her friendship, not to mention her skill in finding obscure references, acquiring books, and providing much-needed coffees between supervisions.

The Bullard would not have been the second home that it has been without my friends here. Thanks to my compatriots Al, Lauren, Ross and Steve, with whom I have shared many trials and tribulations. To Jess and Lizzie for guiding me over many of the hurdles required to succeed in academia, and for teaching me that presenting at conferences is not the same as taking a holiday. Thanks also to Tim and Paula for providing code, calm and a sounding board off which to bounce my ideas. Downtown, I am hugely grateful to Rob Sparkes for his ever-constant friendship, not to mention proofreading skills and giving me a chance to savour the delights of fieldwork in Northern Spain. Without taking up several more pages, I'll never be able to adequately thank everyone in the department and outside; suffice it to say that there are many more postgrad and undergrad students without whom my PhD would have been much less enjoyable.

Annie, Adamos and Mike Rassios (and Terry the dog); Dina Ghikas and Babi; and Anna Mpatsi, an enormous thank you for your hospitality during my many trips to Greece. To Annie and Dina, thank you for showing me the geo-wonders that are your home. I'll always remember the perfect days we've shared in the Pindos, Vourinos and Olympos, and hope for many more.

These acknowledgements could not be complete without thanking my family for their genuine interest during my scientific education, and for buying me books, rocks, fossils, magazines, microscopes and storage for my samples. To my parents, thank you for always encouraging me whatever my new interest, and giving me the gift of wonder in the natural world. Finally, thank you to my sister Anna, for her honesty, patience and kindness at times when the world felt lacking in all three.

For my family

SUMMARY

The mechanisms of deep earthquakes

Robert Myhill

This dissertation uses a variety of seismological and mathematical tools to investigate the mechanisms of deep earthquakes, the properties of fault planes and rupture at high pressure within the Earth, and the local conditions where deep earthquakes occur. This work is split into two parts, focusing respectively on the properties and conditions of deep faulting.

In the first chapter of the first part, waveforms of deep earthquakes beneath the southwest Pacific are investigated. P-waveforms from about 10% of all earthquakes exhibit similar codas extending for over 40 s after the initial arrival. Unlike in local and regional studies, similar teleseismic waveforms can be observed for earthquakes separated by more than 10 km. Similar waveforms can be used to constrain the focal mechanisms of small earthquakes.

In the following two chapters, several techniques are used to integrate earthquake location and gCMT focal mechanism data in order to constrain patterns of faulting, the relationships between faulting and slab shape, and to evaluate the evidence for reactivation of pre-existing features.

Although focal mechanisms can reveal slab stress fields, double-couple moment tensor solutions result in a fundamental ambiguity between fault plane and auxiliary plane. In the fourth chapter of this dissertation, the characteristics of rupture propagation are exploited to determine the fault planes of 20 Izu-Bonin-Marianas deep earthquakes. A predominance of shallowly dipping fault planes is inferred from the waveform shapes and durations. The lack of steeply dipping planes may be a result of deformation of the slab, and resistance to flow at the upper-lower mantle boundary.

In the second part of this dissertation, the conditions under which deep-focus earthquakes occur are modelled using *P-T-composition*-dependent physical parameters. An analysis of several subduction zones shows that the strong temperature dependence of conductivity decreases thermal gradients within the slab. Transition-zone earthquakes are generally confined within material where temperatures do not exceed $\sim$850°C. Differences in modelled temperatures for highly-active (e.g. Tonga) and relatively inactive (e.g. Kamchatka) subducting slabs are generally less than 100°C. Integrating seismic observations with simple stress-strain modelling reveals that differences in seismic activity between slabs with similar temperatures can largely be explained by the unique and evolving morphologies of each slab. Temperature and bending-related strain may be the dominant controls on the depth distributions of deep earthquakes worldwide.

Calvin: The world is a complicated place, Hobbes.

Hobbes: Whenever it seems that way, I take a nap in a tree and wait for dinner.

– Bill Watterson

Publications

From this dissertation

R. Myhill, D. McKenzie, and K. Priestley. The distribution of earthquake multiplets beneath the southwest Pacific. *Earth and Planetary Science Letters*, 301:87–97, 2011. doi:10.1016/j.epsl.2010.10.023.

R. Myhill and L. M. Warren. Fault plane orientations of deep earthquakes in the Izu-Bonin-Marianas subduction zone. *Journal of Geophysical Research (Solid Earth)*, 117:B06307, 2012. doi:10.1029/2011JB009047.

R. Myhill. Slab bending and its effect on the distributions and focal mechanisms of deep-focus earthquakes. *Geophysical Journal International*, submitted.

Arising elsewhere

R. Myhill. Constraints on the evolution of the Mesohellenic Ophiolite from subophiolitic metamorphic rocks, *in Wakabayashi, J., and Dilek, Y., eds., Mélanges: Processes of Formation and Societal Significance: Geological Society of America Special Paper* 480:1–20, 2011. doi:10.1130/2011.2480(03).

Contents

1 Introduction

The processes by which brittle failure occurs in the Earth have been of considerable interest to geophysicists for many decades. Brittle failure is a response to the buildup of stress resulting from deformation of cold lithosphere. The release of this energy is made manifest in the propagation of seismic waves and heating at the site of rupture.

Studies of shallow earthquakes (with hypocentral depths <60 km) dominate both the academic literature and in the public mind. The largest and most destructive earthquakes are shallow. The faults which rupture during these earthquakes can be seen at the surface, offsetting fences, pipelines and railway tracks. Displacement at the Earth's surface triggers tsunamis that cross oceans, and liquefaction that turns solid ground into quicksand. Yet not all earthquakes are shallow.

Since brittle failure is only possible in cold rocks, deeper earthquakes should only be possible within subducting lithosphere. The lack of gigapascal-scale shear stresses suggest that after an oceanic plate is subducted at an oceanic trench, it should become seismically inactive, silently sinking into the aesthenosphere. This is true of the plate interface; earthquakes cease at <40 km depth on the upper interface of warm slabs, corresponding to temperatures of 350–450°C (Oleskevich et al., 1999), while the interfaces of colder slabs become aseismic at ∼40 km depth, possibly as a result of the presence of weak hydrous phases in the mantle wedge (Peacock and Hyndman, 1999). In contrast, the interior of the plate is far from inactive. The cold core of the slab crackles with seismicity, resulting in dipping zones of earthquakes that extend deep into the upper mantle (Wadati, 1935; Benioff, 1949). Between 1960 and 2007, 15835 earthquakes with well determined depths and $M_b > 5.4$ were recorded in the catalogue of Engdahl, van der Hilst and Buland (EHB catalogue; Engdahl et al., 1998). 4097 of these have depths ≥ 60 km. 801 have depths ≥ 300 km. The deepest events rupture material 680–690 km beneath the surface of the Earth (Stark and Frohlich, 1985; Rees and Okal, 1987).

Earthquakes with hypocentral depths greater than 60 km can be large. On the 9th of June 1994, a M_W 8.3, ∼650 km deep earthquake struck beneath Bolivia (Myers et al., 1995). It was felt as far away as Washington State, over 8500 km away from the epicenter (Anderson et al., 1995). Such earthquakes are particularly useful in several realms of geophysical research, since they create large amplitude waveforms that are uncontaminated by near surface complexity, and stimulate normal modes sensitive to deep earth structure.

Despite the number of deep earthquakes, the size of some of the events, and their utility in other areas of the Earth sciences, they remain poorly understood. In Part I of this thesis, I summarise the motivations for studying deep earthquakes (Chapter 2) and the current state of knowledge relating to these phenomena, as derived from observational, experimental and theoretical studies (Chapter 3).

In Part II of this dissertation, I report and integrate observations of earthquake waveforms, locations and focal mechanisms to describe and explain the characteristics of seismically active areas within subducting slabs:

- Chapter 4 investigates the presence and origins of similar waveforms from deep earthquakes within the Vanuatu and Tonga-Kermadec slabs. Several groups of earthquakes with almost identical waveforms are observed along the Tonga-Kermadec slab, especially where seismic density is high.

- Chapter 5 analyses focal mechanisms in the context of areas of high seismic density and slab shape. Large scale trends and minor changes in orientation both reflect observable deformation within several slabs, as does small scale variability. A strong correlation is observed between the orientation of focal mechanism null axes, elongation of areas of high seismic density and the axes of folds in the slab, suggesting that stresses and seismically active areas are controlled by deformation, rather than phase changes or other internal sources of stress.

- Chapter 6 extends the work of the previous two chapters by assessing the likelihood of repeated rupture along localised shear zones. These shear zones are less common than previously reported. Long streaks of seismicity within the Izu-Bonin slab are evaluated as potential surface-formed planes of weakness reactivated at depth.

- Chapter 7 utilises rupture directivity to distinguish the fault and auxiliary plane of earthquakes within the Izu-Bonin-Marianas subducting slab. The majority of identified fault planes have shallow dips, inconsistent with reactivation of dominantly trenchward-dipping normal faults. Fault plane orientation may be controlled by larger scale deformation of the slab and resistance to flow within the lower mantle.

Part III of this dissertation is concerned with the ambient conditions under which faulting is possible.

- Chapter 8 outlines compositional and mineralogical variations in oceanic lithosphere, and the alteration both preceding and following subduction at the oceanic trenches in the context of variations in material properties which may have effects on the potential seismicity in subducting slabs.

- Chapter 9 models thermobaric conditions under which deep-focus earthquakes occur in a self-consistent manner, incorporating pressure, temperature and mineral-assemblage-dependent

enthalpy, conductivity, density and heat capacity. Low thermal gradients and temperatures below 850°C typify subduction zones with abundant deep-focus activity. No consistent trends are observed between *P-T* conditions and the density of seismic activity in cold slabs, suggesting that temperature plays a lesser role than slab deformation in this respect. An apparent step change from broad distribution of earthquakes in cold slabs to strongly localised deformation in warmer slabs suggests a change in deformation mechanism at ∼900°C.

- Chapter 10 compares estimated seismic strain rates with those calculated from a simple kinematic model. The global distribution of seismicity is consistent with most deep-focus earthquakes occuring within localised zones experiencing intense deformation. Much of the total strain within the cold cores of the Tonga-Kermadec and Izu-Bonin slabs is being taken up seismically. Buckling can take up the majority of relative motion between the subducting plate and lower mantle without requiring significant slab thickening.

Finally, in Part IV, the constraints on the underlying physical mechanism of deep earthquakes are discussed in terms of the observations and inferences throughout the dissertation (Chapter 11). In Chapter 12, I summarise the main findings of this dissertation, and propose potential avenues of further research.

Part I

Literature review

2 *The motivation for studying deep earthquakes*

2.1 Introduction

At the turn of the 20th Century, earthquakes represented one of the great mysteries in the Earth Sciences. The connection between earthquakes and faulting was still a topic of active debate (e.g. Oldham, 1909), and hypocentral depths were poorly constrained. These uncertainties are reflected in early estimates of the hypocentral depth of the shallow 1906 San Francisco earthquake ($\lesssim$20 km, $\sim$140 km; Reid, 1910; Pilgrim, 1913), and of 'typical' hypocentral depths ($\sim$1250 km; Walker, 1921). These errors are understandable when the large time errors at recording seismograph stations and a poor understanding of seismic velocities within the Earth are taken into account.

Hypocentral depths only became well constrained in the 1920s. Turner (1922) analysed systematic errors for P-wave arrivals from earthquakes, and ascribed these to deviations of hypocentral depths from those of 'normal' earthquakes. His results indicated a $\sim$500 km depth range of earthquake hypocenters, but didn't include absolute depths relative to the Earth's surface. Differential S-P intervals provided the first accurate estimate of 'normal' earthquake depth beneath Japan (30–50 km) and the first reliable reports of earthquake depths exceeding 300 km (Wadati, 1927, 1928). Soon afterwards, Wadati (1929) discovered that earthquakes beneath Japan exist at all depths from the surface down to $\sim$500 km.

The discovery of inclined zones of deep earthquakes is credited to Wadati (1935) and later to Benioff (1949) (see Uyeda, 1971). While Wadati (1935) followed Holmes (1933) in relating these zones to the theory of continental drift (Wegener, 1915), Benioff (1949) equated them with gravity-driven subsidence of the oceans beneath less dense continental material. Resolving the origin of Wadati-Benioff zones was only possible after the advent of the 'New Global Tectonics' (now plate tectonics). Hess (1960, 1962) noted that spreading of the sea floor implied young oceanic lithosphere in old ocean basins, and that the oceanic trenches marked sites of downwelling. The observations revealing that deep earthquakes marked zones of subduction of cold, strong lithosphere were documented in detail by a series of papers published in the late 1960s (Sykes, 1966; Oliver and Isacks, 1967; Isacks et al., 1968). The first modelling of temperature in subducting slabs followed soon afterwards (McKenzie, 1969a, 1970).

Since the 1970s, many aspects of deep faulting have been studied and constrained (see §3). Nevertheless, the reasons for studying deep earthquakes have largely remained the same. Most research on deep earthquakes focuses on what they can tell us about the rheology, deformation and dynamics of subducting slabs and the upper mantle, or the potential mechanisms by which brittle failure can occur at high pressure.

2.2 *Earth structure and mantle convection*

A detailed knowledge of the locations and deformation of subducting slabs is vital for understanding global geodynamics (e.g. Lay, 1994). In addition to providing first order information on the distribution of cold downwelling material, accurate estimates of slab locations and kinematics can be used to study the influence of mantle phase transitions and compositional changes on dynamics.

Waveform tomography is a useful tool for probing the Earth's deep interior, but the $>$100 km resolution is not high enough for detailed study of subducting slabs. As a result, the locations of deep earthquakes remain the most accurate information from which the morphology of subducting slabs can be constrained.

The primary limitation on determining slab shape from deep earthquake locations, apart from $\sim$20 km location errors, is that subducting slabs aren't always associated with seismicity. The absence of earthquakes in the lower mantle has historically been used as evidence for two-layer convection in the Earth's mantle (e.g. Anderson, 1987); however, high quality tomographic results (e.g. Grand, 1994; Grand et al., 1997) suggest that some slabs penetrate the upper-lower mantle boundary.

2.3 *Deformation in subducting slabs*

Deep earthquakes are the most accurate indicators of deformation within subducting slabs. The consistency in focal mechanism orientations within large volumes led Isacks and Molnar (1971) to suggest that subducting slabs were significantly more viscous than the surrounding mantle and therefore acted as stress guides. They argued that the negative buoyancy of subducted slabs provides a net down-dip extensional force on the slab, while interaction with the upper-lower mantle boundary causes net down-dip compression. Isacks and Molnar (1971) suggested that as subduction continued, the field of down-dip compression expanded to shallower depths, explaining the down-dip extension inferred at intermediate depths beneath the Aleutians and Izu-Bonin Islands and down-dip compression throughout the upper mantle beneath Tonga.

Despite the systematic analysis of Isacks and Molnar (1971), deviations from their intuitive model are relatively common (Apperson and Frohlich, 1987). Although deviations from down-dip extension/compression at intermediate depth can sometimes be explained by slab shape (Chen et al., 2004), it is not clear to what extent this explanation holds true at greater depths. Further complications

include the common presence of intermediate-depth double seismic zones (e.g. Brudzinski et al., 2007), which converge with increasing depth. The upper zone lies mainly within the slab crust and uppermost mantle, while the lower zone typically lies 10–30 km deeper. The two zones usually have different focal mechanisms (although this is not always true, e.g., Rietbrock and Waldhauser, 2004), most commonly representing down-dip extension in the lower zone and down-dip compression in the upper zone (e.g. Hasegawa et al., 1978). Double seismic zones have also been reported at 350–450 km depth within the Tonga slab (Wiens et al., 1993), but these remain poorly studied. The match between local variations in the stress field and models of deformation in subducting slabs may be studied in detail using earthquake moment tensor solutions (e.g. Alpert et al., 2010; Bailey et al., 2012).

By disentangling the effects of temperature, mineralogy and stress on strain rates, the distribution of deep earthquakes may tell us about the rate and style of deformation within subducting slabs. At present, the relative rates of seismic and aseismic strain are poorly known, as is the relative importance of pure and simple shear along subduction zones. Numerical models have suggested that thickening of a factor of two may be expected for cold slabs just above the upper-lower mantle boundary (Gaherty and Hager, 1994; King, 2001). Constraining slab deformation would represent a significant step towards constructing rheological models relevant to the deep Earth.

Deep earthquakes also provide potential insights into the role of heterogeneities and preexisting features in mantle deformation. The concept of surface-formed fault reactivation at depth was suggested by Savage (1969), and revived by Jiao et al. (2000). Two detailed studies of rupture directivity in the Tonga and Middle America subduction zones suggest that reactivation is unlikely to explain fault plane orientations, which have orientations orthogonal to those expected from reactivation of outer rise faults (Warren et al., 2007, 2008). Nevertheless, the persistence of fine grained, altered shear zones within subducting slabs should have some effect on deformation; a hypothesis best addressed by careful observations of deep seismicity.

2.4 *Mechanisms of brittle failure at high pressure*

By the time Wadati published his first English-language paper on deep earthquakes, it was already realised that their presence, if confirmed, presented a serious physical problem. The success of isostasy in predicting surface elevations meant that rocks were weak at depth (Jeffreys, 1928). Although subduction carries cool strong material into the aesthenosphere, the increased pressure should still prevent brittle behaviour in dry rocks. Coulomb fracture at the 2–23 GPa pressures corresponding to deep earthquake is impossible unless large shear stresses can be created and maintained. There is no known geological process that can create such high stresses, and they are ruled out by both gravity and observations of slab morphology. Griggs and Handin (1960) suggested

that for the deepest earthquakes, brittle fracture would require a shear strength four orders of magnitude larger than is considered reasonable for Earth materials. Three mechanisms have been proposed to solve this conundrum.

2.4.1 *Free fluid*

The simplest mechanism for brittle failure under high pressure and $<$200 MPa shear stresses involves the presence of a free fluid. A significant amount of water can be stored within mantle assemblages in the form of serpentinite, raising the possibility that breakdown of this mineral could promote seismic activity. Fluids released by dehydration reactions would be at lithostatic pressure, thus reducing the effective pressure and promoting shear failure (e.g. Hubbert and Rubey, 1959). This was recognised by Isacks et al. (1968), who cited the experiments of Raleigh and Paterson (1965) and Raleigh (1967) which showed that dehydration reactions occurred at 300–1000°C. They pointed out that the objections to dehydration embrittlement at $>$100 km depth raised by Griggs (1967) and Griggs and Baker (1969) were based on normal, non-subduction geothermal gradients, and that subduction geotherms would be significantly cooler, as shown later by McKenzie (1969a, 1970).

The dehydration reactions associated with serpentine at low temperature have been constrained by laboratory experiments. Irifune et al. (1998) showed that there is potential for dehydration at a range of depths, potentially including the base of the upper mantle (Omori et al., 2004). The negative volume change of dehydration reactions doesn't necessarily prevent brittle deformation (Jung et al., 2004), and merely wetting the grain boundaries enables rupture to occur (Zhang et al., 2004).

Publications vary in their proposed mechanism for fluid-related faulting. Some suggest that the dehydration itself results in fracturing (dehydration embrittlement), whereas others suggest that it is the presence of fluid that allows shear fracture (Arkwright et al., 2008; Rutter et al., 2009). The idea that the dehydration process itself causes faulting is not supported by recent experiments, and it may be that faulting is only possible in relatively anhydrous rocks infiltrated by fluids (Chernak and Hirth, 2010, 2011).

2.4.2 *Shear instabilities*

A major problem with faulting induced by an increase in pore fluid pressure is the difficulty of getting water 50 km into the anhydrous oceanic lithosphere. It is unlikely that anhydrous fluids could exist in the deep slab in the upper mantle.

An alternative mechanism for creating earthquakes at high pressure is strain localisation and the development of a mechanical instability (Bridgman, 1936). This instability could develop by shear heating, decreasing grain size, or by mineral amorphisation (Meade and Jeanloz, 1991). Localised melting along the shear zone could create fluids at lithostatic pressure, enabling brittle failure along

or a small distance away from the center of the shear zone (Orowon, 1960).

Although early models suggested that shear zones would have to be tens of kilometers wide to enable thermal runaway (Griggs and Baker, 1969), more recent studies using elastoplastic rheologies have concluded that 10–100 metre-scale zones are sufficient (Ogawa, 1987; Hobbs and Ord, 1988). Using more realistic mineral and grain size models of the mantle, Karato et al. (2001) argue that shear instability models adequately explain the distribution and depth dependence of seismicity, and differences in seismic activity amongst present-day subduction zones.

More recently, simple numerical models suggest that shear instabilities may only occur within a 600–800°C temperature window (Kelemen and Hirth, 2007), consistent with estimated temperatures of intermediate-depth earthquakes (Brudzinski et al., 2007). A consequence of the equations governing these models is that rate-state behaviour is expected, which could explain some of the observed similarities between shallow and deep earthquakes.

A potential problem with the shear instability theory is that models so far require high deviatoric stresses and stress drops. There is little evidence to suggest that static stress drops in deep earthquakes exceed 100 MPa (Frohlich, 2006). Many seismological studies claim higher stress drops, but these are largely dependent on modelling assumptions. For example, estimates of static stress drop during the 1994 Bolivian deep-focus earthquake range from 5–283 MPa (Bouchon and Ihmlé, 1999; Goes and Ritsema, 1995). Small exhumed pseudotachylite-bearing faults in ultramafic rocks appear to have melt compositions and slip dimensions consistent with stress drops up to 580 MPa (e.g. Andersen et al., 2008; John et al., 2009), but slip estimates in the absence of slip vectors or piercing points are minima, leading to overestimates of stress drop. If high deviatoric stresses do exist, they may be transient and/or restricted to small regions such as the tips of larger faults and therefore unrelated to the generation of large earthquakes.

2.4.3 *Metastable phase transformation*

A third hypothesis proposed to explain deep earthquakes is that phase transitions may cause brittle failure. One of the earliest suggestions is that stresses built up during transformation would enable 'normal' brittle failure (Leith and Sharpe, 1936). Although even the largest estimated deep earthquake stress drops are too low to support this hypothesis, transformational faulting remains a popular earthquake-generating mechanism.

The exponential decay in global earthquake frequency and moment release with increasing depth, followed by a secondary rise between 300 and 550 km and fall to zero at 700 km depth has been used to suggest a change in faulting mechanism at about 300 km (Green and Houston, 1995). The deep-focus earthquake depth range of 300–700 km corresponds to the pressure regime where the dominant magnesium silicate phase is wadsleyite or ringwoodite rather than olivine.

Laboratory experiments have revealed that olivine reacts sluggishly to wadsleyite and ringwoodite at temperatures expected in cold subducting slabs. This metastable olivine has been shown in some experiments to produce acoustic emissions and undergo 'transformational faulting' (Green and Burnley, 1989; Green et al., 1990). This faulting does not occur by a normal brittle process, where open or fluid-filled Griffiths cracks coalesce (Tingle et al., 1993). Instead, lens shaped regions of the denser wadsleyite or ringwoodite grow at the expense of olivine, joining to form 'anticracks' (Green and Burnley, 1989), which may nevertheless behave in a similar way to Griffiths cracks (Burnley et al., 1991). It has been argued that the strong effect of strain and temperature on reaction rates might lead to transformational faulting before adiabatic shear instabilities can develop (Kirby et al., 1996).

The transformational faulting hypothesis is not without its problems. Some non-hydrostatic experiments with $(Mg,Fe)_2SiO_4$ olivine have been unsuccessful in reproducing transformational faulting (Dupas-Bruzek et al., 1998; Dobson et al., 2004). The most detailed models of reaction kinetics suggest that metastable wedges could not reach the depths where the deepest seismicity is observed (Mosenfelder et al., 2001; Marton et al., 2005), even in completely dry slabs.

3 Observations

3.1 Introduction

Throughout this dissertation, I shall use the terms shallow and deep to denote regions above and below 60 km depth. When describing earthquake depths, I shall use the term 'intermediate-focus' for events with hypocentral depths between 60–300 km, and 'deep-focus' for events with hypocentral depths $\geq$300 km (Wadati, 1929).

Deep earthquakes rupture sufficiently far from the surface that faults are almost never returned to the surface without first becoming incorporated into the convective mantle. Very rarely, exhumed intermediate-depth faults have been observed in lower crustal continental rocks (Austrheim and Boundy, 1994; Lund and Austrheim, 2003; Steltenpohl et al., 2006) and oceanic upper mantle (Austrheim and Andersen, 2004; John and Schenk, 2006; Andersen et al., 2008). Exhumed oceanic crust hosting eclogite-facies breccias in the Monviso Ophiolite may also represent brittle faulting which occurred at $\sim$70 km depth in a subduction environment (Angiboust et al., 2011).

Without directly observing deep fault zones, there are a limited number of parameters which can be constrained without making assumptions about the rupture process. With an appropriate number and distribution of seismograms sensitive to seismic energy from an earthquake, the location, timing, magnitude, focal mechanism and spatial and temporal distribution of energy release can be determined relatively directly. On the other hand, strain, stress and stress drop are more derived parameters, and are consequently associated with larger errors. Uncertainties related to the mechanism of faulting and fine-scale distribution of energy release can lead to orders of magnitude variation in estimates of stress drop (Frohlich, 2006).

The state of research on deep earthquakes up to 2006 has been thoroughly presented by Frohlich (2006). This chapter seeks not to repeat his excellent summary, but to draw the reader's attention to key points and active areas of debate.

3.2 Earthquake Distribution

3.2.1 Global depth distribution

Wadati (1929) noted that the frequency of earthquakes between 100–200 km depth beneath Japan was lower than that of shallower and deeper events. The explicit confirmation of an intermediate-depth minimum in the global frequency-depth distribution took over 20 years (Koning, 1953). The decrease in seismicity with depth is exponential; between 100 and 200 km depth the frequency of earthquakes drops by a factor of ∼10 (Sykes, 1966; Isacks et al., 1968). At 300–400 km depth, a sharp increase in seismicity is observed (Kirby et al., 1991), with a broad peak in frequency between 550 and 600 km depth (Figure 3.1[1]). No earthquakes are reliably located at >680–690 km depth (Stark and Frohlich, 1985; Okal and Bina, 1998).

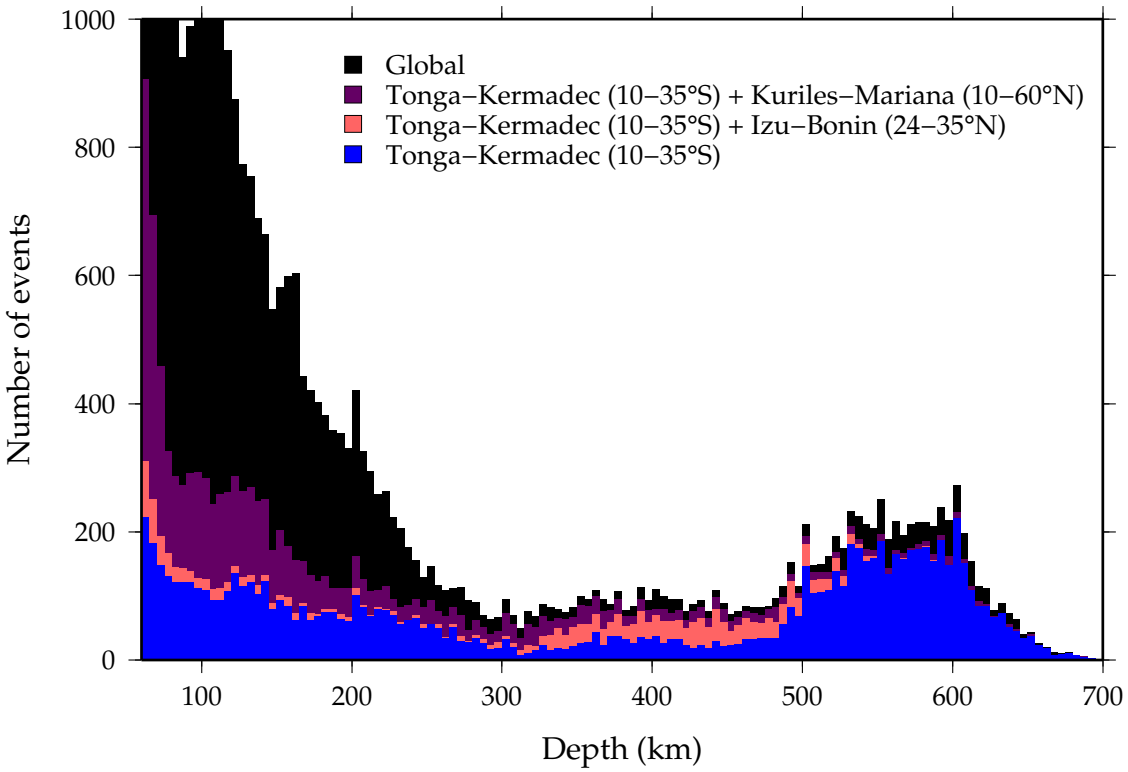

Figure 3.1: The depth distribution of earthquakes with hypocentral depths >60 km, as included in the EHB catalogue for 1960–2007 (Engdahl et al., 1998). The world's deep-focus earthquakes are mostly found in the western Pacific subduction zones.

Although the pattern of decreasing and increasing seismic activity with depth is observed in all global earthquake catalogues, different subduction zones exhibit drastically different behaviour. For example, the Tonga–Kermadec subduction zone system accounts over half of all events over 500 km depth, but only a third of events between 300 and 500 km, a depth range dominated by earthquakes in the Izu–Bonin subduction zone (Figure 3.1).

[1]This figure, and the majority of figures in this dissertation are created using the Generic Mapping Tools package (Wessel and Smith, 1998).

3.2.2 Local distribution

Regional studies reveal more complexity in the distribution of earthquake locations. Some of this complexity may be related to systematic errors in location (Frohlich, 2006); nevertheless, individual regions certainly do not exhibit the same distribution of seismicity as global catalogues. Some Wadati-Benioff zones include large gaps in seismicity, like beneath South America, where almost no earthquakes are observed between 325 and 500 km depth. Isolated deep-focus earthquakes are also present beneath Java (Okal, 2001) and New Zealand (Adams, 1963; Anderson and Webb, 1994; Boddington et al., 2004). Deep-focus earthquakes beneath Spain (Chung and Kanamori, 1976; Buforn et al., 1991, 2011) are also isolated, and not even associated with an active trench.

Gaps in seismicity, particularly between ∼300–500 km depth, have sometimes been interpreted as evidence for slab detachment (e.g. Boddington et al., 2004). However, high resolution tomographic results suggest that parts of the South American subduction zone (Engdahl et al., 1995; Li et al., 2008) are continuous throughout the mantle transition zone. High amplitude T-phases[2] recorded by seismometers in the Pacific Islands after the 1994 deep-focus Bolivian earthquake support the tomographic results (Okal and Talandier, 1997). A continuous slab beneath Java is preferred by Okal (2001). The continuity of the New Zealand slab is currently uncertain (Okal, 2001; Reyners et al., 2006).

Even in slabs without large gaps in seismicity, significant variations in seismic activity are observed. Bands of dense seismicity ∼50 km wide run almost horizontally along the Tonga and Izu-Bonin slabs at 300–600 km depth. A pocket of low seismicity breaks up the band in the deep south Tonga slab (Giardini and Woodhouse, 1984). Narrower trains of seismicity comprise much of the deep-focus seismicity in the Solomons, South America and New Zealand slabs. These bands are investigated in Chapters 5 and 10.

Streaks/lineations of earthquakes cross-cut the mostly horizontal changes in seismic activity within several slabs. Such streaks are observed at intermediate-depth beneath Sumatra (Lange et al., 2010), Japan (Nakajima and Hasegawa, 2006) and South America (Kirby et al., 2001; Kirby and Engdahl, 1993; Kirby et al., 1996), at 400–600 km depth beneath the Izu-Bonin islands (Lundgren and Giardini, 1992) and in a near-horizontal seismic zone 500–650 km beneath Fiji (Sykes, 1964; Isacks and Molnar, 1971; Okal and Kirby, 1998; Chen and Brudzinski, 2001, 2003; Brudzinski and Chen, 2003; Brudzinski and Chen, 2000). These lineations are discussed in more detail in Chapter 6.

Not all clustering of deep seismicity occurs along linear features. One exceptional example of a tight non-linear cluster of deep earthquakes is the nest located 160 km beneath Bucaramanga, Colombia (Tryggvason and Lawson, 1970). Estimated strain rates within this zone reach 10^{-13}–10^{-11}

[2]T-phases are seismic signals which have travelled for significant distances as acoustic waves confined to a narrow low velocity waveguide (the SOund Fixing And Ranging, or SOFAR channel) ∼ 1000 m below the surface of large bodies of water.

s^{-1} within a volume of $<$1000 km^3 (Frohlich et al., 1995).

3.2.3 *Double seismic zones*

At intermediate depths, several Wadati-Benioff zones are split into two subplanar distributions of earthquakes, separated by ∼10–30 km (Tsumura, 1973; Hasegawa et al., 1978; Comte et al., 1999; Shiobara et al., 2010). It has been suggested that these are global features (Brudzinski et al., 2007). Global in this case doesn't mean ubiquitous; some regions only have a single zone of seismicity (Hudnut and Taber, 1987; Comte et al., 1999) and in others, double seismic zones appear to represent overlapping single zones (Kao and Chen, 1994). Beneath Northern Honshu, a triple seismic zone has been reported (Kawakatsu and Seno, 1983). Several double seismic zones are consistent with bending, but sometimes both layers share similar focal mechanism orientations (Rietbrock and Waldhauser, 2004), suggesting that densification (e.g. Wang, 2002) and/or the physical mechanism of faulting (Peacock, 2001; Kelemen and Hirth, 2007) may also be important.

Double seismic zones are not solely restricted to intermediate depths. A deep-focus double seismic zone has been identified within the Tongan slab (Wiens et al., 1993), and another beneath Izu–Bonin (Iidaka and Furukawa, 1994).

3.3 *Aftershocks and triggered events*

Perhaps the most often cited difference between deep earthquakes and their shallow counterparts is the relative lack of deep aftershocks. The largest deep-focus aftershocks tend to be two magnitudes smaller than the mainshock, in contrast to shallow earthquakes like those beneath California, which typically have aftershocks only one magnitude smaller (Wiens et al., 1997). As a result, aftershocks for deep-focus earthquakes tend to be observed only when local networks are operational. Nevertheless, deep-focus earthquakes with $>$10 aftershocks have been observed beneath Tonga (Wiens et al., 1994), Bolivia (Myers et al., 1995) and Marianas (Wu and Chen, 1999).

Although some authors have suggested that aftershocks lie along the same plane as the main shock (e.g. Wiens et al., 1994; Wiens and McGuire, 2000), the results are not significant, and re-analysis of data has been shown to reduce or remove observed clustering (Willemann and Frohlich, 1987; Frohlich, 2006). This could either be because aftershocks do not lie on the mainshock plane, or because errors in location are sufficient to reduce the significance of any observed clustering (Michael, 1989). A study of the 2002 Tonga deep-focus earthquake sequence shows some agreement between the locations of aftershocks and regions where Coulomb stresses should have increased after the first earthquake (Tibi et al., 2003). Changes in focal mechanism between the 1994 Bolivia deep-focus earthquake and aftershock suggest that the mainshock significantly changed the stress regime in the subducting slab, consistent with a near-total release of stress during the mainshock (Tinker et al.,

1995).

One striking similarity between deep and shallow earthquakes is remote triggering of earthquakes by transient stresses due to the passage of seismic waves from large earthquakes several hundred km away (Tibi et al., 2003). This triggering often takes place in regions with very low background seismicity. Just like shallow earthquakes, deep triggered events do not immediately follow the arrival of the seismic waves, but instead take minutes to hours to rupture. These observations suggest that triggered earthquakes lie within regions which are close to failure, but require transient stresses to actually fail (Tibi et al., 2003; Green, 2003).

3.4 Magnitude

3.4.1 Maximum size/rupture width

For most depth ranges within the upper mantle, the maximum size of earthquake is consistent with a single magnitude-frequency relation, such that the largest earthquakes occur in depth ranges where more earthquakes are observed. For 325–400 km and 600–700 km, the largest earthquakes are ∼0.5 magnitude units larger than predicted, but this result is not significant at the 90% confidence interval (Frohlich, 1998). The largest recorded deep-focus earthquake (M_W = 8.2; Bolivia, 1994) had an epicentral depth of ∼650 km. It had roughly equant rupture dimensions and a rupture area of about 1600 km^2 (Kanamori et al., 1998, and references therein).

The largest earthquakes tend to rupture areas with only sparse seismic activity (Lundgren and Giardini, 1994). Figure 3.2 shows the magnitude-frequency relationship for $M_W > 5.5$ earthquakes in the CMT catalogue (Dziewonski et al., 1981) between 01/1976 and 01/2011. When both shallow and deep earthquakes are included in the analysis, isolated events (those where the nearest earthquake is >50 km away) follow the same trend as the full catalogue. Deep-focus earthquakes show a deviation from this trend, with more isolated events above a given magnitude than that expected from the entire catalogue. The seven largest events remain isolated (excluding the aftershocks following the 9 June 1994 Bolivia and 19 August 2002 Tonga earthquakes) even when locations from the more complete EHB catalogue are included.

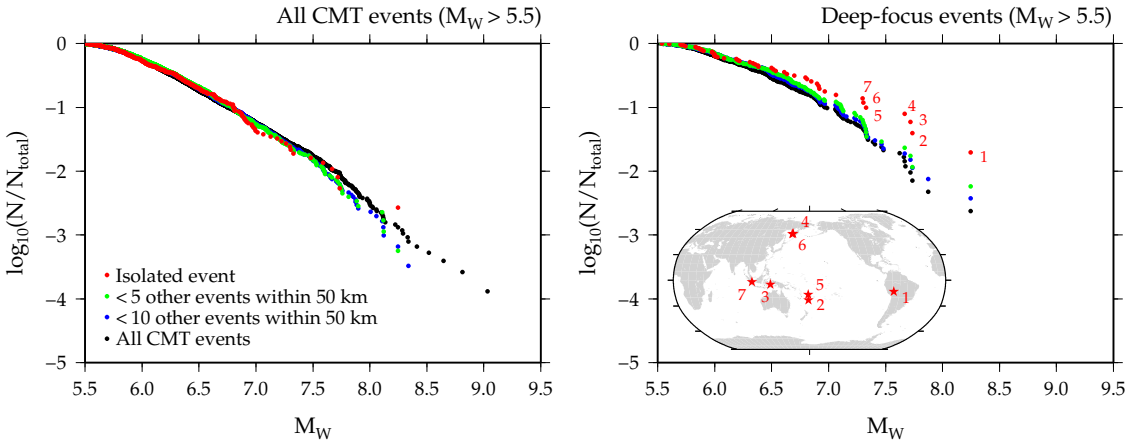

Figure 3.2: Distribution of magnitudes for a) all $M_W > 5.5$ earthquakes in the CMT catalogue (Dziewonski et al., 1981) between 01/1976 and 01/2011, and b) for deep-focus ($z > 300$ km) earthquakes only. Each point corresponds to a single earthquake. N represents the number of earthquakes with a magnitude larger than the selected earthquake. The different colours correspond to different subsets of the data. For example, black dots correspond to the magnitude distribution of the full dataset, while red dots correspond to the group of events which have no other earthquakes within a 50 km radius. The inset map in b) shows the locations of numbered earthquakes.

3.4.2 *β values*

The frequency-magnitude distribution of a group of earthquakes often approximately satisfies the Gutenberg-Richter law describing the relationship between the number of earthquakes N of a given magnitude M_W and moment magnitude M_0:

$$\log_{10} N = a - bM_W \tag{3.1}$$

$$\log_{10} N = A - \beta \log_{10} M_0 \tag{3.2}$$

The Gutenberg-Richter law is only rarely appropriate for the whole range of earthquake magnitudes in any given group. Above a magnitude M_{max}, the distribution is truncated or rolls off as a result of earthquake mechanics or the finite dimensions of the seismogenic zone. There is also a catalogue-dependent lower bound M_{uniform} below which not all earthquakes are recorded.

It has been suggested that b and β values are proxies for physical characteristics of the rock volume undergoing failure. Kanamori and Anderson (1975) suggested that the common observation that $b \sim 1.0$ arises from fault-scaling; the number of ruptures of a given magnitude that can occur on a given area of fault is controlled by the relationship between magnitude and area of faulting. Aki (1981) suggested that $b = 2D$, where D is the fractal dimension of failure (e.g., $b = 1.0$ indicates that the region of faulting is planar).

Since $M_W = (2/3) \log_{10} M_0 - 6.0$, $\beta = 2b/3$. It has been suggested that at all depths below 600 km, worldwide β values are equal to 0.60 ± 0.02 (Kagan, 1999). Nevertheless, at shallow depths, β is a function of geological environment. β values are particularly high beneath volcanic edifices

where magma chambers might be present (e.g. Wyss et al., 2001), and along creeping parts of the San Andreas fault system (Wyss et al., 2004). High β values might correspond to areas of low stress, or where stress is modified by increased pore fluid pressures (e.g. Yamashita, 1999). Both global and local catalogues have revealed that reverse-faulting earthquakes have higher β values than strike-slip events, which in turn have higher β values than normal-faulting events (Schorlemmer et al., 2005).

At intermediate depths, Frohlich and Davis (1993) and Kagan (1999) suggest that β varies little, although the Bucaramanga nest at 160 km depth beneath Colombia appears to have $\beta \sim 0.9$ (Frohlich et al., 1995). Wiemer and Benoit (1996) observe local increases in β at 90–100 km depth which they suggest might be due to dewatering.

Several studies report variations in the regional β value for deep-focus earthquakes. Beneath South America β has been found to be around 0.27, while values reach 0.81 along the Tonga-Kermadec subduction zone (e.g. Okal and Kirby, 1995). Wiens and Gilbert (1996) and Wiens (2001) suggest a correlation between high β values and low slab temperatures.

As Frohlich (2006) points out, in many cases the Gutenberg-Richter law fits the observed frequency-magnitude relationship poorly, such that the obtained values for β are dependent on the chosen values of M_{uniform} and M_{max}. Furthermore, Wyss and Wiemer (2002) show that large numbers of earthquakes are required to detect variations in β with a high statistical significance. 'Large' in this case depends on the distribution and variation in β, but for sample sizes of 50, Wyss and Wiemer (2002) show that the 5% and 95% confidence limits are separated by $\Delta\beta > 0.33$. 100 events are required to resolve $\Delta\beta \sim 0.17$ and 200 to demonstrate a $\Delta\beta \sim 0.13$.

Because the number of events below 60 km depth in most subduction zones is relatively sparse, the extent to which a global picture (e.g Kagan, 1999) obscures regional variations in β is not well constrained. Studies of individual subduction zones binned by depth may have large associated errors and may obscure along-strike variations in β.

It is straightforward to select the closest n events above a chosen M_{uniform} from an event, and find the resulting best-fitting value of β. Areas with denser seismicity can be mapped with a higher resolution than those with lower density or near the edge of a seismically active volume. To ensure that events are only considered if they have sufficient nearby events, a maximum distance can be imposed. The results of this procedure are illustrated for EHB catalogue earthquakes (Figure 3.3).

At intermediate depths beneath the Tonga-Kermadec arc, β values reach maxima of around 0.6 at 26°S and 19°S. These peaks do not mirror shallow variations in β, which reach maxima of around 0.8 at 27°S, 23–22°S and 19–16°S. West of the two more northerly shallow maxima are minima in intermediate-depth β values (~ 0.45 at around 22°S).

At greater depths, β reaches maxima of 0.8 within well-defined pockets at around 25°S and 18°S. The more southerly pocket correspond to areas where the slab may be in the process of tearing (Giardini and Woodhouse, 1984). Further north, where β values decrease to 0.5, the slab has possibly

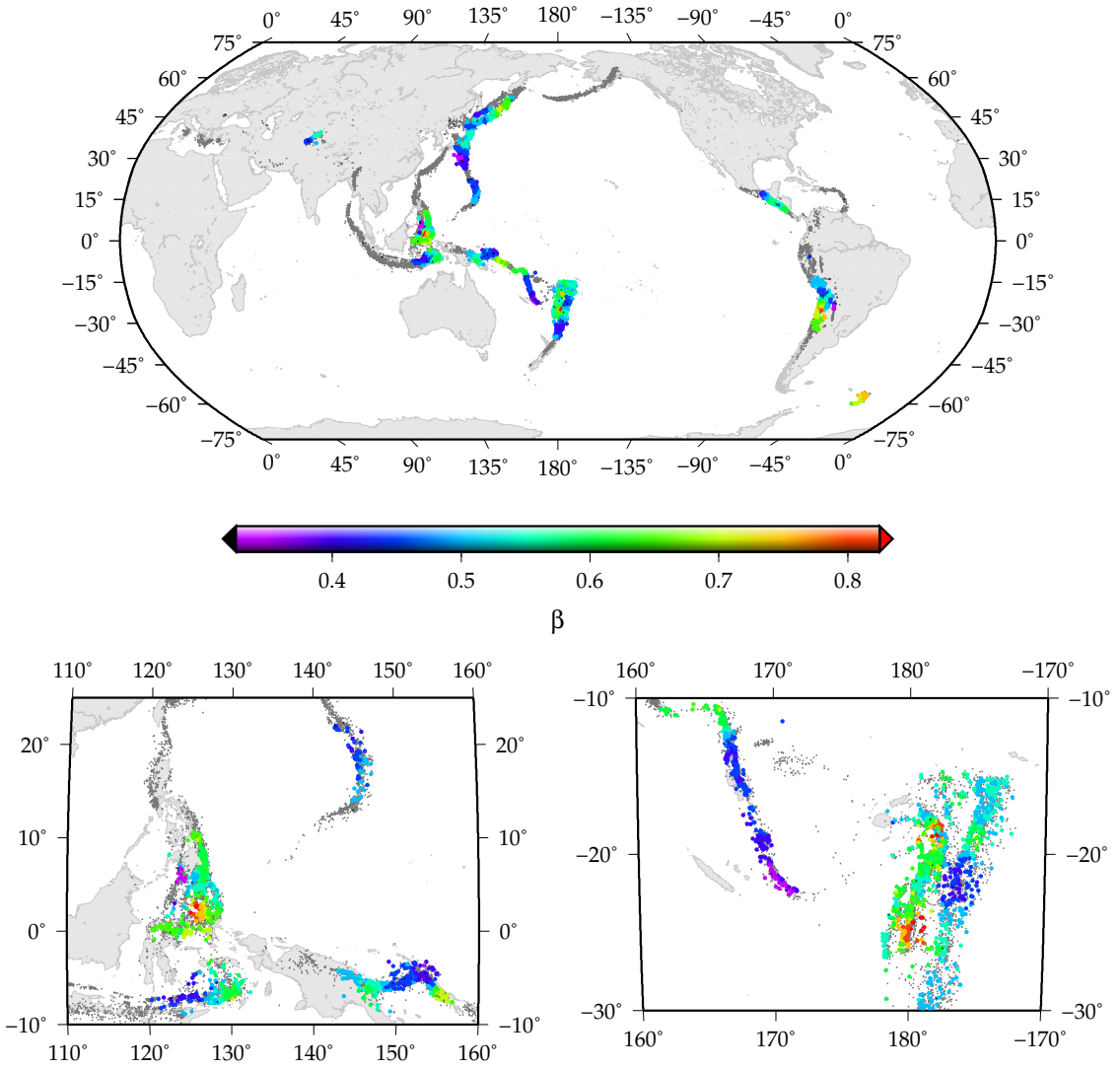

Figure 3.3: A global β value map for deep ($z > 60$ km) earthquakes (top), and further β value maps of subduction zones around the Philippines, Banda, Marianas (left) and Vanuatu and Tonga–Kermadec (right). β values calculated from the nearest 75 earthquakes in the CMT catalogue (up to a maximum distance of 500 km).

torn already. Both regions with high β values are located where the slab has the greatest concave curvature. β values approaching 0.8 are also observed in the Philippines slab within a dense group of earthquakes at around 125.5°E 2.5°N and around 110 km depth, which also corresponds to an area with high concave curvature.

Given the local variability of β values within the Tonga-Kermadec subduction zone, it is unlikely that high values derive from low slab temperatures as proposed by Wiens and Gilbert (1996). There appears to be a correlation between high β values and regions where high deformation rates are expected. Nevertheless, it is unwise to over-interpret the results presented here and in other studies, especially given the lack of understanding of the physics of variations in β, and poor fits to the proposed governing equations.

3.5 Fault plane orientations

3.5.1 Focal mechanisms

Shallow earthquakes occur on near-planar faults. Simple slip on a planar surface results in a double-couple radiation pattern, with two compressional and two extensional quadrants meeting along the intermediate (B) axis of the focal mechanism. Radiation patterns from intermediate and deep-focus earthquakes are also predominantly double-couple in nature; estimated isotropic components are generally smaller than their associated 5–10% errors (e.g. Hara et al., 1996; Kawakatsu, 1996). Compensated linear vector dipole (CLVD) components are generally small (less than 20%), but are sometimes significant (e.g. Kuge and Kawakatsu, 1993). Significant CLVD components are not necessarily evidence for a real non-double-couple component in source mechanism; they may also arise from multiple sources with different fault plane orientations (Frohlich, 1994), or by unmodelled velocity structure (e.g. Kuge and Kawakatsu, 1993; Tada and Shimazaki, 1994).

Deep earthquake focal mechanisms are often oriented such that their principal axes are aligned with the local orientation of the Wadati-Benioff zone. This observation is consistent with the hypothesis that cold slabs act as stress guides (Isacks and Molnar, 1969, 1971). In its simplest form, this hypothesis suggests that the negative buoyancy of the slab and interaction with the convecting mantle result in down-dip extensional or compressional stresses. Strain during faulting acts to relieve those stresses. Despite the success of the hypothesis in describing large scale variations in focal mechanism, deviations from the stress guide hypothesis are common. Only 30% of deep earthquakes have strike-parallel B-axes and down-dip P- or T-axes (Apperson and Frohlich, 1987). For a more detailed review and assessment of focal mechanism orientations, see Chapter 5.

Focal mechanisms have also been used to argue for large active shear zones in the mantle. When earthquakes are projected perpendicular to the B-axis of the earthquake focal mechanism, fine lineations or thicker bands of earthquakes can sometimes be seen parallel to one of the nodal planes of the mechanism (Giardini and Woodhouse, 1984; Lundgren and Giardini, 1992). This observation is revisited in Chapter 6.

3.5.2 Directivity, rupture velocity and fault plane identification

The waveforms of small earthquakes can be modelled by rupture of a point source. For earthquakes with $M_W \gtrsim 5.7$–6.0, teleseismically-recorded waveforms deviate significantly from those expected of a single point source. Rupture propagation along a fault plane results in a Doppler-shift effect, whereby apparent source durations along ray paths parallel to the average rupture direction are shorter than those in other directions. This enables the distribution of energy release and velocity of rupture propagation to be determined. Inversion for peaks in moment release (e.g. Chen et al., 1996;

Antolik et al., 1999; Wu and Chen, 1999; Tibi et al., 1999, 2002, 2003; Park and Mori, 2008) are used to determine the characteristics of rupture.

The speed of rupture V_R varies significantly from deep earthquake to deep earthquake, with a range of at least 20–80% of the local shear wave speed V_S (Lundgren and Giardini, 1995; Park and Mori, 2008, Chapter 7). There are no published examples of deep earthquake rupture exceeding V_S. Although Tibi et al. (2003) suggest that there is a correlation between slab temperatues and rupture velocities, the result is not yet conclusive, especially when outliers such as the fast ($V_R \sim 0.65\ V_S$) 1991 Argentinian event and slow ($V_R \sim 0.20$–$0.40\ V_S$) Japanese deep-focus earthquakes (Park and Mori, 2008) are taken into account.

Some studies have reported consistent directions of rupture relative to the surface of the slab. A study of six $M_W > 7.0$ intermediate-depth earthquakes found a preference for along-strike rupture propagation (Tibi et al., 2002), which presumably reflects a small seismogenic or stress regime width compared to the total area of rupture required for such large events. A more complete study of smaller earthquakes found a preference for intermediate-depth earthquakes beneath Middle America to rupture away from the surface of the slab (Warren et al., 2008).

Rupture modelling of large earthquakes usually requires modelling of slip in two dimensions, but the grid size and large freedom of such inversions is not conducive to studying smaller earthquakes ($M_W \lesssim 7.0$). An alternative approach is to model rupture along a line. The ability to analyse smaller earthquakes enables the construction of larger datasets that can be used to assess the statistical significance of observed patterns in faulting behaviour (Warren and Silver, 2006). Studies on Middle America and Tonga-Kermadec earthquakes show that at intermediate depths, near-horizontal planes are responsible for the majority of seismic activity (Warren et al., 2007, 2008). Deep-focus events beneath Tonga occur on both planes (Warren et al., 2007). A systematic study of earthquakes in the Izu-Bonin-Marianas subduction zone system can be found in Chapter 7.

3.6 Tomography

3.6.1 Large scale velocity structure

Cold subducting slabs have increased body wave velocities and low attenuation (high-Q) relative to the convecting mantle. Under equilibrium conditions, velocities will increase continuously toward the coldest parts of the slab, with somewhat lower velocities in the subducting crust. However, within the slab core, reaction rates might be sufficiently slow that the lowest energy assemblage isn't maintained. A considerable quantity of olivine could exist metastably within the mantle transition zone if slab temperatures and strain rates remain low. Published studies vary in their estimates of conditions required for preservation of metastable olivine, but several groups suggest that reaction rates are sluggish below ~600–750°C. Lower velocities are expected where metastable olivine is

present.

Koper et al. (1998) suggested that travel time data alone is unable to resolve a metastable olivine wedge, at least for the case of the Tonga slab, without modelling waveforms or the differential times between the P wave and later arrivals within the coda created by the wedge. Nevertheless, travel time residuals for 1D (Iidaka and Suetsugu, 1992) and 3D (Jiang et al., 2008; Jiang and Zhao, 2011) velocity models have been used as evidence for a metastable wedge. Jiang and Zhao (2011) used double difference relocation on 78 earthquakes, and a model assuming a constant slab velocity anomaly of 2%. They found that the RMS travel time misfit was reduced by a small amount ($<$0.1 s) by modelling the slab with a wedge with velocity 1–2% slower than the surrounding aesthenosphere, consistent with the presence of metastable olivine. However, the effects of systematic errors in earthquake location (e.g. Syracuse and Abers, 2009) were not assessed. Nor were the effects of incorporating crust and mineral reactions within the mantle sequence.

Kaneshima et al. (2007) studied arrivals within the P wave coda from deep-focus Marianas earthquakes. They used differential travel times to infer a 5% P-wave velocity reduction within a 25 km thick wedge dipping at $\sim$60° within the Marianas slab. Neither the data nor the distance versus differential travel time plots are particularly convincing. Furthermore, since the earthquakes in this region are consistent with a slab dip of $\sim$90°, it is unclear why a wedge with dip $\sim$60° would best fit the data.

Receiver functions have also been used to reveal fine subduction zone velocity structure. Kawakatsu and Yoshioka (2011) conducted vectorial receiver function analysis on waves travelling beneath south-west Japan. At around 400km depth, their RF image the positive ΔV_S '410 km' discontinuity above the slab, followed by a negative ΔV_S, a positive ΔV_S and then a final negative ΔV_S nearly parallel to the surfaces of the slab. Kawakatsu and Yoshioka (2011) compare the locations of these jumps to the JMA seismicity catalogue. They propose that the central negative and positive velocity jumps correspond to the boundaries of metastable olivine in the core of the slab. It is worth noting that their analysis also reveals a negative-positive-negative jump at the '660 km' discontinuity, although only a positive jump should be expected. It is unclear whether the flanking velocity changes are artefacts, or represent real phase-boundary complexity.

Receiver functions have also been used to attempt to resolve compositional changes near the slab-mantle wedge interface. Tonegawa et al. (2008) observed a narrow, prominent low velocity zone above the subducting slab. They argued that this observation can be explained by hydrous minerals entrained along the slab interface.

Polarity reversals in PP precursors resulting from reflections near the '410 km' discontinuity are observed near the Kuriles slab (Schmerr and Thomas, 2011). The impedance drop could imply the presence of metastable olivine, but the Fresnel zones of PP precursors are large, and Schmerr and Thomas (2011) do not observe other indicators of a metastable wedge, such as strong variations in

amplitude and reflector depth.

Two studies report anisotropy in slabs in the mantle transition zone (Iidaka and Obara, 1997; Chen and Brudzinski, 2003). Iidaka and Obara (1997) report shear wave anisotropy in the coldest part of the Izu slab. Chen and Brudzinski (2003) find $V_{SV} < V_{SH}$ in the stagnant slab beneath Fiji. The slab beneath Fiji (north of 22°S) also has a low velocity anomaly of ∼3% in both V_P and V_S (Brudzinski and Chen, 2000; Chen and Brudzinski, 2001; Brudzinski and Chen, 2003).

3.6.2 *Waveguide vs. anti-waveguide*

Elongated or tabular high velocity bodies such as subducting slabs act as anti-waveguides (Vidale, 1987), dispersing seismic energy and causing waveform broadening. The P-wave velocities expected within subducting slabs are up to 10% higher than in the surrounding mantle (Helffrich et al., 1989). Subducting slabs are also high-Q paths, such that seismic waves travelling for long distances inside the slabs will arrive earlier and have greater higher frequency content than would be expected for waves travelling through the aesthenosphere. Early, high-frequency arrivals are observed at stations in New Zealand, which is situated ideally to detect energy from Tonga-Kermadec earthquakes which has travelled along large sections of the subducting slab (Ansell and Gubbins, 1986). These arrivals can be explained by P-wave velocities 4-5% faster than ambient mantle to 300 km and 2% faster to 600 km depth (van der Hilst and Snieder, 1996). Gubbins and Snieder (1991) suggest that the dispersion is most easily matched by a gradual increase in velocity within the slab overlain by a 6–15 km thick even higher velocity layer, which they equate to the oceanic crust.

Opposing the dispersive effect of the high velocity slab, a low velocity metastable olivine wedge would act as a waveguide. Koper and Wiens (2000) compute synthetics for 2D slab models incorporating such a wedge, and show that the signature of the guided energy should be detectable at some stations. A search for a metastable wedge within the Tonga slab failed to observe either late arrivals or evidence of the expected guided energy (Koper et al., 1998).

3.6.3 *Small scale velocity anomalies*

The extremely dense network of stations above the Japan slab allows the resolution of features too small to be observed in other subduction zones. Nakajima et al. (2009) observe low velocity zones around the lower plane of the double seismic zone, and between the two planes around the rupture area of the 1993 Kushiro-Oki earthquake. They interpret this decreased velocity as evidence for hydrated mantle material. Reynard et al. (2010) point out that the V_P decrease in the lower seismic zone is greater than the V_S decrease, and that the region between the two planes of seismicity isn't generally slower than the deeper mantle, as would be expected for a slab with decreasing levels of hydration with increasing depth. They suggest that the velocity anomalies result from

anisotropy of anhydrous olivine and pyroxene with strong lattice preferred orientations. Yet other intermediate earthquakes do occur in regions with pronounced V_S decreases (Nakajima et al., 2011). These observations are discussed in more detail in Chapter 8. More work needs to be done to resolve the respective roles of anisotropy and thermochemical heterogeneity in producing velocity anomalies.

3.7 Discussion

Almost none of the observations listed in this chapter have an interpretation in the published literature that is unanimously agreed on. For example, the distribution of deep earthquakes has been interpreted as evidence for a weak slab (Tao and O'Connell, 1993), strong slab (Alisic et al., 2010), wet (Omori et al., 2004) or dry (Green et al., 2010) slab. It has been proposed that subhorizontal fault plane orientations are indicators of 'isobaric rupture processes' (Antolik et al., 1999), fluid flow (Kiser et al., 2011) and slab deformation (Suzuki and Kasahara, 1996). Low velocity zones have been interpreted variously as evidence for metastable olivine (Brudzinski and Chen, 2003) or hydrous Phase D (Mainprice et al., 2007; Rosa et al., 2011).

At least some of the uncertainty in interpretations of deep earthquake behaviour is the result of small sample sizes. This is especially true of comparisons of earthquake behaviour in different subduction zones. For example, the statement that earthquakes in cold slabs have more aftershocks (Wiens and Stein, 1983; Tibi et al., 2003) may ultimately be proven true, but requires a much larger dataset, especially given the importance of just a few earthquakes in making these conclusions.

The following chapters present several new observations relating to deep earthquakes, and provide a foundation from which a consistent picture of earthquake mechanics and geodynamics can be constructed.

Part II

Focal mechanisms and seismic structure

4 *Waveform similarity*

4.1 Introduction

It has been known for some time that multiple earthquakes can produce similar P-coda waveforms recorded by a single seismometer. This similarity arises only when the focal mechanisms and source-time functions of the earthquakes are comparable, and when hypocentral locations are sufficiently close that scattered waves travel along almost identical paths (Geller and Mueller, 1980; Poupinet et al., 1984).

Similar earthquake waveforms have been shown to originate in a multitude of settings, including along oceanic transform faults (Jordan and Sverdrup, 1981), continental faults (e.g. Waldhauser and Ellsworth, 2002), in volcanic regions (Slunga et al., 1995; Got et al., 1994) and at shallow levels within subduction zones (Igarashi et al., 2003). Large scale relocations have been conducted on such earthquakes (Shearer et al., 2005; Waldhauser and Schaff, 2008) using waveform similarity to improve time delay estimation. Local studies have reported streaks of microearthquakes sub-parallel to the slip vector on faults beneath Kilauea, Hawaii, and along the Calaveras Fault, California (Wolfe et al., 2007; Got et al., 1994; Rubinstein and Beroza, 2007; Rubin et al., 1999). Streaks and earthquake multiplets are also observed in Parkfield microseismicity, along with 'holes' where microearthquakes are not observed (Waldhauser et al., 2004). Seismically defined lineations and detailed fracture patterns have also been observed in a geothermal system (Moriya et al., 2003).

Although most of the above studies are local or regional in scale, teleseismic studies have also revealed a diversity of tectonic environments under which earthquakes producing similar waveforms may be observed. A study of seismicity in China suggests that earthquakes with similar coda waveforms may constitute around 10% of all shallow seismicity (Schaff and Richards, 2004). Similar waveforms have also been reported from intermediate (60 km $<$ hypocentral depth $<$ 300 km) and deep-focus earthquakes (hypocentral depth $>$ 300 km) within subducting slabs (Isacks et al., 1967; Wiens and Snider, 2001; Zhang et al., 2008). Deep-focus earthquake multiplets have been shown to

This chapter is a modified version of the main text from Myhill et al. (2011).

lie along subplanar features (Wiens and Snider, 2001), and may represent repeated rupture on the same fault plane. It has been suggested that short repeat times observed between similar earthquakes implicate shear instabilities as the mechanism behind deep-focus earthquakes (Wiens and Snider, 2001), which occur at pressures thought too high to allow brittle failure in dry rocks.

In addition to helping determine the mechanics of faulting, earthquakes with similar waveforms have been used as repeating sources to monitor temporal variations in crustal velocity (e.g. Poupinet et al., 1984, 2008), and to evaluate the possibility of inner core rotation (e.g. Zhang et al., 2008). The latter studies are potentially flawed, since the earthquakes are used as 'repeating' events without a rigorous assessment of interevent distances.

In this study, we investigate Tonga-Kermadec and Vanuatu subduction zone earthquake P-coda waveforms using a cross-correlation technique and hierarchical clustering algorithm. We determine the distribution of earthquakes producing similar waveforms, and use array data to analyse the origin of the P-wave coda. We also discuss the causes of waveform similarity at teleseismic ranges.

4.2 Data selection and processing

4.2.1 Station and event selection

In order to analyse waveform similarity recorded by stations at different ranges from studied earthquakes and in various geological environments, I have chosen 28 stations with high signal to noise ratios for events within the Southwest Pacific (Figure 4.1 and Supplementary Table 1). These include MSVF, an ocean island station on Fiji, which has relatively high background noise but also high signal amplitude due to its proximity to the study area. Continental stations are also included, such as WRAB in Northern Australia, which has high signal to noise ratios despite being positioned some 5000 km epicentral distance from deep events beneath Fiji.

I processed broadband waveforms for 9951 earthquakes from a region encompassing the Tonga-Fiji-Kermadec and Vanuatu subduction zones as listed in the Engdahl, van der Hilst and Buland (EHB) catalogue (Engdahl et al., 1998, and updates) between January 1994 and October 2007. The analysed earthquakes include 2270 intermediate focus events and 3761 deep-focus events. Preliminary phase picks were assigned according to EHB locations and the IASPEI91 Earth model (Kennett and Engdahl, 1991). Specific events are referred to by their EHB origin times (YYYYJJJHHMMSS).

4.2.2 Cross correlation

To determine the distribution of earthquakes producing similar teleseismically-observed waveforms, the waveform cross correlation methods chosen should be capable of identifying as many similar waveforms as possible. A couple of aspects of the teleseismic waveforms studied are relevant to this choice. Firstly, much of the high frequency power originally present in the waveforms has been

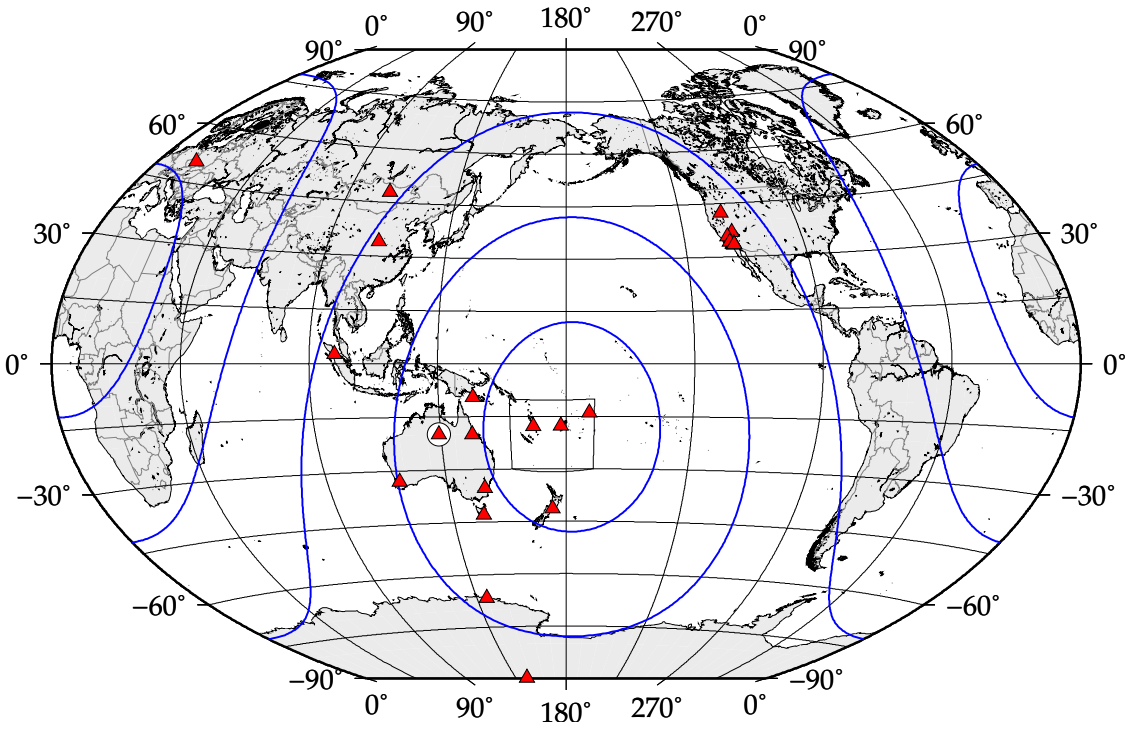

Figure 4.1: Stations selected for waveform analysis are plotted as triangles. The white circle represents the location of the Warramunga arrays used in the beamforming analysis. The black box outlines the study region. Lines are drawn at 30° intervals from 18°S 178°W.

lost via attenuation along the ray path. Secondly, a large number of analysed earthquakes have M_b ~4.5–5.0, for which signal to noise ratios are commonly low. A significant fraction of waveform noise is in the same frequency band as the signal. There are therefore often large stretches of the P-wave coda where the signal is indistinguishable from the noise, regardless of the choice of prefilter.

The properties of the waveforms analysed place constraints on the optimal cross correlation method. To assess similarity between waveforms with variable and often low signal to noise ratios, an appropriate method should:

- Reduce the reduction in cross correlation coefficient caused by noise
- Downweight short duration reductions in waveform similarity (occasional high amplitude noise)
- Upweight the effect of waveform similarity on correlation coefficients at low amplitudes if the signal to noise ratio is high

The second and third points are more easily satisfied in the time domain than the frequency domain. The time series amplitudes are interpolated to yield a uniform sampling frequency of 100 Hz, and band-pass filtered between 1 and 5 Hz. The time-domain cross correlation function $R\left(t, t_w, t_s\right)$ between two waveforms i and j with amplitudes $u(t)$ over a time window of length $2t_w$ is defined as

$$R\left(t, t_w, t_s\right) \equiv \frac{\langle u_i(t) u_j(t+t_s)\rangle}{\left(\langle u_i^2(t)\rangle \langle u_j^2(t+t_s)\rangle\right)^{1/2}} \tag{4.1}$$

where t_s is a time delay imposed on waveform j, and the angle brackets $\langle\rangle$ denote the time average over the employed time window. The reduction in cross correlation function due to noise can be partially negated by using the method of Snieder and Vrijlandt (2005) and Douma and Snieder (2006). A corrected cross correlation function

$$R_{corr} \equiv \frac{\langle u_i(t) u_j(t+t_s)\rangle}{\left(\left(\langle u_i^2(t)\rangle - \langle n_i^2(t)\rangle\right)\left(\langle u_j^2(t+t_s)\rangle - \langle n_j^2(t+t_s)\rangle\right)\right)^{1/2}} \tag{4.2}$$

can be constructed by estimating noise levels (n_i) from 8 second windows starting 16 seconds prior to the direct P arrivals for each waveform.

The cross correlation coefficient is defined as the maximum value of the cross correlation function. I obtain t_s ($|t_s| < 4$ s) by maximising the cross correlation coefficient from a single time window of 44 seconds, starting 4 seconds before the predicted P-wave arrival.

To increase the contribution of waveform similarity from low amplitude parts of the P-coda waveform, a mean cross correlation coefficient is derived from coefficients calculated for 4 second windows offset by 0.05 seconds across the first 44 seconds of the P-coda waveform. The single-window estimate of t_s is used throughout. In other words, the short windows are used only as a means of separating parts of the waveform with differing signal to noise ratios.

4.2.3 Clustering

Large numbers of waveforms recorded at a single station may be grouped based on their cross correlation coefficients by a spectrum of different schemes. To analyse waveform similarity, all events within a single group should share some characteristic properties. Single linkage clustering schemes (where clusters are created by successively linking the two unlinked waveforms with the highest value) is therefore inappropriate, since such schemes are prone to the formation of large clusters with dissimilar waveforms connected by a long series of intermediate links. I have used an agglomerative, dendrogram-based hierarchical pair-group clustering algorithm (e.g. Lance and Williams, 1967; Sneath and Sokal, 1973; Ludwig and Reynolds, 1988; Rowe et al., 2002), which successively 'fuses' pairs of elements (single waveforms or groups of waveforms) into a new element. The similarity values associated with the pair of elements is used to assign a new value to the fused element. The algorithm and equation which governs how the similarity values are calculated at each step are

detailed fully in Appendix A. More information on hierarchical clustering strategies may be found in Rowe et al. (2002).

The dendrogram resulting from the clustering algorithm can be used to find groups of waveforms linked above a given similarity value. A lower bound on this value can be estimated from the maximum cross correlation coefficient achieved between waveforms from distant events. Coefficients obtained between waveforms from south (latitude $< 21.50°$S) and north (latitude $> 19.00°$S) deep-focus Tonga-Fiji-Kermadec events are rarely greater than 0.6 and do not exceed 0.7. Above this value, the exact choice determine the level of similarity between the waveforms (and therefore the source characteristics of the earthquake). We have chosen a value of 0.85, since smaller values produce clusters which include noisy records where signal similarity cannot be clearly observed.

Groups of earthquakes are commonly referred to as clusters if they have similar waveforms. The use of the term cluster in this context is not ideal, since spatially or temporally clustered earthquakes need not have similar waveforms. Cluster analysis strictly refers to the process of grouping similar data, in this case waveforms. We therefore refer to events grouped on the basis of waveform similarity at one or more stations as 'multiplets', rather than 'clusters'.

4.3 Results

4.3.1 Similar waveforms

The results of waveform clustering are shown for waveforms from earthquakes located around 18°S 178.2°W (Figures 4.2 and 4.3), and around 21.9°S, 179.4°W (Figure 4.4), recorded at the station WRAB in north central Australia. Waveforms within single clusters can have a range of magnitudes (from $M_b = 3.6 - 5.2$ in one case).

Waveforms within single clusters are not identical. This is illustrated by the difference between the linear cluster stack and the individual waveforms, which reveals a distinct increase in power at the time of the initial P-arrival. The power spectral density of this difference is of higher frequency than that of the original waveforms (see supplementary materials of Myhill et al., 2011), indicating that the high frequency signal contains most information regarding source differences. The exact nature of these differences is beyond the scope of this work, but is presumably dominated by differences in source properties. The shape of the power spectral density curve does not appear to depend upon earthquake magnitude.

Groups of waveforms recorded at one station usually share members with those recorded at others, but groups recorded at different stations are rarely identical. For example, 47 waveforms recorded at the station TAU cluster above a similarity value of 0.85, whilst 114 recorded at CAN cluster above that value, and 280 at WRAB (Figure 4.5). Gaps in the recording history and differences in signal to noise ratio will evidently preclude identical clustering behaviour in some cases. However,

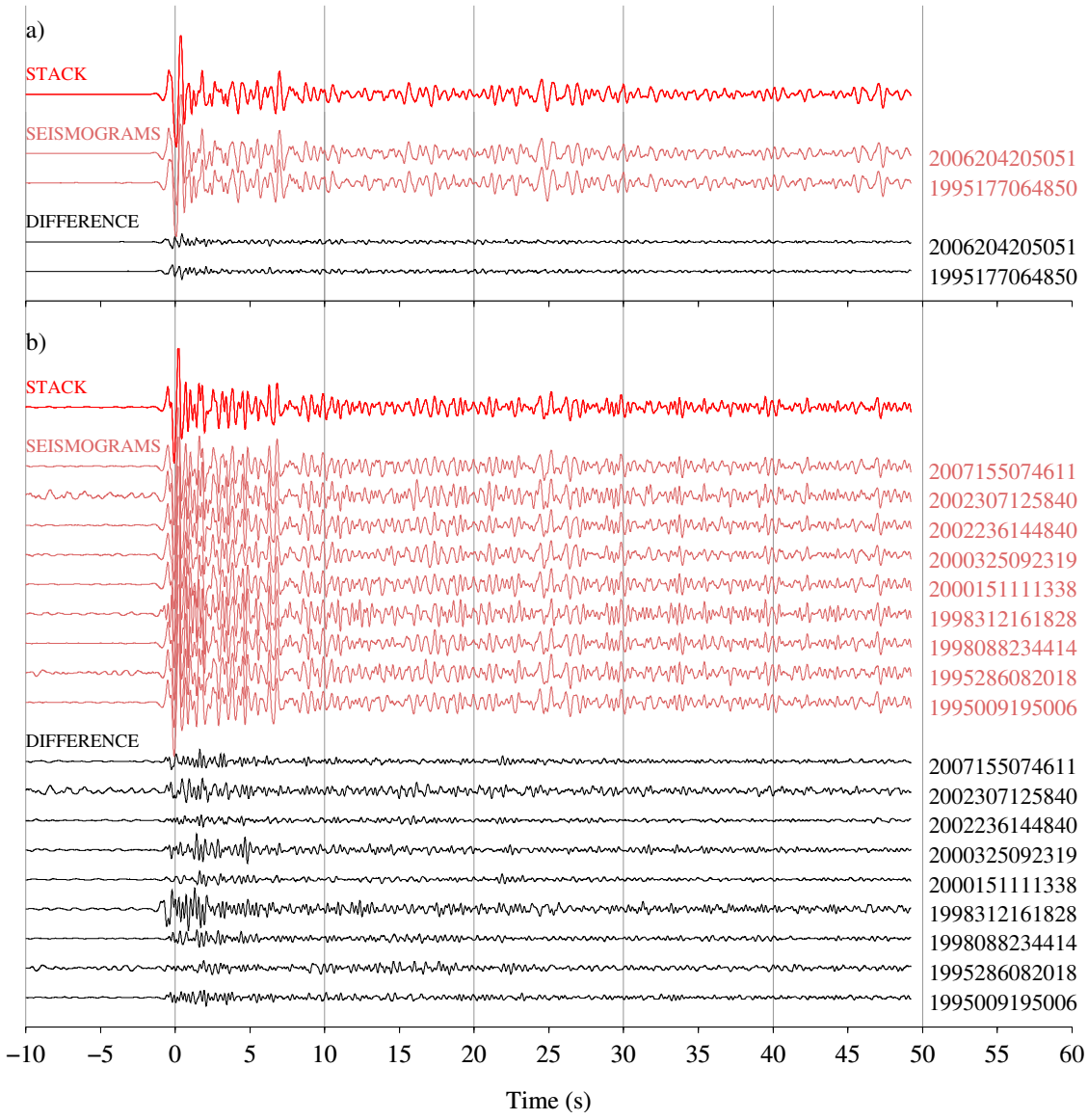

Figure 4.2: Waveforms recorded at the station WRAB and clustered into two groups according to the algorithm detailed in the text. Time zero is aligned on the predicted P-wave arrival time for the first event based on the EHB location and IASPEI91 Earth Model. The events producing these waveforms were located at around 18°S 178.5°W. a) Waveforms from two magnitude 5+ events. Top: A linear stack of all the records, stacked after normalising the amplitudes. Middle: Filtered records, normalised to the maximum amplitude of each record. Bottom: The difference between each seismogram and the linear stack, plotted using the same normalisation factor as the filtered records. b) Waveforms from part of a large group of events with similar waveforms. Traces arranged as in a).

differences in the nature of scattering will also contribute to the difference in cross correlation values. Furthermore, similarity will also depend on the parts of the focal sphere sampled by the waveform ray paths. If the station is positioned such that rays pass near one of the nodal planes of the focal mechanism, even small changes in focal mechanism between events will result in dissimilar P-coda waveforms. When rays leave the focal sphere close to the P and T-axes, variations in focal mechanism can be larger without significantly affecting the P waveform.

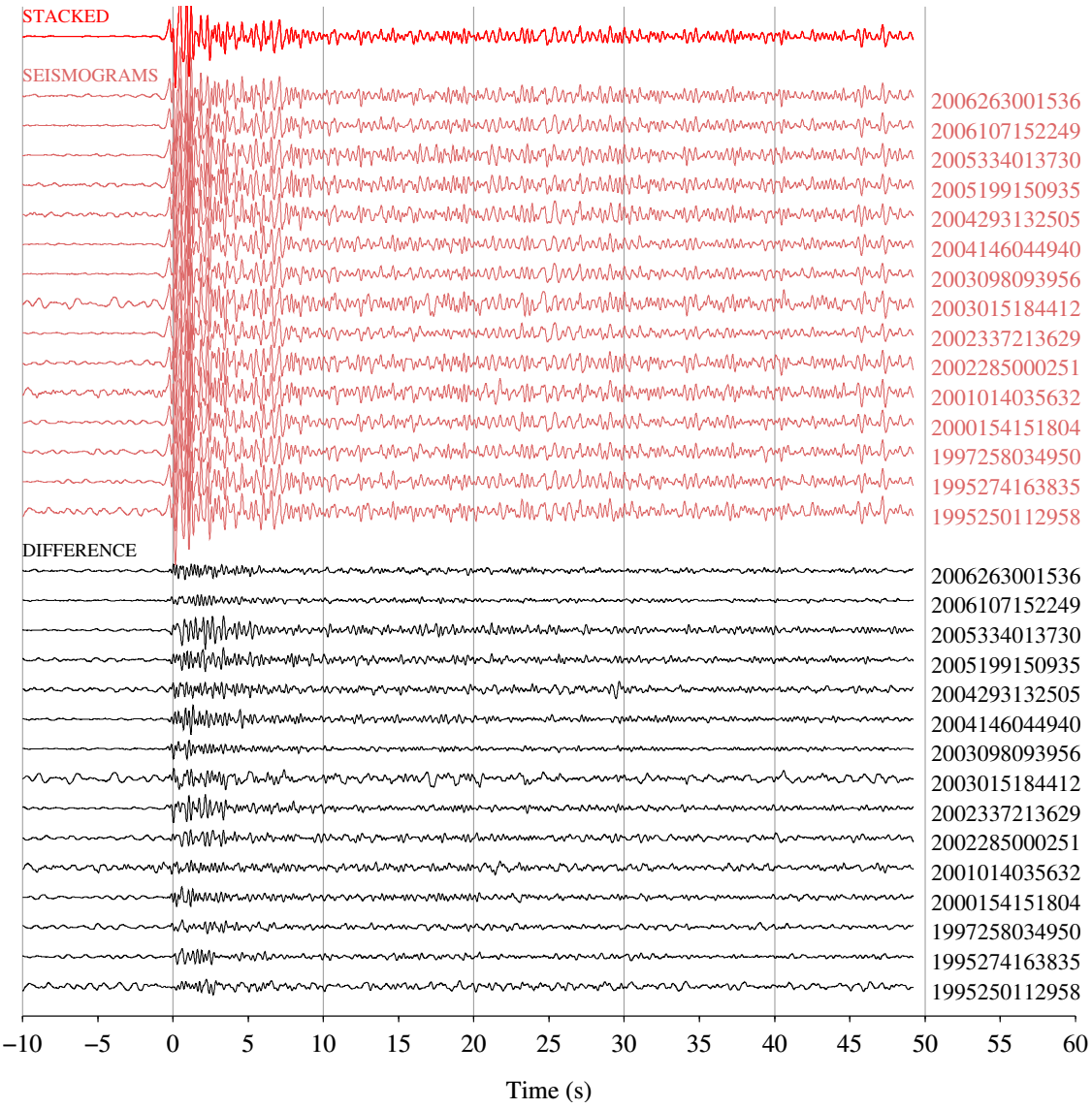

Figure 4.3: Similar waveforms recorded at the station WRAB from a cluster situated at around 575 km depth at the northern end of the Tonga-Fiji-Kermadec subduction system. These events clustered above a cross correlation coefficient cut-off of 0.85. Traces are plotted and scaled as in Figure 4.2a.

4.3.2 *Origin of coda waveform similarity*

A better understanding of teleseismic coda waveform similarity is required before analysing the spatial and temporal distribution of earthquake multiplets. The results of Wiens and Snider (2001) illustrate that the presence of similar teleseismic waveforms does not preclude event separations of 30 km or greater. An obvious reason for this is that scatterers contributing significant amounts of energy to the coda waveforms are not evenly distributed around the source. In fact, Randall and Owens (1994) suggest that the P-wave coda from deep events is predominantly composed of energy scattered near to the receiver.

One way of analysing the effect of near-receiver scattering is to use an array to determine the directionality of incoming energy (Green et al., 1966). Broad-band frequency-wavenumber spectrum

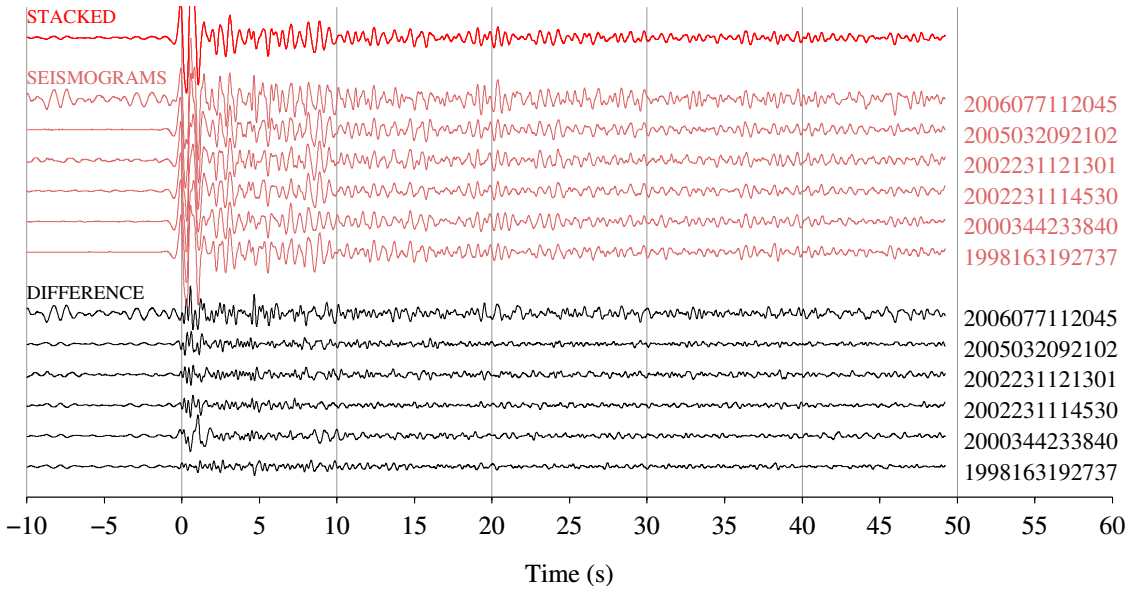

Figure 4.4: Similar waveforms recorded at the station WRAB from part of a cluster situated at around 590km depth in the central region of the Tonga-Fiji-Kermadec subduction system at around 21.9° S. These events clustered above a cross correlation coefficient cut-off of 0.85. Traces are plotted and scaled as in Figure 4.2a.

analysis (BBFK) (Nawab et al., 1985) allows the power spectrum of the waveforms at an array to be visualised in terms of back azimuth and radial wavenumber of the incoming energy. This is illustrated for an M_b 5.6 deep-focus earthquake in Figure 4.6. The analysis uses waveforms recorded by the Australian Warramunga arrays (WB, WC and WR) positioned close to station WRAB (Figure 4.1). Coherent energy from the source is observed throughout the P-coda and into the pP-coda, although the power of this energy decreases significantly after the initial arrival. Waveforms from smaller events produce a similar pattern, although coherent energy is often lost within certain sections of the coda. The decrease in power after the initial arrival is much greater than that expected if all the coda waveform energy originated from near-source.

By directing the array beam (Green et al., 1966) along the ray path of the P-arrival, we can remove much of the incident energy from scatterers located close to the array. We repeated our similarity analysis on beamforms constructed from deep-focus waveforms recorded by the Warramunga arrays between February 2005 and October 2007. Seven doublets and one triplet of beamed waveforms exhibit cross correlation values above 0.7; three doublets above 0.85. In contrast, the same group of earthquakes yield five doublets and two triplets with cross correlation values above 0.85 prior to beamforming at the nearby station WRAB. The pair of events with the highest beamform cross correlation coefficient occured almost two years apart (2005149093445 and 2007137121252). The appearance of the beamed waveforms differs from that observed prior to beamforming (Figure 4.7). As expected from the BBFK analysis, much of the power in the raw P-wave coda is lost on beamforming, suggesting that most of the incident energy is scattered through large angles close to the receiver.

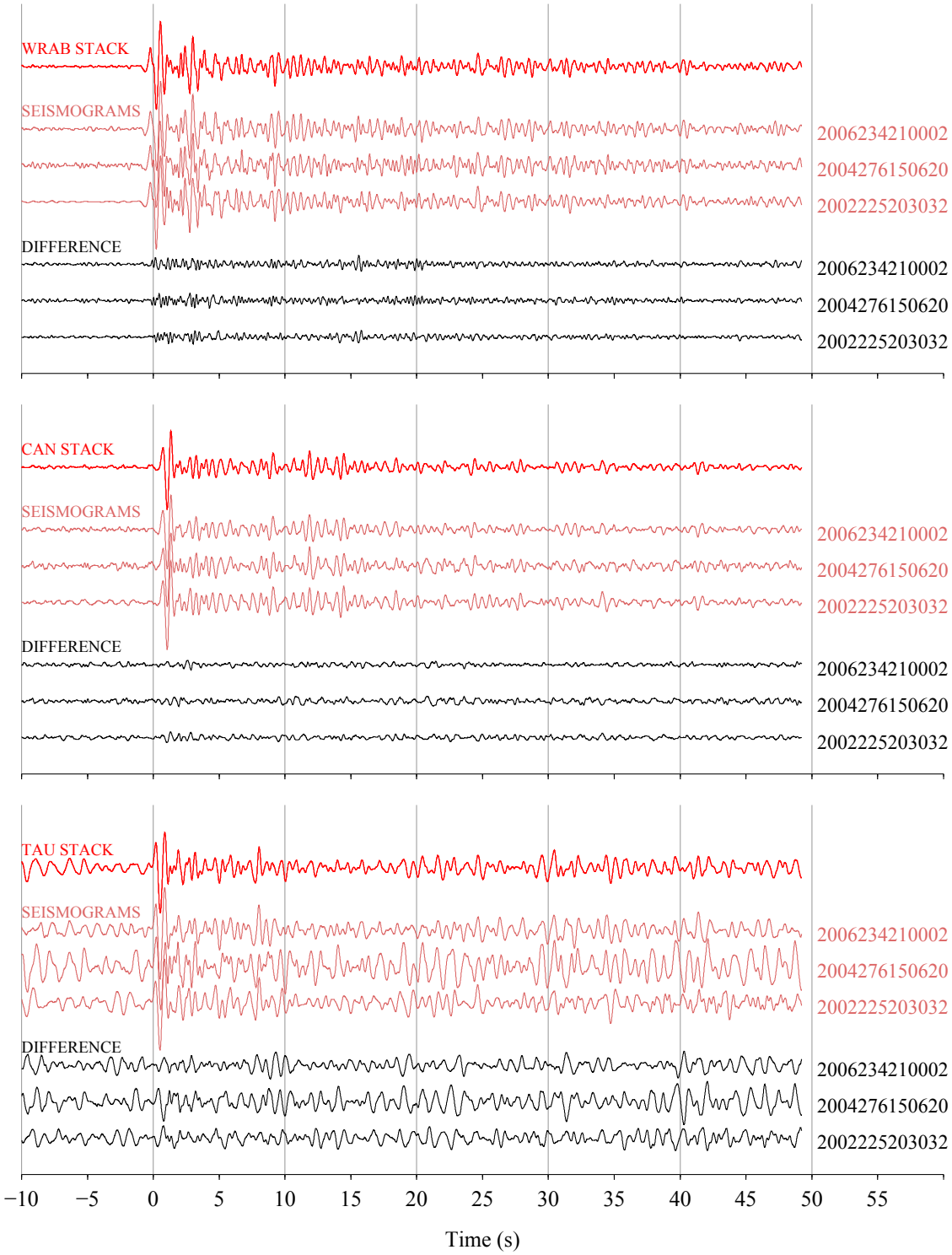

Figure 4.5: Waveforms for three events recorded at the stations WRAB (top), CAN (middle) and TAU (bottom). These events cluster above a coefficient cutoff of 0.85 at both WRAB and CAN. Although our noise-corrected cross-correlation procedure is effective for relatively low levels of noise, at higher levels waveform similarity cannot be discerned. High noise levels at TAU are thus a possible reason for failure of the triplet to cluster above a cutoff of 0.33. Traces are plotted and scaled as in Figure 4.2.

The beamform in Figure 4.7 does not necessarily reflect the form of the P-coda wavetrain as it left the source region. Scatterers will add to coda complexity along the entirety of the ray path; some of the power in the beamform coda may originate from scattering at the 410 and 660 discontinuities, in

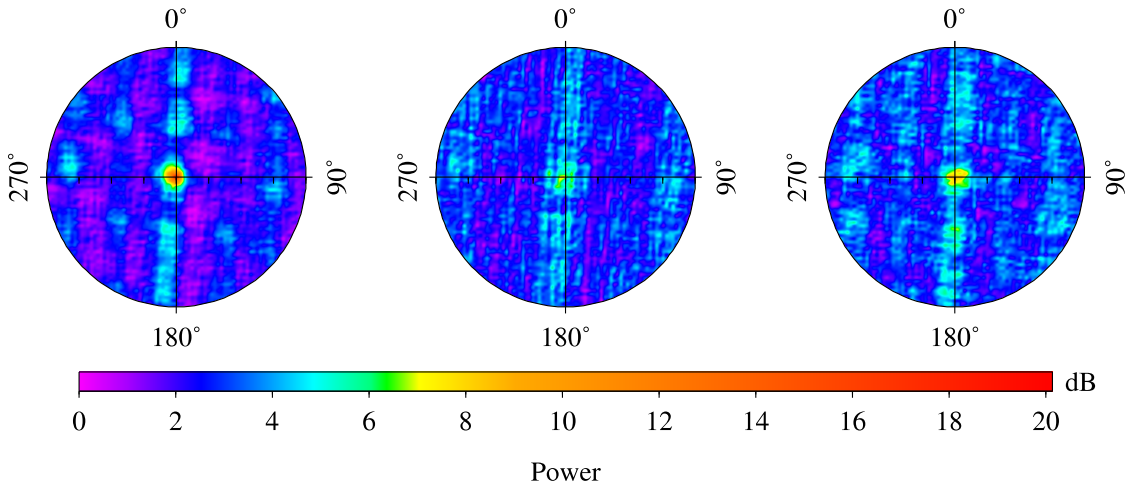

Figure 4.6: Broad-band frequency-wavenumber spectrum analysis on event 2006204205051, for the Warramunga Arrays WR, WA and WB. The array waveforms for frequency wavenumber analysis were first aligned on the arrival time of P at each of the array stations, as estimated using the IASP91 Earth model and EHB location. Energy coming directly from source should therefore be apparent as a high power signal in the center of the diagrams. The outer edge of the diagrams correspond to a wavenumber of 1. From left to right: Analysis of 0–10 seconds, 20–30 seconds and 40–50 seconds after the direct P-arrival. All three time windows are well before the pP arrival. The central figure shows a loss of coherent energy direct from source despite significant overall coda energy, indicating that some coda similarity arises from near receiver scattering.

addition to other interfaces between the source region and crust and uppermost mantle beneath the receiver.

The importance of receiver side scattering in creating the P-coda indicates that little information regarding source separations is contained in the P-coda, other than that pertaining to differences in the ray path take-off angle. Teleseismic waveform similarity is instead a better indicator of similar focal mechanisms and rupture propagation characteristics.

4.3.3 The distribution of earthquake multiplets beneath the Southwest Pacific

The spatial distribution of analysed earthquake multiplets is nonuniform. Figure 4.8 illustrates the locations of multiplets obtained using the chosen similarity value (0.85) on waveforms recorded at station WRAB. The locations correspond to the centroid of event positions as recorded in the EHB catalogue.

Perhaps the most striking feature of Figure 4.8 is the marked increase in the density of multiplets at 0–60 kilometers and again at 520–620 kilometers depth within the Tonga-Fiji-Kermadec Slab. Scattered multiplets are also observed at around 150 kilometers depth within the Vanuatu region, and in several more isolated regions, including beneath the Kermadec Arc towards the south of the study area and within a finger of outboard deep-focus earthquakes at ∼600 km depth to the east of the Vanuatu Arc (labelled in Figure 4.8). These events may have occurred within a stagnant slab subducted 5–8 Myr ago (e.g. Chen and Brudzinski, 2001).

Zones with a high density of multiplets also have a high overall density of earthquakes. It is

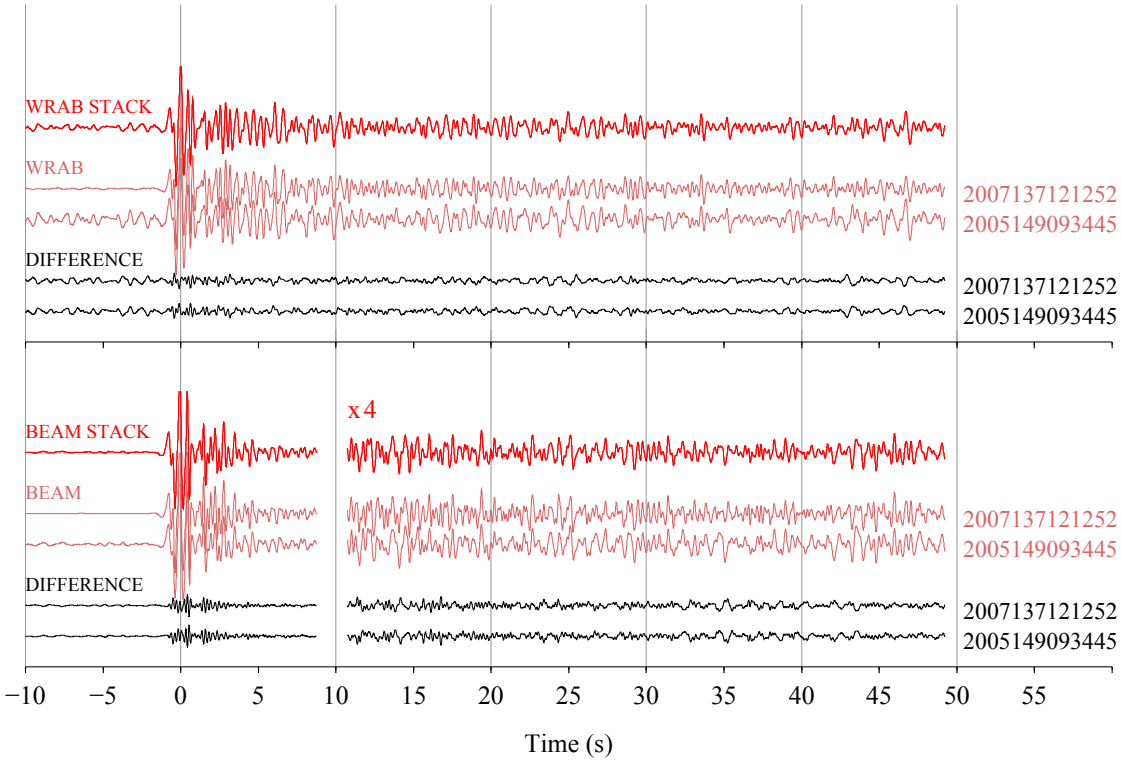

Figure 4.7: Waveforms from a pair of events recorded by the Warramunga arrays (WR, WA, WB) and station WRAB. The upper plot shows the filtered waveforms recorded at WRAB. The lower plot shows the same two events with waveforms obtained by beamforming data recorded by the arrays. The beamform trace amplitudes more than 10 seconds after the main P-wave arrival are increased by a factor of four for clarity. Beamforming results in significant changes to the waveform, suggesting that much of the coda results from scattering through high angles close to the receiver. Nevertheless, in both cases the waveforms have cross correlation values above 0.9. The similarity of the filtered unbeamed waveforms is thus a result of both a similarity in energy propagation close to the source and to the receiver. Traces are plotted and scaled as in Figure 4.2a.

important to establish whether multiplet density is a function of earthquake density alone, or whether regional differences in earthquake mechanism, stress or deformational regime also play a role.

Given the sparsity of multiplets at intermediate depths, and uncertainties in earthquake location, it is difficult to illustrate statistically the effect of earthquake density on earthquake multiplets within the southwest Pacific subduction zones. It is impossible to be certain that the 14-year recording period is not unusual in terms of the number and distribution of multiplets, or whether different patterns might be observed on longer timescales. Nevertheless, a preliminary investigation can be made for different regions by considering the number of multiplets present within each region in a time span shortened such that the number of earthquakes per slab unit area within that time frame is equal in each region. The time frame may be shifted from the start to the end of the 14-year recording history to estimate the average number of multiplets.

Shallow, intermediate and deep-focus regions have been chosen (Figure 4.9), and earthquake densities normalised to approximate that of the intermediate depth region over the full 14-year window. The time frames shown in Figure 4.9 start at the beginning of the recording period studied

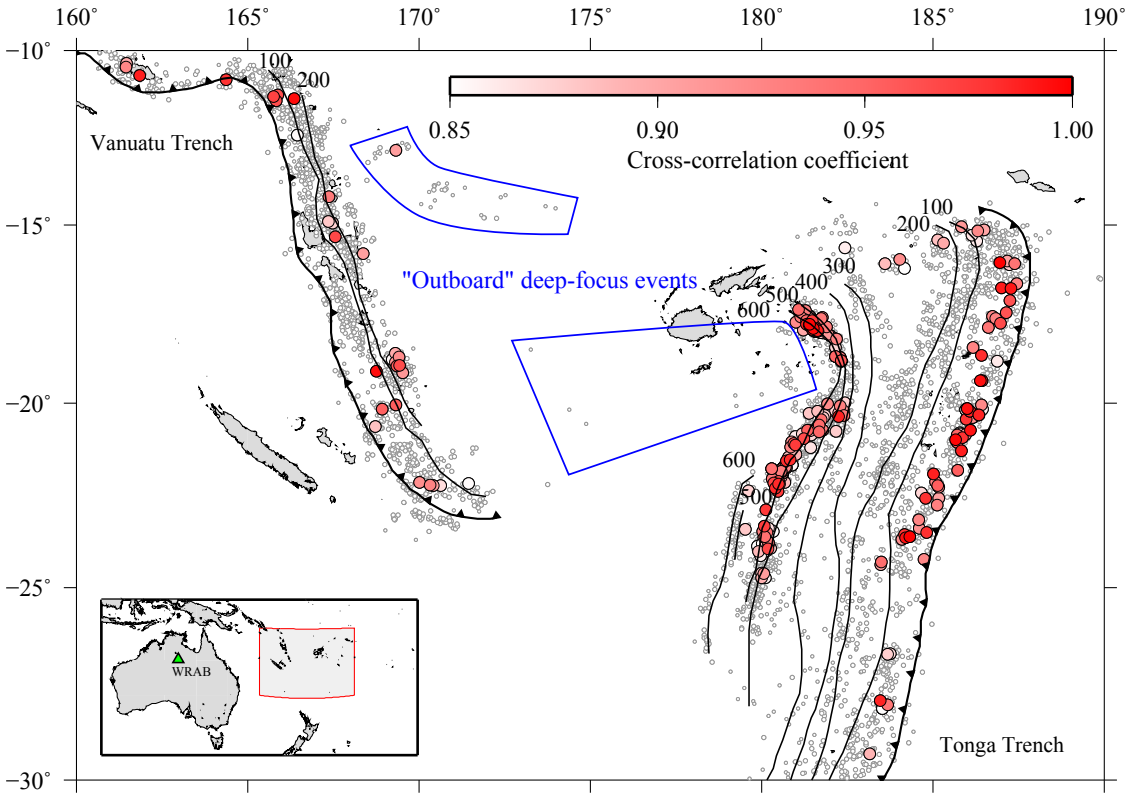

Figure 4.8: Map of the study region, with the depth of the best-fitting surface to seismicity within the Vanuatu and Tonga-Kermadec slabs contoured every 100 km. Shaded locations correspond to the centroids of groups of earthquakes recorded in the EHB catalogue with waveforms recorded at WRAB (see inset for location) which cluster above a similarity value of 0.85. The shading corresponds to the maximum cross correlation value between any pair of waveforms within the group. These are superimposed on the overall seismicity for the region during the time period studied.

(1994). The density-normalised number of earthquakes in the shallow, intermediate, north deep-focus and south deep-focus regions are 55, 344, 34 and 102 respectively (inversely proportional to the areas of each part of the slab). The resulting average number of multiplets within each region (standard deviation in brackets) are 1.20 (1.38) for the shallow region, 3.54 (1.89) for the northerly deep-focus region, and 7.16 (3.54) for the southerly deep-focus region. The marked differences not only between the shallow and deep regions, but also between the two deep regions suggest that neither regional earthquake density nor depth dependent processes are the sole control on clustering. Local slab structure, small scale variations in earthquake density and/or stresses are also important. Without extremely accurate locations, it is impossible to determine whether small scale heterogeneities in earthquake distribution have an effect on the number of multiplets observed.

4.3.4 Relocation

The largest multiplet of earthquakes observed in our catalogue is located between 540–580 km depth near 18°S 178.2°W. Selected waveforms from the multiplet are shown in Figure 4.2b. This multiplet is suitable for relative relocation. The effect of velocity structures outside the region of interest

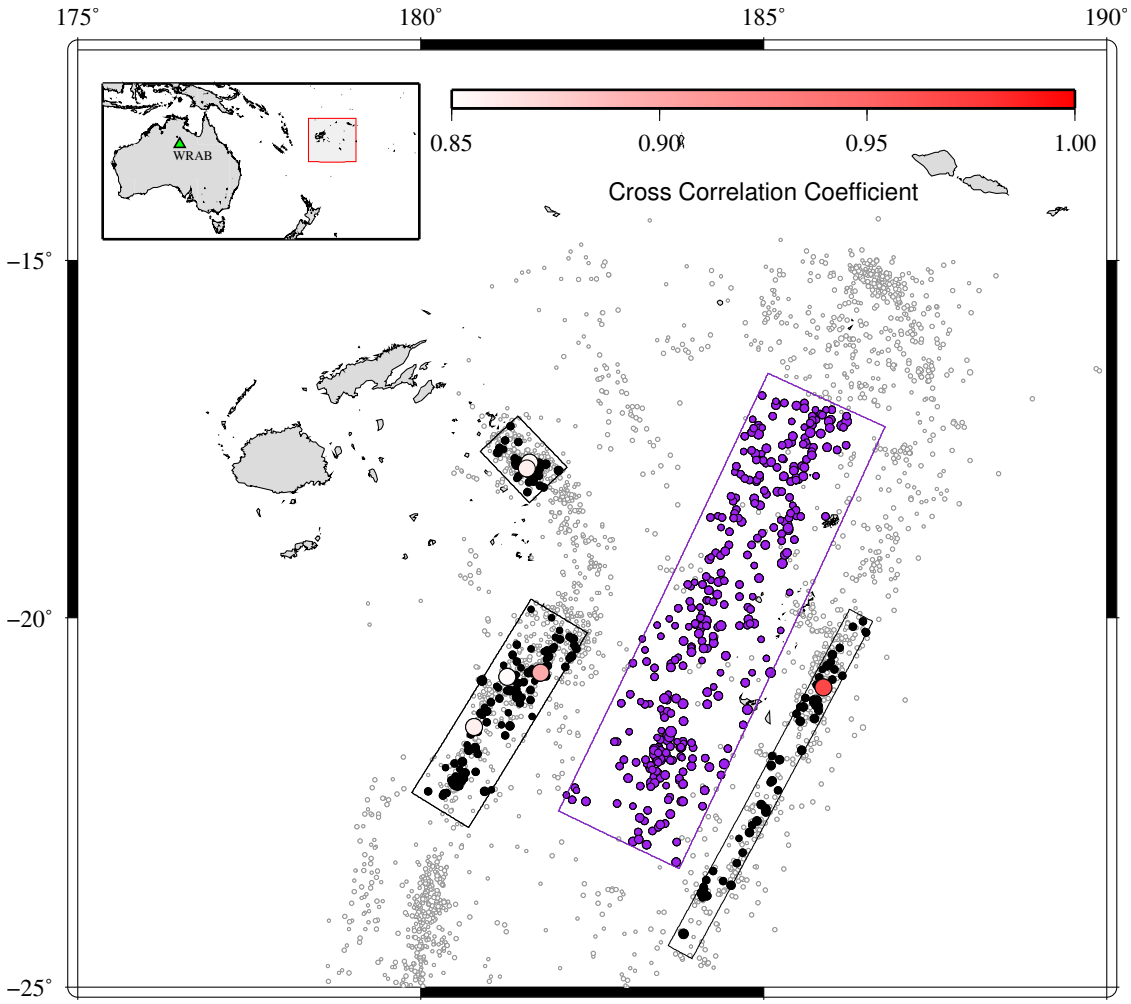

Figure 4.9: Map showing regions used to study the effect of earthquake density on the observation of similar waveforms at WRAB. Events shaded according to their cross correlation values (white–red) represent some of those displayed in Figure 4.8. Slab areas were calculated from slab dip in each outlined region (42° from the one at intermediate depth, 45° at shallow depth, and 63° and 58° for the northern and southern deep-focus regions respectively). The observation time for each of the regions was shortened so that the earthquake density was equal to that of the intermediate depth region. Shaded groups of earthquakes represent those with waveforms that clustered in the first time frame applied to each region.

can be minimised by using double-difference times, which are the residuals between observed and calculated differential travel time between two events Waldhauser and Ellsworth (2000)

To relocate N events relative to each other using M double-difference observations, we use a method derived from Frechet (1985) and Got et al. (1994). In the coordinate system [x, y, z, T], where x, y, and z are spatial coordinates, and T is the difference in origin times we find the system of linear equations

$$\mathbf{Ax} = \mathbf{d} \tag{4.3}$$

where A is the M x 4N matrix containing the partial derivatives of the travel times of the events with respect to their locations and origin times, x is the 4N-vector containing the changes in hypocentral parameters to be determined $[\Delta x, \Delta y, \Delta z, \Delta T]$ and d is the M-vector of double-difference

times determined by the maximum cross correlation coefficient of the first 4 seconds after the initial P-wave arrival. Since the source region is small compared with the station-source distance, the travel times between two events recorded at a station far from the source region may be calculated from the ray-path azimuths and slownesses using a single event location corresponding to the centroid of the initial EHB locations. We add four extra rows to the matrix A and vector d to constrain the mean x, y, z and T offsets to zero. The system of equations is solved by weighted damped least squares via singular value decomposition. The weighting matrix values are taken from the waveform cross correlation coefficients.

The relative locations of earthquakes within the multiplet are shown in Figure 4.10. Also plotted are 95% confidence error ellipses calculated from the covariance matrix. The hypocenters appear define a sub-planar feature striking around 120° clockwise from north and dipping almost vertically. Notably, although the separation between the shallowest and deepest events is over 40 km, the shallowest events are located at the northwest limit of imaged seismicity, and the deepest at the southeast, such that the events mark a narrow subvertical zone about 20 km in down-dip length and less than 10 km in width, deepening to the northeast at an angle of $\sim$45 degrees. Regional hypocentral locations in the EHB catalogue (Engdahl et al., 1998) are consistent with scatter around a feature of this shape. Independent relocations by Gesserman and Wiens (2010) also indicate the presence of a shear zone about 5 km in width.

Location errors are sufficiently small to suggest that the vertically elongated pattern of hypocenters is not an artefact of the relocation procedure. The trend of seismicity in this region is nearly parallel to the sub-vertical nodal planes of several Centroid Moment Tensor (CMT; Dziewonski et al., 1981) solutions. One of the CMT solutions corresponds to an event (2007145172611) within the relocated multiplet. The steeply dipping nodal plane has a strike of 126°, dipping 76° to the southwest with a rake of 61°. The other two focal mechanisms plotted in Figure 4.10 correspond to the earthquake doublet with waveforms illustrated in Figure 4.2a. This doublet does not cluster within the larger multiplet at any station at a similarity value of 0.85, but waveforms recorded at several stations are sufficiently similar that they may be relocated relative to the other events. The strike, dip and rake of the steeply dipping nodal planes of the events 1995177064850 and 2006204205051 are 321, 76, -50 and 323, 81, -54 respectively. The change in strike and opposite dip direction may reflect doublet focal mechanisms distinct from those of the larger multiplet.

One interpretation is that the earthquakes plotted in Figure 4.10 represent shear facilitating down dip motion of the slab mantle relative to the crust. If true, this would be a unique observation, since most deep focus earthquakes have P-axes in the plane of the Wadati-Benioff zone. An alternative suggestion is that the trend of earthquakes in this region does not indicate a planar Wadati-Benioff zone, but one which is folded about an axis parallel to the B-axis of the three plotted CMT focal mechanism solutions. This would result in in-plane P-axes, as observed in other slabs. Evidence to

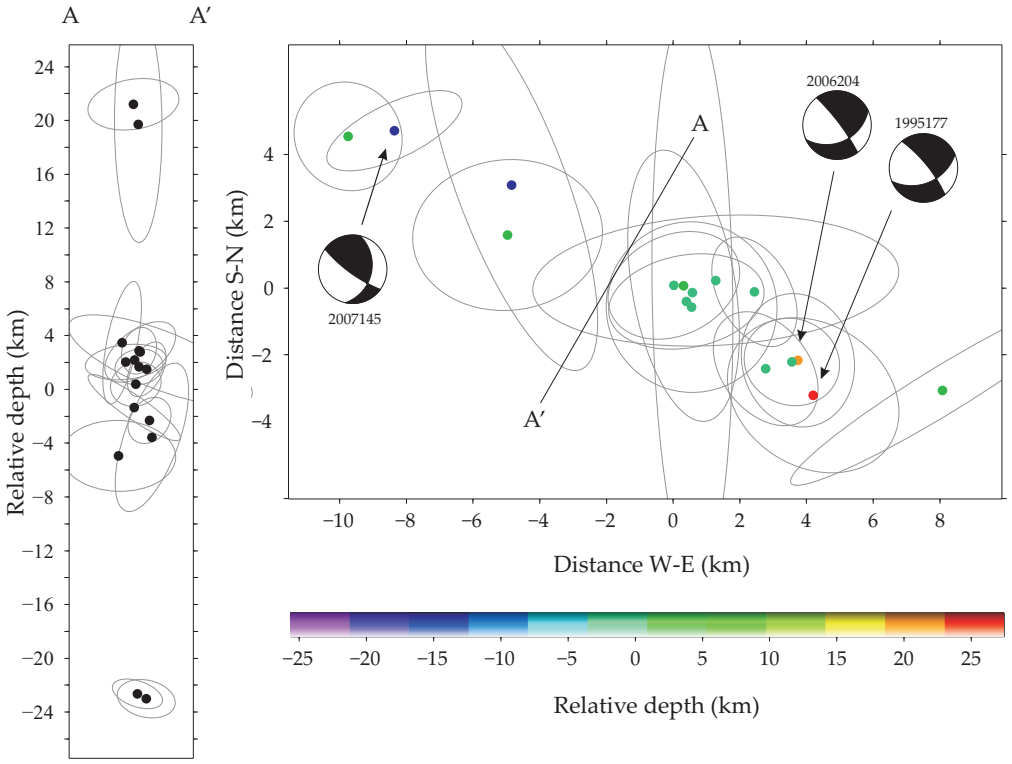

Figure 4.10: Relocated events at around 18°S within the Tonga-Fiji-Kermadec Wadati-Benioff zone. Only hypocenters with a good azimuthal coverage of stations are plotted. Azimuths and slownesses were calculated using an event location of 17.91°S, 178.55°W at 567.13 km depth (the centroid of the EHB hypocenters).

support this hypothesis is presented in Chapter 5 (§5.4.5).

One of the earthquakes within the relocated multiplet (1995286082018) is shared with a 21-event multiplet reported in a 2-year regional study by Wiens and Snider (2001). At least two further earthquakes in the EHB catalogue are also within their multiplet, but are grouped into distinct multiplets in this study. One of the events is the earlier of the two doublet earthquakes previously mentioned (1995177064850), The other (1995274163835; Figure 4.3) has only one station (out of 16; PMG) with a cross correlation coefficient of over 0.85 (0.897744) with event 1995286082018. WRAB-recorded waveforms from the clusters containing each event only become grouped together when the similarity value for clustering is less than 0.500.

The differences in cluster sizes between studies suggests that the sensitivity of clustering to small changes in source properties depends on the choice of cross correlation technique, clustering technique, and the locations of the recording stations. The curved surface and corresponding $\sim 30^\circ$ rotation of sub-vertical CMT nodal planes in the multiplet identified by Wiens and Snider (2001), is matched in the present study if a similarity value lower than about 0.80 is used.

4.3.5 *Temporal characteristics*

The repeat times of earthquakes within multiplets are most consistent with a semi-random distribution, contrary to the short interevent times reported by Wiens and Snider (2001). Histograms of interevent time within deep-focus earthquake waveform clusters from several stations (Figure 4.11) show few interevent times less than 10 days ($\sim 10^6$ s). The peak in interevent time frequency between 10^7 and 10^8 s is present within both large single clusters and the combined interevent times for all clusters. The decay at long interevent times is a result of the 14-year span of analysed events ($10^{8.6}$ s).

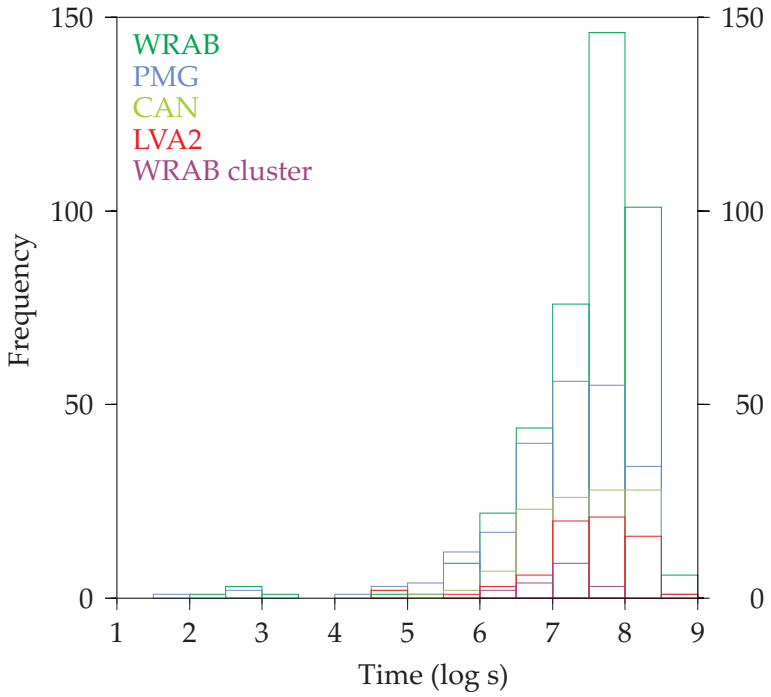

Figure 4.11: Histograms illustrating the distribution of interevent times within deep-focus clusters identified at different stations. The histogram labelled 'WRAB cluster' corresponds to events within the same cluster as the waveforms shown in Figure 4.2a.

Despite interevent times generally being $> 10^6$ s, there are some notable exceptions. Several aftershocks occuring within days of the M_W 7.6 2002 Tongan deep-focus earthquake studied by Tibi et al. (2003) (2002231110101) are contained within a single multiplet defined at several stations (including 2002231114530, 2002231121301 and 2002232014457). Four events within the deep-focus outboard earthquakes east of the Vanuatu Slab (around 13°S 169°W) occuring within the weeks of each other also have similar waveforms (1999292044326, 1999307013037, 1999307013641 and 1999312103658), and thus presumably similar focal mechanisms. Despite a lack of preferred focal mechanism in the region (Okal and Kirby, 1998; Chen and Brudzinski, 2001) some earthquakes may nevertheless occur on related fault planes.

The data in this study suggest a range of different repeat-time behaviour for deep earthquakes. The temporal behaviour within multiplets is usually semi-random, but also includes aftershocks and the swarms of events of similar magnitude observed in the regional study by Wiens and Snider

(2001).

4.4 Discussion

4.4.1 The origin and significance of waveform similarity

As stated in the introduction, waveform similarity of earthquakes with identical rupture properties are observed when hypocentral locations are sufficiently close that complexly scattered waves travel along almost identical paths (Geller and Mueller, 1980; Poupinet et al., 1984; Snieder, 2002). The exact interpretation of the phrase depends on the specific source-scatterer-receiver geometries. In local studies, an oft-stated rule of thumb is that event separations are within around one quarter of the dominant wavelength of energy arriving at the station (Geller and Mueller, 1980). Synthetic wave-field simulations in laterally heterogeneous media (Baisch et al., 2008) have shown that for this criterion to be applied, time windows significantly greater than the S-P time difference should be used, and coefficients resulting from waveform cross correlation must exceed 0.95. These conditions ensure that waveform energy leaves the source at multiple azimuths even in the absence of scatterers along the ray path, constraining locations within the vertical 2D plane containing the source and receiver.

There are two key problems with using long-window techniques on teleseismic waveforms. Firstly, single window cross correlation coefficients on long time windows will be dominated by the high amplitude arrivals. Secondly, as we have shown, much of the power in the coda is generated by receiver-side scatterers, weakening the connection between coda similarity and source separation. If one seeks to ascertain differences in source separation, relative relocation techniques may be used.

One strength of waveform similarity observations is the ability to easily determine earthquakes with similar focal mechanisms. Changes in orientation are reflected not only in the initial arrival but the whole coda. The range of moment magnitudes within single multiplets suggests that similar waveforms may be of use in estimating focal mechanisms for small events where there are insufficient observations to obtain a good moment tensor solution. Minor changes in focal mechanism can result in decreased but not small cross correlation coefficients, so care should be taken to ascertain the significance of waveform similarity in specific cases.

4.4.2 The distribution and behaviour of earthquake multiplets

The heterogeneous distribution of earthquake multiplets could be a result of a variety of processes. Certainly the difference in number of multiplets in a given region is not solely controlled by depth dependent mechanisms, since intermediate depth multiplets are relatively common in the Vanuatu subduction zone, yet rare along the Tonga-Fiji-Kermadec slab. The regional density of earthquakes plays a primary role, since if earthquakes are distributed such that none occur within about 30-40

km of each other, there will be no similar events. The present dataset cannot reveal all the factors controlling the presence of multiplets, but it may be that if a region is seismically active, dominant shear zones form along which earthquakes with similar mechanisms are more likely to occur.

The presence of so many deep-focus earthquakes which belong to multiplets east of Fiji (between 19°S and 14°S, and 175°E and 170°W), where 286 out of 1341 events belong to a multiplet at a similarity value of 0.85 at station WRAB (726 with a similarity value of 0.6) suggests that the contorted slab is deforming in an organised way. CMT solutions support this conclusion, since the orientation of many of the earthquake B axes rotate as the strike of the Wadati-Benioff zone rotates around the northern end of the Tonga slab. An analysis of this observation can be found in §5.4.5.

The diversity in clustering behaviour at great depths is intriguing. The semi-random distributions with time and occasional aftershock behaviour seen in earthquake multiplets in the present study is akin to shallow earthquake behaviour. The swarm-like behaviour observed by Wiens and Snider (2001) is reminiscent of fluid-influenced seismicity at shallow depths.

4.5 Conclusions

Earthquakes producing similar waveforms beneath the southwest Pacific are not rare. Shallow, intermediate and deep-focus multiplets are all observed, and the number of multiplets in a given region strongly correlates with the overall seismic density. There is a predominance of earthquake multiplets between 0–60 km and 520–620 km depth within the Tonga-Fiji-Kermadec Wadati-Benioff zone. Particularly strong clustering is observed in waveforms from deep-focus events at the north end of the Tonga 'hook' (northeast of Fiji), where intense seismic activity illuminates a sub-vertical seismic zone in the slab.

The physical implications of waveform similarity at teleseismic stations are fundamentally different from those inferred in local studies. The coda is primarily composed of energy from receiver-side scatterers, and therefore similarity tells us little about relative location on kilometer length scales. Similar waveforms are a stronger constraint on focal mechanism, and so earthquake multiplets determined through the study of teleseismic waveforms reveal the extent of activity on single or closely related shear systems.

5 *Deep earthquake focal mechanisms*

5.1 Introduction

The first systematic overview of focal mechanisms within subducting slabs (Isacks and Molnar, 1971) revealed a consistent relationship between the maximum depth of seismicity and focal mechanism orientation. In slabs where seismicity is restricted to <300 km depth (e.g. Nicaragua), earthquakes typically have focal mechanisms with T axes indicating down-dip extension. Wadati-Benioff zones with deeper seismicity often have intermediate-focus (60–300 km) earthquakes indicating down-dip extension and deep-focus (300–700 km) events indicating down-dip compression (e.g. South America). This separation of focal mechanism behaviour into two depth bins (60–300 and 300–700 km) is consistent with an exponential decline in global intermediate-depth seismic activity with increasing depth and a broad peak in deep-focus seismic activity at ∼550 km depth (e.g. Sykes, 1966; Isacks et al., 1968). For slabs that reach the upper-lower mantle boundary (e.g. Tonga, North Kuriles), Isacks and Molnar (1971) and Vassiliou (1984) reported that the entire slab experiences down-dip compression. They argued that this is the result of increased resistance to subduction imposed by a viscosity jump across the upper-lower mantle boundary. Consistency in deep earthquake fault plane orientations is best explained by fracture of a homogeneous material (McKenzie, 1969b).

The data contained in modern earthquake catalogues support the inferences made in early studies of deep seismicity, but they also reveal significant complexity in earthquake distributions and focal mechanisms. Individual subduction zones have unique patterns of seismicity which vary with depth and along-strike. At intermediate depths, double seismic zones are commonly observed, many (but not all) of which indicate compression in the upper plane and extension in the lower plane (e.g. Engdahl and Scholz, 1977; Brudzinski et al., 2007). Earthquakes in several slabs have focal mechanisms with principal axes not aligned with the local slab reference frame, or aligned in a way not expected from a slab experiencing down-dip compression or extension (e.g. Marianas, Aleutians; see Apperson and Frohlich, 1987; Chen et al., 2004). Apperson and Frohlich (1987) reported that 50% of all deep-focus earthquake P axes lie more than 28° away from the down-dip direction. These complexities can be used to test models of stress and strain development in subducting slabs.

This chapter is a modified version of the main text from Myhill (2012).

5.1.1 Potential controls on the distribution of seismicity

A variety of models have been proposed to explain the distributions and focal mechanism variations of deep earthquakes. The negative buoyancy driving subduction and viscous resistance to flow are vital components of most of these models. Vassiliou et al. (1984) and Vassiliou and Hager (1988) show that the depth distributions of earthquakes and down-dip compression/extensional behaviour in Wadati-Benioff zones can be simulated in numerical models of negatively buoyant planar slabs 10 times more viscous than the upper mantle (Vassiliou et al., 1984; Vassiliou and Hager, 1988). Density driven slab-pull promotes down-dip extension, while viscous resistance to penetration into the lower mantle results in down-dip compression. In these models, slabs become seismically inactive after penetrating the lower mantle (Wortel and Vlaar, 1988; Willemann, 1991). Tao and O'Connell (1993) show that deformation rates can even be explained by the subduction of slabs with the same viscosity as the surrounding aesthenosphere. In contrast, much of the behaviour observed in subduction zones can also be modelled with highly viscous slabs if a stress-limiting rheology is used (e.g. Alisic et al., 2010).

Deviations from the equilibrium density structure of a homogeneous slab and surrounding aesthenosphere may also affect deformation in subducting lithosphere. It has been suggested that a bending moment induced by the presence of a relatively low density metastable olivine wedge could increase seismicity in cold subducting slabs at $>$300 km depth (Bina, 1997; Bina et al., 2001). Low density upwelling plumes have been proposed as a potential influence on deformation in the Tonga slab (Gurnis et al., 2000).

Slab shape is likely to play an important role in determining the distribution of stress and strain in subducting slabs. At intermediate depths, bending and unbending have been invoked as the cause of double seismic zones with opposing stresses in the upper and lower planes (e.g. Engdahl and Scholz, 1977). Changes in slab shape have been invoked to explain along-strike tension and compression in (for example) the Marianas and Aleutians slabs (Creager and Boyd, 1991; Chen et al., 2004). Bailey et al. (2012) compare the results of three-dimensional numerical modelling with summed gCMT data. They find that seismic data are generally consistent with slabs having viscosities 10–100 times that of the lower mantle.

Not all studies support the hypothesis that strain is controlled by slab shape. Some double seismic zones exhibiting different states of strain are seen where changes in slab dip are small, suggesting that bending may not be the only contributor to focal mechanism variations (e.g. Fujita and Kanamori, 1981). For a large fraction of deep-focus earthquakes, Apperson and Frohlich (1987) conclude that focal mechanisms are not controlled by slab shape in any simple way. Nothard et al. (1996b) calculate the gaussian curvature along the Tonga slab, and show that the distribution of earthquakes cannot be explained by deformation of a slab moving under a rigid template.

The physical mechanism of deep earthquakes has also been invoked to explain spatial variations in deep seismicity. For example, the minimum in seismic activity at ∼300 km depth in global catalogues has been used to suggest that a new mechanism becomes active at greater depths. The 320–410 km depth range corresponds to the pressures where olivine becomes unstable within cold mantle. The transformational faulting hypothesis states that deep-focus earthquakes occur when narrow lenses of wadsleyite or ringwoodite coalesce and shear during sluggish reaction from olivine (Kirby et al., 1991; Furukawa, 1994; Kirby et al., 1996; Green, 2007). It has been argued that large stresses accompany the volume decrease associated with the transformation, which could further promote seismicity (Guest et al., 2003, 2004). Wiens et al. (1993) suggest that stresses resulting from olivine transformation may be responsible for double seismic zones at 350–450 km depth in the Tonga slab. A secondary increase in moment release at ∼530 km depth in both warm and cool slabs has been attributed to transformational faulting of garnet to perovskite (Estabrook, 2004).

An alternative possibility is that deep earthquakes arise from adiabatic shear instabilities[2]. Karato et al. (2001) argue that such instabilities may be promoted in the upper half of the mantle transition zone by weak, fine-grained wadsleyite. They also suggest that slab shapes, deep-focus earthquake stress drops and gravity measurements support the idea that cold slabs are weaker than warm ones, as expected if grain growth is more sluggish in cold slabs.

A third hypothesis for earthquake generation at high pressure involves the presence of free fluids. Isacks et al. (1968) suggested that the *P-T* locations of dehydration reactions may control the depth distribution of seismicity. The relative sparsity of seismicity between 200 and 350 km depth has been linked to a gap in dehydration reactions, with intermediate depth earthquakes enabled by partial dehydration of the slab during antigorite breakdown and deep-focus earthquakes promoted by the decomposition of phase A or brucite (Omori et al., 2004).

Despite the range of reaction-specific explanations for the global depth distribution of seismicity, the broad maximum in seismic activity at 550 km depth represents a composite of different regional maxima that do not correlate well with known mineral reactions (e.g. Sykes, 1966). Throughout the upper mantle, the interplay between temperature, mineralogy, stress and strain may be complex. To understand these relationships fully, a better understanding of the relationships between the locations, focal mechanisms, fault planes and rupture characteristics of deep earthquakes is required.

5.1.2 *Aim*

The models summarised above interpret the same seismological data in very different ways. Many incorporate only the broadest features of deep earthquake behaviour, so it seems likely that a more detailed interrogation of the available earthquake data will be able to determine the relative importance of various controls on brittle deformation within subducting slabs.

[2]Adiabatic in this case implies that heat is not exchanged between the shear zone and its surroundings.

This study is concerned with the relationships between slab shape and the distribution and focal mechanisms of deep earthquakes. As many slabs are non-planar and presumably undergoing deformation related to their shape, it might be expected that the uneven distribution of seismicity and complex variation in mechanisms are somehow related to slab morphology. If this is true, then the relationships between slab shape and deformation help constrain the current kinematics and dynamics of subducting slabs, and provide a foundation on which to build and assess models of slab evolution through time.

5.2 Methodology and data sets

Any assessment of subduction zone seismicity in terms of slab morphology requires a technique to constrain slab shape. Tomographic images currently have insufficient resolution to accurately map the locations of subducting slabs. A more accurate technique is to use the locations of deep earthquakes themselves (e.g. Apperson and Frohlich, 1987; Gudmundsson and Sambridge, 1998; Chen et al., 2004).

Wadati-Benioff zones in the mantle transition zone are three-dimensional. Zones undergo abrupt changes in dip and strike angle (e.g. Izu-Bonin, Solomons), and exhibit morphologies which cannot be approximated as two-dimensional planar or axisymmetric bodies (e.g. Tonga). Unlike analyses of intermediate-depth earthquakes, which can be conducted satisfactorily by assuming that the down-dip direction is perpendicular to the trench or volcanic arc (e.g. Chen et al., 2004), rotation of deep-focus focal mechanisms into the local slab reference frame requires consideration of these 3-D complexities in slab shape.

I use well constrained locations for earthquakes in the EHB catalogue (Engdahl et al., 1998, and recent updates) to approximate the best-fitting surface to seismicity. Assuming the location of subduction zone earthquakes is controlled primarily by temperature and stress, this best-fitting surface approximates the locus of points defining the coldest parts of the slab. The steps required to approximate this plane are shown in Figure 5.1. The best-fitting surface to the seismicity is found using an adjustable tension continuous-curvature surface-gridding algorithm (Smith and Wessel, 1990), where $z = 0$ corresponds to the predetermined best-fitting plane to seismicity. Individual earthquake locations are subject to location errors, and scatter around the cold core of the slab, so the surface to seismicity is fitted to average earthquake locations, which are found for a series of blocks within the xy-plane. The slabs investigated in this study have earthquake distributions sufficient to determine the shape of the slab with a block spacing of 50–100 km. The resolution of slab shape is sufficient to see small changes in slab orientation on length scales comparable to or slightly smaller than the plate thickness. Most slabs can be modelled as a single sheet, but extreme curvature in the Tonga and Izu-Bonin-Marianas slabs requires analysis to be conducted in several parts.

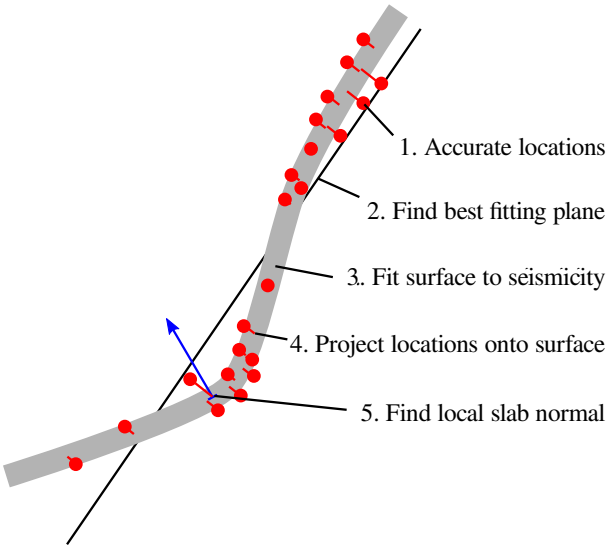

Figure 5.1: A graphical representation of the seismicity surface-fitting and slab-normal-finding procedure. The procedures shown on this two-dimensional cross section are simplifications of the three-dimensional fitting method. The distance from seismicity to the best fitting surface is slightly exaggerated.

5.2.1 *Focal mechanism rotation into the slab reference frame*

Once the best-fit surface to seismicity has been found, the locations of earthquakes with gCMT fault plane solutions (Dziewonski et al., 1981; Ekström et al., 2012) are projected onto the surface, by translating the EHB catalogue location for that earthquake (or the gCMT catalogue location for events after October 2007) onto the best-fitting surface to seismicity along the direction perpendicular to the average slab plane (Figure 5.1). Most events are positioned less than 20 km from the surface, so the difference in location between this plane-orthogonal mapping and the surface-orthogonal (least-distance) mapping is small. The local pole to the surface is used to rotate each focal mechanism into the coordinate system of the slab.

5.2.2 *Visualisation*

A visual analysis of the spatial distributions of focal mechanisms is difficult in regions of dense seismicity. Plotting the mechanisms themselves is to be avoided, since resulting plots are cluttered and difficult to analyse. Summing focal mechanisms within regions (e.g. Bailey et al., 2012) aids visualisation at the risk of averaging dissimilar mechanisms. Some studies overcome this problem by plotting P and T axes on lower hemisphere plots in a slab coordinate frame, preserving information from individual events but removing spatial information (e.g. Vassiliou, 1984; Chen et al., 2004).

A desired solution to this problem retains both individual mechanisms and their spatial information, but encodes the focal mechanism information into a single variable. The conventional description of earthquakes as down-dip P, T or B (or any intermediate) enables focal mechanism information to be plotted on a ternary diagram (Frohlich, 1992), and therefore mapped to a colour

using the RGB palette. Although powerful, this technique cannot uniquely assign a colour to any mechanism. For example, down-dip P axis events would be coloured the same regardless of the angle between the T (or B) axis and along-strike vector. Although brightness or saturation could be used as added discriminants, any resulting figure would be difficult to interpret.

If some non-uniqueness in mapping can be tolerated, colour-coding of mechanisms can be based on mechanism similarity, rather than an explicit relationship between the principle axes and the orientation of the slab. The 3D rotation angle θ can be used to describe the similarity between two focal mechanisms (Kagan, 1991). I use the group-mean hierarchical clustering scheme of Rowe et al. (2002) described in Appendix A to sort the earthquakes into groups according to their dissimilarity $(1 - \theta/90)$. The number of clusters can be varied to provide a balance between variability in focal mechanisms in single clusters and the required level of interpretation. Each cluster is assigned a unique colour for plotting purposes.

5.2.3 *Comparison with slab shapes*

Recently, finite element simulations have been used to compare the focal mechanisms of deep earthquakes with the deformation expected for real slab morphologies and subduction velocities using a variety of mantle rheologies (Alisic et al., 2010; Alpert et al., 2010; Bailey et al., 2012). The calculations are sufficiently involved that it is sometimes difficult to isolate the effects of the various inputs. Model boundary conditions and rheology can both be treated in a variety of potentially realistic but often poorly constrained ways.

In this study, I take the alternative approach of combining the seismic observations (shapes of Wadati-Benioff zones, earthquake locations and focal mechanisms), in order to directly compare the characteristics of different subducting slabs.

5.3 *Study regions*

In order to study the relationship between slab shape and seismicity, the morphology of the slab must be sufficiently constrained by the seismicity. For this reason, the present analysis is restricted to the Kuriles-Kamchatka, Izu-Bonin, Marianas, Tonga-Kermadec and Solomons slabs, which all have seismicity extending to the base of the upper mantle (Figure 5.2). With the exception of the Solomons slab, all of these subduction zones have almost continuous distributions of seismicity from the surface to 600–700 km depth. The Solomons slab is included in the present analysis because despite relatively low levels of seismic activity the distribution of deep earthquakes in the region is sufficient to estimate the shape of the slab.

Rejected Wadati-Benioff zones have few deep-focus earthquakes. They include the Philippines and Java-Sunda-Banda subduction zones, which exhibit little variation in deep-focus earthquake

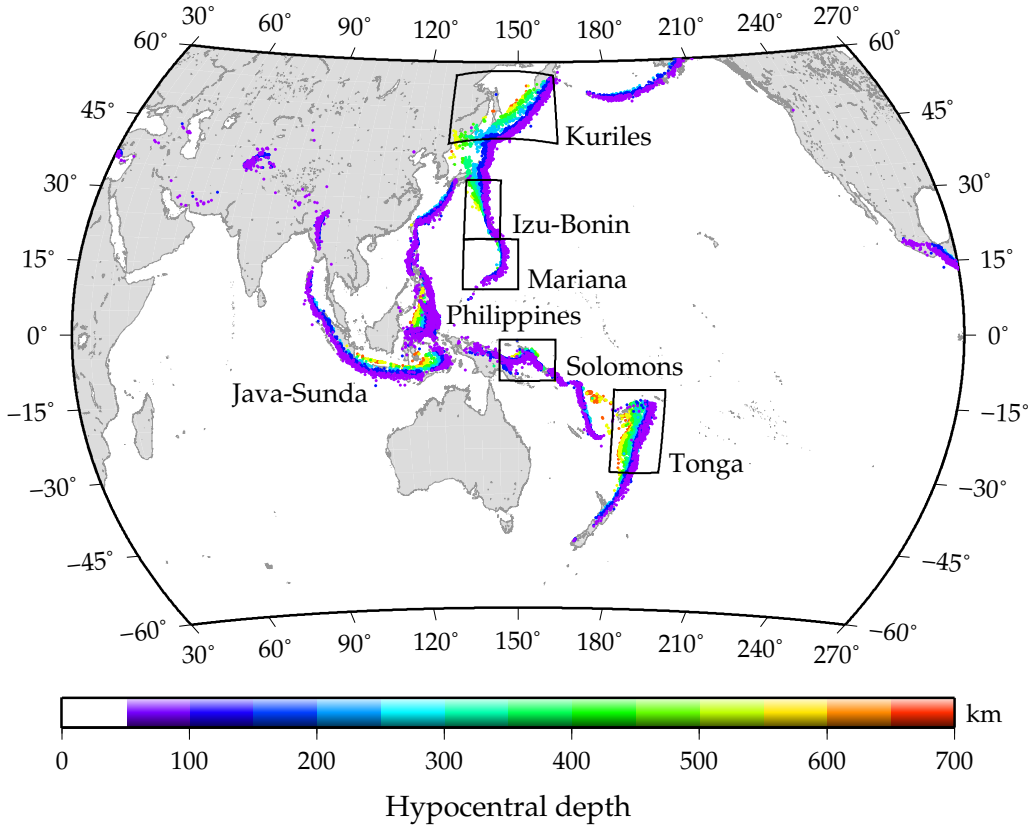

Figure 5.2: Map of western Pacific and East Asian seismicity. Coloured dots correspond to EHB locations, coloured according to depth. Major subduction zone systems which are active throughout the upper mantle are named. The regions analysed in this study are outlined.

focal mechanism, and South America, New Zealand and Spain, where slab shape and continuity are poorly constrained as a result of large gaps in the distribution of seismicity.

5.4 *Results*

5.4.1 *Izu-Bonin*

The Pacific Plate subducts beneath the Philippines plate between Japan and Guam. At 100–300 km depth beneath the Izu and Bonin Islands, the dip of the slab increases from 40–50° in the north to subvertical in the south. At 300–500 km depth, the dip of the slab decreases to 0–30° along a bend whose hinge plunges 10–20° southeastwards from 34°N to 26°N (marked by synform symbols in Figure 5.3). Where the slab is almost planar, seismicity is sparse. A broad, dense band of seismic activity plunges at 10–20° to the southeast, following the bend in the slab.

Throughout the Izu–Bonin slab, earthquake focal mechanisms mostly indicate in-plane compression (orange in Figure 5.3). A few intermediate depth earthquakes have focal mechanisms with down-dip T axes (blue), and several more have in-plane P and T axes taking up along-strike shortening (cyan), especially south of 30°N. The deepest earthquakes mostly have gCMT solutions with P axes oriented approximately down-dip and B axes slab-normal (pink, red events). The intersections

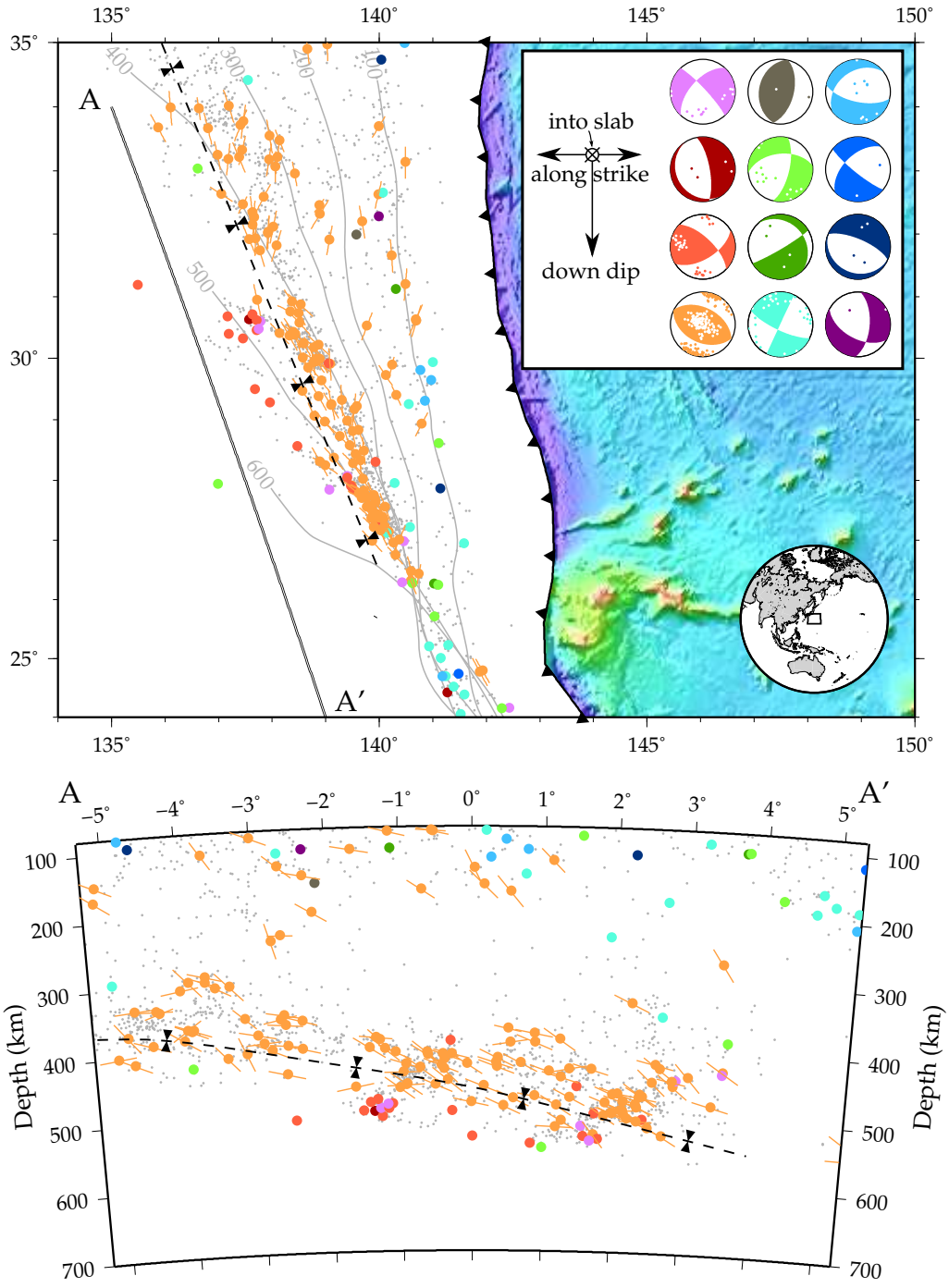

Figure 5.3: Locations and focal mechanisms of deep earthquakes in the Izu-Bonin slab in plan view and cross section projected along the line A–A′. Grey contours correspond to the best-fitting surface to seismicity. Bathymetry is shown east of the trench. The dashed black line with synform symbols marks a concave-up fold in the slab. EHB locations are plotted as grey dots, while earthquakes with gCMT solutions are plotted as larger coloured dots. Each colour represents a different focal mechanism type, as shown in the inset (upper right). For 'down-dip' compressional events (orange), B axes are also drawn. Individual P and T axes are superimposed on each focal mechanism type. Down-dip is down, and inward-facing slab-normal into the page.

of the northeast-striking nodal planes and the best-fitting surface to seismicity are co-linear with narrow streaks of deep-focus earthquakes, which may represent shear zones within the subducting slab (Lundgren and Giardini, 1992).

The dense band of seismicity at 300–500 km depth is dominated by earthquakes with in-plane

P and B axes (orange). These compressional earthquakes have B axes which are rotated by 10–20° clockwise from the along-strike direction, ∼parallel to the hinge of the bend in the slab . This observation is most easily explained by continued bending of the slab, with high strain rates and alignment of the principal strain axes around the hinge.

5.4.2 *Kuriles-Kamchatka*

To the north of Japan, the Pacific Plate subducts beneath the Sea of Okhotsk. The Wadati-Benioff zone is almost planar in the north (beneath Kamchatka), but is kinked about a northeast plunging hinge to the south of 50°N.

The results of the focal mechanism analysis for deep Kuriles-Kamchatka earthquakes are shown in Figure 5.4. There is a wider variation in focal mechanisms than observed in the Izu-Bonin slab, but the variety of mechanisms can still be adequately represented by 12 gCMT focal mechanism clusters.

As observed in the Izu-Bonin slab, a dense band of seismicity is associated with the bend in the south Kuriles slab between 250 and 500 km depth. In the north, where the slab is almost planar, seismicity is diffuse between 200 and 700 km depth.

From south to north, in-plane compressional events become more common. At <200 km depth, down-dip extensional (blue) and compressional (pink) events are observed between 43.5°N and 54°N, with extensional events dominating further south and compressional events dominating further north. Kao and Chen (1994) showed that this central region exhibits a double seismic zone, with a zone of down-dip compression overlying a zone of down-dip extension. They argued that the change in the dominant focal mechanism from south to north along the slab reflects the increasing interaction between the slab and the viscous lower mantle.

At greater depths, a different transition in focal mechanisms is observed. In-plane shear gCMT solutions (green) dominate south of 47°N. Between 47°N and 49°N, in-plane compressional events appear (orange, red), with P axes directed down-dip north of 49°N (pink). The in-plane compressional events in the zone of transition (marked by grey arrows in Figure 5.4) have B axes rotated 30–45° anticlockwise from the along-strike direction. As observed in the Izu-Bonin slab, these B axes are aligned with both the distribution of seismicity, and the bend in the slab.

Despite the variability in focal mechanism, the technique used in the present study reveals several patterns in seismic behaviour within the Kuriles-Kamchatka slab. A down-dip compressional strain field dominates in the north, where the slab is almost planar and reaches the 670 km discontinuity. Further south, a transition to in-plane shear is consistent with the decreasing importance of slab interaction with the upper-lower mantle boundary, as proposed by Kao and Chen (1994). In the zone of transition between 47°N and 49°N, the rotation of P axes away from the down-dip direction is consistent with deformation by bending of the slab, as seen beneath the Izu-Bonin Islands.

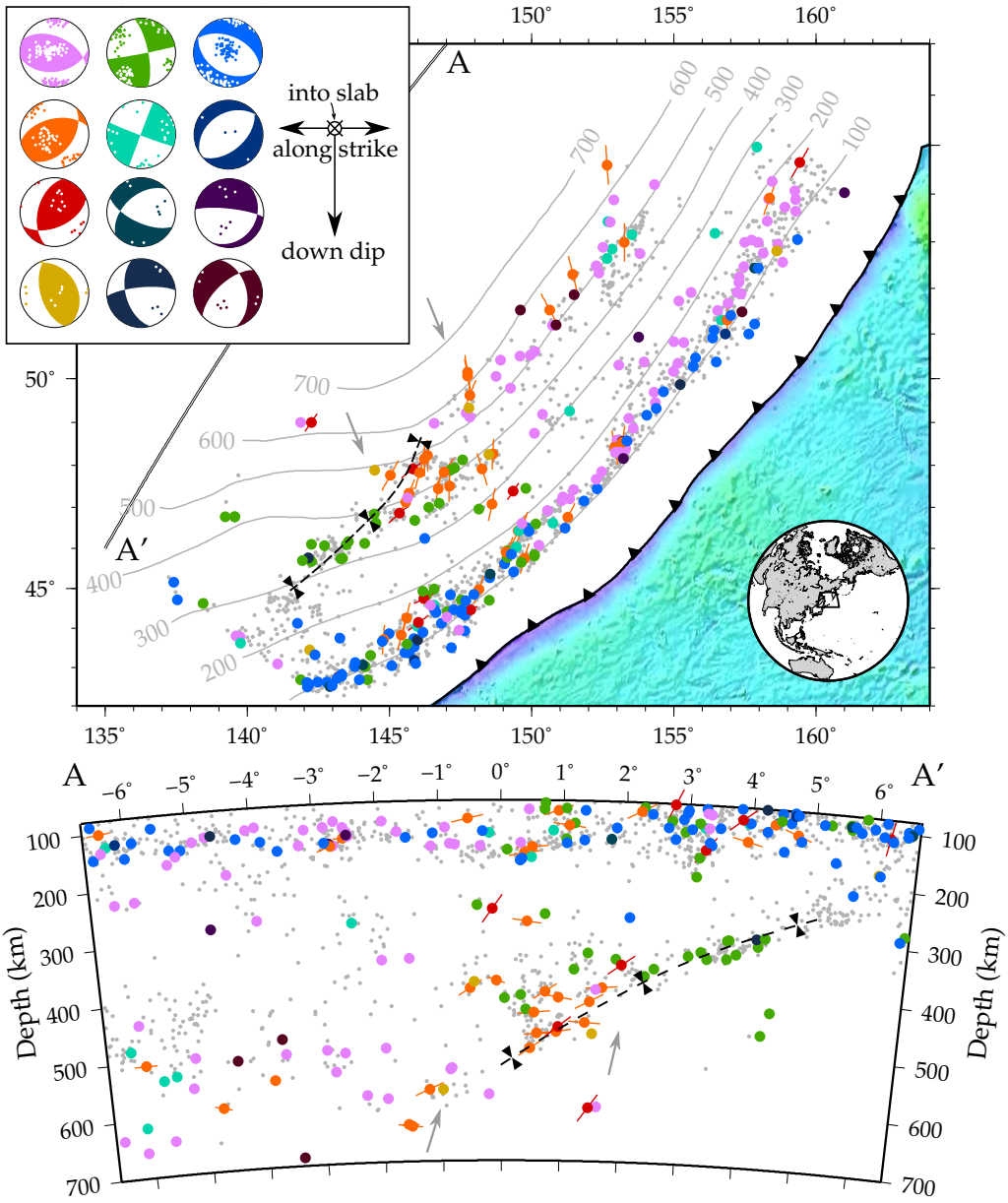

Figure 5.4: Locations and focal mechanisms of deep earthquakes in the Kurile-Kamchatka slab in plan view and cross section projected along the line A–A′. Grey contours correspond to the best-fitting surface to seismicity. Bathymetry is shown southeast of the trench. The dashed black line with synform symbols marks a concave-up fold in the slab. EHB locations are plotted as grey dots, while earthquakes with gCMT solutions are plotted as larger coloured dots. Each colour represents a different focal mechanism type, as shown in the inset (upper left). For in-plane compressional focal mechanisms represented by earthquakes close to the concave bend in the slab (orange, red), B axes are also drawn. Grey arrows represent an along strike transition in focal mechanisms (described in the text). Individual P and T axes are superimposed on each focal mechanism type. Down-dip is down, and inward-facing slab-normal into the page.

5.4.3 Marianas

To the south of the Izu-Bonin trench, subduction continues along the arcuate Marianas trench. The Marianas slab dips steeply between 100 and 700 km depth, and at the base of the upper mantle appears to be slightly overturned (Figure 5.5).

Deep-focus earthquakes are restricted to an arc of ∼400 km length between 16°N and 20°N. The Wadati-Benioff zone has no dense bands of seismicity, and is therefore more similar to the zone beneath Kamchatka than beneath the Kuriles and Izu-Bonin Islands.

gCMT solutions for deep-focus earthquakes indicate that the slab is undergoing down-dip compression. Although most of the focal plane solutions have T-axes perpendicular to the slab surface (red), there are a few earthquakes which have along-strike T-axes (blue, cyan, green). These two groups of events appear in different parts of the slab, with the along-strike extension / down-dip compressional events clustered within a 40–50 km wide strip at 480–530 km depth. The upper boundary of this zone plunges shallowly toward the south at a similar angle to the B axes of the shallower in-plane compressional earthquakes.

The similarities between the north Kuriles and Marianas slabs are striking. The deep Marianas slab is almost planar, with diffuse seismicity dominated by near-down-dip compressional events. A few events indicate along-strike extension. The zone dominated by earthquakes with in-plane shear mechanisms corresponds to an overturned segment of slab below a gentle bend at 300–400 km depth. The single in-plane extensional event suggests that the slab may be bending along-strike as well as down-dip. Whatever the reasons for the different mechanisms, the spatial segregation of events with different mechanisms suggests that this behaviour is controlled at least in part by subtle complexities in slab shape.

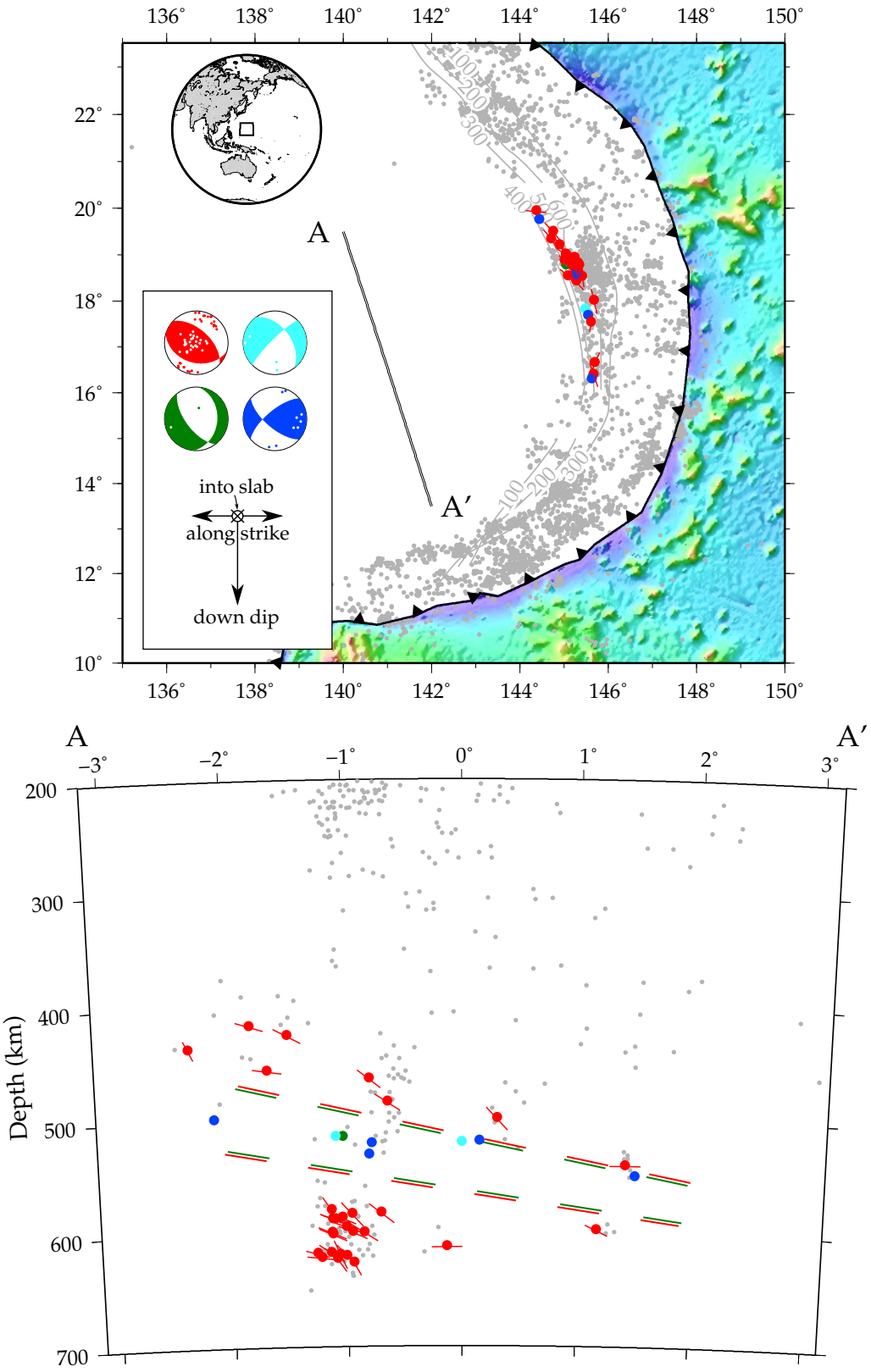

Figure 5.5: Locations and focal mechanisms of deep earthquakes in the Marianas slab in plan view and cross section projected along the line A–A′. Grey contours correspond to the best-fitting surface to seismicity. Bathymetry is shown east of the trench. EHB locations are plotted as grey dots, while earthquakes with gCMT solutions are plotted as larger coloured dots. Each colour represents a different focal mechanism type, as shown in the inset (upper right). For 'down-dip' compressional events (red), B axes are also drawn. The paired red and green lines represent the boundaries between different tectonic regimes in the slab. Individual P and T axes are superimposed on each focal mechanism type. Down-dip is down, and inward-facing slab-normal into the page.

5.4.4 New Britain-Solomons

The Solomon Sea Plate is currently subducting beneath New Britain and the Solomon Islands. It is probably early to mid-Tertiary in age (see review in Honza et al., 1987), subducting at 55–130 mm/yr along the New Britain Trench (Wallace et al., 2004). It is therefore relatively young; temperatures within the slab are probably higher than those in other slabs investigated in this study.

Deep seismic activity beneath New Britain and the Solomons is sparse but sufficient to estimate the shape of the subducting slab from the surface down to ∼600 km depth (Figure 5.6). The Wadati-Benioff zone is split into northwest and northeast dipping segments. The eastern segment beneath the Solomon Islands dips almost vertically at 200–400 km depth, striking north-northwest. It then shallows abruptly, and the strike rotates anticlockwise. The western segment dips steeply beneath New Britain. The shape of the deepest part of the slab is poorly constrained.

The level of seismic activity within the Solomons slab decreases rapidly between 200 and 300 km depth. At >300 km depth, most earthquake activity within the Solomons Wadati-Benioff zone is clustered along narrow bands or lineations. Within the eastern segment, the most prominent lineation is almost horizontal, trending toward the north-northwest. Its location is consistent with marking a sharp concave-up bend in the slab. This hypothesis is supported by available focal mechanisms, which indicate in-plane compression with B axes parallel to the lineation (red). At 450–500 km depth, a possible short eastward-plunging lineation, is marked by in-plane extensional earthquakes which have B axes parallel to the lineation and T axes in-plane (cyan). A larger dataset and more accurate locations are required to confirm the presence of this second lineation.

Within the western segment, another lineation is observed, plunging at ∼40° toward the west. Earthquakes again indicate the slab is undergoing extension perpendicular to the hinge, with focal mechanism B axes parallel to the lineation (purple). The focal mechanisms and distribution of earthquakes are consistent with a convex-up bend in the slab.

The seismic lineations and rotation of B axes away from a horizontal orientation in the Solomons Slab can both be explained by folding of the slab. The deep-focus earthquakes indicating in-plane extension are unusual, but these can also be explained if convex-up (antiformal) bending induces in-plane tension in the upper seismogenic part of the slab. In this model, the lower mantle is still resisting subduction, but the shape of the slab modifies the local strain field. The sparse seismic activity and earthquake clustering along narrow lineations rather than broad bands may be the result of higher temperatures within the Solomons slab at 300–600 km depth (see §5.5).

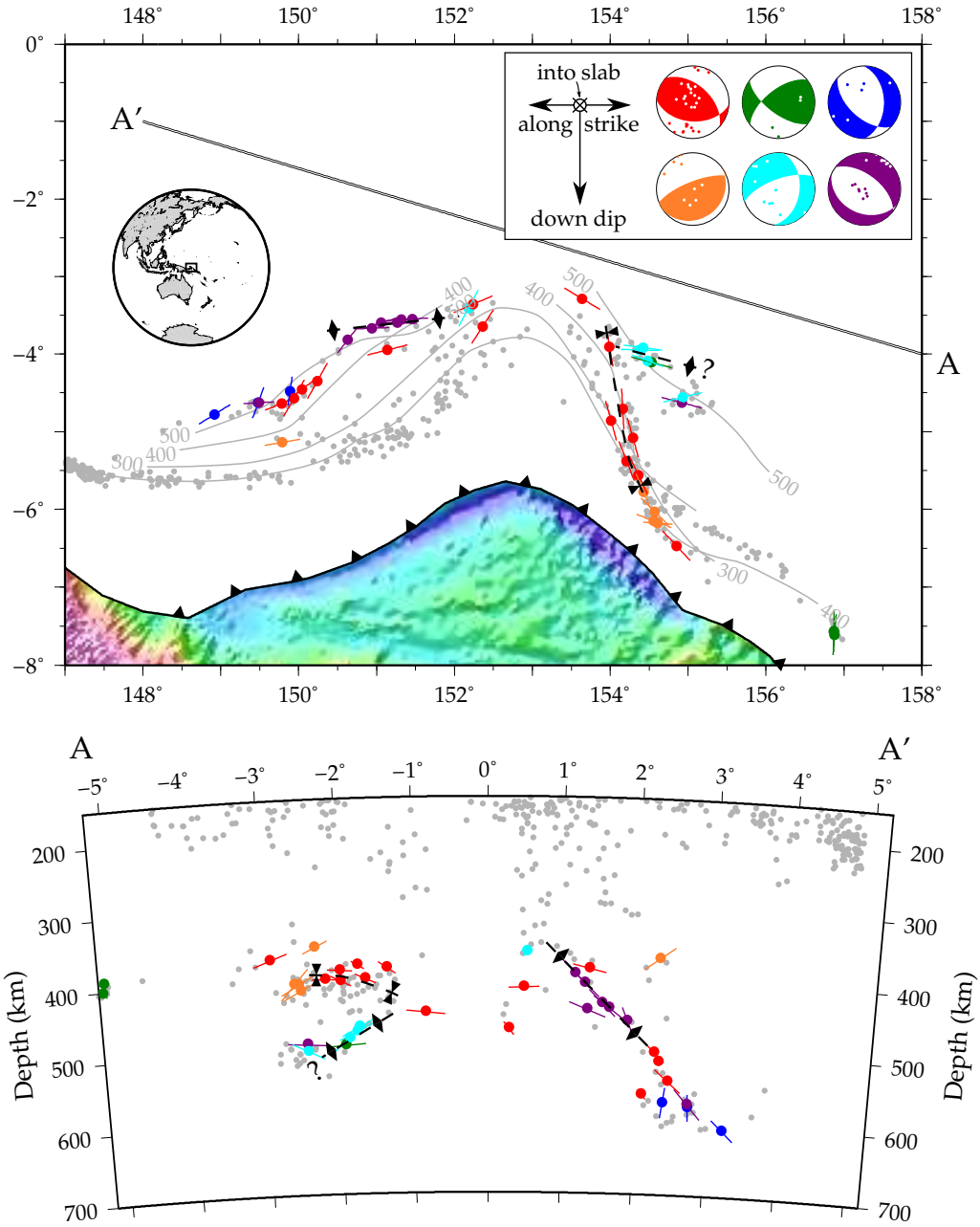

Figure 5.6: Locations and focal mechanisms of deep earthquakes in the New Britain-Solomons slab in plan view and cross section projected along the line A–A′. Note that as in other figures the cross section is drawn looking at the upper surface of the slab, with the eastern limb on the left hand side of the section. Grey contours correspond to the best-fitting surface to seismicity. Bathymetry is shown south of the trench. The dashed black line with synform symbols marks a concave-up fold in the slab, and the lines with antiform symbols mark inferred convex-up folds. EHB locations are plotted as grey dots, while earthquakes with gCMT solutions are plotted as larger coloured dots with lines representing the orientation of the B axes. Each colour represents a different focal mechanism type, as shown in the inset (upper right). Individual P and T axes are superimposed on each focal mechanism type. Down-dip is down, and inward-facing slab-normal into the page.

5.4.5 Tonga

The Tonga-Kermadec subduction zone accounts for more than half of all deep-focus seismicity worldwide. These high levels of seismicity are probably partially due to cold slab temperatures (e.g. Emmerson and McKenzie, 2007) and high strain rates imposed by the high relative plate velocities at the Tonga Trench. Pacific Plate subduction velocities increase from south to north, and exceed 100 mm/a when back-arc spreading in the overriding plate is taken into account (Müller et al., 2008).

The shape of the Tonga slab is complex (Figure 5.7). North of 22°S, the deep slab is hooked, with the slab dip increasing with depth below 300–400 km depth. South of 22°S the Wadati-Benioff zone is warped, but is no longer hooked. A marked decrease in dip is observed at 500 km depth, followed by an increase at 550–600 km depth. There may be a tear in the slab propagating southwards at ∼500 km depth at ∼23°S (e.g. Giardini and Woodhouse, 1984).

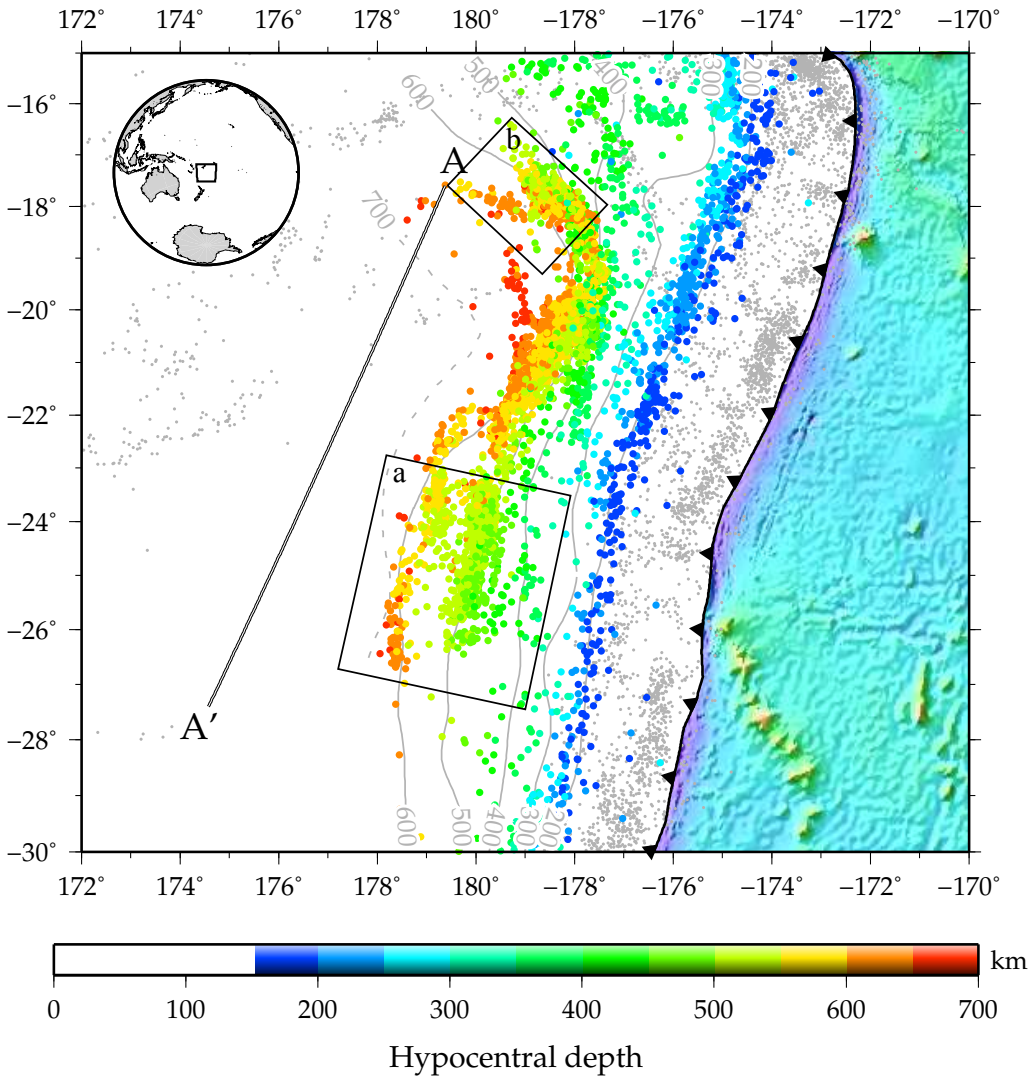

Figure 5.7: Study areas along the Tonga subduction zone. Contours of seismicity are calculated as described in the text. A depth profile through A–A′ is shown in Figure 5.8. Regions marked a and b correspond to the south and north Tonga areas discussed in the text.

Seismic activity within the Tonga slab varies with depth and along-strike. Levels of seismicity decrease between 150 and 250 km depth. A weak increase in seismic activity at 400 km depth is observed in the northern half of the Wadati-Benioff zone. Between 500 and 650 km depth, an extremely dense band of seismicity plunges at 10–20° toward the north.

The Tonga slab has the largest variation in gCMT focal mechanisms of any subduction zone worldwide. Figure 5.8 illustrates the range of mechanisms relative to the local slab reference frame along most of the slab, except for the region marked (b) in Figure 5.7 (addressed in §5.4.5). Although there must be multiple factors influencing the distributions of different focal mechanism orientations, several important features can be identified:

- The most common mechanism type is one with P axes 'down-dip' and T axes 'slab-normal', indicating down-dip compression as per Isacks and Molnar (1971).

- The north end of the Tonga subduction zone (near A) has a large number of in-plane shear mechanisms between 300 and 400 km depth which have a nearly vertical nodal plane.

- Far from being restricted to shallow depths, earthquakes with in-plane extensional focal mechanisms are observed along the subduction zone system at >400 km depth, especially along the southern end of the slab. Unusually, several of the deepest in-plane extensional events have down-dip B-axes.

The large variation in focal mechanisms on the scale of the whole subduction zone makes a single coherent analysis difficult. Instead, I present a detailed analysis of two large subregions (marked (a) and (b) in Figure 5.7) where a range of focal mechanisms are observed.

a) South Tonga, 350–700 km depth

At the southern end of the Tonga subduction zone, the slab is not planar, but has low gaussian curvature. Slab dip varies with depth (Figure 5.9a), decreasing slightly between 200 and 350 km depth, and increasing at 450–500 km. Another decrease and subsequent increase in dip occur between 500 and 600 km depth. This second paired bend becomes tighter from south to north. At 26°S the slab is almost planar, while at ∼23°S the slab between the two bends appears to form a near-horizontal bench. Fischer and Jordan (1991) and Fischer et al. (1991) treat 'outboard' earthquakes between 22 and 26°S as a separate fragment of slab, but EHB catalogue locations suggest that the slab is continuous between the main Wadati-Benioff zone and outboard events, at least in the south (see also Figures 5q and 5r of Giardini and Woodhouse, 1984).

Seismic activity is generally low between 200 and 300 km depth, and increases only slightly down to ∼480 km depth (Figure 5.9c). An extremely dense band of seismicity plunges at ∼5° toward the

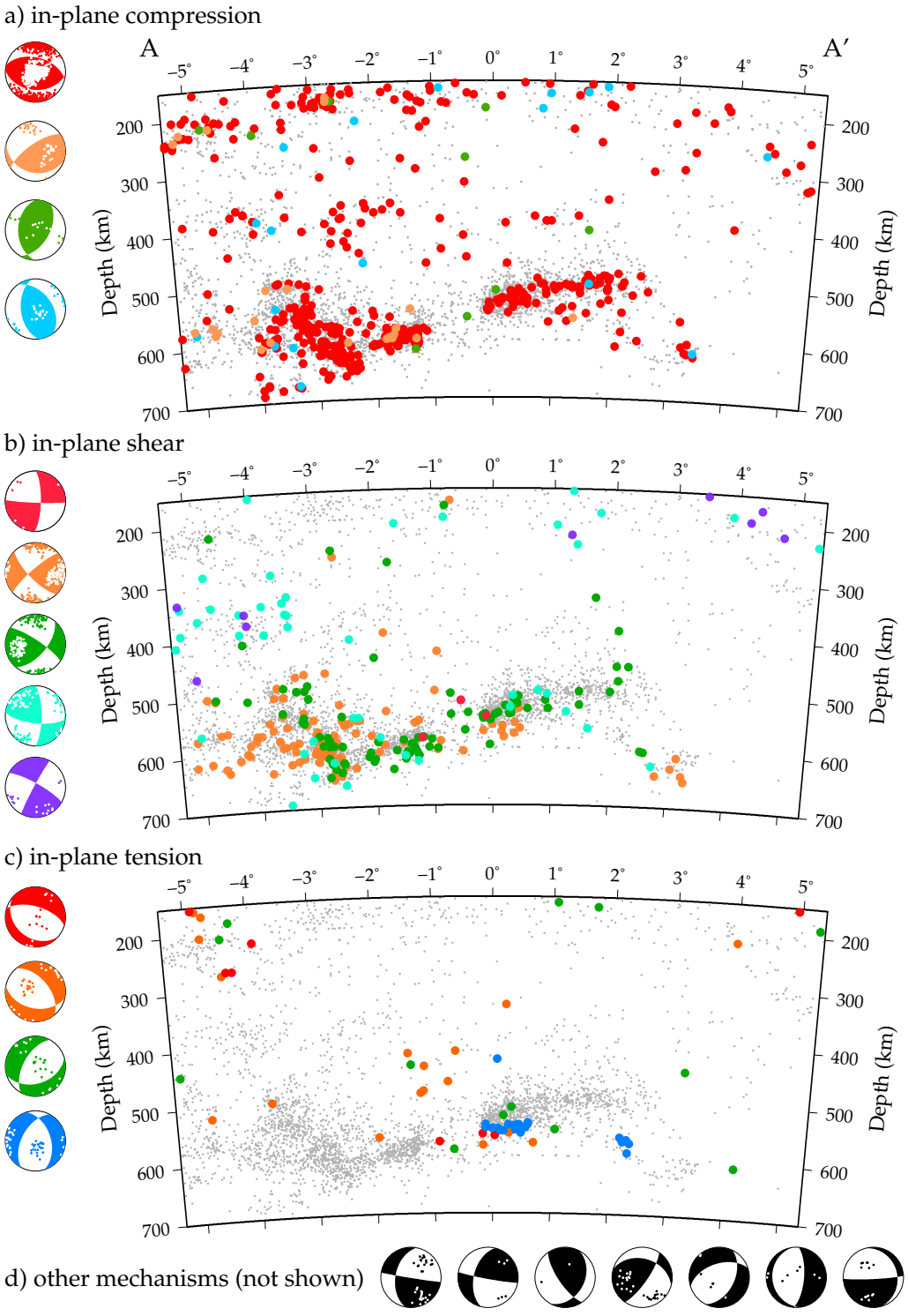

Figure 5.8: Locations and focal mechanisms of deep earthquakes along the profile A–A′ from Figure 5.7, parallel to the Tonga-Kermadec trench. EHB locations are plotted as grey dots, while earthquakes with gCMT solutions are plotted as larger coloured dots. The three plots show the distribution of earthquakes with a) compressional, b) in-plane shear and c) extensional focal mechanisms. Each colour represents a different focal mechanism type, represented to the left of each image. Individual P and T axes are superimposed on each focal mechanism type. Down-dip is down, and inward-facing slab-normal into the page.

north at 480–550 km depth, following the hinge of the prominent concave-up (synformal) bend in the slab. Another less-active band of earthquakes marks the convex-up (antiformal) bend (Figure 5.9d).

The majority of earthquakes within the main Wadati-Benioff zone indicate in-plane, approximately

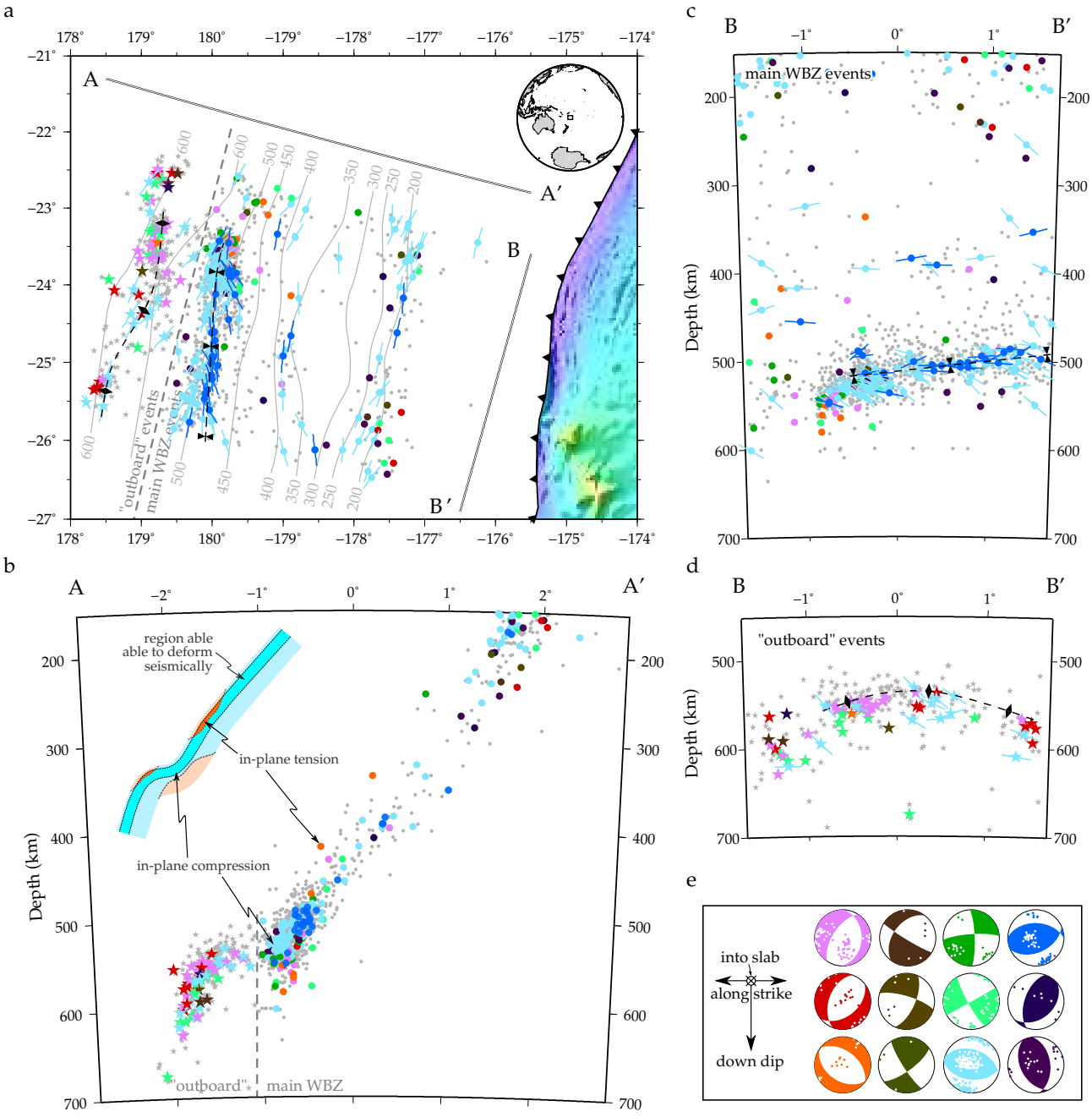

Figure 5.9: a) Locations and focal mechanisms of deep earthquakes in the south Tonga slab. Grey contours correspond to the best-fitting surface to seismicity. Bathymetry is shown east of the trench. The dashed black line with synform symbols marks a concave-up fold in the slab, and the line with antiform symbols marks a convex-up fold. EHB locations are plotted as grey dots, while earthquakes with gCMT solutions are plotted as larger coloured dots, where each colour corresponds to a different focal mechanism orientation. 'Down-dip' compressional events (blue,cyan) also have B axis orientations plotted. b) Cross section along profile A–A′. c) Cross section along profile B–B′, including earthquakes to the east of the grey dotted line in (a). d) Cross section along profile B–B′, including earthquakes to the west of the grey dotted line in (a). e) Focal mechanisms corresponding to each colour in subfigures a–d. Individual P and T axes are superimposed on each mechanism type. Down-dip is down, and inward-facing slab-normal into the page.

down-dip compression (blue, cyan). A few events at 300–500 km depth indicate in-plane extension (orange, pink). These correspond to a double seismic zone reported at 350–420 km depth, with in-plane extension in the upper plane (Wiens et al., 1993). Although Wiens et al. (1993) prefer to

explain this double seismic zone by transformational faulting, bending cannot be ruled out, and the best-fitting surface to seismicity tentatively supports this alternative explanation.

Within the synform in the slab, in-plane compression dominates. A subset of the earthquakes within the synform (blue) have focal mechanisms with B axes parallel to the elongation of seismicity and the shallowly northward dipping hinge of the bend. These events cluster along the top edge of the densest seismicity. Deeper events (cyan) have B axes rotated clockwise. The increased along-strike component of compression may also be related to the continued development of the conical folds. North of 24°S, where the slab may be torn (Giardini and Woodhouse, 1984), the pattern of focal mechanisms is more complex. In plane extensional (pink, orange) and shear events (green) become more common.

West of 180°E, 'outboard' earthquakes indicate a mixture of in-plane tension (pink, red, orange), shear (green) and compression (blue, navy blue, purple). The presence of both in-plane tensional and compressional events is consistent with bending of the slab (see cross-section cartoon in Figure 5.9). An unusual feature of the in-plane tension focal mechanisms is that the B axes are most commonly oriented down-dip and perpendicular to the convex-up fold in the slab. One possible explanation for this along-strike extension is the superposition of bending strains on an in-plane compressional strain field.

b) North Tonga, 500–650 km depth

The deep-focus earthquakes at the northernmost end of the Tonga slab represent the most seismically active volume in the Earth. They include some of the largest earthquakes with the most prolific aftershock sequences. For example, the M_W 7.6 event earthquake on 9 March 1994 had 40 aftershocks with $M_W > 4.5$ (Wiens et al., 1994).

Although plan views and cross sections of seismicity suggest that the zone of greatest earthquake density is planar (Giardini and Woodhouse, 1984; Wiens and Snider, 2001), it is better described as a band plunging ∼40–45° to the southeast (Figures 5.10 and 5.11). Seismicity above this band is nearly vertical, while below, earthquakes are scattered and include several 'outboard' events displaced southwards from the main seismicity.

If the deep north Tonga slab is taken to be subplanar and almost vertical, then many of the focal mechanisms have nodal planes sub-parallel to the slab surface (Figure 5.10a–d, brown, red, orange mechanisms). Giardini and Woodhouse (1984) suggest that this nodal plane corresponds to a narrow shear zone, facilitating slab movement down and to the west relative to the juxtaposed aesthenosphere. Further from the slab surface, the majority of earthquakes have gCMT focal mechanisms with in-plane P- and T-axes (blue, cyan), indicating extension parallel to the band of densest seismicity.

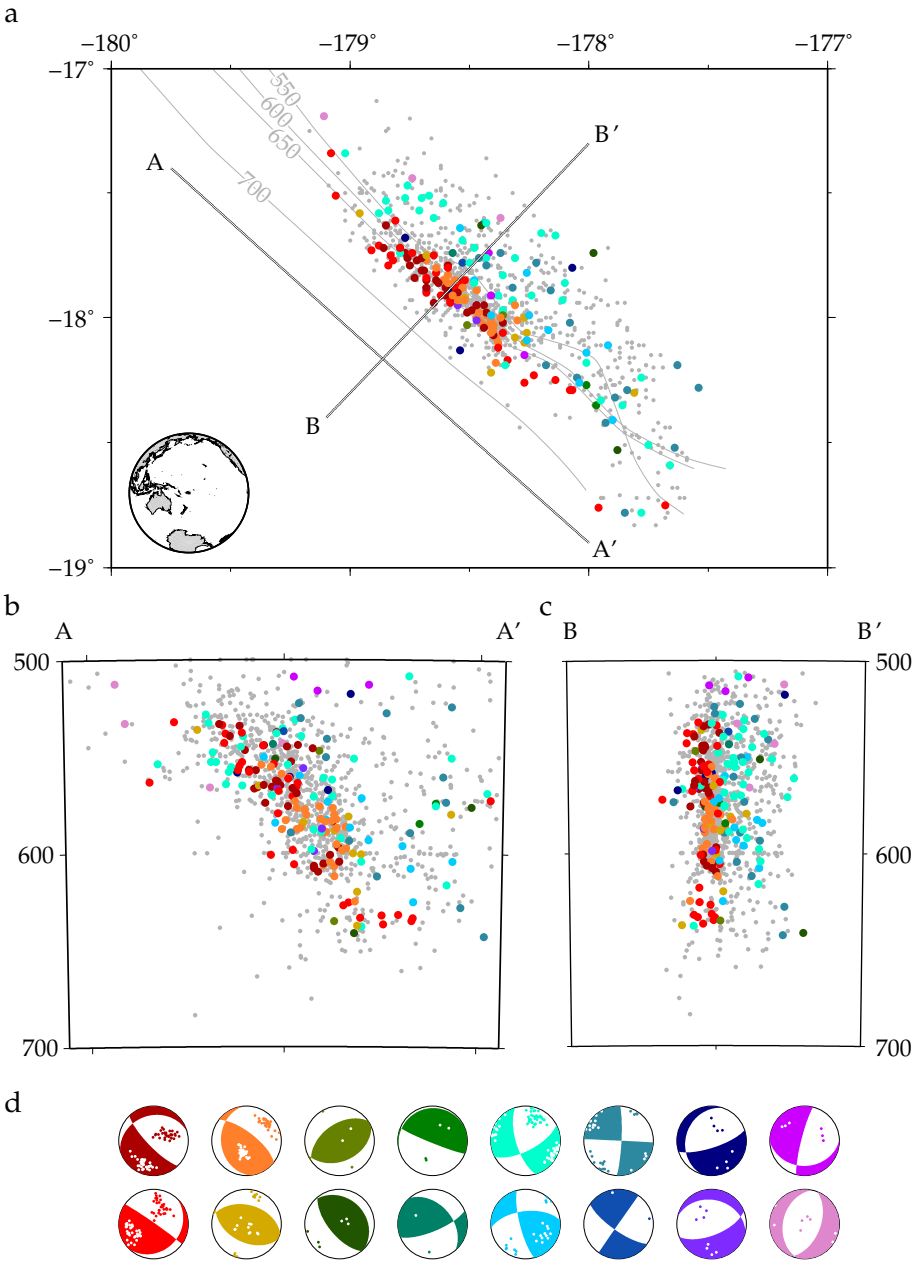

Figure 5.10: Results of focal mechanism analysis conducted for the best-fitting surface to deep North Tonga seismicity without including outboard earthquakes. a) Earthquake locations. Contours of the best-fitting surface to seismicity are shown in black. EHB locations are plotted as grey dots. EHB/gCMT locations for earthquakes with gCMT solutions are plotted as larger coloured dots, where each colour corresponds to a different focal mechanism orientation. b) Cross section along profile A–A′. c) Cross section along profile B–B′. d) Focal mechanisms corresponding to each colour in subfigures a–c. Individual P and T axes are superimposed on each mechanism type. Down-dip is down, and inward-facing slab-normal into the page.

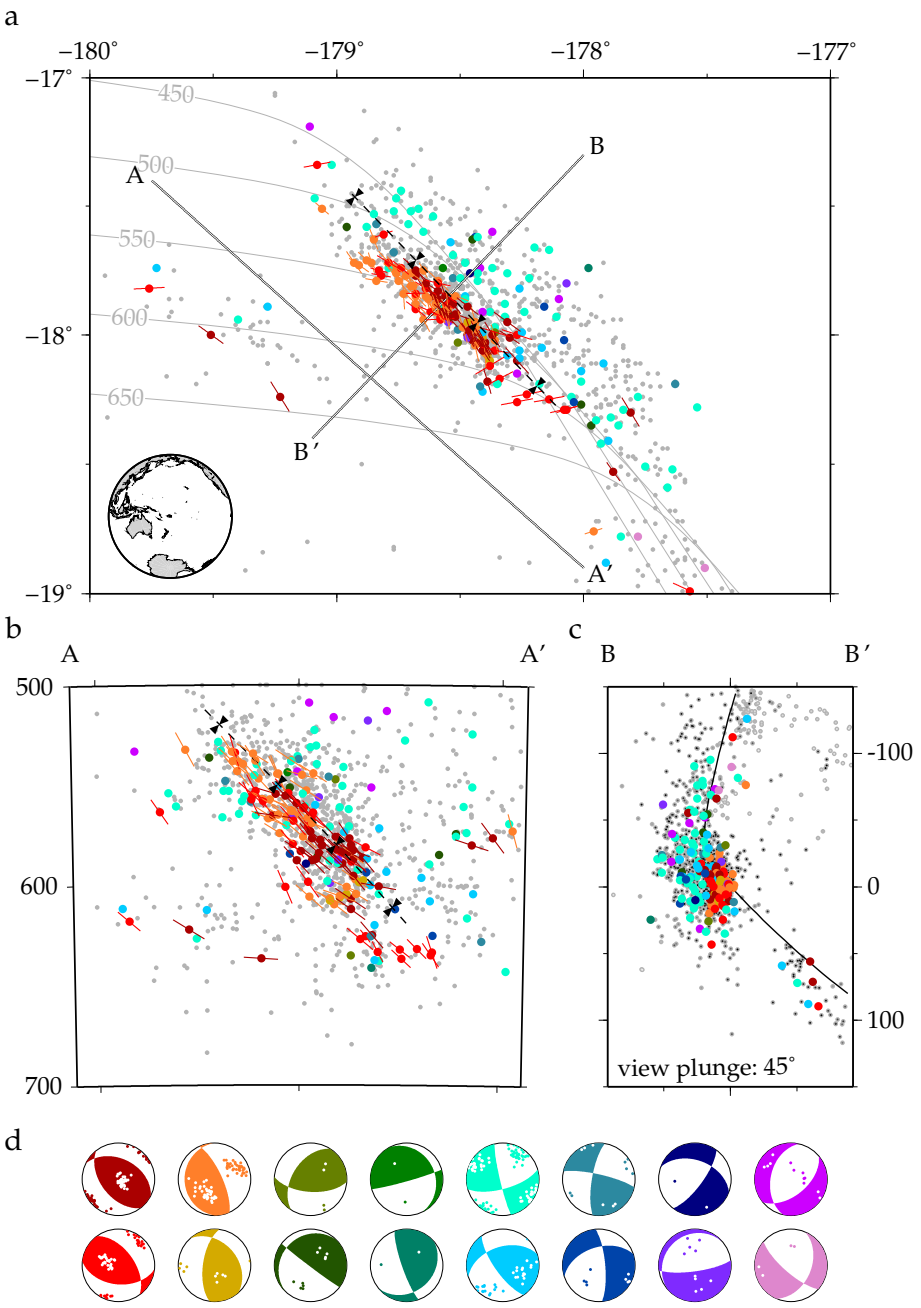

Figure 5.11: Results of focal mechanism analysis conducted for the best-fitting surface to deep North Tonga seismicity as in Figure 5.10 but the shape approximating the surface to seismicity has been adjusted to account for a bend in the slab along the band of densest seismicity. a) Earthquake locations. Contours of the best-fitting surface to seismicity are shown in black. EHB locations are plotted as grey dots. EHB/gCMT locations for earthquakes with gCMT solutions are plotted as larger coloured dots, where each colour corresponds to a different focal mechanism orientation. In-plane compressional events (brown, red, orange) have B axes plotted. b) Cross section along profile A–A′. c) Cross section along profile B–B′, looking along the hinge line of the inferred fold in the slab at an angle of 45° from the horizontal. EHB locations are shaded according to their distance from the profile plane. d) Focal mechanisms corresponding to each colour in subfigures a–c. Individual P and T axes are superimposed on each mechanism type. Down-dip is down, and inward-facing slab-normal into the page.

The insights gleaned from the Kuriles, Izu-Bonin, Solomons and south Tonga slabs can be used to advance an alternative to the slab-parallel shear-zone interpretation. The southeastward-plunging band of seismicity is reminiscent of the clustering of earthquakes observed along the hinges of bends in other slabs. Looking along this band, the distribution of seismicity resembles a fold, with the previously neglected 'outboard' earthquakes contained within the lower limb (Figure 5.11a–d). Re-analysing the earthquake focal mechanisms with this modified slab shape, the events which have subvertical nodal planes (brown, red, orange) now indicate in-plane compression, with B axes parallel to the band of seismicity and the inferred fold in the slab, just as observed in other subduction zones. With increasing distance from the surface of the slab, the focal mechanism axis closest to slab normal evolves from T to B to P, again consistent with bending. It should be noted that the in-plane bend-perpendicular axes evolve from P to B, rather than from P to T. This mechanism change is identical to that observed in the antiformal bend in the south Tonga slab. Like the south Tonga slab, this variety and spatial distribution of focal mechanisms may be explained by the superposition of bending strain on an in-plane compressional strain field.

5.5 Discussion

5.5.1 Slab bending and buckling

This joint study of slab shape and seismic activity has revealed that bending or buckling is a common feature of subducting slabs in the mantle transition zone. The orientation and high amplitude of the strain field within zones of bending is revealed by increased seismic activity and a common co-linearity between the focal mechanism B axes and the hinge of the lithospheric-scale fold. Synforms in the Kuriles, Izu-Bonin, Solomons and south Tonga slabs are dominated by earthquakes with in-plane P axes, while an inferred antiform in the Solomons slab has earthquakes with in-plane T axes. An antiform in the south Tonga slab has a mixture of earthquakes with in-plane P axes and in-plane T axes, consistent with the zero-strain surface lying within the seismogenic zone.

The bands of seismicity highlighted in this study constitute a large proportion of all deep-focus earthquakes within several subduction zones. The broad, extremely dense bands of seismicity present along the Izu-Bonin and Tonga-Kermadec subduction zone systems constitute more than half of all deep-focus earthquakes recorded in the EHB catalogue, and therefore make up the majority of the broad peak of seismicity around 550 km in global depth distributions of seismicity. Global compilations are commonly used to support a physical mechanism of deep earthquake generation (e.g. Omori et al., 2004; Green et al., 2010). Specifically, the proposition that different physical mechanisms govern intermediate and deep-focus earthquake generation is largely founded on the relative sparsity of earthquakes at $\sim$300 km depth, and may therefore be incorrect.

When added to the accepted roles of negative slab buoyancy and resistance to flow at the base

of the upper mantle, bending of stiff slabs is capable of explaining much of the variation in focal mechanisms reported by Apperson and Frohlich (1987). Internally-derived stresses from phase transitions (e.g. Wiens et al., 1993) and thermal expansion are not explicitly required to explain any of the patterns reported in this present study and may be largely relaxed, as suggested by Bina (1997).

5.5.2 *Deformational styles*

Some studies of subduction zone seismicity use moment-slip relationships to suggest that slabs may thicken by 50–100% as they traverse the upper mantle (e.g. Fischer and Jordan, 1991; Holt, 1995; Nothard et al., 1996a; King, 2001). These estimates are based on the assumption that slab deformation is homogeneous with depth through the slab and occurs by pure shear. If much of the deformation within the Izu-Bonin and Tonga subducting plates can be attributed to bending, compression in the seismogenic part cannot be attributed to whole slab thickening. A further consequence of continued bending in the same region over 10^5–10^6 years is that large parts of the slab may escape significant deformation.

Even within zones of localised deformation, shortening may be accommodated by simple shear or pure shear. Both of these modes may be important in plate bending, but result in a different relationship between the hinge and the locus of deformation. Simple shear accommodating compression can accentuate bending if the zone of shear within one limb makes a $< 45^\circ$ angle with the other limb. The distribution of earthquakes suggest that sub-vertical shear may be responsible for the majority of seismic activity in the north Tonga slab (Figure 5.11c).

Bending can also resolve differences between seismic strain rates and estimates of slab-lower mantle convergence. Holt (1995) suggested that seismic deformation accounts for no more than $\sim$60% of the subduction velocity of the south Tonga slab. The subduction velocity was calculated without back-arc spreading, so this bound almost certainly represents an overestimate. Without bending, the remainder of the plate convergence rate must be accommodated by aseismic deformation or penetration into the lower mantle, for which there is little evidence. Bending of the Tonga slab allows most of the relative convergence between the slab and lower mantle to be taken up by relative motion between the upper and lower parts of the slab, without requiring significant aseismic deformation of the cold slab core or lower mantle penetration.

Previous studies have suggested that in-plane rotation of focal mechanisms provides evidence for along-strike shear of the Tonga slab (e.g. Giardini and Woodhouse, 1984; Bailey et al., 2012). Giardini and Woodhouse (1986) propose that the gap in deep focus seismicity at $\sim$23°S represents the continuation of the Louisville Ridge; an interpretation that requires 500 km of southwards shear of the deep Tonga slab relative to the surface. The present study illustrates that in-plane rotation of focal mechanisms is more simply explained by slab bending. Consequently, the gap in seismicity in

the deep Tonga slab is unlikely to represent a subducted ridge. The absence of dense seismicity may be related to propagation of the tear in the slab recognised by Giardini and Woodhouse (1984).

5.5.3 *The role of temperature*

Within cold slabs, such as Izu-Bonin and Tonga, extremely dense seismicity around bends in the slab implies that it is brittle yielding that facilitates changes in slab shape. Material viscosity within cold slabs may therefore be much higher than the 'slab viscosity' values in numerical models designed to match observed deformation (e.g. Zhong and Gurnis, 1995; Alisic et al., 2010; Bailey et al., 2012). Highly viscous slab material is predicted by experimental data (e.g. Mei et al., 2010), and is not at odds with geoid highs above subducting slabs (Moresi and Gurnis, 1996; Zhong and Davies, 1999) if brittle processes control deformation. As a result, neither high aesthenospheric viscosities nor large frictional stresses are required to support slabs in the upper mantle (Davies, 1980).

The Solomons slab is probably the youngest of the subducting oceanic plates analysed in this study. Slab temperatures will be higher than the cold western Pacific slabs and in the mantle transition zone they may be similar to those within the South American slab. This increased temperature is reflected in low seismic activity and clustering of earthquakes along the hinge lines of inferred slab folds. The implication is that ductile processes can accommodate higher strain rates in warmer slabs. Although grain size may influence slab strength (Karato et al., 2001), there is little evidence to suggest that cold slabs have lower material strength than warm slabs.

Narrow belts of earthquakes like those observed in the Solomons slab typify deep-focus activity in other subduction zones. Within the South American slab, long trains of earthquakes are observed at 500–650 km, roughly parallel to the strike of the subduction zone (e.g. Barazangi and Isacks, 1976). A lineation of earthquakes is also observed at $\sim$603 km depth beneath New Zealand (Boddington et al., 2004). By analogy with the Solomons slab, these earthquake lineations signify high strain rates accommodating slab buckling at the base of the upper mantle.

5.5.4 *Lower mantle penetration*

It is notable that the Marianas and north Kuriles slabs are almost planar, with diffuse intermediate and deep-focus earthquake distributions. Tomographic images indicate that both slabs may be subducting directly into the lower mantle (van der Hilst et al., 1991; Li et al., 2008; Koulakov et al., 2011). Rather than being controlled solely by slab age (e.g. Goes et al., 2008), the penetration of slabs into the lower mantle may be controlled more directly by the total negative buoyancy force that can be transmitted to the upper-lower mantle boundary. Bent slabs act as largely broken plates, unable to transmit forces along the full slab length. If these hypotheses are accurate, the penetration of subducting lithosphere into the lower mantle will be episodic.

5.6 Conclusions

In this study, I show that the shapes of subducting slabs are intimately related to seismic deformation. The hinges of folds in the Kuriles, Izu-Bonin, Solomons and Tonga slab are sites of intense seismic activity, which have focal mechanisms rotated such that the principal axes are aligned parallel and perpendicular to the slab and hinge. Many of the systematic deviations from down-dip compression or extension can be explained in terms of slab bending. As suggested by Isacks and Molnar (1971), the negative buoyancy of the slab and resistance to flow in the lower mantle remain the primary forces acting on the slab. However, the effect of these forces on the stress and strain field is controlled by slab morphology.

Focal mechanisms along subduction zone systems such as Tonga-Kermadec and Izu-Bonin do not require significant along-strike shear. Internal stresses and strains resulting from phase transitions or thermal expansion do not appear to control deformational styles.

The frequency of earthquakes in zones of bending dominates seismic catalogues of deep-focus earthquakes. Consequently, the global depth distribution of deep earthquakes may be controlled by changes in slab morphology, rather than by the physical mechanism behind brittle failure.

The shapes of subducting slabs are constantly evolving. High viscosity in the coldest slabs is offset by their ability to undergo seismic deformation, resolving the apparent conflict between experimental results and geophysical observations of the geoid and slab contortions. In warmer slabs, viscous creep can accommodate higher strain rates. Narrow lineations of seismicity beneath the Solomons, South America and New Zealand may represent localised slab buckling.

If much of the seismicity within subducting slabs represents strain due to bending then slabs may undergo less thickening than previously suggested. Localised shortening in the seismically active part of slabs such as Tonga may be coupled to in-plane extension in aseismic parts of the slab. Bending provides a potential explanation for discrepancies between estimates of seismic strain rate and convergence velocities between the slab and lower mantle (e.g. Holt, 1995).

This study describes how slab shape controls seismic activity and deformation within subducting slabs, but not the factors influencing the initiation and development of bending. It is hoped that further study may elucidate the factors influencing this development, which may include phase changes (Willemann and Davies, 1982), variations in grain size (e.g. Karato et al., 2001), pre-existing plate structure, subduction velocity and plate age.

6 *Active shear zones within subducting slabs*

6.1 Introduction

The frictional and elastic properties of rocks close to the surface, coupled with the decrease in mechanical strength when rocks become fractured, results in a situation where faults grow over time, and where large shallow earthquakes only occur on pre-existing faults. Arrays of tensile cracks advance in front of fault tips, and are progressively linked by shear faults as the faults grow (Pollard et al., 1982; Cox and Scholz, 1988a,b).

The strength of dry rocks at high pressure precludes the maintenance and growth of a network of open cracks. If deep faults do not form by the same mechanism as their shallow counterparts, then large deep earthquakes in subduction zones may no longer occur on long-lived faults. The seismic properties of seismically active regions may help determine whether fault reactivation is possible (Reynard et al., 2010; Nakajima et al., 2011), but the high resolution tomography required to do this is rarely feasible. Determining whether deep earthquakes lie along fault-like structures is more straightforward, as it requires only high quality locations and focal mechanisms. Wiens and Snider (2001) argued that earthquakes with similar waveforms provided evidence for repeated fault plane rupture (see also Chapter 4). Giardini and Woodhouse (1984) projected earthquake locations onto a plane perpendicular to the B axis of a CMT solution (Dziewonski et al., 1981). They presented several examples of areas where lineations of earthquakes aligned with one or both of the two nodal planes of the focal mechanism. They argued that these lineations corresponded to long-lived shear zones within the slab. Several extremely large lineations were observed within the Tonga slab, some reaching lengths $>$600 km. The method was later used by Lundgren and Giardini (1992) for the Bonin slab.

It is now two decades since the work of Giardini and Woodhouse (1984) and Lundgren and Giardini (1992). Earthquake catalogues have increased greatly in size and accuracy (Engdahl et al., 1998). It is therefore an opportune time to revisit the concept of shear zones at great depths within subducting slabs.

6.2 Data and methodology

Centroid moment tensors are obtained from the gCMT catalogue (formally Harvard CMT; Dziewonski et al., 1981) from January 1978 to January 2011. Earthquake locations used in this study are those contained in the EHB catalogue 1960–2007 (Engdahl et al., 1998, and updates). Post-2007 earthquake locations are taken from the gCMT catalogue.

For each earthquake in the gCMT catalogue, I select all EHB catalogue earthquakes within a cylinder with axis of length 100 km parallel to the B axis and a 180 km radius. Following Giardini and Woodhouse (1984), I plot these earthquakes and the focal mechanism in the plane perpendicular to the B axis (Figure 6.1). The presence or absence of lineations of earthquakes parallel to each of the nodal planes of the 31 March 1994 earthquake can be assessed by eye. A potential lineation can be seen plunging almost vertically, almost parallel to the steeply dipping nodal plane of the earthquake focal mechanism. In areas of dense seismicity, some earthquakes may be superimposed, and so I also plot the one dimensional estimate of the gaussian kernel density (KDE, $\sigma = 5$; bottom left) of earthquakes versus the angle clockwise from vertical. The identification of the steeply dipping lineation is confirmed in the KDE plot, which reveals a single peak corresponding to an almost vertical lineation (0 and 180°on the y-axis) centered on the CMT solution (0 km along the x-axis).

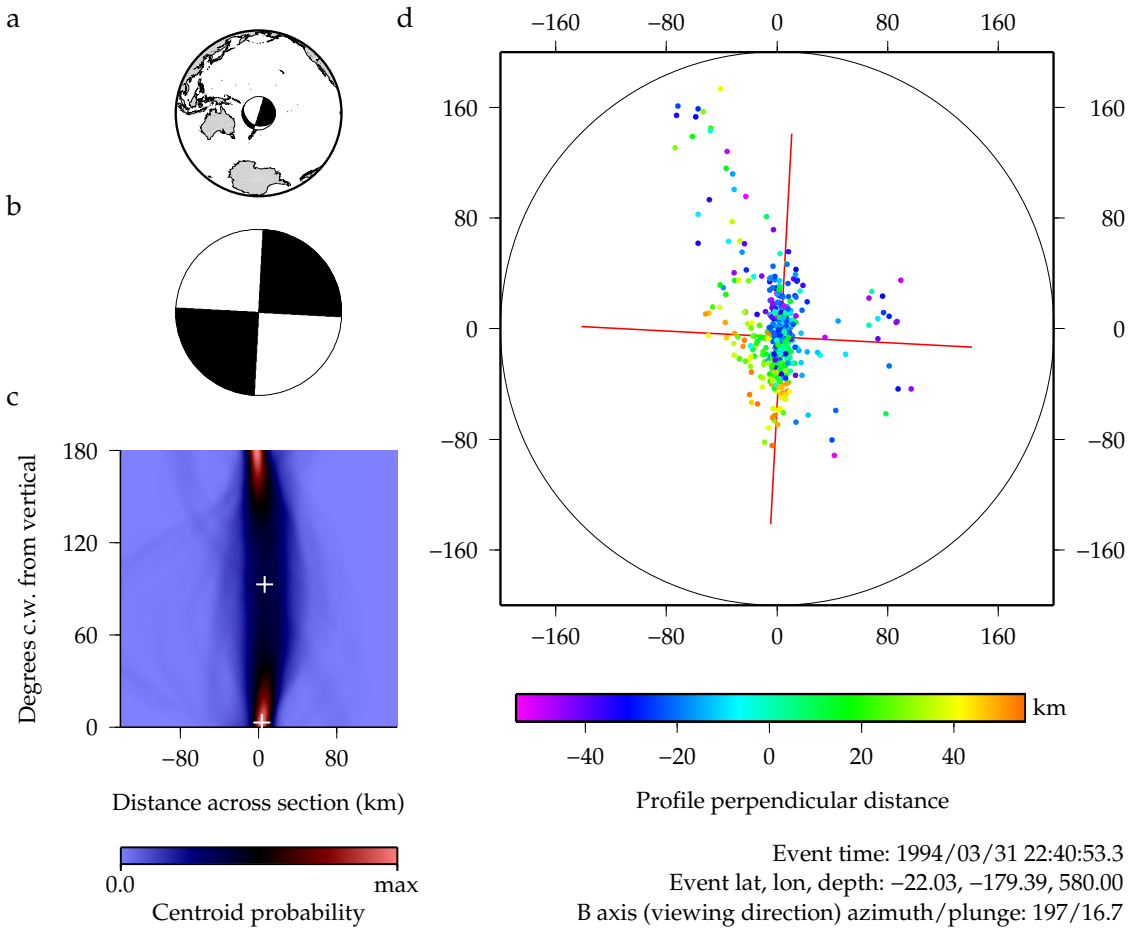

Figure 6.1: Earthquakes close to the EHB location of the 31 March 1994 deep earthquake. a) Location map showing the focal mechanism of the earthquake. b) Focal mechanism rotated into the projection plane, which is perpendicular to the B axis. c) Kernel density estimate for earthquake density at different angles and distances across the section. Each position on this plot represents the probability of an earthquake appearing along a given line in the projection plane. The vertical axis provides the angle of that line relative to vertical, while the horizontal axis gives the offset of that line relative to the center of the projection plane. White crosses mark the maxima of the density function at the angles corresponding to each nodal plane. In this example, a single peak is observed in the bottom center of the plot, very close to the lower of the two white crosses. This suggests the presence of a near-vertical streak of earthquakes in the center of the projection plane. d) The EHB earthquake distribution around the 31 March 1994 earthquake projected into the plane perpendicular to the B axis. The inscribed circle represents a section through the cylinder from which events were selected. The 31 March 1994 earthquake is in the center of this cylinder. The two red lines correspond to the positions of the two white crosses in (c). As previously inferred, the more steeply dipping plane of the focal mechanism solution is co-linear with a dense streak of seismicity.

6.3 Results

6.3.1 Tonga

Giardini and Woodhouse (1984) reported several lineations of earthquakes within the Tonga slab. One of the densest of these lineations is located within the main Wadati-Benioff zone at ∼22°S (their Figure 5l, constructed using the 8 July 1979 earthquake). The same lineation is shown in Figure 6.1. Earthquakes within this lineation represent motion of the shallower slab down relative to the deeper more westerly slab.

Despite the remarkably clear lineation in Figure 6.1, strong lineations or planar features perpendicular to gCMT mechanism B axes are less common than implied by the results of Giardini and Woodhouse (1984). Figure 6.2 shows the distribution of earthquakes around the hypocenter of the 21 March 1993 earthquake at 589 km depth at the northern end of the Tonga slab. The earthquakes in this region reveal a curved Wadati-Benioff zone, with the 21 March 1993 earthquake and densest seismicity in the inner bend. The KDE plot reveals a high earthquake density in the center of the selected region with no particular direction of elongation. The overall earthquake distribution is therefore best described as a single equant cluster in this orientation. The earthquakes are distributed along a band roughly parallel to the B axis.

The absence of a well-defined lineation parallel to one of the nodal planes of the 21 March 1993 earthquake is surprising, because plan views and cross sections of seismicity both reveal apparently planar features (e.g. Billington and Isacks, 1975, Figures 4.10 and 5.10). Additionally, Giardini and Woodhouse (1984) report a lineation parallel to the steeply dipping nodal plane of the nearby 21 January 1977 and 28 July 1988 earthquakes (their Figures 5a and 5b).

The variation in apparent alignment of earthquakes highlights the importance of using appropriate projections to view seismicity. Presenting earthquake locations using plan views and cross sections can be misleading, but so too can selecting earthquakes that best reveal lineations parallel to nodal planes. The mechanism of the 21 January 1977 earthquake selected by Giardini and Woodhouse (1984) is unusual. Their figure 5b uses a more typical focal mechanism; despite plotting many of the same earthquakes, the identified lineation is much shorter.

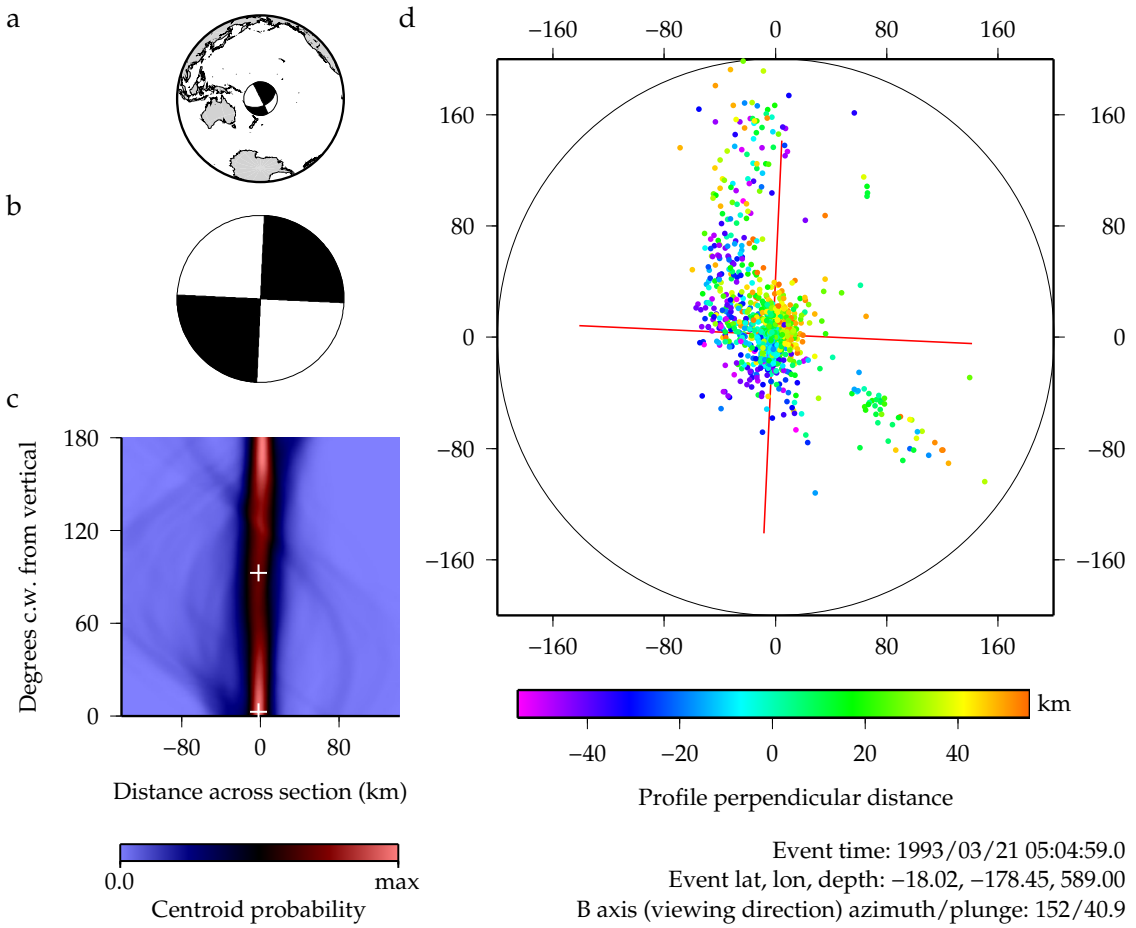

Figure 6.2: Plane of seismicity parallel to one of the nodal planes of the 21 March 1993 deep earthquake. Subplots are as described in Figure 6.1. The kernel density estimate in (c) reveals a region of high earthquake density, with no well-defined angular maximum. There is no clear lineation parallel to either nodal plane in this projection (d).

Another example of the problems associated with viewing angle is illustrated in Figure 6.3. The subplots are constructed using four earthquakes separated by less than 100 km located in a dense region of seismicity along the South Tonga arc at ∼23°(see §5.4.5). The first subplot (top left) reveals a broad band of seismicity running for more than 100 km parallel to the more shallowly dipping nodal plane of the 17 June 1978 earthquake. This plot is an updated version of Figure 5j in Giardini and Woodhouse (1984). Although this earthquake was used as evidence for an extremely active shear plane, the mechanism is not representative of most of the earthquakes plotted. The densest seismicity in the second subplot (marked by the intersection of the two red lines) reveals no evidence of a lineation. One potential lineation parallel to the more steeply dipping nodal plane is marked by a dotted line, but is unconvincing. The other two subplots again fail to reveal clear lineations parallel to one of the nodal planes. The last of the earthquakes represents a more common focal mechanism for the area.

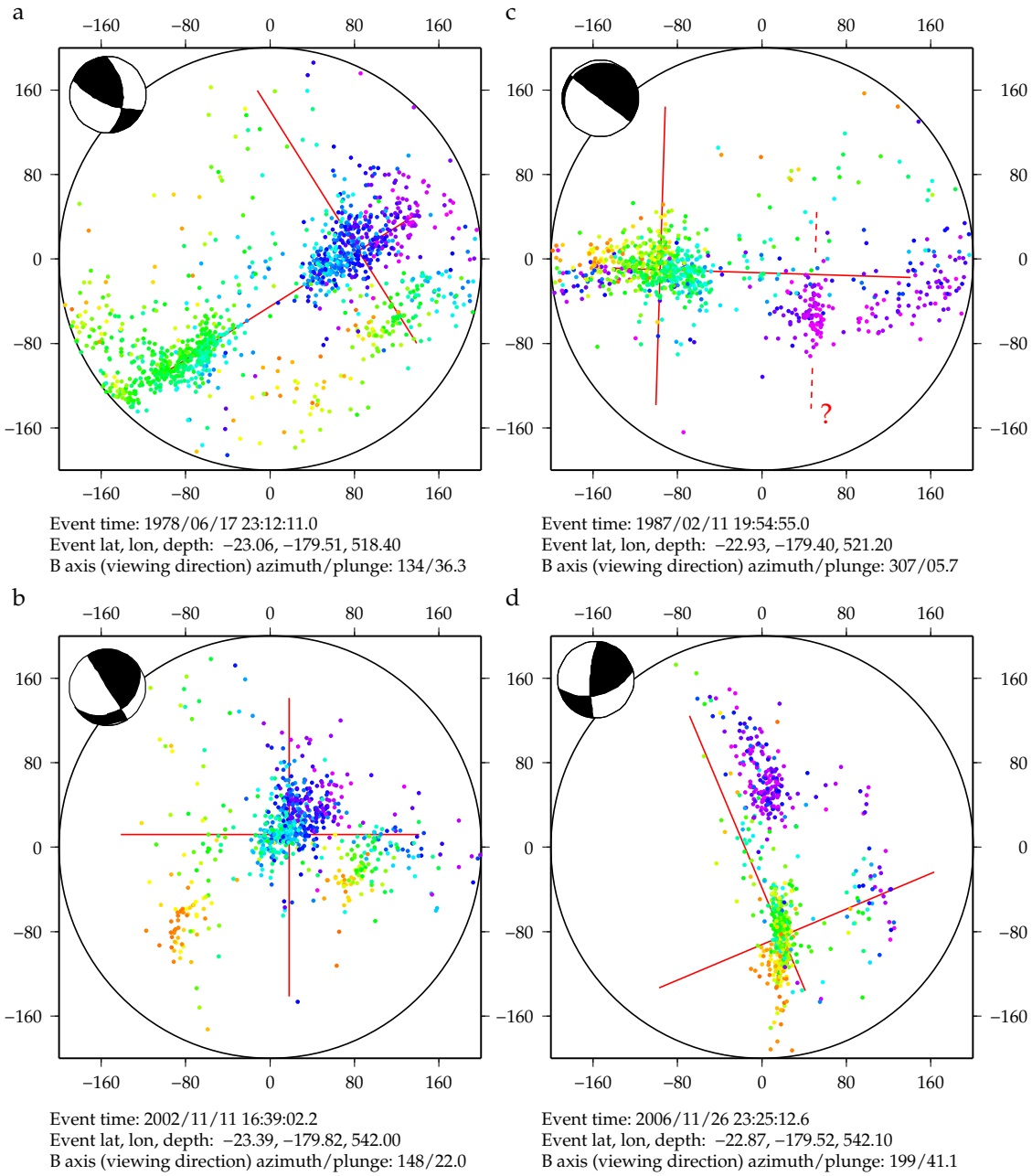

Figure 6.3: Comparison of the apparent distribution of south Tongan deep earthquakes when viewed along the B axis of four nearby earthquakes. Focal mechanisms for each earthquake are shown in the top left hand corner of each subplot. Horizontal and vertical scales are in kilometers. a) The 17 June 1978 earthquake was used by Giardini and Woodhouse (1984) to infer a large northeastward dipping shear zone along the south Tonga subducting slab. b) The nearby 11 November 2002 earthquake reveals no clear lineations parallel to either of the nodal planes. c) The 11 February 1987 earthquake is only 20 km away from (a), yet it has a completely different focal mechanism. A possible subvertical lineation is observed, but does not pass through the location of the master event. d) Projection the earthquakes perpendicular to the B axis of the 26 November 2006 earthquake reveals the same broad lineation as in (a), but the lineation is not parallel with either nodal plane.

Earthquake locations and focal mechanisms can also be visualised by plotting the intersection of the nodal planes with any given plane. This technique has the potential to reveal the relationship between deep earthquake fault planes and (for example) the slab surface. The plot is equivalent to a map of fault traces at the surface of the Earth — except that deep fault planes cannot in general be distinguished from their auxiliary planes, so both nodal planes are plotted. An example of this plotting procedure is shown in Figure 6.4. The shape of the south Tonga slab is modelled after discarding the outboard events deeper than 500 km and west of ∼180°E. The lines for each nodal plane are coloured to reflect the angle between the nodal plane and the local best-fitting plane to seismicity. The simplest form of the stress guide hypothesis (Isacks and Molnar, 1971) predicts that the nodal planes should intersect the slab along-strike at an angle of ∼45° (green-cyan).

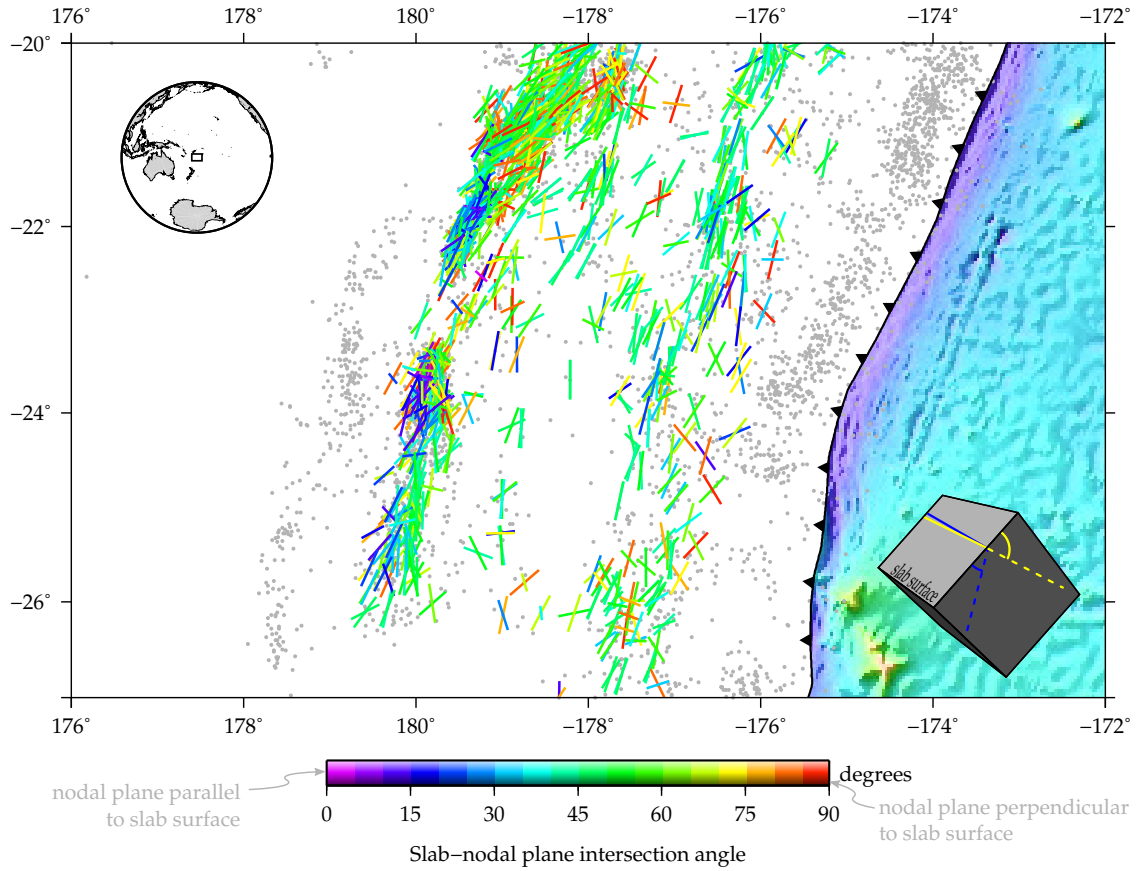

Figure 6.4: Nodal plane - seismic surface intersections along the south Tonga slab. Outboard deep-focus earthquakes (which form the NNE-SSW band of seismicity west of 180°W) are not included in the estimation of the seismic surface. The cartoon in the lower right-hand corner illustrates the geometric relationship between the plotted intersections, the nodal planes and the slab surface. Earthquakes with one nodal plane sub-parallel to the modelled plane of seismicity are observed to the east of the outboard events. Including the outboard events in the slab modelling procedure changes the angle of slab intersection of most these nodal planes to ∼45° (further discussion in main text).

Figure 6.4 reveals that most deep-focus earthquakes are in good agreement with the stress guide hypothesis. However, the deepest part of the main Wadati-Benioff zone to the east of the outboard events is typified by earthquakes with one nodal plane sub-parallel to the modelled surface of seismicity. This observation is consistent with shear accommodating downward motion of the main

Wadati-Benioff zone relative to the outboard events, or alternatively indicates that the outboard events are actually attached to the main part of the Wadati-Benioff zone. South of 22°S, the latter proposition is preferred in this study and by Giardini and Woodhouse (1984), for the reasons discussed in §5.4.5. North of 22°S, the continuity of the slab is less well constrained. Some of the events with slab-parallel nodal planes in Figure 6.4 correspond to the lineation in Figure 6.2. The two figures therefore provide support for small regions of the deep Tonga slab undergoing repeated shear failure; in this case perhaps facilitating the propagating tear in the slab proposed by Giardini and Woodhouse (1984).

6.3.2 *Izu-Bonin*

After the Izu-Bonin slab bends at 350–450 km depth, prominent seismic lineations are observed (see §5.4.1). These lineations plunge shallowly to the northwest, and continue for over 100 km; in others they appear to be split into several shorter sub-parallel segments. Figure 6.5 reveals several lineations within the Bonin slab, all of which are parallel to the steeply dipping nodal plane of the 5 August 1990 deep-focus earthquake.

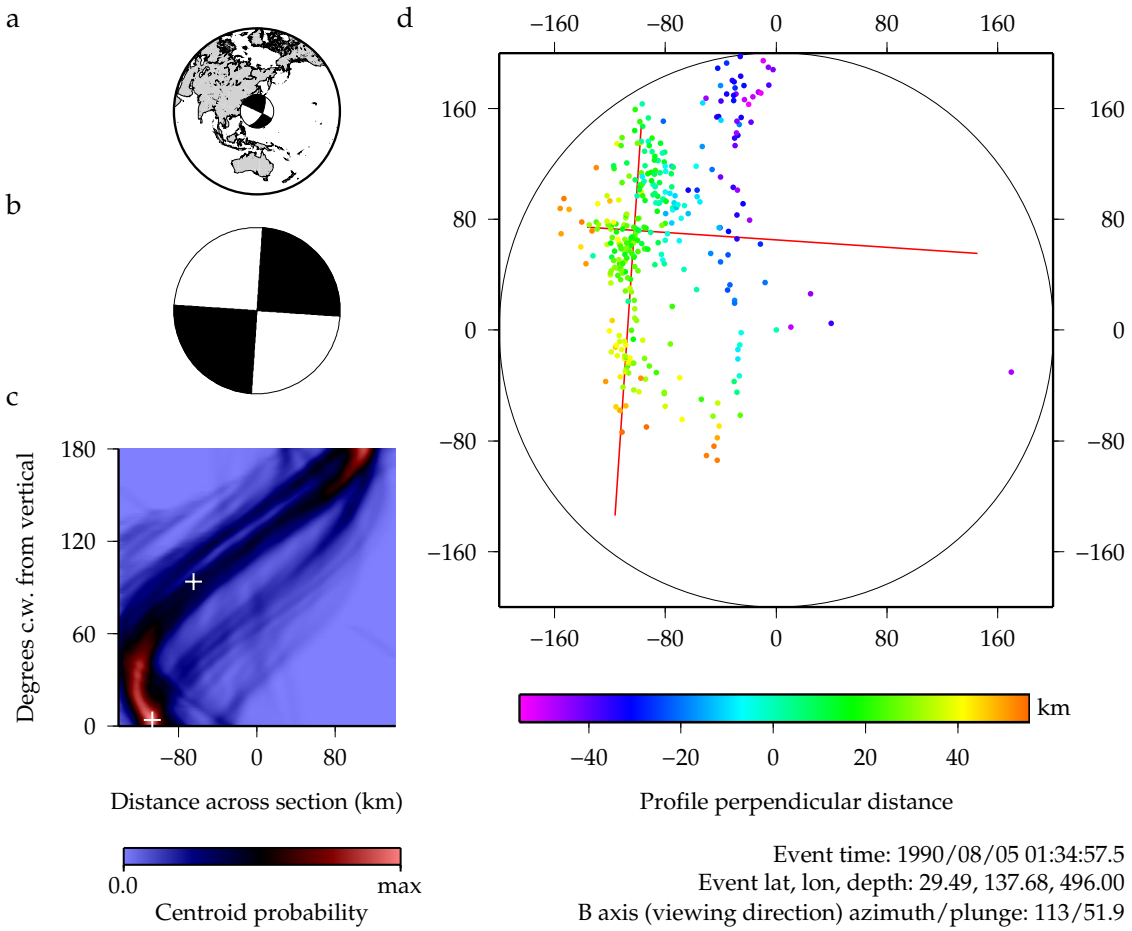

Figure 6.5: Plane of seismicity parallel to one of the nodal planes of the 5 August 1990 deep-focus earthquake. Subplots are as described in Figure 6.1.

Unlike the lineations in the Solomons slab (§5.4.4), the lineations in the Bonin slab do not appear

to be associated with slab bending. Similar lineations are observed at intermediate depths beneath South America (Kirby and Engdahl, 1993; Kirby et al., 1996), Japan (Nakajima and Hasegawa, 2006; Hasegawa et al., 2007; Nakajima et al., 2009) and Sumatra (Lange et al., 2010). In these regions, it has been argued that the observed lineations correspond to subducted features such as seamount chains (Kirby et al., 1996) or fracture zones (Hasegawa et al., 2007; Lange et al., 2010).

To assess the possibility that seismic streaks within the deep Bonin slab correspond to features created at the surface, the streaks must be extrapolated through the largely aseismic region between 100 and 350 km depth. In order to do this, two assumptions must be made. First, we must make the assumption that the orientations of pre-subduction features have remained the same for several million years. Second, the general pattern of deformation within the slab must be constrained. The Bonin slab is not planar, so it must be undergoing some deformation at depth. I approximate the slab as a 2D incompressible sheet, i.e. one with zero Gaussian curvature.

I construct the shape of the Bonin slab using the following algorithm (Figure 6.6):

1. As described in Chapter 5, the locations of seismicity are rotated into the best fitting plane of the slab, and the best-fitting surface to seismicity found using the fitting procedure of Smith and Wessel (1990).

2. Bounding lines are drawn along the north-basal and south ends of the seismicity parallel to the best-fitting plane to seismicity.

3. Each line is sampled 100 times along its length.

4. For each point along the north-basal section, a line is drawn to every point along the southern end of the section. The gradient and height of this line are varied to find the minimum misfit with the slab surface.

5. For each point along the north-basal section, the non-overlapping line to the southern section with the minimum overall misfit is selected. The maximum RMS misfit is 13.4 km.

6. The new model slab surface is constructed from the complete set of best-fitting lines.

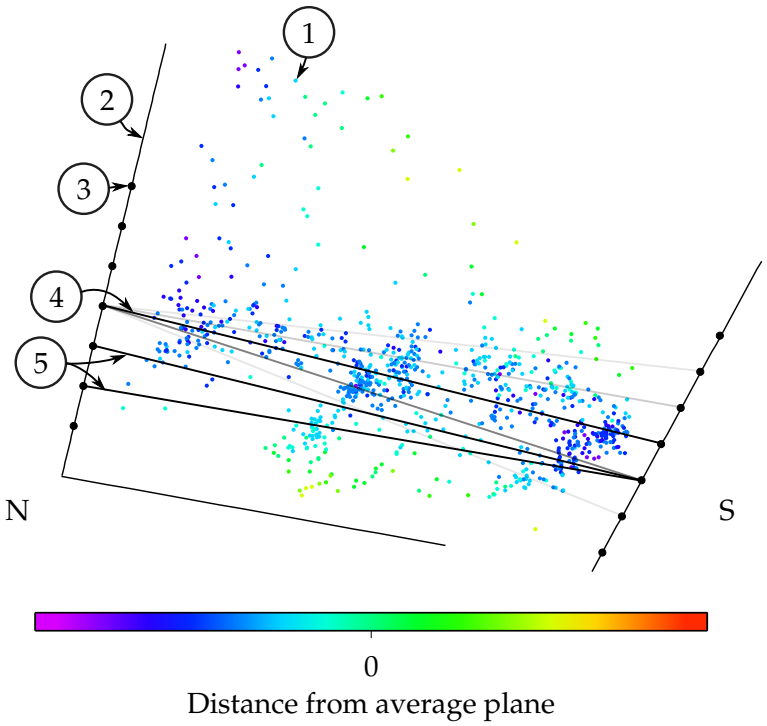

Figure 6.6: Cartoon illustrating the algorithm to model subducting slabs as incompressible (zero Gaussian curvature) sheets. Seismicity projected onto the average plane of the Wadati-Benioff zone is plotted as dots, coloured according to the distance to the average plane. Numbers correspond to the steps described in the main text.

One consequence of the assumption that the slab cannot undergo distortion or shear after subduction is that features approximating great circles before subduction will continue to represent the shortest path between two points. In differential geometry, the shortest path between two points on a curved surface is called a geodesic. An efficient technique to determine geodesics on arbitrary surfaces in three-dimensional Euclidean space has been outlined by Mitchell et al. (1987). I have used their algorithm[1] to extend the streaks of earthquakes within the Bonin slab to the surface (Figure 6.7).

The extensions of the deep seismic streaks are parallel to two short streaks in seismicity at 31–32°N. The extension of the two northernmost deep seismic streaks meet sets of active outer rise normal faults. These faults have strikes which do not parallel the trench where they will eventually subduct. Instead, they are parallel to the segment of trench between 22 and 24.5°S, and to the southern part of the paired Kashimi Fracture Zone. Finally, in the deepest parts of the Wadati-Benioff zone, the steeper of the two slab-nodal plane intersections is commonly parallel to the nearest streak. None of these gCMT-recorded earthquakes are large enough to observe sufficient rupture directivity to conclusively identify the more steeply-dipping nodal planes as the fault planes (Chapter 7), but it would be surprising if this were not the case.

There are two possible origins of the trench-oblique normal faults in the outer rise. Firstly, they might represent reactivation of transform faults. The orientation of stress is probably within 30° of

[1]Implemented in C++ by Danil Kirsanov; `http://code.google.com/p/geodesic/`

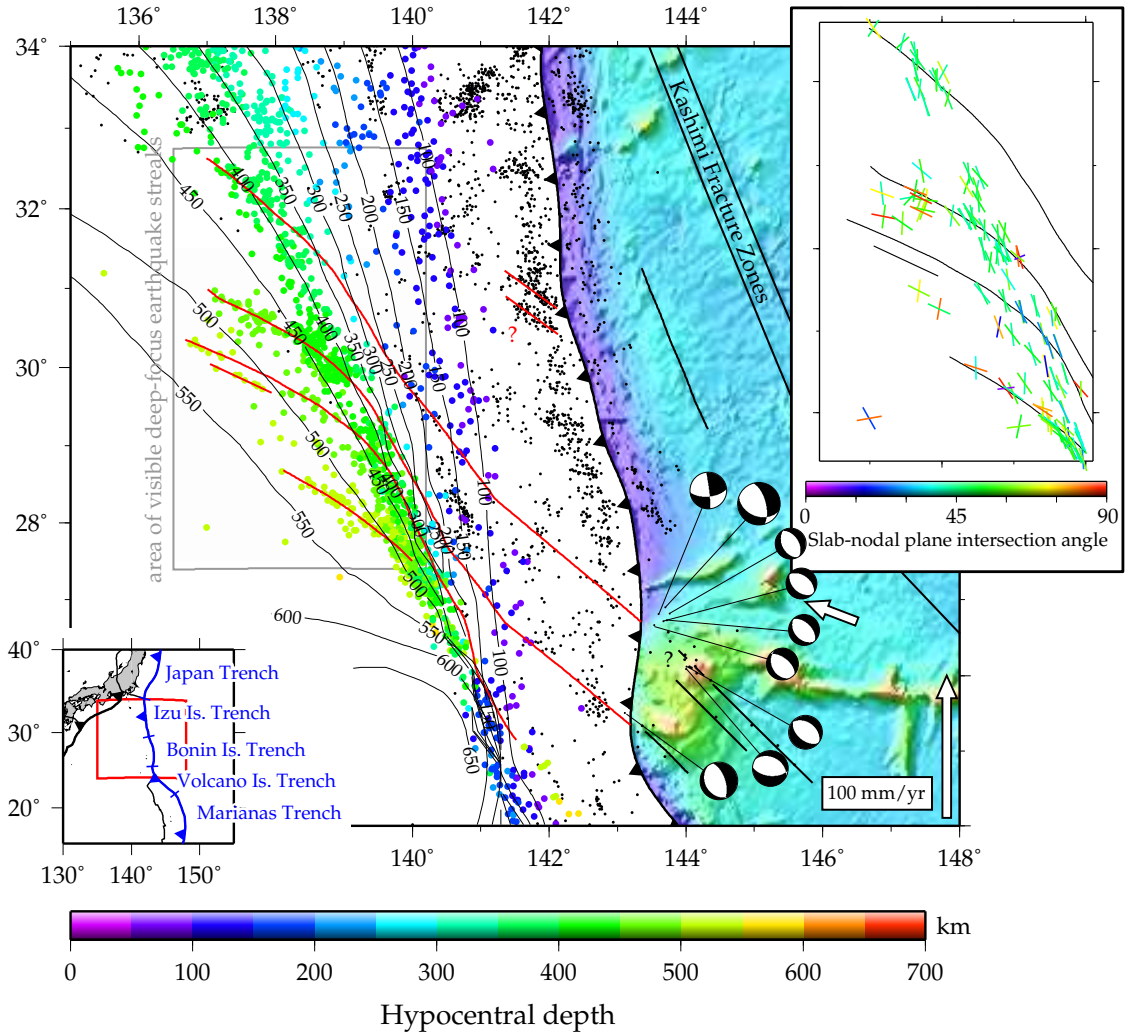

Figure 6.7: Izu-Bonin seismicity as recorded in the EHB catalogue 1960–2007 and colour-coded according to hypocentral depth. The best-fitting surface to seismicity is contoured in kilometers. Prominent streaks of deep-focus earthquakes can be seen in the grey box. Geodesics aligned with these seismic streaks are shown in red, plunging to the northwest. To the east of the trench, oceanic bathymetry and major fracture zones are plotted. The velocity vector corresponds to the relative motion between the Pacific and Philippine Plates. Outer rise earthquake gCMT focal mechanisms are plotted south of 28°N. All but three of the earthquakes clustered around 26.5°N are aftershocks of the 21 December 2010 M_W 7.4 normal faulting earthquake. The focal mechanism south of 26°N corresponds to the 21 December 1977 M_W 6.5 earthquake. Inset: Slab-nodal plane intersection angles for deep-focus earthquakes in the highlighted region of the main map.

the ideal orientation for movement on these faults, favouring reactivation (Masson, 1991). Igneous activity has obscured the gravitational expression of fracture zones in the area in the dataset of Sandwell and Smith (2009), but magnetic anomalies indicate that one or several fracture zones must take up ∼400 km and 11 Ma of displacement along the trench between 23 and 25°N (Nakanishi et al., 1992). Alternatively, the normal faults might represent deformation at a curved trench.

The two hypotheses have different implications for potential reactivation at depth. The paired Kashimi Fracture Zone is kinked at ∼ 29°N, and fracture zones further south are also expected to undergo a change in strike. Any subducted fracture zones would cut across the slab more obliquely than the observed seismic streaks. Reactivation of outer rise faults created parallel to the Volcano

Islands trench might present a more attractive explanation for the orientations of the deep-focus seismic streaks. The convex kink in the trench has become more pronounced with rapid spreading in the Marianas back-arc basin, but has probably existed for at least 10 Ma (Sdrolias and Müller, 2006).

6.3.3 Vitiaz

The stagnant slab between the Vanuatu and Tonga subduction zones also exhibits deep-focus seismic streaks which are not clearly associated with slab bending (Figure 6.8). Earthquakes in this region have hypocentral depths >500 km and scattered focal mechanisms (Brudzinski and Chen, 2005), although a sequence of four earthquakes in October-November 1999 may have had similar mechanisms (Chapter 4). Travel time anomalies suggest that these earthquakes occur in a continuous stagnant slab (Okal and Kirby, 1998; Brudzinski and Chen, 2000; Brudzinski and Chen, 2003), which was probably subducted about 5–8 Myr ago at the Vitiaz Trench (e.g. Chen and Brudzinski, 2001). The strike of the lineations of earthquakes is similar to the strike of fracture zones associated with the Nova Canton Trough. If subduction has had little effect on the orientation of the flat lying slab, it is possible that these seismic streaks represent subducted fault zones. As with the Izu-Bonin slab, reactivation of large normal faults created at the outer rise is also possible.

The lack of consistency in focal mechanism orientation, and the rarity of earthquakes with nodal planes parallel to the seismic streaks suggests that the location of the streaks are not determined by the local stress field. The distribution of these deep-focus earthquakes may instead be determined by small scale mineralogical or rheological heterogeneity in the stagnant slab.

6.4 Discussion

Identifying active fault zones in subducting slabs is associated with several potential problems. Even high-quality hypocentral locations can be associated with location errors >10 km that could obscure fault zones. Systematic errors in location can create spurious changes in the orientation of such zones (Syracuse and Abers, 2009).

In looking along the B axis of large earthquakes to identify shear zones at depth, care must be taken to pick master events which accurately reflect the orientations of the majority of analysed seismicity (for example, see Figure 6.3). Because many earthquakes have B axes approximately in-plane, and errors in seismic locations are comparable or greater than the thickness of the seismically active slab, many fault zones would look like diffuse clusters of seismicity when viewed down the B axis. The broad 'lineations' of Giardini and Woodhouse (1984) and Lundgren and Giardini (1992) are 50–100 km wide zones of high-strain, rather than single shear zones (see Chapter 5). In some cases (e.g. south Tonga) these zones have significant variations in focal mechanism orientation.

A small fraction of subduction zone earthquakes unambiguously represent repeated shear

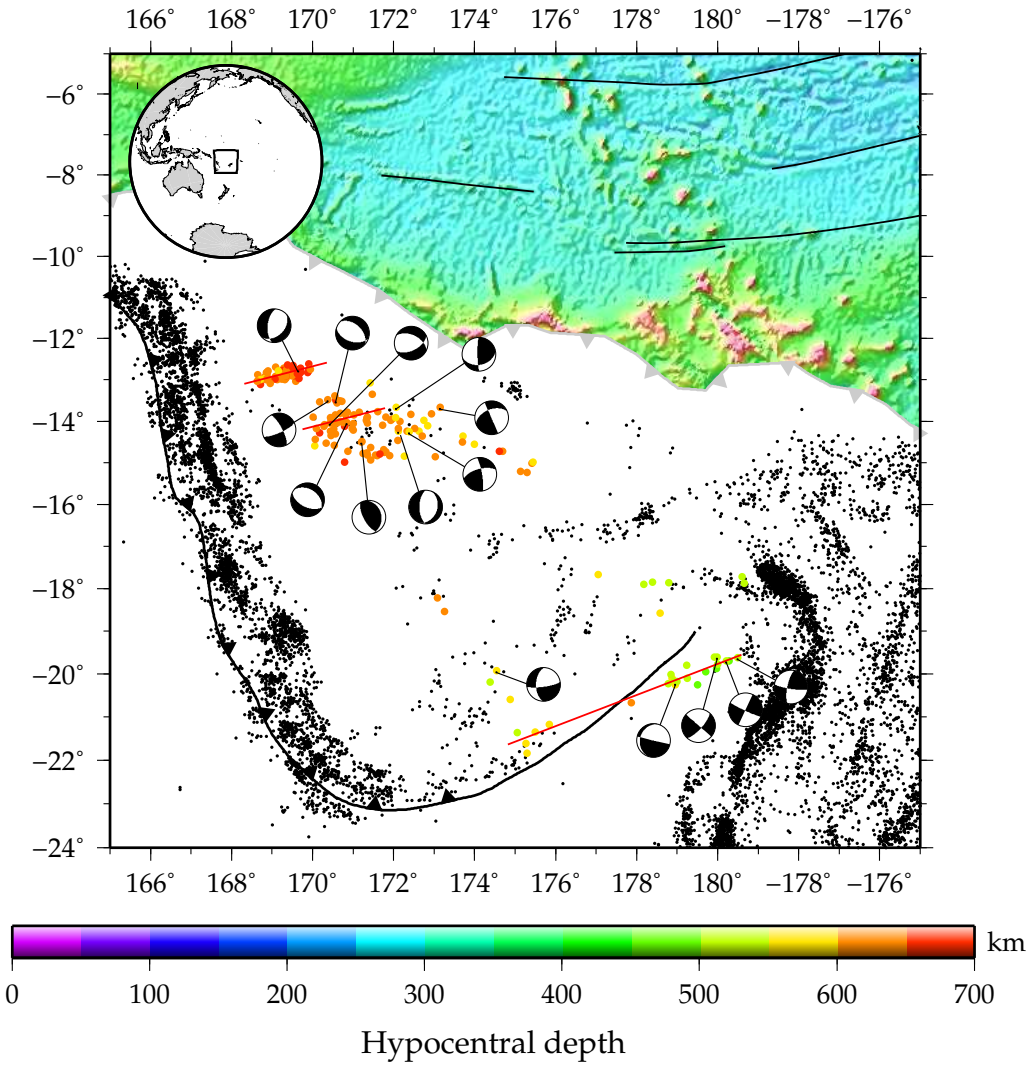

Figure 6.8: Seismicity in the southwest Pacific, as recorded in the EHB catalogue 1960–2007. Bathymetry is shown to the north of the extinct Vitiaz Trench (grey). Fracture zones associated with the Nova Canton Trough are outlined in black. Coloured events lie within a stagnant slab in the mantle transition zone. Three elongate streaks of seismicity are outlined in red.

failure within narrow linear or planar zones of high seismicity apparently unrelated to large scale deformation of the slab. Particularly impressive are the long seismic streaks within the Bonin slab. These zones are only observed within the deepest part of the subduction zone, and the earthquakes along them are of a different orientation to shallower seismicity. It may be that the regional stress field in the deepest part of the slab is oriented favourably to allow slip along these zones within the slab. They may represent preferential activation of material that is rheologically distinct from the rest of the slab, perhaps due to chemical or grain size variations.

Faults are prime locations for physical and chemical alteration prior to subduction (see Chapter 8). For faulting to penetrate deep into the mantle, the oceanic lithosphere must be cool; the 600°C isotherm represents the cessation of seismicity in mid-ocean and outer rise environments (McKenzie et al., 2005; Tilmann et al., 2008). Hydrothermal circulation may be an important contributor to cooling along transform faults (Roland et al., 2010).

6.5 Conclusions

This study revisits and extends the work of Giardini and Woodhouse (1984) and Lundgren and Giardini (1992), who combined focal mechanisms with earthquake locations to identify planes of shear failure within subducting slabs. Some of their identified lineations remain visible with more recent earthquake catalogues, but several are absent. With the greatly expanded gCMT database (1977–2011) it is clear that some of the identifications in earlier studies are spurious; resulting from choosing unusual focal mechanisms or sparse seismicity.

Despite these problems, some earthquakes do lie along elongated trains of seismicity that can't be explained by warping or buckling of the slab. These earthquakes may represent preferential failure of rheologically distinct material, such as fine grained or mineralogically-distinct fault gouge or the presence of free fluid phases.

The decreased number of identified planes of shear failure does not imply that large earthquakes rupture pristine slab material. It would be surprising if the presence of fine grained regions or hydrated regions in subducting slabs had no effect on the local distribution of strain. Nevertheless, the seismic streaks in the Bonin and Vitiaz slabs represent a minority of deep earthquakes, distinct from the majority of earthquakes which appear to rupture along developing fault systems formed as a result of recent slab deformation.

7 *Rupture directivity*

7.1 Introduction

Shallow ($z_h \leq 60$ km), intermediate (60 km $< z_h \leq 300$ km) and deep-focus ($z_h > 300$ km) earthquakes are typified by double-couple radiation patterns. These patterns indicate that energy release during earthquakes is a consequence of slip along planar surfaces, regardless of hypocentral depth (e.g. Honda, 1932; Frohlich, 1989). Identical double-couple radiation patterns can be produced by slip along one of two orthogonal nodal planes. In order to distinguish the fault plane from the auxiliary plane, extra information is required.

Determining which of the two nodal planes of an earthquake focal mechanism corresponds to the fault plane is important in several respects. Firstly, fault plane orientations may tell us about compositional and rheological variations within subducting slabs. Although we know some details of the structure of oceanic material entering a subduction zone system at the trench, there are few constraints on how structural heterogeneities behave or influence deformation of the slab. It is not known whether deep earthquakes occur on pre-existing planes of weakness (e.g. Savage, 1969; Jiao et al., 2000; Ranero et al., 2005; Kiser et al., 2011) or on newly formed faults (e.g. Isacks et al., 1968; Isacks and Molnar, 1971; Zhang et al., 2004).

Secondly, the rupture characteristics of subduction zone earthquakes provide constraints on the physics of brittle failure on faults under high pressure. Analysis of Tonga-Kermadec earthquakes reveals a change in focal mechanisms relative to the slab down-dip direction (Jiao et al., 2000) and in fault plane orientation from near-horizontal at intermediate depth to a mixture of near-horizontal and subvertical planes at greater depth (Warren et al., 2007). External forces, slab geometry, rates of subduction, thermal structure and inherited seafloor structure could all potentially affect seismic activity and the orientation of fault planes in subducting slabs. A comparison of fault plane orientations in several subduction zones is required before competing hypotheses for differences in behaviour can be assessed.

Finally, fault plane orientations govern and are governed by the style of deformation within seismically active slabs. Conjugate sets of faults are common features of several tectonic regimes.

This chapter is a modified version of the main text from Myhill and Warren (2012).

If both sets accommodate strain equally, deformation can be viewed as pure shear on scales much greater than typical fault lengths. If one set dominates, the slab either experiences a larger component of simple shear or rotation of fault-bounded blocks.

In this study, I conduct a regional study of deep earthquake directivity to determine the orientations of fault planes active in the Izu-Bonin-Marianas (IBM) subduction zone.

7.2 *Regional Overview*

Between Japan and Guam, the Pacific Plate subducts westwards beneath the Philippines Plate along a 2800 km long intra-oceanic subduction zone (Stern et al., 2003, Figure 7.1). The age of the subducting plate at the trench increases southwards from around 120 Ma at 35° N to over 150 Ma at 13° N (Müller et al., 2008). The oceanic plate entering the Marianas Trench is the oldest known material currently undergoing subduction on Earth (Nakanishi et al., 1992; Müller et al., 2008).

Several fracture zones are subducted along the IBM trench (Nakanishi et al., 1992). The offset along these transform faults contributes significantly to the increase in plate age along the trench, but their locations are not well constrained by existing geophysical data. The original topographic expression of these faults has been overprinted by the later formation of seamounts and plateaus, including the prominent Ogasawara Plateau, which meets the Izu-Bonin Trench at ∼25–26° N.

Close to the plate boundary, numerous bending-related normal faults are observed. Fault offsets increase toward the trench (Oakley et al., 2008). As exemplified by the 5 April 1990 earthquake (Yoshida et al., 1992), trenchward dipping faults tend to contribute more to total moment release and become more abundant close to the trench, though there is significant variation along strike (Nakanishi, 2011). Systematic changes in typical fault offset are observed, ranging from 400–600 m along the Izu-Bonin and Central Marianas Trenches and decreasing to 150–325 m at the northern and southern margins of the Marianas Trench (Oakley et al., 2008).

The subducting slab, as defined by seismicity (e.g. Engdahl et al., 1998) and tomography (e.g. Li and van der Hilst, 2010), is far from planar. At intermediate depths, the slab dips at ∼45° at the northern end of the study area. Further south, the dip of the slab increases, and is nearly vertical below 100 km depth to the south of ∼26° N. A bend in the slab at 350–500 km depth results in a decrease in dip along the leading edge of the Bonin Wadati-Benioff zone (e.g. Fukao et al., 1992). In contrast, the distribution of seismicity in the Marianas slab indicates that the subducting lithosphere is nearly vertical between 200 km depth and the base of the upper mantle.

Focal mechanisms of deep-focus earthquakes rotated into the orientation of the slab have strongly clustered T axes normal to the slab surface and P axes down-dip. Intermediate-depth earthquakes along the Izu-Bonin section tend to have T axes normal to the slab surface and P axes oriented north of down-dip, approximately aligned with the direction of motion (Chen et al., 2004). Beneath the

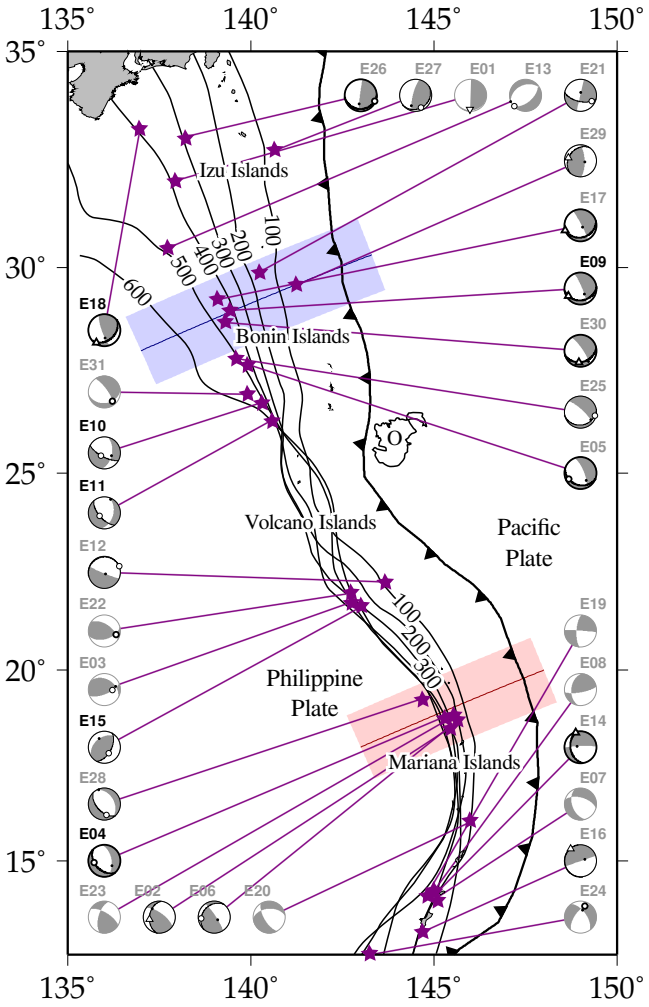

Figure 7.1: Overview map of the IBM subduction zone system. The trench is marked with ticks on the upper Philippine Plate. Thin black contours represent a fit to the EHB seismicity (Engdahl et al., 1998), approximating the shape of the subducting slab. The region marked 'O' denotes the part of the Ogasawara Plateau where the ocean depth is <3 km. Event identification numbers above each focal mechanism correspond to those in Table 7.1. The events discussed in the main text have black event IDs. Best-fitting rupture vectors are shown with a circle (downward-propagating) or triangle (upward-propagating). Identified and preferred fault planes have thick and thin black outlines respectively. Earthquakes with rupture propagation along the null axis have focal mechanisms marked only with the best fitting rupture vectors on each plane. Mechanisms without marked vectors have observed directivity, but insufficient station coverage to constrain the directivity to either plane. Shaded swaths correspond to the two cross sections in Figure 7.11.

Marianas Islands, intermediate-depth earthquake focal mechanisms are more scattered (Apperson and Frohlich, 1987), though P axes generally plunge steeply into the slab.

Convergence within the IBM system has been ongoing for the last 50 Myr (Bloomer et al., 1995; Stern and Bloomer, 1992), with true subduction beginning at about 43 Ma (Richards and Lithgow-Bertelloni, 1996). At the present day, the Pacific Plate is moving northwest at 20–30 mm/yr relative to the Philippines Plate at the southern end of the system. At the northern end, the relative motion is 40–50 mm/yr west-northwest (Sella et al., 2002). Subduction velocities are higher than these relative plate motions as a result of back-arc spreading in the Marianas, Bonin and Izu Basins.

7.3 Fault plane identification by analysis of rupture directivity

Several methods have been employed to determine the orientation of deep earthquake fault planes. Aftershock locations (e.g. Wiens et al., 1994) and second-degree moments (e.g. Silver, 1983; McGuire et al., 2001) have both been used. A more common technique is to determine the distribution and progression of moment release along the fault surface during the earthquake (e.g. Chen et al., 1996; Antolik et al., 1999; Tibi et al., 1999, 2002, 2003; Park and Mori, 2008). At a magnitude threshold dependent on the frequency content of recorded seismic waves from an earthquake, brittle rupture can no longer be modeled as a point source. This source finiteness results in an apparent variation in rupture duration and relative timing of subevents when recorded by seismometers positioned at a variety of azimuths and distances from the earthquake.

Rupture directivity can be modelled in several ways. If there are distinct subevents, they can be located relative to each other (e.g. Tibi et al., 2003) and the relative locations compared with potential fault planes for the earthquake. Alternatively, the best-fitting double couple solution may be used as a starting point for inversion, with slip modelled in two dimensions on both of the potential fault planes (e.g. Antolik et al., 1999). This second technique avoids the need to consistently identify subevents, but the greater number of degrees of freedom of the inversion can lead to non-unique moment distributions.

If rupture propagation during an earthquake is sufficiently simple it can be modelled as a sequence of sources along a line, rather than a plane. Unilateral and bilateral rupture both result in differences in apparent rupture duration at stations with variable angular separations between take off vector and rupture direction (Haskell, 1964). Restricting the rupture to having a constant (but unconstrained) velocity greatly decreases the degrees of freedom of the problem over the more general two dimensional case. This single-velocity approach is adopted by Warren and Silver (2006). Their semi-automated scheme does not require the user to input a preferred fault plane orientation. The stricter constraints on the rupture distribution enables the method to be applied to earthquakes with magnitudes too small to be analysed with more traditional methods. Warren (2010)

has conducted synthetic tests to estimate errors in rupture vector determination. She found that station distribution is the most important factor in constraining the rupture vector and fault plane. Specifically, the technique requires a good distribution of takeoff vectors around the rupture vector. Local stations provide increased resolution of directivity, but are not required to reliably identify active fault planes.

The technique of Warren and Silver (2006) has previously been applied to intermediate-focus earthquakes beneath Central America (Warren et al., 2008) and to intermediate and deep-focus earthquakes within the Tonga-Kermadec subduction zone (Warren et al., 2007). Intermediate-depth earthquakes in both regions tend to rupture on near-horizontal fault planes. The onset depth of this near-horizontal faulting begins at ∼75 km depth in both regions, despite large thermal differences and both down-dip compressional and down-dip extensional focal mechanisms (Warren et al., 2008). Between 300–600 km depth, earthquakes in the Tonga-Kermadec subduction zone rupture on both near-horizontal and subvertical planes. At depths >600 km, a predominance of near-horizontal fault planes is again observed (Warren et al., 2007).

7.3.1 Technique

In this study, I extend the analysis of earthquake directivity to the IBM subduction zone system. I selected all IBM subduction zone earthquakes (10°N–35°N) with hypocentral depths exceeding 50 km and magnitudes exceeding M_W 6.0 between January 1993 and January 2011, and some additional earthquakes with M_W between 5.7 and 6.0. In total, I identified for analysis 58 earthquakes with M_W ranging from 5.7–7.6 at depths between 50–595 km. My selection criteria are chosen to ensure good station coverage, avoid *P*-wave contamination by other phases, and filter out the majority of events which are indistinguishable from a point source. I use data from all available stations within the epicentral distance range 0–100 degrees (see Supplementary Materials of Myhill and Warren, 2012, for a list and map of station locations), and process the data using the technique of Warren and Silver (2006).

Unilateral rupture at constant velocity v_r along a fault of length L results in an apparent rupture duration

$$\tau(\theta) = \frac{L}{v_r} - \frac{L\cos\theta}{c} \tag{7.1}$$

where θ is the angle between the direction of rupture propagation and the takeoff vector to the station and c is the local seismic velocity (Bollinger, 1968). Since the rupture duration $a = L/v_r$, Equation 7.1 can be rewritten as

$$\tau(\theta) = a(1 - \frac{v_r}{c}\cos\theta) \tag{7.2}$$

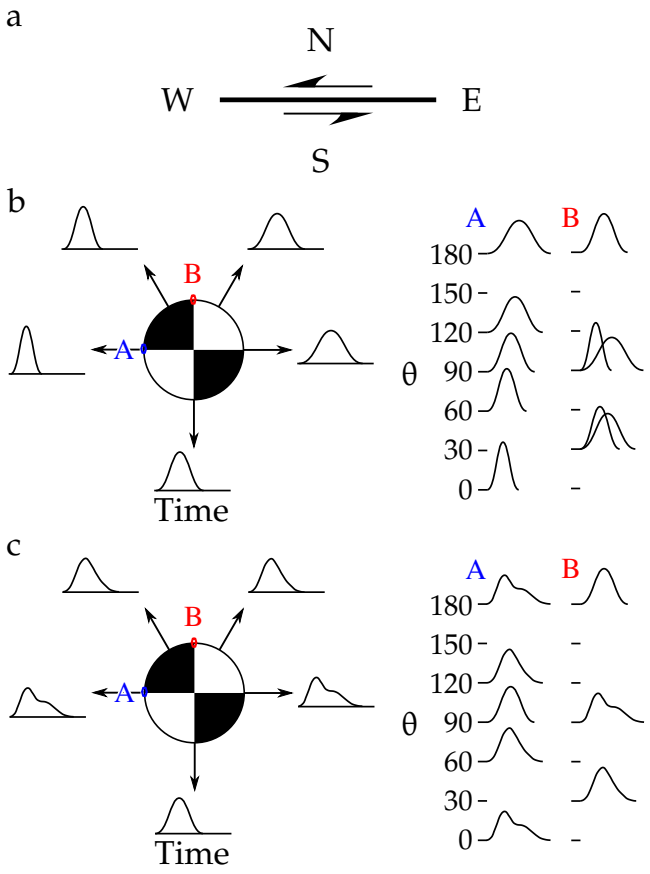

Figure 7.2: Cartoon showing variations in pulse width recorded at different take-off angles for a simple rupture propagating along an east-west striking fault. a) Map view of the fault, with arrows indicating the sense of motion. b) Polarity-corrected displacement waveforms corresponding to a rupture propagating unilaterally westwards. c) Polarity-corrected displacement waveforms corresponding to a rupture propagating bilaterally. In both cases, the rupture propagates at a velocity of $\alpha/3$. Diagrams on the right hand side show the same seismograms aligned on the first motions. Θ corresponds to the angle between the takeoff vector and a candidate rupture vector (labelled "A" and "B" on the focal mechanisms). The symmetrical distribution of stations about "B" leads to two pairs of seismograms being plotted at the same value of Θ. A coherent variation in pulse width is observed only for candidate rupture vector "A", which corresponds to the actual rupture vector.

A similar expression can be derived for bilateral rupture:

$$\tau(\theta) = a(1 + \frac{v_r}{c}|\cos\theta|) \tag{7.3}$$

A graphical illustration of the effects of rupture directivity on pulse width can be seen in Figure 7.2.

To find the rupture velocity most consistent with the measurements of differential rupture duration, a search is conducted over candidate rupture velocities $\mathbf{r}$, specified by trend $0 \leq \phi_r < 360$, plunge $-90 < \gamma_r < 90$ and speed relative to the local P-wave velocity $0 < v_r \leq 0.8\alpha$. Rupture velocity is unlikely to exceed the S-wave velocity ($\sim 0.57\alpha$). The RMS misfit M for P-wave measurements is defined as

$$M(\mathbf{r}) = \sqrt{\frac{1}{m}\sum_{i=1}^{n}\sum_{j=1}^{n,\neq i}\left[s_{ij,measured} - s_{ij,predicted}\right]^2} \tag{7.4}$$

where s_{ij} is the stretching factor between seismograms recorded at stations i and j and m is the number of measurements with high cross-correlation coefficients. For unilateral rupture

$$s_{ij} = \frac{1 - \frac{v_r}{\alpha} \cos\theta_i}{1 - \frac{v_r}{\alpha} \cos\theta_j} \tag{7.5}$$

and for bilateral rupture

$$s_{ij} = \frac{1 + \frac{v_r}{\alpha} |\cos\theta_i|}{1 + \frac{v_r}{\alpha} |\cos\theta_j|} \tag{7.6}$$

80% and 95% confidence intervals for the rupture vector and velocities are determined through bootstrap resampling. The analysis is repeated 1000 times using different subsets of the data.

The misfit function is then compared with the orientations of fault planes as reported by the Global Centroid Moment Tensor (CMT) Project (Dziewonski et al., 1981). Identification of the fault plane follows if the following criteria hold:

1. The misfit is < 0.85, and the 95% confidence region overlaps only one nodal plane. If the 95% confidence region overlaps both planes, but the 80% region only intersects one plane, that plane is designated a preferred fault plane.

2. There is a coherent increase in apparent rupture duration with increasing rupture–takeoff angle for the best-fitting fault plane. The moveout in rupture time is markedly clearer for this plane than for the auxiliary plane.

3. The errors in rupture vector and velocity can be replicated with synthetics.

Synthetic seismograms are generated for the best-fitting rupture vector on each nodal plane, using the estimated rupture velocity and approximating the rupture history with either a single finite source or up to three point sources of variable duration, onset time and amplitude. Each trace is convolved with the appropriate upper mantle attenuation operator (Warren and Shearer, 2002) and noise is added from the observed seismogram prior to the initial arrival.

7.4 Results

7.4.1 General Results

I observed directivity for 31 of the 58 analyzed earthquakes. I present in Table 7.1 the best-fitting unilateral rupture vectors for these events. The rupture vector for 20 earthquakes was constrained sufficiently to identify a preferred fault plane. A further 6 earthquakes ruptured almost parallel to the null axis of the focal plane solution (E01, E03, E13, E22, E24, E31), while the directivity of the remaining 5 was insufficiently clear to determine a well-constrained rupture direction (E7, E8, E19,

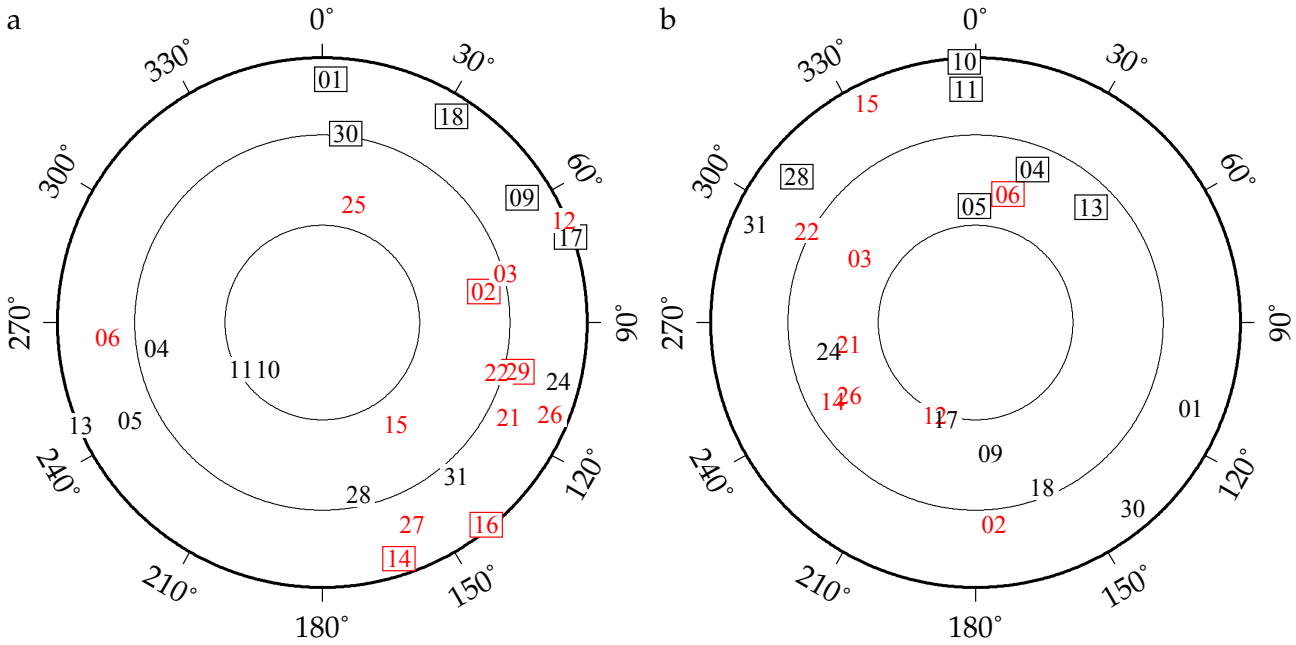

Figure 7.3: Rupture directivity for the 22 events with hypocentral depths >100 km. Vectors are plotted relative to the surface (a; 0° is north), and to the local slab orientation (b; 0° is down-dip, with the center of the plot normal to the slab). Numbers correspond to the unique event IDs in column one of Table 7.1. Red and black symbols correspond to events with hypocentral depths <300 km and >300 km respectively. Events with and without enclosing boxes are plotted using an upper and lower hemisphere projection respectively. All events with well-constrained directivity are plotted. Concentric circles are plotted at 30° intervals.

E20, E23). In agreement with studies of other subduction zones (Warren et al., 2007, 2008), unilateral rupture is preferred over bilateral rupture in all cases.

I failed to determine rupture directions for 27 analyzed earthquakes (Table 7.2). Short rupture durations and poor station distribution were the most common causes of failure to constrain rupture directivity. Analysis of the October 27 2000 event (R20) was prohibited by a large negative displacement after the main arrival at some stations, which has undesirable effects on stretching factors during waveform cross correlation. Other than earthquake magnitude and the distribution of takeoff vectors over the focal sphere, I found no systematic differences between events with and without identified directivity.

Using an estimate of slab shape determined from the distribution of seismicity at depths >100 km (Figure 7.1), 16 of the 26 well-constrained best fit rupture vectors indicate rupture into the slab (Figure 7.3). The results suggest that only one of the nine earthquakes with depths 100–300 km (E06) ruptured toward the surface of the slab, consistent with previous studies (Warren et al., 2007, 2008). In contrast, 6 of the 13 earthquakes with depths 300–700 km have best-fitting rupture vectors directed toward the surface of the slab (E04, E05, E10, E11, E13, E28). The dataset reveals no strong preference for along-strike rupture propagation reported for $M_W > 7.0$ intermediate-depth earthquakes in other subduction zones (Tibi et al., 2002). This result presumably reflects the width of the seismogenic zone relative to the total length of rupture.

Table 7.1: Intermediate and deep earthquakes in the Izu-Marianas subduction system with observed directivity. Pre-10/2007 times and locations are from the EHB catalogue (Engdahl et al., 1998). Magnitudes, focal plane and 10/2007–present event parameters are from the Global CMT catalogue (Dziewonski et al., 1981). Identified fault planes are indicated in **bold**, preferred fault planes in ***bold italics*** and events which ruptured close to the B axis in *italics*; M is misfit; p and t are the plunge and trend of rupture vector; γ is the angle between rupture vector and slip vector; v_r/α is rupture velocity/P wave velocity.

	Event details						Best fitting vector		Best fitting rupture vector on shallower plane					Best fitting rupture vector on steeper plane				
ID	Date	Time	Lat	Lon	Depth	M_W	M	p / t	str/dip/rake 1	M	p / t	γ	v_r/α	str/dip/rake 2	M	p / t	γ	v_r/α
E01	19931011	15:54:22.30	32.03	137.93	351.00	6.9	0.84	-30 / 010	*093 / 09 / -179*	0.84	-9 / 002	270 ± 16	0.38 ± 0.11	*002 / 90 / -081*	0.84	-14 / 002	272 ± 31	0.47 ± 0.16
E02	19941230	15:12:26.40	18.51	145.45	219.00	6.3	0.58	-40 / 080	***187 / 39 / 144***	0.58	-38 / 079	226 ± 16	0.67 ± 0.16	306 / 68 / 057	0.67	-31 / 140	281 ± 42	0.33 ± 0.09
E03	19950408	17:45:14.00	21.75	142.79	267.00	6.2	0.60	70 / 060	*302 / 37 / 138*	0.64	29 / 075	85 ± 32	0.53 ± 0.12	*067 / 66 / 061*	0.63	48 / 096	75 ± 27	0.53 ± 0.11
E04	19950823	07:06:03.80	18.81	145.32	595.00	7.0	0.49	30 / 260	**136 / 42 / -118**	0.51	37 / 261	0 ± 5	0.47 ± 0.04	351 / 53 / -067	0.91	-45 / 302	220 ± 31	0.45 ± 0.27
E05	19960626	03:22:04.10	27.67	139.92	468.00	6.2	0.61	20 / 240	**110 / 25 / -135**	0.61	20 / 243	6 ± 12	0.41 ± 0.07	338 / 72 / -071	0.91	41 / 142	89 ± 42	0.44 ± 0.25
E06	19960715	16:51:23.00	18.72	145.67	176.00	6.2	0.67	40 / 270	***218 / 26 / 159***	0.75	20 / 266	33 ± 31	0.45 ± 0.08	327 / 81 / 065	0.86	-69 / 303	174 ± 40	0.74 ± 0.12
E07	19970423	19:44:29.80	13.99	145.04	101.00	6.5	0.67	-50 / 190	159 / 48 / -049	0.71	28 / 187	348 ± 13	0.35 ± 0.06	286 / 56 / -126	0.67	-55 / 181	226 ± 6	0.77 ± 0.08
E08	19980515	05:58:07.90	14.19	144.99	158.00	6.0	0.84	50 / 180	187 / 43 / 023	0.85	-8 / 178	173 ± 36	0.44 ± 0.18	080 / 75 / 131	0.87	74 / 186	45 ± 20	0.57 ± 0.15
E09	19980820	06:40:55.50	28.97	139.40	425.00	7.0	0.44	-10 / 050	**083 / 27 / -162**	0.44	-12 / 058	192 ± 7	0.29 ± 0.02	337 / 82 / -064	0.99	78 / 116	24 ± 54	0.16 ± 0.10
E10	19990112	02:32:26.60	26.74	140.30	441.00	5.9	0.75	80 / 210	010 / 51 / -027	0.94	50 / 112	78 ± 34	0.31 ± 0.16	***118 / 69 / -138***	0.76	68 / 229	44 ± 16	0.41 ± 0.10
E11	19990703	05:30:11.20	26.31	140.59	431.00	6.0	0.83	60 / 240	015 / 44 / -043	0.87	-9 / 205	152 ± 11	0.62 ± 0.12	***139 / 62 / -125***	0.84	61 / 240	29 ± 10	0.40 ± 0.05
E12	20000328	11:00:20.40	22.26	143.68	102.00	7.6	0.60	70 / 080	***255 / 06 / -127***	0.78	1 / 067	314 ± 11	0.31 ± 0.05	112 / 85 / -086	0.87	80 / 141	352 ± 7	0.48 ± 0.09
E13	20000609	23:31:45.90	30.47	137.75	485.00	6.2	0.85	10 / 230	*245 / 36 / -077*	0.86	1 / 247	290 ± 22	0.30 ± 0.07	*049 / 55 / -100*	0.85	5 / 226	284 ± 15	0.34 ± 0.07
E14	20000621	16:25:08.00	14.10	145.02	117.10	5.9	0.71	-30 / 160	**171 / 38 / -008**	0.72	-7 / 162	342 ± 19	0.46 ± 0.10	268 / 85 / -128	0.92	-72 / 104	238 ± 40	0.70 ± 0.20
E15	20010703	13:10:43.90	21.64	143.04	290.00	6.4	0.49	30 / 140	234 / 39 / 111	0.71	-39 / 149	203 ± 10	0.56 ± 0.16	***028 / 54 / 074***	0.54	51 / 144	2 ± 4	0.46 ± 0.03
E16	20020426	16:06:05.13	13.11	144.67	54.00	7.0	0.72	-20 / 140	***172 / 03 / 11***	0.73	-2 / 141	200 ± 10	0.63 ± 0.13	071 / 89 / 093	0.82	67 / 072	333 ± 26	0.39 ± 0.10
E17	20020802	23:11:39.40	29.23	139.10	418.00	6.2	0.69	00 / 070	**073 / 25 / -168**	0.70	-1 / 071	166 ± 21	0.39 ± 0.07	332 / 85 / -065	0.83	74 / 134	46 ± 27	0.53 ± 0.11
E18	20031112	08:26:44.70	33.24	136.98	381.00	6.3	0.34	-10 / 030	**050 / 34 / 156**	0.34	-12 / 032	317 ± 3	0.34 ± 0.02	160 / 77 / 059	0.97	-50 / 356	244 ± 46	0.40 ± 0.31
E19	20050202	02:30:25.90	14.07	144.79	159.10	6.3	0.46	60 / 150	183 / 70 / -003	0.54	-48 / 159	316 ± 27	0.61 ± 0.19	274 / 87 / -160	0.87	-65 / 100	275 ± 22	0.80 ± 0.03
E20	20050205	03:34:26.00	16.03	146.00	143.70	6.6	0.23	-10 / 280	266 / 46 / -144	0.24	6 / 272	133 ± 11	0.64 ± 0.05	149 / 65 / -050	0.31	61 / 272	56 ± 14	0.72 ± 0.05
E21	20070308	05:03:32.10	29.89	140.24	139.60	6.1	0.76	30 / 110	***102 / 59 / 179***	0.76	22 / 117	26 ± 16	0.39 ± 0.05	193 / 89 / 031	0.88	76 / 008	45 ± 8	0.51 ± 0.09
E22	20070928	13:38:59.60	21.97	142.70	277.50	7.5	0.67	20 / 110	*073 / 49 / 050*	0.67	32 / 106	85 ± 8	0.23 ± 0.02	*305 / 55 / 126*	0.67	25 / 106	97 ± 10	0.23 ± 0.02
E23	20071031	03:30:25.50	18.83	145.59	211.00	7.2	0.87	-50 / 090	196 / 60 / 152	0.87	-58 / 083	232 ± 8	0.46 ± 0.12	301 / 66 / 033	0.89	30 / 106	353 ± 23	0.21 ± 0.05
E24	20080509	21:51:35.90	12.36	143.28	83.30	6.7	0.53	20 / 050	*325 / 59 / -147*	0.53	52 / 015	80 ± 9	0.51 ± 0.06	*216 / 62 / -36*	0.54	26 / 021	113 ± 13	0.49 ± 0.07
E25	20080720	21:30:31.80	27.81	139.60	485.60	5.8	0.61	10 / 100	***079 / 22 / -142***	0.61	9 / 104	118 ± 13	0.42 ± 0.05	313 / 76 / -072	0.67	22 / 127	77 ± 21	0.48 ± 0.07
E26	20090809	10:55:58.80	33.05	138.19	301.80	7.1	0.53	-10 / 110	**086 / 17 / 168**	0.54	8 / 112	17 ± 4	0.35 ± 0.02	187 / 86 / 073	0.95	47 / 191	61 ± 17	0.21 ± 0.05
E27	20090812	22:48:55.90	32.74	140.68	55.2	6.6	0.54	20 / 160	***055 / 18 / 130***	0.53	18 / 156	51 ± 10	0.45 ± 0.06	194 / 76 / 079	0.75	31 / 202	90 ± 46	0.55 ± 0.18
E28	20100308	09:47:11.40	19.26	144.67	432.20	6.1	0.75	40 / 170	332 / 39 / -078	0.77	-5 / 158	110 ± 8	0.55 ± 0.11	***136 / 52 / -100***	0.75	34 / 168	55 ± 10	0.50 ± 0.08
E29	20100503	10:27:48.80	29.58	141.28	98.9	6.1	0.67	-40 / 090	***217 / 27 / 127***	0.72	-22 / 093	185 ± 8	0.48 ± 0.13	358 / 69 / 73	0.84	68 / 92	16 ± 8	0.33 ± 0.09
E30	20101130	03:24:49.10	28.69	139.26	460.60	6.8	0.50	-30 / 010	**076 / 31 / -157**	0.50	-29 / 007	229 ± 3	0.30 ± 0.05	326 / 78 / -061	0.99	-19 / 323	298 ± 50	0.09 ± 0.07
E31	20110112	21:32:58.20	26.94	139.94	511.50	6.5	0.52	10 / 150	*084 / 31 / -147*	0.52	26 / 144	83 ± 4	0.41 ± 0.03	*325 / 74 / -063*	0.51	5 / 144	110 ± 9	0.45 ± 0.04

Table 7.2: Rejected events

ID	Date	Time	Lat	Lon	Depth	M_W	str/dip/rake 1	str/dip/rake 2	Reason for rejection
R01	19930118	01:18:08.00	18.38	145.71	169.00	6.2	233/43/-159	127/76/-049	Poor station distribution
R02	19930722	12:15:37.30	21.73	144.32	125.30	5.7	263/19/-144	138/79/-075	Rupture duration too short
R03	19930808	08:34:26.07	13.00	144.87	59.00	7.7	312/18/ 147	075/80/ 075	pP, sP overlap
R04	19950707	21:15:18.50	33.95	137.12	324.00	5.9	328/15/ 075	163/75/ 094	Rupture duration too short
R05	19950824	01:55:34.60	18.92	144.95	589.00	6.2	117/46/-116	332/50/-066	Poor station distribution
R06	19950824	07:54:41.70	18.86	144.98	598.00	6.1	353/60/-031	099/63/-146	Poor station distribution
R07	19950824	07:55:25.60	18.86	145.01	580.00	6.2	099/62/-150	353/64/-032	Poor station distribution
R08	19951001	17:06:03.00	29.31	138.95	427.00	6.1	073/19/ 175	168/88/ 071	Poor station distribution
R09	19960214	21:26:56.20	29.22	140.38	142.00	5.6	034/47/ 050	265/56/ 125	Rupture duration too short
R10	19960316	22:04:06.20	28.98	138.94	477.00	6.6	068/23/-163	322/84/-068	No clear directivity
R11	19960609	01:12:16.60	17.44	145.46	149.00	6.5	218/44/ 168	317/82/ 047	Poor station distribution
R12	19960706	21:36:28.60	21.97	142.83	241.00	6.2	064/55/ 043	306/56/ 137	No clear directivity
R13	19971110	23:06:42.72	31.22	140.47	60.00	6.1	071/13/ 157	184/85/ 078	Poor station distribution
R14	19980101	06:11:23.75	23.95	142.06	92.00	6.3	020/57/-011	116/81/-146	Poor station distribution
R15	19980207	01:18:59.50	24.82	141.75	525.30	6.4	101/36/-145	342/71/-059	No clear directivity
R16	19991205	22:00:34.00	29.92	138.69	448.90	5.7	085/41/-178	354/89/-049	Rupture duration too short
R17	20000215	02:05:00.50	17.67	145.40	521.50	5.8	201/29/-114	048/64/-077	Rupture duration too short
R18	20000226	08:11:48.30	13.80	144.78	132.20	6.1	161/46/-009	257/83/-135	No clear directivity
R19	20000806	07:27:12.90	28.86	139.56	394.80	7.3	108/27/-142	344/74/-068	No clear directivity
R20	20001027	04:21:51.60	26.27	140.46	388.00	6.0	142/24/ 148	262/78/ 070	Problematic waveform shape
R21	20010114	08:58:25.80	22.09	143.88	87.00	5.9	007/27/ 025	255/79/ 115	Rupture duration too short
R22	20010604	22:41:04.87	17.06	146.08	96.80	5.7	053/30/-041	180/71/-113	Rupture duration too short
R23	20020107	13:26:26.50	18.96	144.96	599.40	5.9	349/44/-082	158/47/-098	Rupture duration too short
R24	20031111	18:48:23.80	22.32	143.25	101.00	5.9	012/19/ 066	217/73/ 098	Rupture duration too short
R25	20060103	12:27:54.95	13.85	145.41	55.00	5.8	313/24/ 158	064/81/ 067	Rupture duration too short
R26	20071207	00:47:36.79	29.95	141.01	77.50	5.9	359/61/ 031	253/64/ 147	Rupture duration too short
R27	20081202	12:31:44.90	19.17	145.99	118.70	5.9	220/39/-171	123/84/-052	Rupture duration too short

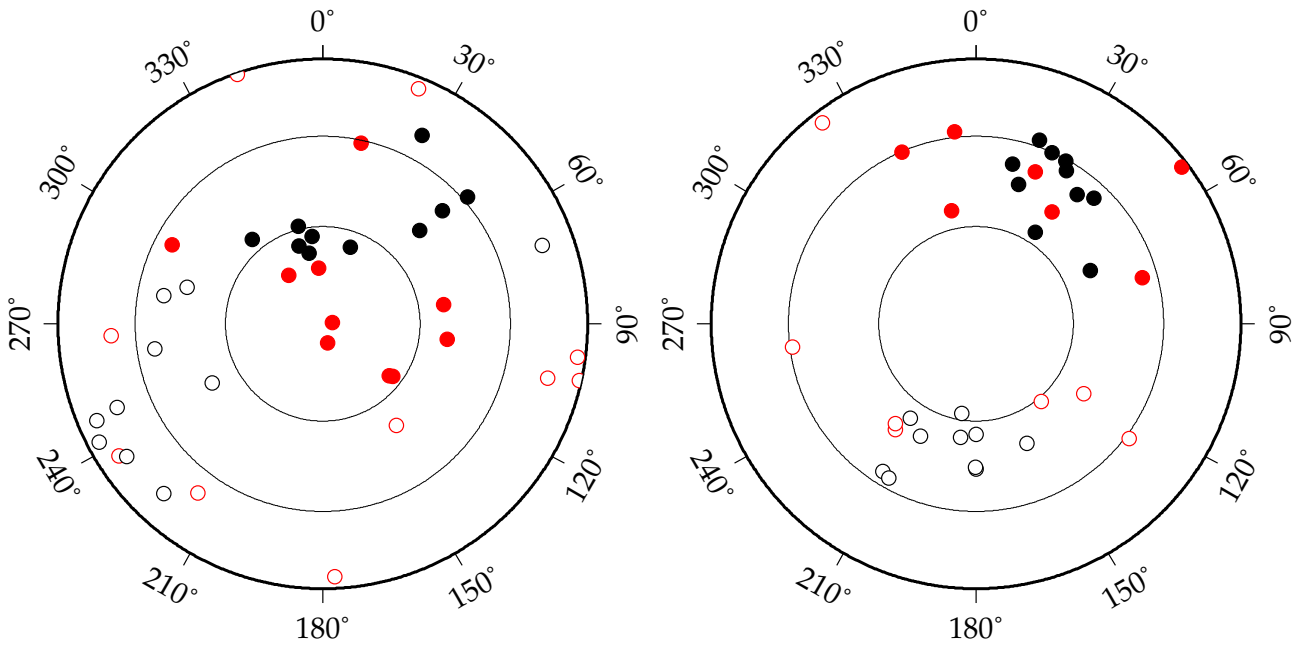

Figure 7.4: Poles to nodal planes of the 17 analyzed earthquakes with hypocentral depths >100 km for which observed directivity led to identification of fault planes. Poles are plotted relative to the surface (a), and to the local slab orientation (b). Lower hemisphere projection. Down-dip is at 0° with the center of the plot representing the vector into and normal to the slab as drawn in Figure 7.1. Red and black symbols correspond to events with hypocentral depths <300 km and >300 km respectively. Filled symbols represent the preferred or definitively identified fault planes. Events with directivity close to the null axis are not plotted. Concentric circles are plotted at 30° intervals.

The data in this study provide little evidence for a systematic variation in rupture vectors along the IBM subduction system. Nevertheless, three pairs of earthquakes with small hypocentral separations rupture along a similar vector (Figure 7.1; pairs [E03,E22], [E09,E17], [E10,E11]). A larger dataset is required to test the significance of this observation.

There is a strong tendency for the identified fault planes of both intermediate-focus and deep-focus earthquakes to dip up the slab (towards the trench) relative to the slab surface (Figure 7.4). Along the Izu subduction zone, which dips at 30–60°, the nodal planes which I identify as planes of rupture are near-horizontal. Along the Marianas and Volcano Islands arc, where the slab dips almost vertically, the preferred planes of rupture dip at moderate angles to the south or southwest. Four earthquakes are modelled better by rupture on the steeper of the two possible CMT nodal planes (E10, E11, E15, E28). The dip of these planes is 50–70°. Only the 3 July 2001 intermediate-depth Volcano Islands earthquake (E15) has a southeast-dipping preferred fault plane.

Near-horizontal planes of rupture also dominate catalogues of fault planes at intermediate depths beneath Middle America (Warren et al., 2008) and Tonga-Kermadec (Warren et al., 2007). The Tonga-Kermadec study identified both near-horizontal and subvertical rupture planes for deep-focus earthquakes, in contrast to the results presented here.

Throughout the rest of this paper, I refer to nodal planes as near-horizontal and subvertical or

shallow and steep if the two planes have markedly different dips. Otherwise, I describe the nodal planes in terms of their dip direction.

7.4.2 Rupture velocities

The velocities of the definitively identified ruptures are between 0.29–0.47 α, with errors of $\pm$ 0.02–0.10 α. In every case, the error on the best-fitting rupture velocity on the auxiliary plane is higher, supporting my choice of rupture plane.

With the exception of two events, all of the preferred rupture vectors (including those events which ruptured parallel to the null axis) have velocities between 0.23–0.53 α and associated errors of $\pm$ 0.03–0.13 α. The events with small associated errors ($<$0.05 α) have a range of velocities 0.23–0.47 α (or 0.4–0.8 times the local shear wave velocity), suggesting that these variations in rupture velocity are real.

The remaining two events are the intermediate-depth 30 December 1994 Marianas earthquake (E02; M_W=6.3, v_r=0.67 α $\pm$ 0.16 α) and the shallow 26 April 2002 Marianas event (E16; M_W=7.0, v_r=0.63 α $\pm$ 0.13 α). The best-fitting velocities exceed the local shear wave velocity ($\sim$0.58 α), but have large errors. In each case, the best-fitting velocity on the other plane is lower, but the misfit is higher. My identification of the fault plane for these events, and similarly for the 3 May 2010 intermediate-depth Izu-Bonin earthquake (E29; M_W=6.1, v_r=0.48 α $\pm$ 0.13 α) is therefore tentative.

7.4.3 Individual and previously analyzed earthquakes

I present the results of my analysis of the M_W=7.0 23 August 1995 Marianas event (E04, z_h=595 km). This earthquake has previously been analyzed by Antolik et al. (1999), Wu and Chen (1999) and Tibi et al. (2001). Wu and Chen (1999) suggested that the eastward dipping nodal plane of the focal mechanism corresponded to the rupture plane, with an apparent rupture velocity of 3–4 km/s toward the west between the two subevents. Their identification of the rupture plane was based on the more consistent orientations of the eastward dipping nodal planes for earthquakes in the aftershock sequence following the mainshock. In contrast, both Antolik et al. (1999) and Tibi et al. (2001) suggest the mainshock ruptured a southwestward dipping plane. Like Wu and Chen (1999), they observe two distinct subevents separated by $\sim$2.5 s. Tibi et al. (2001) estimated that the second subevent was located 13 $\pm$ 2 km west of the first, similar to that of Antolik et al. (1999) ($\sim$ 15 km). My analysis also identifies the southwestward dipping plane as the plane of rupture (Figure 7.5). The best-fitting rupture velocity of 0.47 α $\pm$ 0.04 α (4.7 km/s at 595 km depth) corresponds to an offset of 11.7 $\pm$ 1.0 km between subevents, in agreement with the estimate of Tibi et al. (2001).

Seismograms recording energy from the M_W=6.1 12 November 2003 Izu Islands earthquake (E18, z_h=385 km) also reveal two main subevents. The first subevent of this earthquake peaked 3–3.5 s

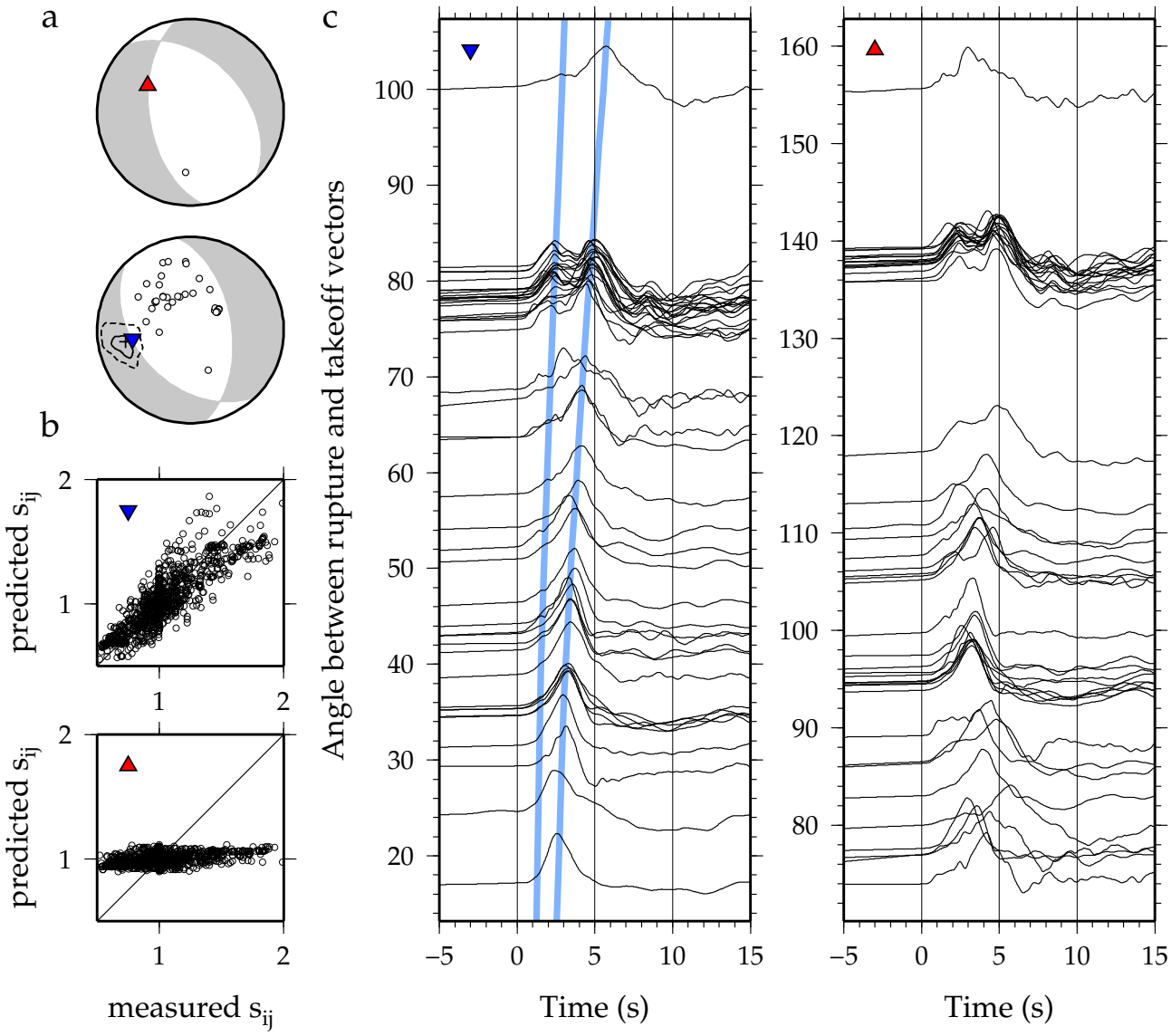

Figure 7.5: Results for the 23 August 1995 Marianas earthquake (E04). a) Focal mechanism and station takeoff vectors (circles) on upper and lower hemisphere equal area projections. A cross marks the best-fitting rupture vector over the whole focal sphere, and triangles mark the best-fitting rupture vector on each of the nodal planes. 80% (solid line) and 95% (dashed line) confidence intervals for the rupture vector orientation are also shown. b) Measured and predicted stretching factors for rupture on each of the nodal planes. The symbols in the upper left corner match those in (a), and denote the vector from which the predicted stretching factors were calculated. c) Seismograms aligned relative to the best fitting rupture direction on each of the nodal planes. Thick shaded lines emphasise the change in arrival times corresponding to distinct subevents for the preferred rupture vector.

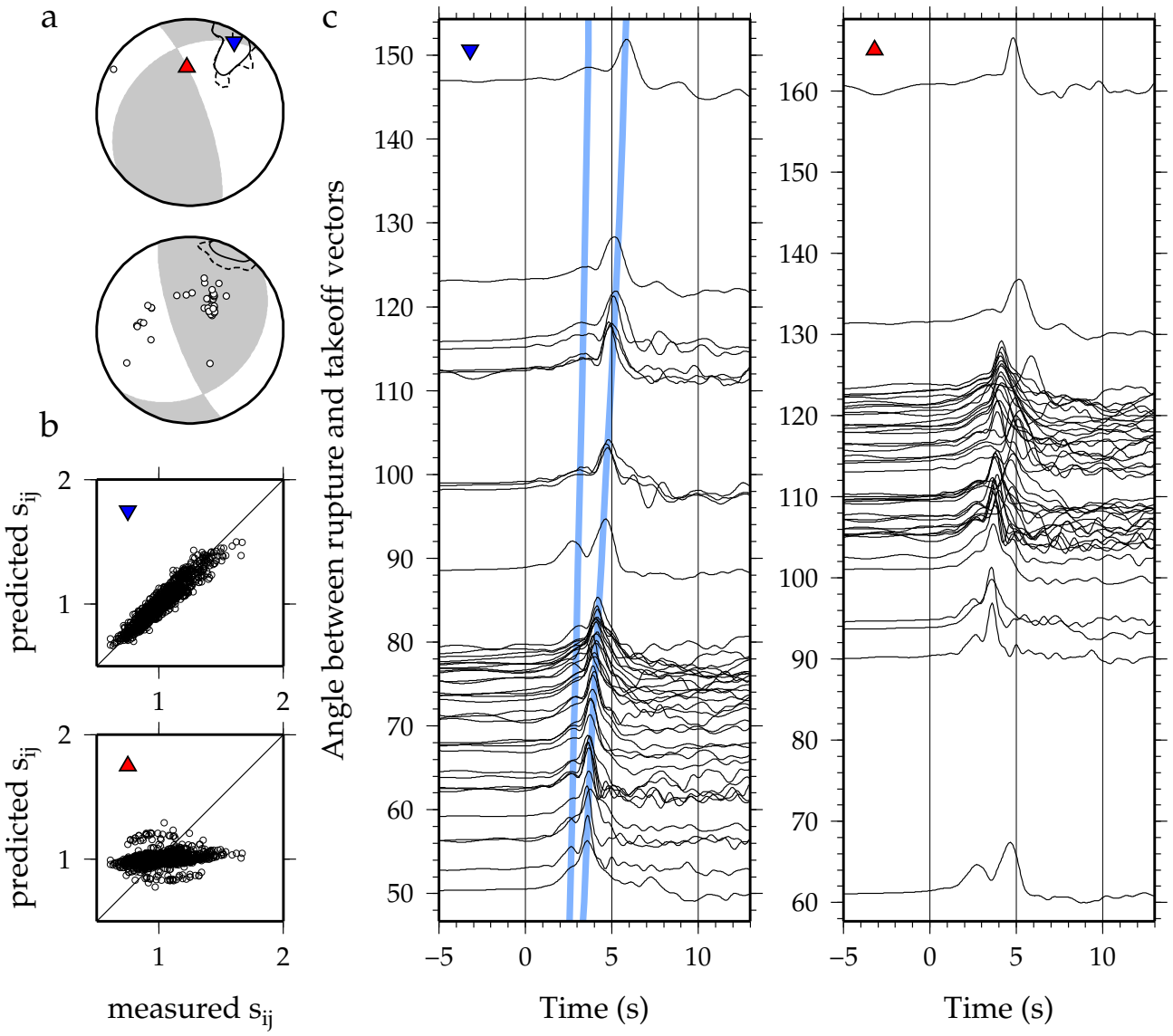

Figure 7.6: Results for the 12 November 2003 Izu Islands earthquake (E18). Subplots are as described in Figure 7.5.

after the nucleation time, and was followed 2–2.5 s later by another subevent. The earthquake is best described as a unilateral rupture propagating almost horizontally toward the northeast at a speed of 0.34 α ± 0.02 α (Figure 7.6).

A more complex earthquake with observable directivity occurred on 20 August 1998 (E09, z_h=425 km, α=9.4 km/s). This event comprised a long, low-amplitude signal, followed 9 s later by three subevents. Each of the large amplitude subevents exhibits moveout relative to the onset of the first (Figure 7.7). The shallow southward-dipping plane is identified as the fault plane, with a best-fitting rupture vector having a velocity of 0.29 α ± 0.02 α (2.7 ± 0.2 km/s), a plunge of -12° and trend of 058°. For the subvertical plane, the best-fitting rupture vector is downward. The station distribution covers rupture-takeoff angles from ∼20–120 degrees on this plane, which is an ample range to identify vertically-propagating unilateral rupture. The high misfit and lack of coherent moveout in subevent

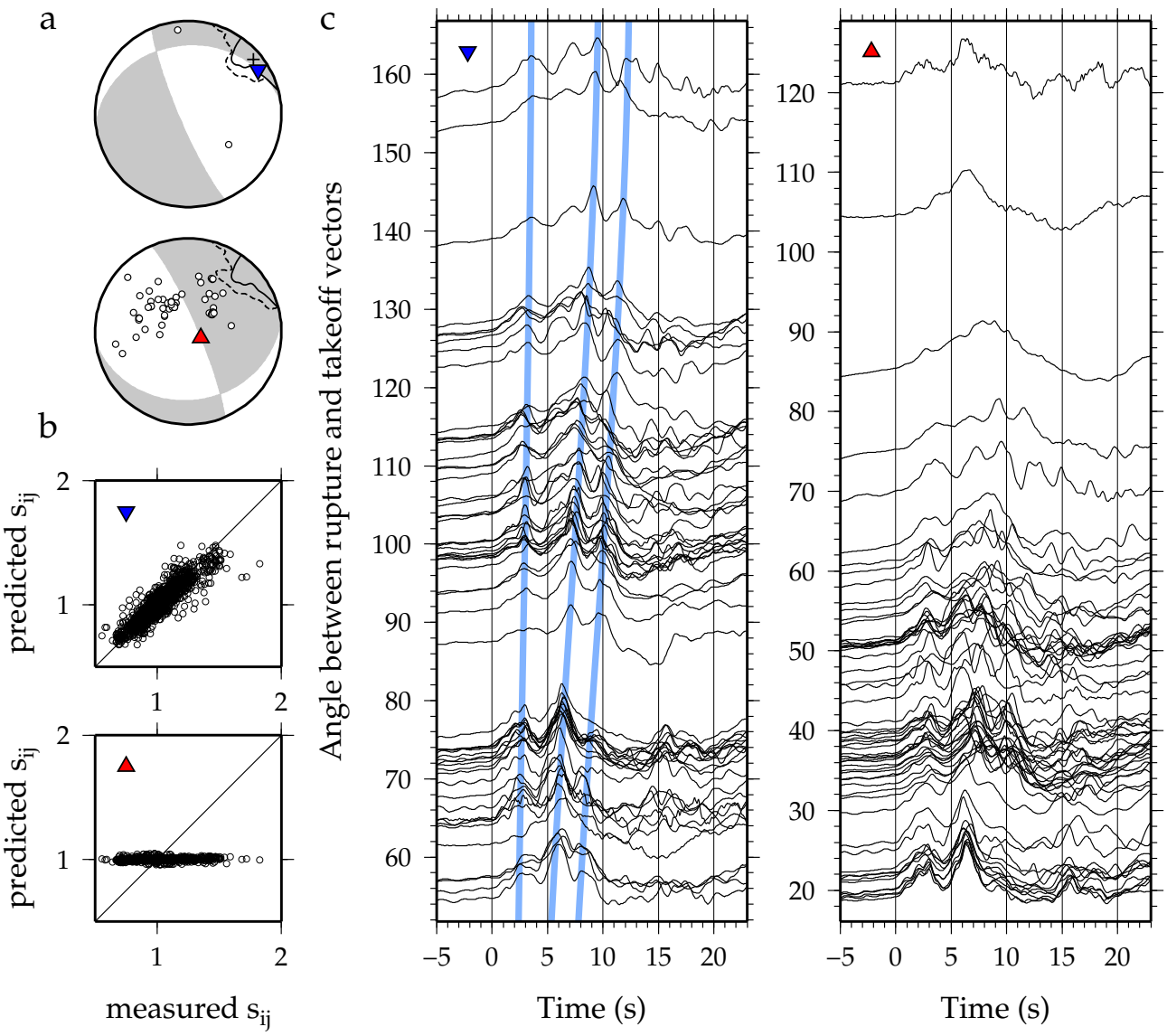

Figure 7.7: Results for the 20 August 1998 Bonin Islands earthquake (E09). Subplots are as described in Figure 7.5.

arrivals plotted on the record section corresponding to this vector is sufficient to conclusively rule out rupture on the steeply dipping plane. My fault-plane identification is further supported by synthetics constructed to match the 3 main subevents (Figures 7.8 and 7.9).

Including the initial 9 s low amplitude event increases the minimum misfit (0.60 instead of 0.44) and reduces the best-fitting rupture velocity (0.14 α $\pm$ 0.02 α), but results in little change in the best-fitting rupture direction (plunge/trend of $-18/043$). Windowing between the onset of the low amplitude event and the first large subevent reveals moveout consistent with propagation along the null axis toward the south at a velocity of 0.20 α $\pm$ 0.05 α, equivalent to a rupture 17 $\pm$ 4 km long (see Supplementary Materials of Myhill and Warren, 2012).

The 20 August 1998 earthquake was previously studied by Tibi et al. (2003), who selected the steeply dipping nodal plane as the fault plane. They picked the P wave arrival time for first

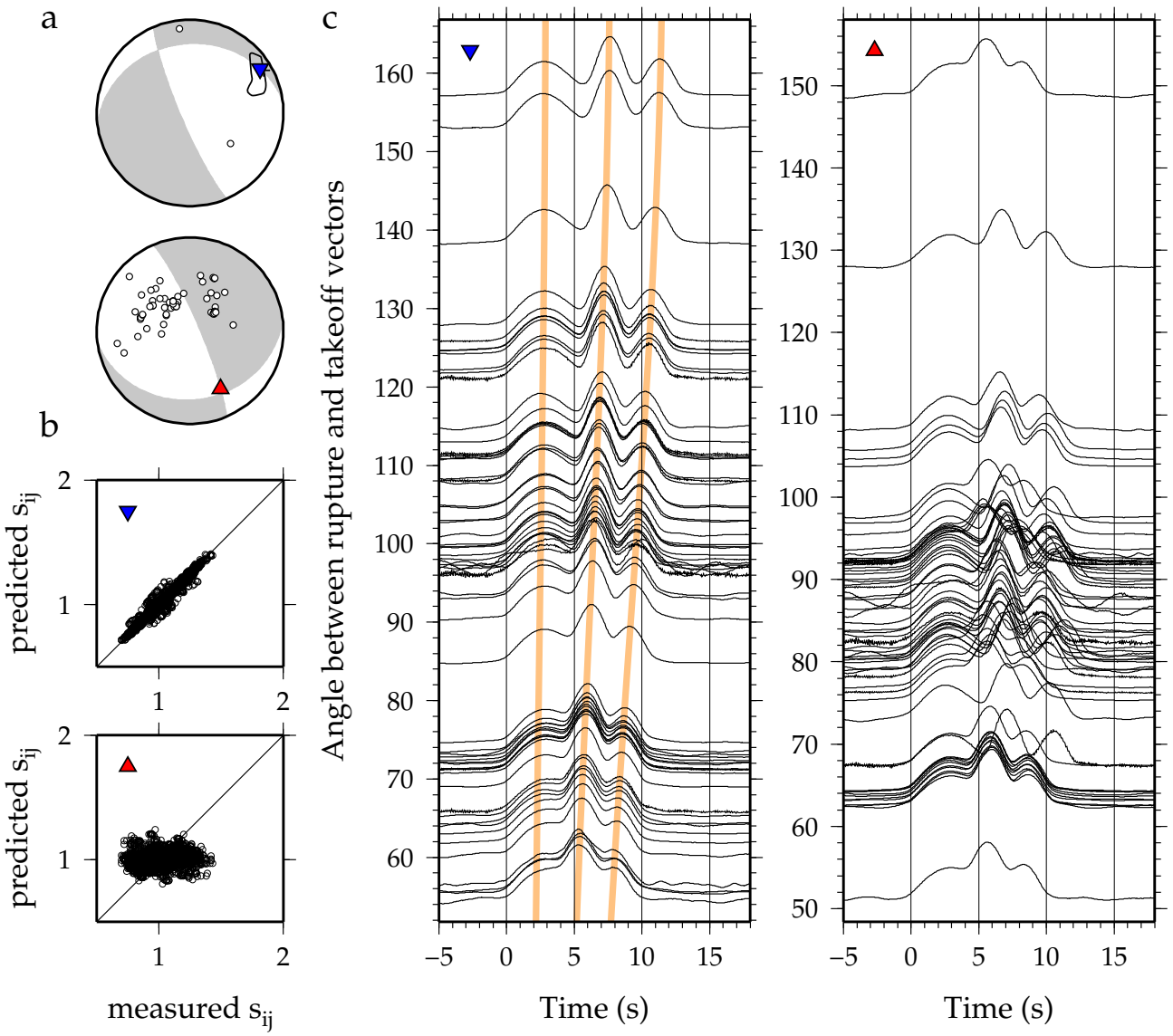

Figure 7.8: Synthetic seismograms for the 20 August 1998 earthquake (E09) assuming rupture on the shallower nodal plane. Subplots are as described in Figure 7.5. Thick lines emphasise moveout in the three synthetic subevents on the shallow rupture plane. The form of the cross correlation graphs in (b) closely mirrors those for the observed seismograms (Figure 7.7).

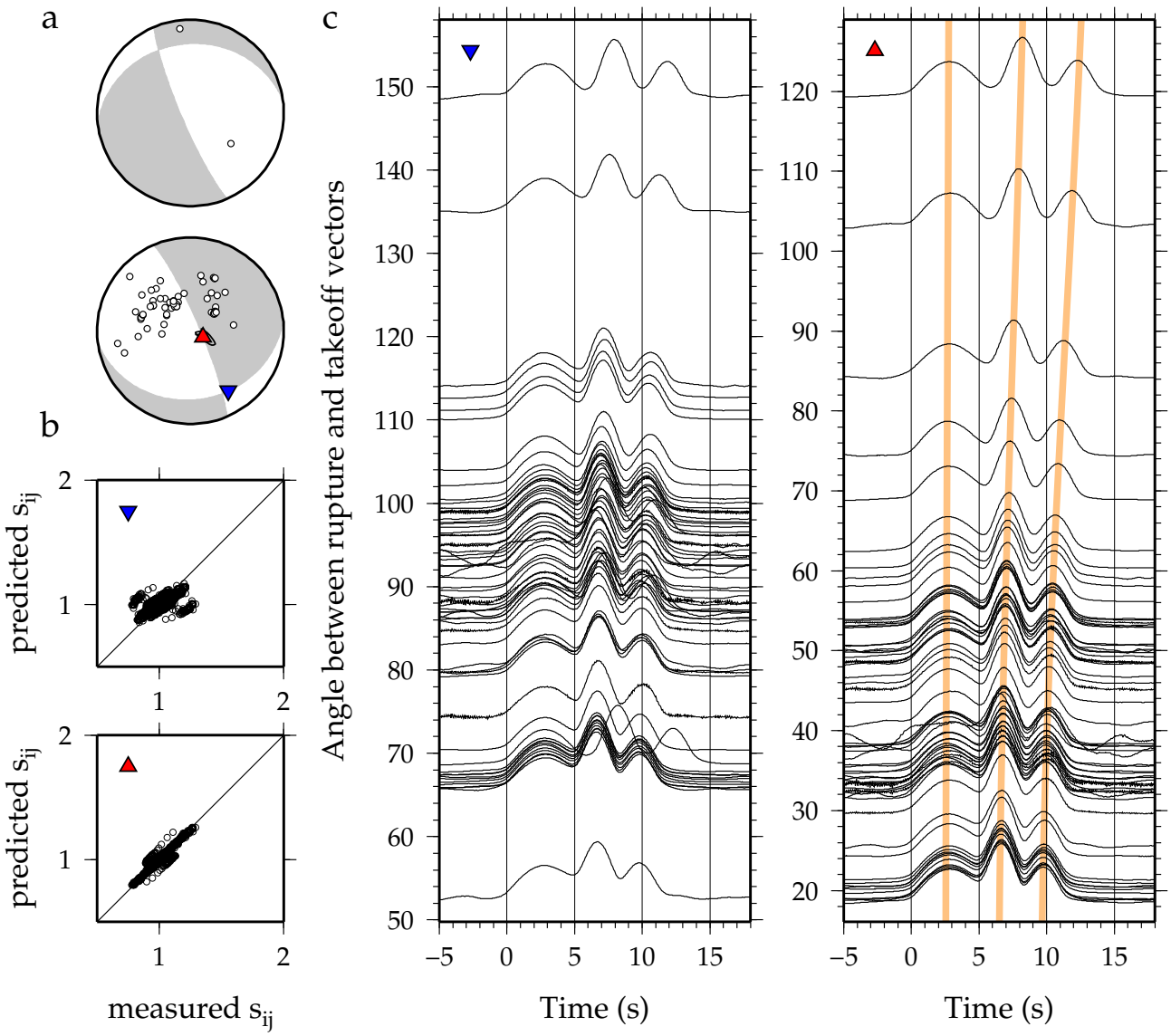

Figure 7.9: Synthetic seismograms for the 20 August 1998 earthquake (E09) assuming rupture on the steeper nodal plane. Subplots are as described in Figure 7.5. Thick lines emphasise moveout in the three synthetic subevents on the steep rupture plane. The form of the cross correlation graphs in (b) are dissimilar to those for the observed seismograms (Figure 7.7).

motion, a single aftershock and the three subevent centroids, locating each using both local and teleseismic stations and a hypocentroidal decomposition method (Jordan and Sverdrup, 1981). Despite identifying the opposite plane to that preferred in this study, there are several similarities between my results and theirs. Their locations for the three main subevents indicate rupture propagation towards the northeast along a shallowly dipping vector. The 6 s and 9 s between the onset of the first and second, and first and third subevents at my estimated velocity of 0.29 $\alpha \pm 0.02\ \alpha$ implies offsets of 16.4 $\pm$ 1.1 and 24.5 $\pm$ 1.7 km, which are comparable to the location offsets of Tibi et al. (2003).

The choice of the steeply dipping nodal plane as the fault plane in the study of Tibi et al. (2003) depended strongly on the nucleation point, which they located 24 km above the centroid of the first large subevent. This relative offset is inconsistent with slip on a near-horizontal plane. I note that their best-fitting plane through the nucleation point lies outside the 95% confidence intervals of all three of the main subevents (their Figure 11). If their location of the nucleation point relative to the mainshock centroid is accurate, I suggest that rupture on a single fault plane is unable to explain all the moment release associated with the 20 August 1998 earthquake.

The 20 August 1998 earthquake was also studied by Park and Mori (2008), who picked the shallowly dipping nodal plane as the fault plane. Park and Mori (2008) inverted waveform data from teleseismic and regional stations using a constant velocity slip-on-a-grid scheme. They achieved a good fit to waveform shape and amplitudes with a velocity of 1–2 km/s, similar to the 1.3–2.7 km/s obtained from my inversion. My values are not directly comparable to their preferred range, because the nucleation point is not co-linear with the main subevents. Nevertheless, the distribution and progression of rupture are in good agreement with my results.

Tibi et al. (2003) and Park and Mori (2008) also analyzed the 6 August 2000 earthquake, one of the earthquakes rejected in my study (R19). Tibi et al. (2003) observed no unambiguous rupture directivity, only slightly narrower triangular pulses for stations with south and southeast takeoff azimuths. Modelling the earthquake as an asymmetric bilateral rupture with constant velocity on the steeply east-northeast dipping nodal plane produced a slightly better fit to the 21 P and 5 SH waveforms than the more shallowly dipping plane. The 2-D slip distribution of Park and Mori (2008) on the steeply dipping plane also reproduces the waveform shapes more closely than the shallowly dipping plane (their Figure 19), although the quality of fit for individual subevent peaks is sometimes quite low.

The timing and duration of individual peaks in displacement for event R19 cannot be matched well by either unilateral or symmetric bilateral rupture at constant velocity, and so I am unable to use the technique of Warren and Silver (2006) to determine the characteristics of rupture for this earthquake. Coherent changes in waveform shape are observed when waveforms are plotted relative to a near-horizontal southwest-northeast vector, but I stress that this observation may not necessarily be indicative of rupture on either plane (see Supplementary Materials of Myhill and Warren, 2012,

for further discussion). The 6 August 2000 earthquake therefore remains a possible exception to the general findings of this study.

Not all of the earthquakes with observed directivity are best explained by rupture on the shallower of the two nodal planes of the CMT solution. Four south dipping planes are also identified as preferred fault planes. Two of these events are located at 26.5°N and 140.5°E, ~435 km beneath the southern end of the Bonin arc. Seismograms which recorded the 12 January 1999 (E10) and 3 July 1999 (E11) events reveal rupture propagation to the southwest. Short waveform durations preclude definitive identification of the fault plane, but the minimum misfit rupture direction for both events is down-dip on the steep southwest dipping plane. The misfit pattern over the focal sphere for each event is replicated in the computed synthetics only for the steeper planes. These two events are separated by less than 100 km, less than a year, and have almost identical best-fitting rupture directions and velocities (Table 7.1).

The 3 July 2001 Volcano Islands earthquake (E15) at 30°N, 140°E and 140 km depth is a third event for which rupture on the more steeply dipping plane is preferred. The earthquake consisted of two main subevents separated by about three seconds (Figure 7.10). Rupture on either plane fits the data satisfactorily, but the steeper plane yields a smaller misfit, better constrained rupture direction and velocity, and more consistent moveout.

7.4.4 Comparison with previously identified fault lineations

I compare my results with the work of Lundgren and Giardini (1992), who projected well-located deep earthquakes onto a plane perpendicular to the null axes of CMT double-couple solutions of nearby earthquakes. Their analysis revealed lineations of earthquakes parallel to one of the nodal planes of the best-fitting double-couple solution, which they equated to planes of shear failure within the subducting slab.

For a $M_W = 5.6$ earthquake which occurred on the 14 April 1990 earthquake at 27.22°N, 140°E and at 450.6 km depth, Lundgren and Giardini (1992) identify the shallow east-southeast-dipping nodal plane as a plane of shear failure. The 12 January 1999 event (E10) is the closest analyzed event to the 14 April 1990 earthquake, with a preferred steep southwest dipping plane of failure. The closest earthquakes with definitively identified planes (E09 and E30) are 1–2° further north; both have shallow south-dipping fault planes.

Lundgren and Giardini (1992) presented two further analyses for the Bonin region. They report a prominent steep north-dipping lineation parallel to one of the nodal planes of the 29 December 1977 $M_W = 5.2$ earthquake at 28.55°N, 138.47°E, 543.2 km depth, with a potential conjugate lineation. For the nearby $M_W = 5.0$ event on 9 September 1990 (28.03°N, 139.4°E, 531.6 km depth), Lundgren and Giardini (1992) note that the north dipping plane is aligned well with prominent northwest-

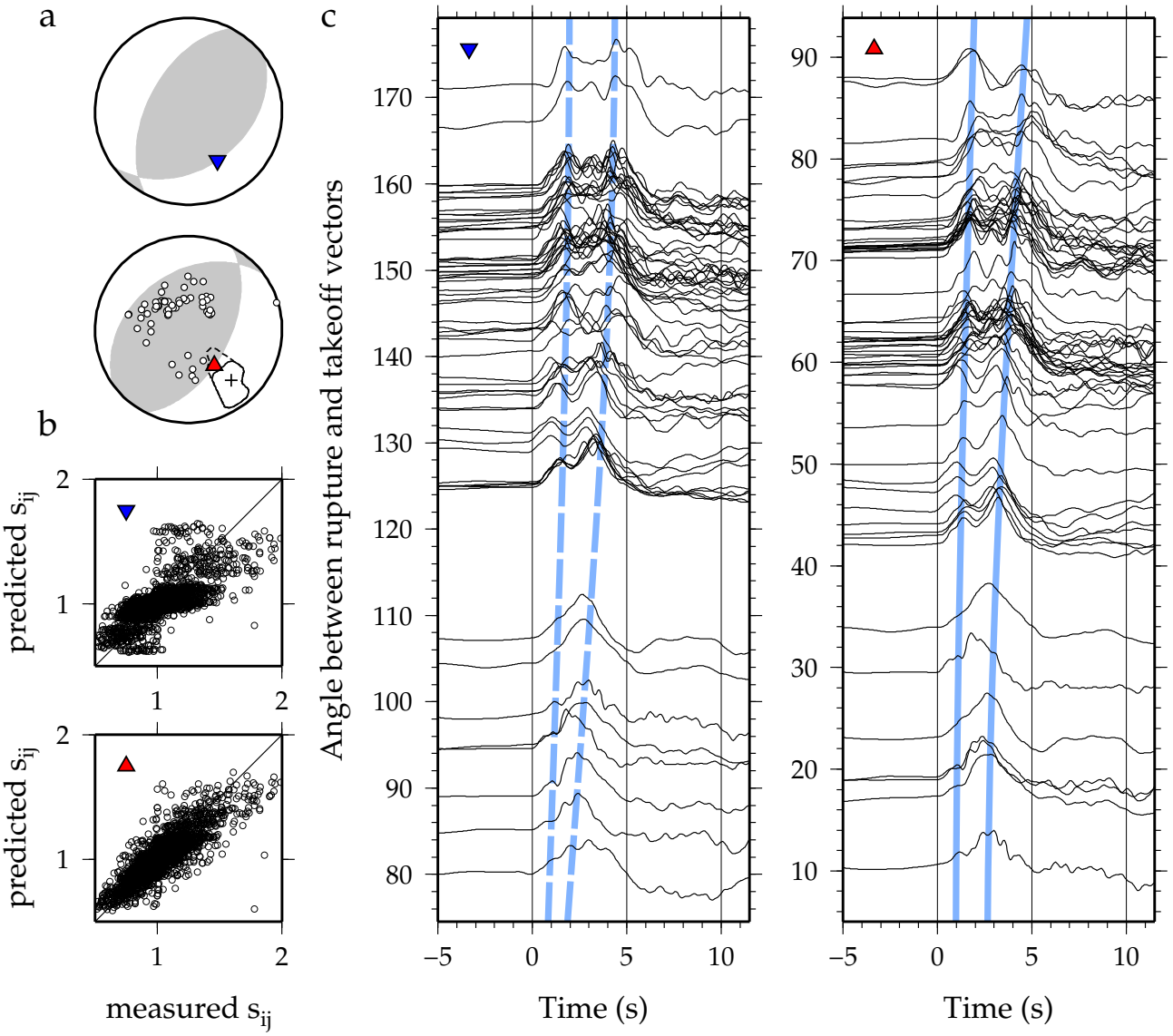

Figure 7.10: Results for the 3 July 2001 Volcano Islands earthquake (E15). Subplots are as described in Figure 7.5. The solid lines in (c) show moveout in peaks of displacement peaks on the southwest dipping plane, and the dashed lines show moveout on the northeast dipping plane. Rupture on the southwest dipping plane appears to fit waveform shapes better than rupture on the northeast dipping plane, consistent with the higher correlation between expected and observed stretching coefficients illustrated in (b).

striking lineations which can be seen on large-scale maps. These earthquakes ruptured a part of the subducting slab which is shallowly dipping, beneath a prominent kink in the Wadati-Benioff zone. Although the orientation of these inferred fault planes is different from those identified in the present study, I have observed no unambiguous directivity in any of the earthquakes from this part of the slab. If the lineations identified by Lundgren and Giardini (1992) represent major shear planes, a change in faulting style is required as the dip of the slab decreases.

Beneath the Marianas Islands, Lundgren and Giardini (1992) reported the presence of a conjugate set of lineations. A $M_W = 5.1$ event on 13 August 1991 (18.93°N, 145.24°E, 617.80 km depth) occurred on an eastward dipping lineation, while the 17 October 1979 $M_W = 6.1$ event (18.52°N, 145.41°E, 583.00 km depth) occurred on a shallower westward dipping lineation. The 17 October 1979 earthquake has an EHB location 12 km shallower and to the east of the 23 August 1995 earthquake analyzed in this study (E04), which ruptured down-dip on a shallow west-southwest dipping plane. This is consistent with the 1979 and 1995 earthquakes occurring on the westward dipping shear plane identified by Lundgren and Giardini (1992).

7.5 Discussion

7.5.1 Rupture processes

The greater success in modelling rupture with unilateral propagation rather than bilateral propagation is primarily a result of the analyzed earthquakes commonly having two distinct subevents. Although no events are better modelled by bilateral rupture than unilateral rupture, full 2D inversions could improve rupture resolution for the larger of my studied events. In particular, the 20 August 1998 $M_W > 7.0$ earthquake (E09) is better modelled by three non-co-linear subevents. The 6 August 2000 $M_W > 7.3$ earthquake (R19) may have had considerable source complexity. It should be noted that "unilateral rupture" in this study is shorthand for unilateral progression of observable seismic energy release. Actual slip distributions may be significantly more complicated.

Although the success of unilateral rupture modelling says little about the rupture processes, the directionality of rupture propagation is more significant. Intermediate depth earthquakes have a tendency to rupture away from the surface of the subducting slab. One possibility is that the upper edge of the plane of seismicity often reaches a critical failure condition before the lower edge, triggering failure progressively deeper into the slab. Deep-focus earthquakes do not show the same preference for rupture into the slab.

7.5.2 Fault plane orientations

Most of the studied earthquakes have one of the principal axes of the focal mechanism aligned with the slab down-dip direction. The analyzed deep-focus earthquakes have down-dip P axes, indicating

that the slab is undergoing compression. The analyzed intermediate depth earthquakes beneath the Marianas and Volcano Islands are mostly down-dip extensional events.

The orientations of identified fault planes are similar for both intermediate and deep-focus earthquakes. The majority of analyzed earthquakes with observed directivity involved energy release on faults which dip up the slab (toward the trench) relative to the slab surface. For all but four of the earthquakes in this study, this orientation corresponds to the more shallowly dipping nodal plane of the CMT solution.

Near-horizontal faulting appears to dominate by 100 km depth. Horizontal faults are active by 50 km depth, but whether there is asymmetry at 50–100 km depth is impossible to deduce from the two earthquakes for which directivity was observed in this depth range. The well-constrained changeover in fault behaviour beneath Middle America occurs at 75 km. Above 75 km depth, faulting occurs on both horizontal and vertical planes (Warren et al., 2008).

Two further deep-focus earthquakes not included in the current study were analyzed by Yoshida (1988). Waveforms from the 446.0 km deep 6 March 1984 (29.60°N 139.11°E) and the 394.8 km deep 24 April 1984 (30.81°N 138.46°E) earthquakes were inverted for slip distributions. In both cases, the more shallowly dipping plane provided a better fit to the waveform data. These two events therefore contribute to the asymmetry in fault plane orientations reported in the current study.

7.5.3 *Assessing potential bias*

Correct identification of the fault plane

The potential for the method of Warren and Silver (2006) to incorrectly identify the fault plane, or distort the confidence intervals was critically assessed by Warren (2010). She conducted a series of experiments using synthetic waveforms with and without noise to demonstrate the resolution of the technique. It was shown that for realistic station distributions without local data, there is no large shift of the minimum misfit away from the true rupture direction. Ruptures with steep and shallow plunges were both recovered successfully. It was shown that improving the distribution of teleseismic stations tightens the constraints on the best-fitting rupture direction. The rupture characteristics of earthquakes with multiple subevents are generally better constrained than more simple events, largely because of the effect of noise on apparent duration of single subevents.

For the current study, synthetics like those plotted in Figures 7.8 and 7.9 were constructed for each of the earthquakes in Table 7.1. The complete set of synthetics are published as Supplementary Materials of Myhill and Warren (2012). As discussed in the methodology section, these synthetics were used as tests of rupture vector resolution and fault plane identification. Misfit surfaces over the focal sphere for synthetics constructed for ruptures on the preferred/identified fault planes closely mirror those constructed from the real data. The misfit surfaces for the best-fitting rupture vectors

on the auxiliary planes rarely match the real data as closely. Both waveform shapes and station distributions are therefore important in defining the shape of the misfit function. In comparing synthetic waveforms with real data I provide an additional discriminant from which I can make my selection of the rupture plane for each earthquake.

Resolvability of subvertical rupture vectors

Despite the discussion above, the possibility remains that the predominance of near-horizontal faults is an artefact produced by failing to identify directivity on more steeply dipping planes. Although many of the rejected events are small, ten rejected events (five of which were deep-focus) had $M_W \geq 6.2$, and there were five events (E07, E08, E19, E20, E23; none of which were deep-focus) for which directivity was observed but insufficient to sufficiently constrain rupture propagation to a single nodal plane or the focal mechanism null axis.

A key requirement for resolving a rupture in any direction is a good range of station-event azimuths and takeoff-rupture angles. This is true for any technique designed to constrain patterns of fault slip, and is not unique to the technique of Warren and Silver (2006). If ruptures occur with a large component of vertical motion, apparent durations recorded at large epicentral distances do not vary very much, because $d\tau/d\theta$ is low at $\sim 0^\circ$ and $\sim 180^\circ$ (Equation 7.2). The lack of a large number of regional and local stations has a larger effect on the resolvability of subvertical than near-horizontal rupture. This is particularly true for downward-propagating ruptures, for which stations at large epicentral distances will have low takeoff-rupture angles and record short apparent rupture durations, making it less likely that individual subevents will be visible.

For well recorded IBM earthquakes, the range in rupture-takeoff angles for candidate rupture directions on either nodal plane exceeds 60°, which is sufficient to observe directivity for most M_W >6.0 earthquakes. Only five earthquakes in Table 7.1 have much poorer ranges of candidate rupture-takeoff angles on the steeply dipping plane (E06,E08,E12,E14,E19); these are all intermediate depth earthquakes.

The resolution of rupture directivity for analyzed earthquakes on each of the nodal planes can be determined by constructing a further set of synthetics. I use the rupture characteristics on the preferred and identified planes (velocity, duration and sub-event properties) to create synthetics for an identical rupture propagating instead along the best-fitting rupture vector on the auxiliary plane. By doing this, I make the assumption that rupture characteristics are independent of rupture orientation, but make no assumptions about the effects of location and depth on propagation. All the synthetics created are included as Supplementary Materials of Myhill and Warren (2012).

There are 25 events in my dataset for which the best-fitting rupture vectors are distinct from the null axis. Only one of these identified ruptures would have been difficult to identify had it occurred

instead on the auxiliary plane (21 June 2000, synthetic misfit 0.59, contrasting with a synthetic misfit of 0.26 on the identified plane of rupture). One of the preferred ruptures would also probably have been missed or rejected (28 March 2000, synthetic misfit 0.61, contrasting with a synthetic misfit of 0.24 on the identified plane of rupture). Considering the effects of noise, the other 23 events would probably have resulted in the same confidence in identification as in the actual dataset; increases in synthetic misfit are ≤ 0.12 where a plane of rupture has been identified or preferred, and in some cases the misfit is actually smaller for synthetics on the auxiliary plane than for the preferred fault plane (e.g. the 20 August 1998 and 3 May 2010 earthquakes).

I cannot rule out the possibility that rupture on the steeply dipping nodal plane occurred during many of the earthquakes for which I have been unable to adequately constrain directivity to a single plane. Nevertheless, the difference in my ability to resolve shallowly versus steeply dipping ruptures does not appear to be sufficient to explain the dominance of one fault orientation as inferred from the results summarised in Table 7.1.

7.5.4 *Possible interpretations*

Reactivation of pre-existing faults

Several hypotheses have been proposed to explain the dominance of one set of fault planes in subduction settings. One proposal is that normal faults created at the outer rise are reactivated during subduction (Savage, 1969; Silver et al., 1995). Nakajima et al. (2011) present one potential case of reactivation of an oceanward dipping normal fault within the slab beneath Japan.

In several different subduction zones, the outer rise faults with larger offsets dip towards the trench. This is true along the Middle America Trench offshore Costa Rica and Nicaragua (Ranero et al., 2003), and along the Tongan Trench (Masson, 1991; Wright et al., 2000). If these faults are reactivated at depth, as proposed by Ranero et al. (2005) and Nakajima et al. (2011), then a predominance of subvertical planes should be expected. This is not observed, and statistical analyses on focal mechanisms suggesting a dominance of subvertical faults (e.g. Jiao et al., 2000) have been proven to be incorrect (Warren et al., 2007).

Despite the lack of subvertical planes, it is still possible that reactivation of pre-existing faults occurs at intermediate depth. The IBM outer rise exhibits normal faults dipping both towards and away from the trench (Oakley et al., 2008). However, even if oceanward-dipping normal faults are reactivated after subduction, a modification to the theory is required to explain the lack of reactivation of trenchward-dipping faults.

Fluid/hydrous phase accumulation

If shear parallel to the slab surface has a significant effect on the slab stress field, any planes of weakness in a near-horizontal orientation would be approximately perpendicular to the minimum compressive stress. Savage (1969) suggested that free fluids would concentrate along such zones, reducing the effective pressure and allowing faulting. A key problem with this hypothesis is that it is at odds with the stress guide hypothesis, in which the strength of the slab results in either σ_1 or σ_3 being parallel to the down-dip direction (Isacks and Molnar, 1971). The stress guide hypothesis has been successful in explaining focal mechanism orientations within many subduction zones (e.g. Christova and Scholz, 2003; Chen et al., 2004) and stress guide behaviour is reproduced in numerical models of subducting slabs (e.g. Billen et al., 2003).

In an alternative model, accumulation of fluids arises not as a result of shear but by channelisation along zones of reduced grain size (Wark and Watson, 2000; Kiser et al., 2011). Kiser et al. (2011) propose that fluids released at greater depth within subducting slabs will migrate rapidly up near-vertical planes, but reside for long enough along near-horizontal faults to become incorporated into hydrous minerals. The relative weakness of hydrous minerals may promote shear localisation and instability (Kelemen and Hirth, 2007), followed by a temperature increase by frictional heating and strain hardening (Chernak and Hirth, 2010). The resulting destabilisation of hydrous phases will release fluids along the shear zones, enhancing slip.

This hypothesis was proposed to explain only the orientation of intermediate depth faulting. The role of fluids and hydrous minerals at depths exceeding 300 km is subject to debate. Results from high pressure experiments suggest that dehydration of hydrous minerals in subducting slabs above 300 km is only partial, and that significant water may be carried deeper (e.g. Komabayashi and Omori, 2006). It has been suggested that fluid release in the mantle transition zone may cause deep seismicity (Omori et al., 2004). In contrast, Green et al. (2010) suggest on the basis of seismic distributions and the olivine transformation hypothesis for deep seismogenesis that negligible water is carried beyond 300 km. As such, it is unclear whether fluid accumulation can explain the dominance of near-horizontal planes along the IBM subduction zone system down to 500–600 km depth.

Lattice preferred orientation (LPO)

Fluid weakening is not the only mechanism by which rupturing of near-horizontal faults could be promoted. The orientation of fault planes could be controlled by the LPO of major mineral constituents, such as olivine (Sugimura and Uyeda, 1967). Although studies of seismic anisotropy have the potential to determine LPO in subducting slabs, an extremely good distribution of stations and range of ray paths are required to constrain the 3D nature of this anisotropy. Potential changes in LPO with increasing pressure and temperature (e.g. Raterron et al., 2011) make the possibility of

horizontal shear promoted by LPO throughout the upper mantle less likely.

Isobaric rupture processes

Isobaric rupture processes have been suggested as a reason for rupture on near-horizontal faults (e.g. Antolik et al., 1999). There is little data to support this hypothesis; indeed, three of the preferred fault planes with steeper dips in this study exhibit down-dip rupture directivity.

External forces and slab morphology

The above proposals assume that chemical or structural variations within the slab cause the observed asymmetry in faulting orientations. Although such variations certainly exist, their structure, location and orientations are not well known, and they may have little influence on the orientation of deep fault planes. An alternative possibility is that the asymmetry is imposed by forces acting on the slab.

In most subduction zones, the alignment of one of the principal stress axes down the dip of the slab indicates the importance of the slab as a stress guide. A homogeneous slab and stress field will yield a conjugate fault system. The superposition of bending or unbending stresses on the down-dip stress field may result in the slab preferentially breaking along just one orientation of fault. In the outer rise prior to subduction, this preference is seen in the increase in numbers of and displacement along trenchward-dipping faults as distance to the trench decreases. A similar process may operate after subduction.

Suzuki and Kasahara (1996) studied three intermediate-depth earthquakes which ruptured on faults with shallow dips beneath Hokkaido. One of these earthquakes was the 1994 Kushiro-Oki event, which had a prominent aftershock sequence demarcating the mainshock rupture. Suzuki and Kasahara (1996) suggested the cause of horizontal rupture was unbending within the slab. This is consistent with the results from the present study, and those in Warren et al. (2007, 2008).

Within the deeper part of the mantle transition zone, resistance to penetration beyond 700 km depth could explain the near-horizontal fault planes within the IBM slab. The difference in deep fault orientations within the IBM and the Tonga-Kermadec slab is consistent with control by evolving slab morphology. In this scenario, there is no reason why slabs deforming by pure shear should not exhibit both fault plane orientations. Highly contorted regions of the slab might be expected to exhibit changes in fault orientation on short ($<$300 km) length scales.

7.5.5 Slab deformation

If the fault plane orientations of deep earthquakes within subduction zones are dependent on external forces and deformation of the slab, they provide independent observations which can be used to constrain subduction zone dynamics. The well defined peak of deep-focus seismic activity within

the Izu-Bonin slab lends some support to this idea; it occurs close to a well-defined bend in the Wadati-Benioff zone where compressive stresses should be highest, and where near-horizontal fault formation should be strongly favoured. After the slab has flattened out (below ∼500 km), there are fewer earthquakes. I note the absence of $M_W > 5.7$ earthquakes after 1994 with sufficient directivity to indicate the orientation of earthquakes within the toe of the seismically active slab north of 27°N. If the prominent lineations identified by Lundgren and Giardini (1992) do delineate active shear zones, they indicate a change in fault plane orientation. Perhaps this is related to unbending of the deep slab, similar to the unbending observed at intermediate depth.

7.6 Conclusions

I use the technique of Warren and Silver (2006) to analyse the directivity of 58 earthquakes within the Izu-Bonin-Marianas subduction zone system. I improve on previous studies of the region by more efficiently using waveform shape to resolve directivity, enabling the analysis of smaller earthquakes and greatly increasing the number of studied events.

I observe directivity for 31 of the analyzed earthquakes. For 20 of these earthquakes, the rupture vector is sufficiently constrained to identify the fault plane. Comparing estimated and observed stretching factors between waveforms, constructing synthetics and monitoring variations in waveform shapes increases confidence in the selection of the preferred rupture planes.

Waveform shapes of the studied earthquakes are fit better or equally well by unilateral as bilateral rupture. At intermediate depths, earthquake ruptures exhibit a strong preference for propagation away from the surface of the slab. The ruptures of deep-focus earthquakes show no such preference. Well-constrained rupture velocities are 0.4–0.8 times the local shear wave velocity.

All of the identified (8) and preferred (12) fault planes reported in this study dip either at low angles, or to the south and west (Figure 7.11). This behaviour is observed for both intermediate-depth (60–300 km) and deep–focus (300–700 km) earthquakes, in contrast to a previous study of the Tonga-Kermadec region (Warren et al., 2007) where both near-horizontal and subvertical fault orientations are observed at >300 km depth. Only 4 earthquakes are modelled better by rupture on the steeper of the two possible CMT nodal planes. These events occur where the slab is steeply dipping, such that the preferred rupture planes have similar orientations to the more shallowly dipping fault planes when rotated into the local orientation of the slab.

There are a wide range of possible interpretations of these observations. Chemical or rheological differences on asymmetrically oriented pre-existing features (such as faults) could result in a dominance of one orientation of deep fault planes. However, the data presented here are most compatible with deep fault planes being oriented to most effectively relieve stresses developed as a result of slab deformation. Pre-existing structures may be reactivated in deep earthquakes, but only if they

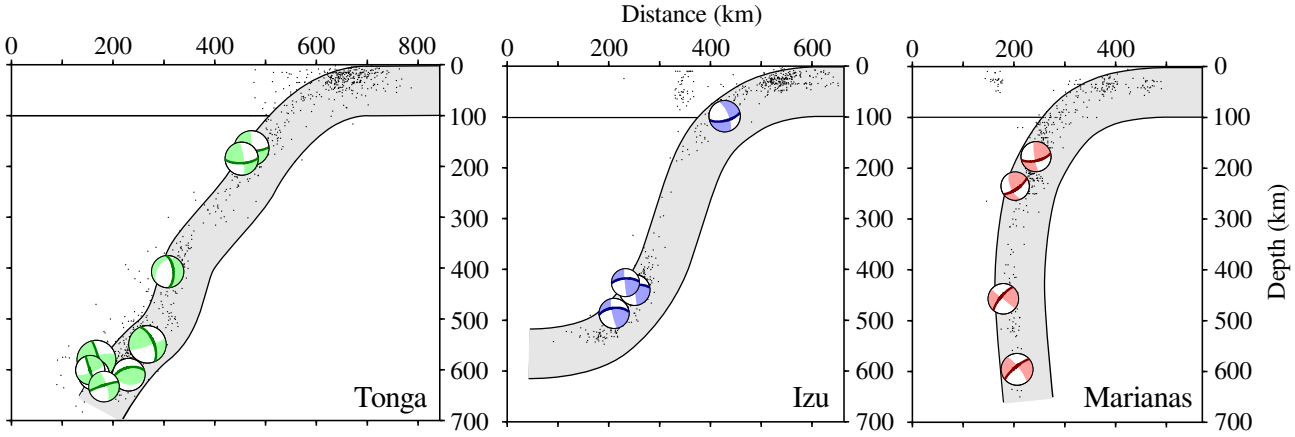

Figure 7.11: Cartoon cross sections through the Tonga, Bonin and Marianas slabs perpendicular to the trench. The Bonin and Marianas profiles correspond to the swaths drawn in Figure 7.1. Focal mechanisms of earthquakes are projected onto the plane of the cross section. Identified and preferred fault planes are marked in bold. The focal mechanisms on the Tonga section are taken from (Warren et al., 2007), those on the Izu and Marianas sections are from the analysis presented here.

are favourably oriented. I hope that further study and modelling will help confirm or reject this hypothesis.

Part III

Local conditions

8 Composition and mineralogy

8.1 Introduction

The vast majority of deep earthquakes occur within oceanic lithosphere. Exceptions to this rule include a few earthquakes which occur in the Indian plate 60–100 km beneath Tibet and possibly those forming the intermediate-depth Wadati-Benioff zone beneath the Hindu-Kush (e.g. Roecker, 1982; Searle et al., 2001).

The composition and structure of oceanic lithosphere is reasonably well understood. Even without direct access or detailed information about the source region of deep earthquakes, the protolith compositions of the rocks undergoing brittle failure can be inferred with a degree of confidence.

In this chapter, I will outline the structure and composition of subducting oceanic lithosphere and potential sources of alteration. This information will be used in simple thermal and kinematic models of subducting slabs (Chapters 9 and 10).

8.2 Composition

8.2.1 Oceanic pseudostratigraphy

Oceanic lithosphere created at intermediate and fast-spreading ocean ridges is layered. The uppermost lithosphere consists of a thin veneer of sediments, typically $\sim$0.5 km thick but with a thickness dependent on the proximity of the ocean floor to sources of sediment throughout the history of the plate. These sediments overlie $\sim$0.5 km of basalts, and a further $\sim$1.5 km of diabase dykes. Beneath the dykes lies a $\sim$5 km thick section of coarse grained mafic and ultramafic cumulates. Mineral assemblages typical of the oceanic crust include calcic plagioclase (anorthite-rich) and clinopyroxene (augite), often accompanied by lesser olivine, orthopyroxene and iron oxide.

The underlying mantle consists of ultramafic rocks depleted by melt removal during isentropic upwelling at the mid ocean ridges. Because mid-ocean ridge melting is polybaric, the solid residue evolves as it upwells, becoming increasingly depleted as it decompresses. Decompression melting of a lherzolitic olivine-garnet-clinopyroxene-orthopyroxene source results in the loss of clinopyroxene and garnet, and a new generation of olivine. Harzburgites and dunites are typical residua of the

melting process, consisting of olivine and variable amounts of orthopyroxene.

Sample compositions for basalt, harzburgite and 'pyrolite' (an idealised lherzolite representing the bulk mantle) are provided in Table 8.1.

Oxide	Pyrolite[a]	Basalt[a]	Harzburgite[b]	Modified harzburgite
SiO_2	38.71	51.75	36.07	36.04
MgO	49.85	14.94	56.51	56.54
FeO	6.17	7.06	6.07	5.97
CaO	2.94	13.88	0.81	0.79
Al_2O_3	2.22	10.19	0.53	0.65
Na_2O	0.11	2.18	0.00	0.00

Table 8.1: Molar percentage of oxides for bulk compositions used in thermal models. Compositions after Workman and Hart (2005)[a] and Baker and Beckett (1999)[b]. The modified harzburgite composition was calculated by subtraction of basalt from pyrolite under mass and phase balance at 1600 K and 0 GPa by Xu et al. (2008). It is shown only for comparison with the natural harzburgite.

8.2.2 *Metamorphism of unaltered lithosphere*

After subduction, slab crust and mantle undergo significant changes in mineralogy. If chemical equilibrium is maintained, dry basaltic compositions grow pyrope and grossular-rich garnet and omphacitic pyroxene at the expense of plagioclase. Kyanite is also common. Quartz transforms to coesite and finally to stishovite with increasing pressure. In the mantle transition zone at $<1000^\circ$C, ringwoodite is stable. At the base of the upper mantle, crustal assemblages include magnesiowüstite, akimotoite and perovskite.

Peridotites in the upper mantle also exhibit changes in equilibrium assemblage during subduction (Figure 8.1). At 30–60 km depth, garnet grows at the expense of plagioclase. It should be noted that the composition used to calculate Figure 8.1 does not include chromium, which stabilises spinel at the expense of garnet (e.g. Klemme, 2004).

Before reaching the mantle transition zone, orthopyroxenes undergo a transformation to high pressure clinopyroxene (C2/c). Within cold slabs, stishovite becomes stable at 400–500 km depth, despite the lack of quartz at low pressure.

The most significant changes in peridotite assemblage occur within the olivine component. Within the convecting mantle, olivine transforms to wadsleyite at about 410 km depth, then to ringwoodite at 520 km, and finally ringwoodite decomposes into perovskite and ferropericlase at 670 km. In cold slabs, the wadsleyite phase field narrows and migrates to lower pressure. At $<600^\circ$C, wadsleyite is stable at <350 km depth. The ringwoodite-in reaction also migrates to lower pressure at low temperatures, and within the coldest slabs ringwoodite could grow directly from olivine. In the coldest slabs, Figure 8.1 suggests that ringwoodite could break down to stishovite and ferropericlase, rather than perovskite and ferropericlase.

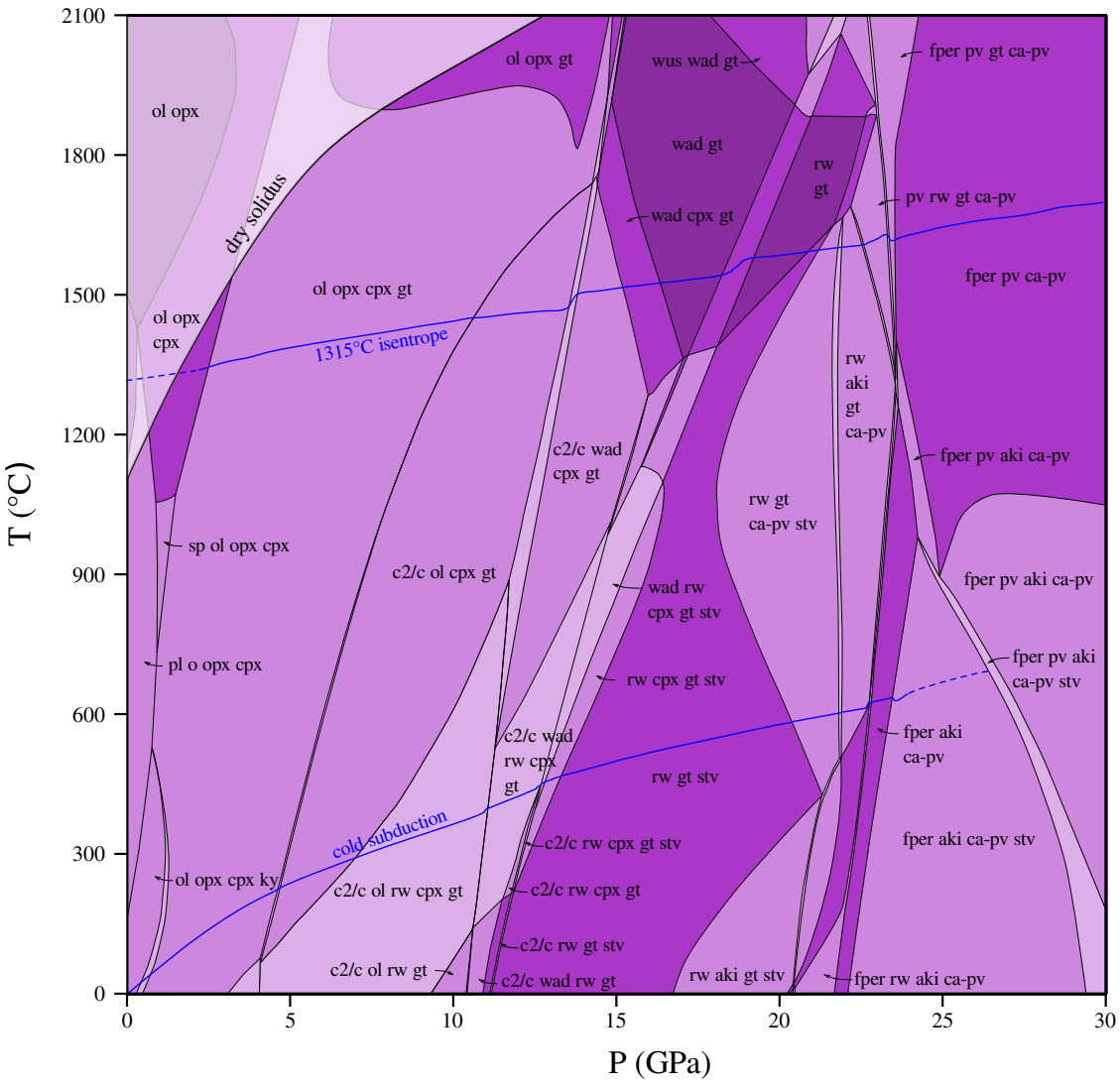

Figure 8.1: Isochemical *P-T* phase diagram for a dry harzburgite. Diagrams like this one show the equilibrium (minimum Gibbs free energy) mineral assemblage for a given bulk composition under varying pressure and temperature conditions. Gibbs free energy minimisation was undertaken using Perple_X (Connolly, 2005, 2009) with the thermodynamic database of Stixrude and Lithgow-Bertelloni (2011). The *P-T* region where melting is expected is shaded more lightly. Blue lines correspond to the geotherms for convecting mantle (calculated from the pyrolitic composition in Table 8.1 with T_P=1315°C) and cold subducting slabs (minimum estimated temperature within the north Tonga slab; see Chapter 9). Mineral abbreviations are as follows: ol = olivine, opx = orthopyroxene, cpx = clinopyroxene, pl = plagioclase, sp = spinel, gt = garnet, c2/c = high pressure clinopyroxene (C2/c space group), wad = wadsleyite, rw = ringwoodite, stv = stishovite, fper = ferropericlase (or magnesiowüstite), pv = perovskite, ca-pv = calcium perovskite, aki = akimotoite (high pressure ilmenite-group mineral).

8.3 Fluid alteration

Hydrogen is incompatible in mantle minerals at high temperatures and low pressures, such that decompression melting effectively dehydrates the mantle. The solubility of water in mafic melts is ~2500 times greater than in olivine, such that even small fraction melting leaves only a few p.p.m. H_2O in the residue that becomes the lithospheric mantle (Hirth and Kohlstedt, 1996). Small fraction melts may crystallise hydrous minerals such as amphibole, but the low concentration of hydrogen in the convecting mantle (125 ± 75 p.p.m.; Hirth and Kohlstedt, 1996) means that any concentrations of hydrous minerals formed in this way will make only a very small contribution to the total volume of the lithosphere.

Significant bodies of hydrated material cannot be primary features of the oceanic lithosphere. If large volumes of hydrated material are present in oceanic plates, the hydrogen must have been added after formation at the mid-ocean ridges. Furthermore, hydration of the crust and uppermost mantle is only possible at <700°C, where hydrous minerals are stable (e.g. Yang and Powell, 2008). Lower temperatures encourage greater hydration, as orthoamphibole, talc, serpentine (antigorite) and brucite successively become stable. Serpentine is the major product of hydration reactions at <600°C, and contains 13 wt% H_2O. Providing serpentinisation is not limited by water availability, hydration fronts may advance at velocities on the order of 1 mm/a (MacDonald and Fyfe, 1985; Rudge et al., 2010).

8.3.1 Hydration near the ridge

Hydrothermal circulation close to the mid-ocean ridges reintroduces water to the uppermost lithosphere. Although vigorous and pervasive convection is probably limited to the upper 200–300 m of extrusives where small scale permeabilities are greater than $\sim 10^{-14}$ m^2, large-scale networks of cracks and faults probably enable fluid flow and advective cooling to greater depths (Becker and Davis, 2004), but probably no deeper than 5 km (e.g. Bach and Früh-Green, 2010). The lack of hydrothermal circulation in the lowermost crust and oceanic mantle close to the ridge is a result of low strength and the lack of brittle failure at >600°C, which precludes the opening and maintenance of high-permeability crack networks.

Hydrothermal circulation and alteration may extend to greater depths around oceanic fracture zones, where newly formed crust and uppermost lithosphere are cooled dynamically. Because transform faults have large displacements and are active over millions of years, damage zones are able to become well developed. Single hydrothermal fields can exist for tens of thousands of years (Früh-Green et al., 2003). Depending on the efficiency of cooling by hydrothermal cooling, hydrothermal alteration may reach depths of over 15 km on long or slow slipping fracture zones (Roland et al., 2010). Thin or absent crust along fracture zones revealed by dredged peridotite

encourages more intense hydration of mantle rocks, evidenced by white smokers (Kelley et al., 2001).

Direct mantle hydration is also possible at slow spreading ridges such as the Gakkel or Southwest Indian Ridges, where conductive cooling at the ridge is sufficient to inhibit decompression melting (Dick et al., 2003). Slow spreading ridges are also host to oceanic core complexes, where large normal faults expose lower crust and mantle at the sea floor (Escartín et al., 1997; Ildefonse et al., 2007).

8.3.2 *Hydration prior to and following subduction*

The feasibility of large scale hydration of the oceanic uppermost mantle remains controversial. Borehole projects have so far failed to reach the Moho in lithosphere created at an intermediate or fast-spreading mid-ocean ridge. The negligible porosity and permeability of intact lower crustal cumulates (Becker and Davis, 2004) implies that if any fluids do penetrate down to the mantle, they must do so through faults, or where the crust is thin or absent. Any hydrothermal alteration may therefore be restricted to the damage zones of these faults.

Far from ridges, trenches and active fracture zones, oceanic lithosphere remains largely undeformed. It has been suggested that long-term cooling and contraction may lead to thermal cracking and subsequent hydration down to 50 km depth (Korenaga, 2007). However, there is currently little geological evidence to support this hypothesis. Localised hydration may occur on faults formed by flexure in the vicinity of volcanic edifices, but the bulk of the lithosphere probably remains largely unchanged as it cools and subsides.

As oceanic plates approach a trench, deformation rates again increase. Within the outer rise (a low rise seaward of the trench), faults cut more than 20 km into the plate. Close to the trench, they can be spaced as little as 2–3 km apart (Ranero et al., 2003; Lefeldt and Grevemeyer, 2008). Rare large normal faulting earthquakes such as the 1977 Sumba earthquake may cut even deeper, perhaps 30–50 km into the plate (Lynnes and Lay, 1988). Large outer rise faults may be conduits for water penetration into the mantle (Kirby et al., 1996; Peacock, 2001; Ranero et al., 2003).

It has been suggested that deeply penetrating slab hydration may continue after subduction (Oxburgh and Turcotte, 1976). Numerical models suggest that fluids may be drawn into the slab from the overlying subduction channel (Faccenda et al., 2009), or they could rise buoyantly and penetrate the slab more deeply after being released during dehydration at greater depths (Faccenda et al., 2012). Whether these results reflect real Earth processes strongly depends on how closely the governing equations reflect the complex and variable rheology of oceanic lithosphere, and the mechanisms by which porosity and permeability develop in compact media during strain, both of which remain poorly understood.

8.4 Metamorphism of hydrated lithosphere

8.4.1 Mineralogy

Even if slab hydration is restricted to the uppermost 5–10 km of the upper mantle, significant water can still be transported to >100 km depth. Many hydrous minerals are capable of transporting water beyond 100 km depth within mafic and ultramafic rocks (Table 8.2).

Table 8.2: Hydrous minerals

Name	End-member chemical formula	wt % H_2O
Brucite	$Mg(OH)_2$	30.89
Serpentine (Clinochrysotile)	$Mg_3Si_2O_5(OH)_4$	13.00
Chondrodite	$Mg_5Si_2O_8(OH)_2$	5.30
Hydroxylclinohumite	$Mg_9Si_4O_{16}(OH)_2$	2.90
Talc	$Mg_3Si_4O_{10}(OH)_2$	4.75
Amphibole (Mg-anthophyllite)	$Mg_7Si_8O_{22}(OH)_2$	2.31
10 Å	$Mg_3Si_4O_{14}H_6$	13.01
Phase A	$Mg_7Si_2O_8(OH)_6$	11.84
Phase B	$Mg_{12}Si_4O_{19}(OH)_2$	2.43
Superhydrous Phase B (C)	$Mg_{10}Si_3O_{14}(OH)_4$	5.82
Phase D (F, G)	$Mg_{1.14}Si_{1.73}H_{2.81}O_6$	14.45
Phase E	$Mg_{2.3}Si_{1.25}H_{2.4}O_6$	11.41
Chlorite	$Mg_5Al_2Si_3O_{10}(OH)_8$	12.97
Topaz-OH	$Al_2SiO_4(OH)_2$	10.01
Diaspore	AlOOH	15.02
Phase δ	AlOOH	15.02
Phase Π	$Al_3Si_2O_7(OH)_3$	9.00
Phase Egg	$AlSiO_3OH$	7.50
Lawsonite	$CaAl_2Si_2O_{10}H_4$	11.47

In basic assemblages, the mineral that can transport significant amounts of water to greatest depths is lawsonite, which breaks down at about 10 GPa (300 km depth; Poli and Schmidt, 2002, Figure 8.2). Small amounts of water may be carried as far as the lower mantle in aluminous phase D (Boffa Ballaran et al., 2010). In contrast, peridotites are capable of carrying significant amounts of water in superhydrous phase B, hydrous phase D and brucite well into the mantle transition zone and into the lower mantle, providing the *P-T* path passes through 5–6 GPa at $\lesssim$580°C (Figures 8.3 and 8.4).

8.5 Discussion

8.5.1 Chemical heterogeneity in dry oceanic lithosphere

Although the layering in the crust and uppermost mantle constitutes the most laterally continuous heterogeneity within the oceanic lithosphere, there are significant deviations from this 1D structure. Exposures of ophiolitic mantle sequences reveal complex distributions of lherzolite, harzburgite and

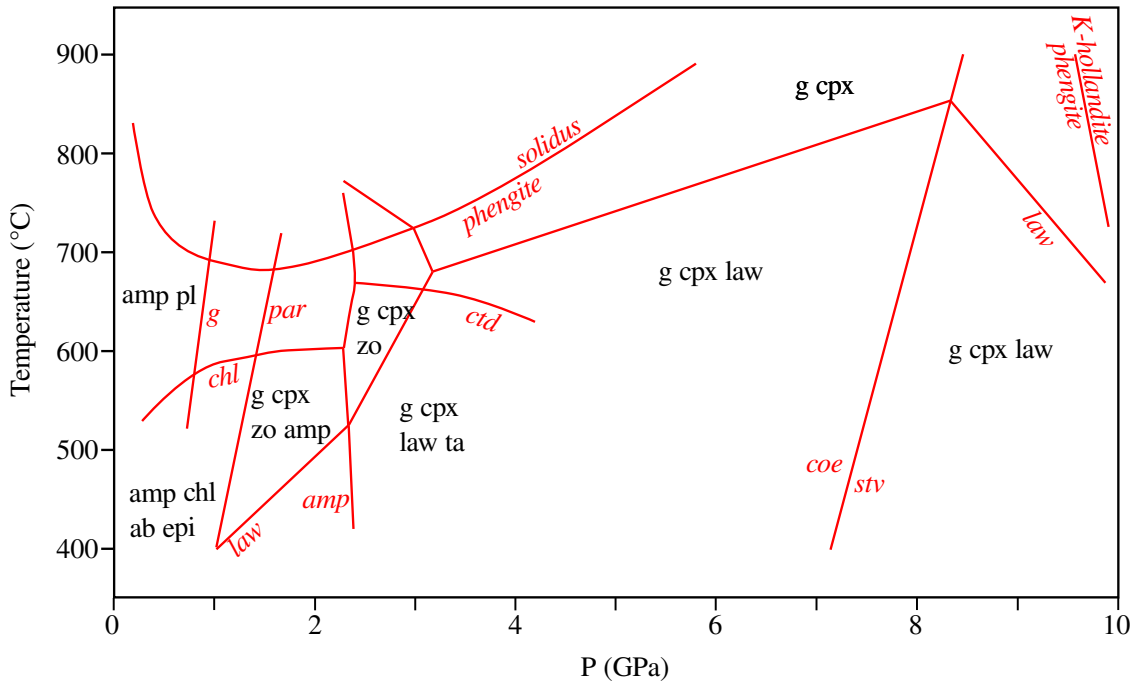

Figure 8.2: Phase diagram of the H_2O-saturated basaltic rocks deduced from the compilation of experimental results. Redrawn from Poli and Schmidt (2002). Lines with italic labels correspond to the edge of the stability field of specific minerals. Other labels show typical assemblages at specific pressures and temperatures.

dunite. Although it is unclear how similar ophiolites are to 'normal' oceanic lithosphere, similar complexity is expected. The convecting mantle from which the oceanic lithosphere is derived is heterogeneous, consisting of large amounts of recycled crust and depleted mantle (Allègre and Turcotte, 1986) in addition to lherzolite. Recycled crustal rocks may have undergone chemical alteration to pyroxenite in the convecting mantle (Sobolev et al., 2007).

8.5.2 *Evidence for and against mantle hydration*

Before subduction

Seismic tomography of the outer rise provides evidence for the existence of fluids and/or hydrous minerals within the uppermost mantle of oceanic plates prior to subduction. Velocities beneath the north Chile outer rise are 7.6 ± 0.2 km/s in the upper 1 km of mantle, much lower than the 8.1 km/s of unaltered mantle peridotite (Ranero and Sallarès, 2004) and consistent with ∼15% serpentinisation (∼2–3 wt% mineral bound water; Carlson and Miller, 2003). A similar reduction in mantle velocity beneath the Middle America outer rise implies at least 2–3 km of the mantle are 10–15% serpentinised (Grevemeyer et al., 2007; Ivandic et al., 2008, 2010; Van Avendonk et al., 2011). Micro-earthquake seismicity about 5 km into the mantle section offshore southern Chile has high-b values, implicating fluids in the seismic activity (Tilmann et al., 2008). The temperatures here are ∼600°C, around the upper limit for serpentinisation. The Pn velocity drops from >8.1 to 7.8 km/s where earthquake activity increases (Contreras-Reyes et al., 2008; Tilmann et al., 2008). Similar behaviour is observed at

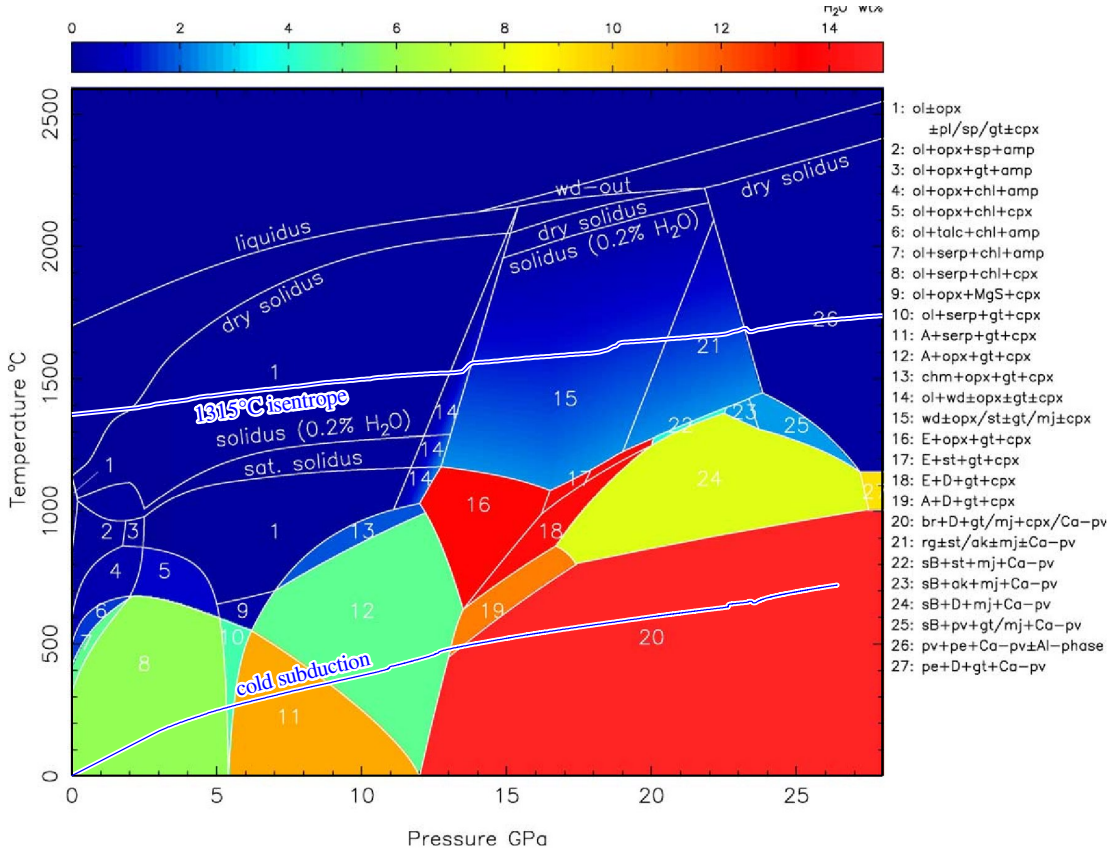

Figure 8.3: Phase diagram of the H_2O-saturated peridotitic rocks deduced from the compilation of experimental results. The maximum H_2O contents bound in the solid phases are calculated from the phase assemblages and the chemical composition of the phases based on mass balance. The phase assemblages of fields '1' to '27' are shown on the right-hand side of the figure. Blue lines correspond to the geotherms for convecting mantle (calculated from the pyrolitic composition in Table 8.1 with T_P=1315°C) and cold subducting slabs (minimum estimated temperature within the north Tonga slab; see Chapter 9). The abbreviations of the phases are as follows: ol=olivine, opx=orthopyroxene, cpx=clinopyroxene, pl=plagioclase, sp=spinel, gt=garnet, amp=amphibole, chl=chlorite, serp=serpentine, MgS=Mg-sursassite, A=phase A, chm=clinohumite, wd=wadsleyite, rg=ringwoodite, st=stishovite, mj=majorite, E=phase E, D=phase D, br=brucite, Ca-pv=Ca-perovskite, ak=akimotoite, sB=superhydrous phase B, pv=perovskite, pe=periclase/magnesiowüstite, Al-phase=Al-rich phase. Taken from Iwamori (2004).

offshore Nicaragua (Lefeldt et al., 2009).

No existing outer rise studies have succeeded in identifying alteration more than a few kilometers into the mantle. The imaging of mantle fault zones 20 km below the surface of the plate (e.g. Ranero et al., 2003) requires an impedance contrast which may be the result of localised hydration (Ranero et al., 2003; Nedimović et al., 2009), but there is no direct evidence for mantle hydration $>\sim$5 km below the Moho.

After subduction

Water contents of blueschist facies metabasic rocks exhumed from subduction zones during continental collision are significantly more hydrated than their ODP borehole counterparts collected far from the oceanic trenches (see Peacock, 2004, and references therein).

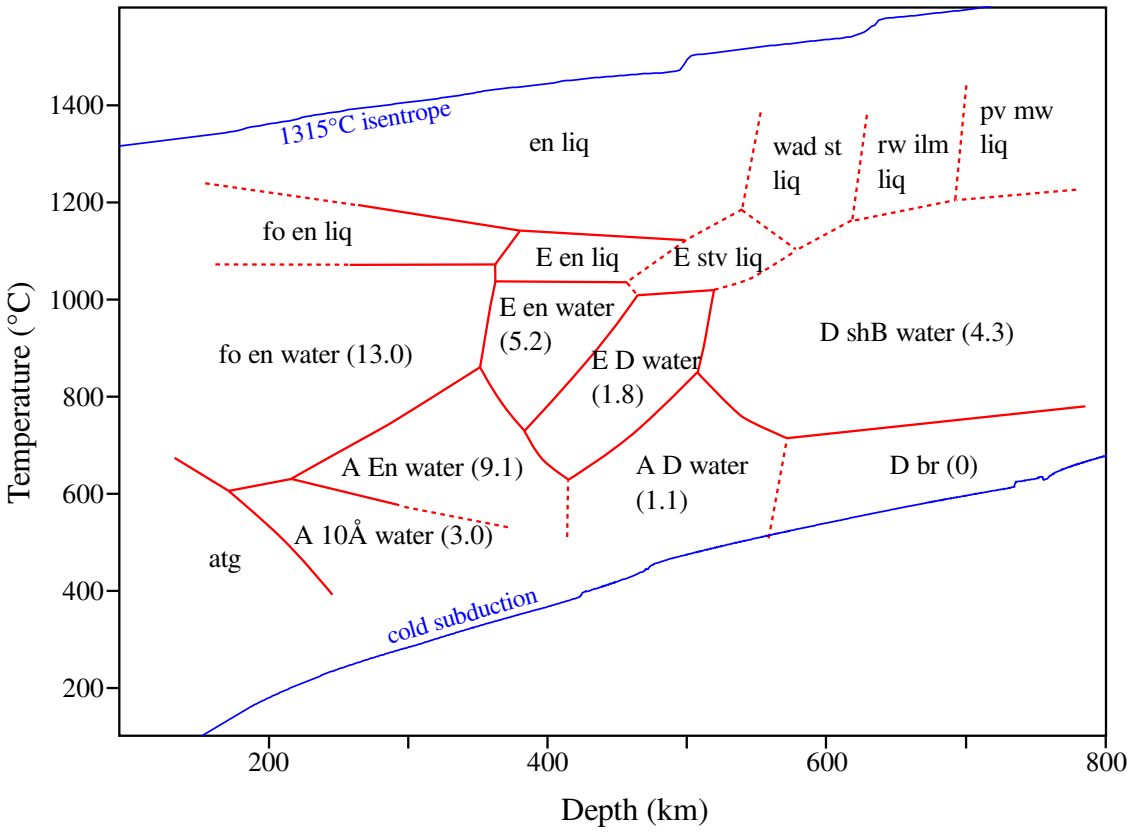

Figure 8.4: Phase diagram of serpentine and associated weight percent of water released from the initial assemblage, derived from experimental results. Redrawn from Irifune et al. (1998). Blue lines correspond to the geotherms for convecting mantle (calculated from the pyrolitic composition in Table 8.1 with T_P=1315°C) and cold subducting slabs (minimum estimated temperature within the north Tonga slab; see Chapter 9).

High resolution tomographic images of subducting slabs are potentially able to reveal deeper hydration of the mantle than outer rise studies, which are typically designed to image only the top 10 km of the oceanic plate. S-wave velocities are significantly reduced around the sites of large intermediate depth earthquakes beneath Japan; specifically the 1993 Kushiro-Oki earthquake (Suzuki and Kasahara, 1996; Nakajima et al., 2009) and a M_W 7.1 aftershock of the 2011 Tohoku earthquake (Nakajima et al., 2011), both of which cut 15–20 km into the slab mantle.

Anomalous phases may also help determine the chemical and mineralogical structure of downgoing lithosphere. Savage (2012) argued that <70 s long high frequency arrivals recorded at Tonga but not Fiji could only be explained by large amounts of water heterogeneously distributed within the Tonga-Kermadec slab down to at least 600 km depth. However, the model presented only considered an isothermal, isochemical slab, isobaric phase changes and water within a layer 8 km thick. Savage did not publish synthetics for alternative explanations, such as structure immediately above the slab surface, complexity in slab shape at ∼20°S, or crustal effects.

Not everyone believes that water is the cause of low velocity anomalies within subducting slabs. Reynard et al. (2010) suggest that anisotropy of deformed anhydrous peridotite explains low-V_P high-V_S anomalies observed along the lower plane of the double seismic zone beneath Japan (Nakajima

et al., 2009, Figure 8.5) better than the presence of hydrous minerals.

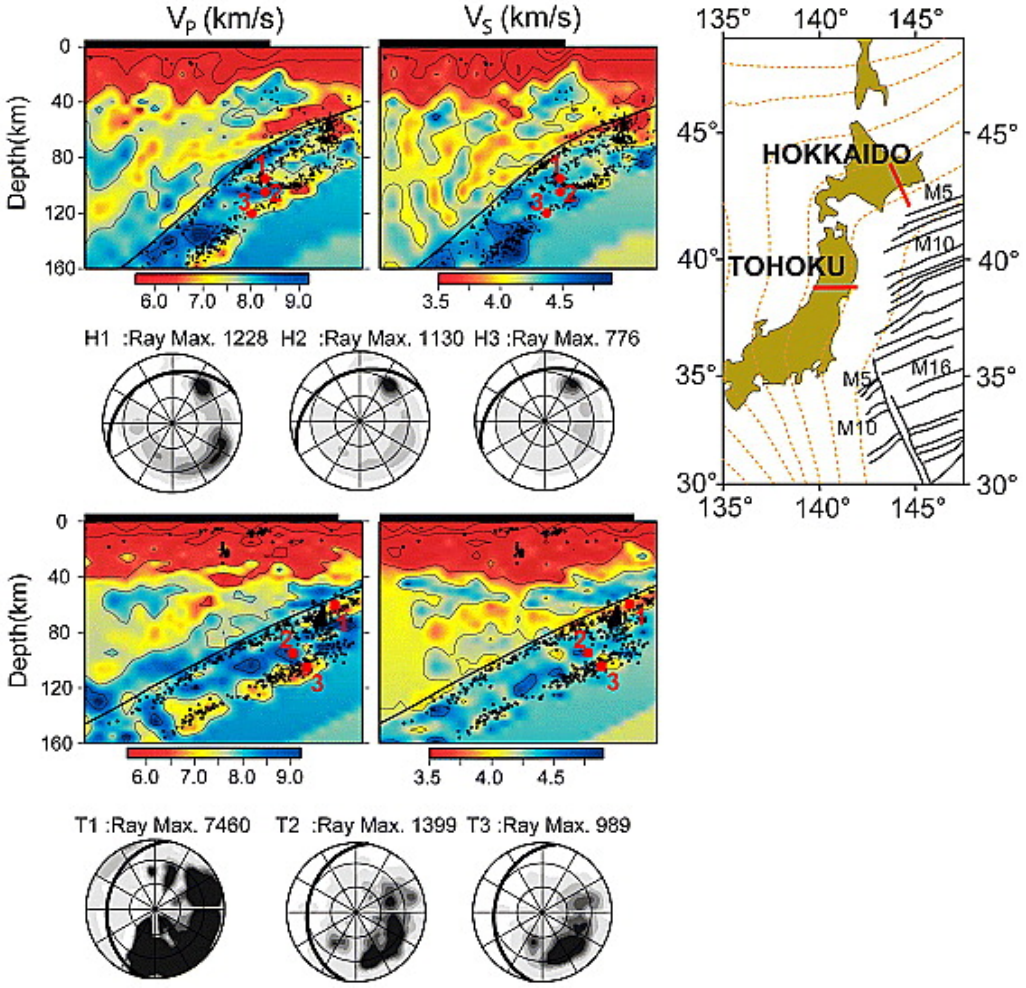

Figure 8.5: Tomographic cross sections of the Pacific subduction under northeast Japan, taken from the study of Reynard et al. (2010). Low-velocity patches with higher velocity contrast for V_P than for V_S occur along the lower seismicity plane (hypocenters: black dots), about 20–30 km beneath the slab surface (black line) both in (top) Hokkaido and (bottom) Tohoku. Orientations of the seismic rays used in tomographic reconstruction (shown as lower hemisphere stereographic projections) are distributed for areas well above the lower seismicity plane (point T1) whereas they cluster around specific directions when approaching it (points T2, T3, H2, and H3). The horizontal high-seismicity plane with low-V_P anomaly (point H1) is associated with the source and aftershock propagation zone of the 1993 Kushiro-oki earthquake.

There are two potential problems with the inference of Reynard et al. (2010). The first problem is with the tomographic technique. Much of the low V_P streak lies beneath the deepest earthquakes used in the inversion, and is therefore an artefact of smoothing. The very thin remaining low velocity zone is almost devoid of crossing ray paths, and may therefore reflect small errors in earthquake location rather than local velocity. The earthquakes used are relocated during the double-difference tomographic inversion (Zhang and Thurber, 2006), but the lack of crossing ray paths results in a trade off between near-source velocity and location.

Assuming that there is a low V_P zone coincident with the lower plane of the double seismic zone, a second problem presents itself. High V_S is not necessarily an indicator of anhydrous lithologies. Even hydrous minerals such as antigorite have high P and S wave velocities in some orientations,

and studies of hydrated mantle rocks in the field reveal a well developed foliation in antigorite (e.g. Padrón-Navarta et al., 2010) that could lead to misinterpretations of tomographic images. Seismic velocities for the antigorite elastic stiffness tensor (Bezacier et al., 2010) are calculated using MTEX (Bachmann et al., 2010) and plotted in Figure 8.6. For antigorite foliated along active near-horizontal fault planes (see Chapter 7) dipping at an angle of 15° to the southeast, the seismic waves used by Reynard et al. (2010) would mostly sample paths making a 60–90 degree angle with the c^* axis. These paths would have relatively high V_S values. Even pure antigorite could produce the range of P and S-wave velocities observed in Figure 8.5 (orientations bounded by the two thick black lines in Figure 8.6c).

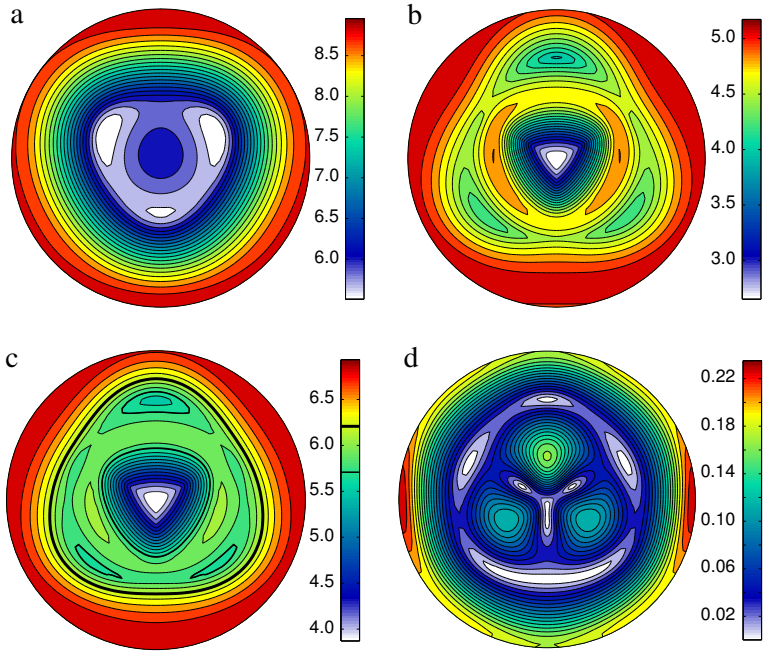

Figure 8.6: Seismic velocities for foliated antigorite with a density of 2.6g/cc, using the elastic stiffness tensor of Bezacier et al. (2010). The c^* axis is oriented perpendicular to the plane of the page. a) V_P, b) V_{S1}, c) $V_P/5 + V_{S1}$, all in (in kms^{-1}). d) $(V_{S1} - V_{S2})/(V_{S1}V_{S2})$, corresponding to the shear wave splitting delay in skm^{-1}.

More work is required to improve tomographic images and better constrain seismic anisotropy before a convincing argument can be made for or against deep hydration of subducting slabs.

8.5.3 *The relationships between mineralogy and seismicity*

Mineralogy and metamorphism may play a significant role in slab seismicity:

- Temperature within subducting slabs is controlled by material properties (see Chapter 9). As temperature appears to be the primary factor controlling whether deformation occurs by ductile or brittle processes, mineralogy may determine the areas of subducting slabs that can be seismically active.

- Thermal conductivity may also have a more direct effect on seismicity. If shear heating is an

important aspect in triggering deep earthquakes, increased conductivity may inhibit rupture nucleation (Hobbs and Ord, 1988).

- Shear modulus is also controlled by mineralogy, and increases with increasing pressure and decreasing temperature. A higher shear moduli results in a higher seismic moment for an earthquake with a given areal extent and slip distribution (see Chapter 10).

- The presence of hydrous minerals may affect seismicity within subduction zones, both because they tend to be weaker than anhydrous phases, and may therefore promote stable sliding rather than brittle faulting (e.g. Chernak and Hirth, 2010, 2011), but also because any fluids released during dehydration reactions will be at lithostatic pressure and may therefore promote brittle faulting (Hubbert and Rubey, 1959).

- The olivine $\rightarrow$ wadsleyite (and olivine $\rightarrow$ ringwoodite) reactions have been implicated in causing earthquakes by transformational faulting (e.g. Green and Burnley, 1989). Whether this is the case or not, the strength of olivine will encourage reaction to the denser polymorphs along planar surfaces, to more easily accommodate the volume change.

- The polymineralllic nature of subducting slabs may affect rupture nucleation and propagation.

8.6 Summary

The general pseudostratigraphy of oceanic lithosphere is well known. The 7 km thick crust can be approximated as basaltic, with lavas and sheeted dykes overlying mafic and ultramafic cumulates. This crust is underlain by peridotite, which is most depleted close to the surface. This simple structure is complicated by variations in thickness of the layers, and also by small scale heterogeneities throughout the lithosphere. These are unlikely to significantly affect the thermal structure of subducting slabs, but they could have significant effects on the distribution of stress and strain.

Before oceanic plates approach the trench, they are mostly dry. Hydration of the plate close to the trench is not well documented, but seismic evidence suggests that pervasive hydration is probably restricted to the upper few kilometers of the mantle. Localised and potentially high-percentage hydration may extend to $>$20 km depth along fracture zones or large normal faults formed at the outer rise. This hydration could have profound effects on deformation of the slab, because hydrous minerals tend to be much weaker than anhydrous minerals and fluid release promotes brittle failure. Conversely, the localised hydrated mantle will make up a relatively low fraction of the total plate volume, such that the unique physical properties of hydrous minerals will have a negligible effect on the large-scale thermal structure of subducting slabs.

9 *Pressure and temperature*

9.1 Introduction

Temperature is plays a dominant role in determining whether the lithosphere deforms in a brittle or ductile manner. Estimates of geotherms using constant conductivity analytic plate cooling models suggest that shallow earthquakes in the oceanic mantle are restricted to ambient temperatures $<$750°C (Chen and Molnar, 1983; Wiens and Stein, 1983). Repeating this analysis with temperature dependant conductivity, expansivity and heat capacity reduces this estimate to $<$600°C (McKenzie et al., 2005). The 600°C seismicity cutoff appears to be relevant throughout the oceanic plate: near the ridges, far from plate margins (McKenzie et al., 2005), and close to the trenches (Tilmann et al., 2008).

The temperature control on seismicity is a consequence of rock rheology, and specifically the interplay between rates of stress buildup and viscous relaxation. The observation that brittle deformation in volcanic regions occurs at higher temperatures than in non volcanic regions is an indicator of higher transient stresses induced by melt movement (e.g. Soosalu et al., 2009).

Since deep earthquakes appear to be constrained to regions where lithosphere has recently been subducted, temperature is probably a key factor in controlling seismicity at all depths. In this chapter, I investigate thermal evolution within subducting slabs, and discuss the potential effects of metamorphism on slab seismicity and geodynamics.

9.2 Motivation

There have been many attempts to determine the thermal conditions in subduction zones, and to estimate the temperature at which seismicity ceases. Several observational studies relate seismicity to the thermal parameter ϕ, defined as the product of the age of the lithosphere at the time of subduction t_{age} and the vertical component of the subduction velocity $v_{\perp}$. The value of the thermal parameter at the depth of maximum seismicity d_{max} varies for different subduction zones. Above around 150 km depth, $\phi \sim 4.5\, d_{\text{max}}$ (Kirby et al., 1991; Kirby et al., 1996; Gorbatov and Kostoglodov, 1997). Between 150 and 300 km depth there is a marked deviation from this linear relationship towards higher values of ϕ. Deep-focus earthquakes (with hypocentral depths in excess of 300 km)

appear to be restricted to regions where ϕ exceeds 3500–5000 km (Gorbatov and Kostoglodov, 1997).

In order to directly relate earthquakes to temperature, explicit thermal modelling is required. McKenzie (1969a) used an analytic model to estimate the minimum potential temperature T_P (the temperature the rock would acquire if decompressed to 0 GPa along an adiabat) within a subducting slab at a given depth. He concluded that earthquakes are not present within material where T_P exceeds ~680°C (McKenzie, 1970). Soon afterwards, the data of Schatz and Simmons (1972) was used to study the effects of temperature-dependent thermal conductivity on slabs, also including the effects of the latent heat of reaction of olivine → wadsleyite → ringwoodite → spinel plus magnesiowüstite (Minear and Toksöz, 1970; Toksöz et al., 1971; Toksöz et al., 1973). Wortel (1982) followed the same approach as McKenzie (1969a), but incorporated both temperature dependent conductivity and a constant 135 K jump in temperature at the olivine → wadsleyite phase transition.

The effect of dehydration reactions in the crustal section has also been extensively studied (Anderson et al., 1976, 1978, 1980; Oxburgh and Turcotte, 1976; DeVore, 1983; Peacock, 1990). These reactions are mostly endothermic, decelerating the rate of slab heating during the first few hundred kilometers of subduction. The total effect of these reactions on *P-T* paths is probably only a few kelvin (Peacock, 1990). Hydrothermal circulation within the slab crust may further lower slab temperatures (Kummer and Spinelli, 2008), but would need to be unexpectedly vigorous to have a significant cooling effect (Peacock, 1990). Recent estimates of the locations of dehydration reactions in subducting slabs at intermediate depths have been made without including the effects of these reactions (van Keken et al., 2002; Syracuse et al., 2010).

Thermal models of subduction zones like the ones described above are commonly constructed using constant or simply varying physical parameters, from which stable mineral assemblages are then determined using isochemical *P-T* phase diagrams (e.g. Iwamori, 1998; Peacock, 1993; Peacock and Wang, 1999). Similar models have been used to assess the locations of metastable reaction boundaries (Stein and Stein, 1996; Kirby et al., 1996). This approach ignores the effect of pressure, temperature and composition on the material properties relevant to thermal conduction. Pyrolite increases in density from around 3300 $\mathrm{kgm^{-3}}$ to 4500 $\mathrm{kgm^{-3}}$ at room temperature between 0 and 30 GPa, with smaller decreases with increasing temperature. Heat capacity varies mostly with temperature, increasing from 900–1000 $\mathrm{Jkg^{-1}K^{-1}}$ at room temperature to almost 1300 $\mathrm{Jkg^{-1}K^{-1}}$ at 2300 K. A factor of two decrease in conductivity with increasing temperature (between 300 K and 1500 K) in olivine (Fujisawa et al., 1968; Kanamori et al., 1968; Schatz and Simmons, 1972) and pyroxene (Kobayashi, 1974) is responsible for an oceanic mid-lithosphere 100 K cooler than predicted from constant conductivity models (Denlinger, 1992; McKenzie et al., 2005).

A few studies have sought to improve the accuracy of thermal models of subduction zones by making full use of available mineral physics data. These studies have mostly focused on the potential presence of metastable olivine within subducting slabs, by incorporating equations approximating

the sluggish kinetics of the olivine → wadsleyite and olivine → ringwoodite phase transformations at low temperatures (e.g. Däßler and Yuen, 1996; Mosenfelder et al., 2001). Marton et al. (2005) extended this work further, by including a pressure and temperature dependence on the conductivity of olivine, wadsleyite and ringwoodite. In their model, slab conductivity doubles between 400 and 650 km depth as a result of phase changes and the increase in pressure.

The recent incorporation of deep Earth mineral physics data into thermodynamic datasets (e.g. Stixrude and Lithgow-Bertelloni, 2011) for use in Gibbs' Free Energy minimisation programs such as THERMOCALC (Holland and Powell, 1998, 2011) or Perple_X (Connolly, 2005, 2009), has greatly simplified the procedures required to conduct thermal modelling in realistic chemical systems in a fully self-consistent manner. In deriving material properties using Gibbs' Free Energy minimisation, the variables used in thermal modelling can be refined such that quoted uncertainties reflect real world processes (such as the approach to equilibrium) rather than derived parameters.

9.3 *Modelling the thermal structure of subducting slabs*

9.3.1 *The heat equation*

The flow of heat energy through a surface is proportional to the temperature gradient normal to that surface, where the constant of proportionality k is defined as the thermal conductivity ($\mathbf{q} = -k\nabla T$). The heat Q added to a system of unit volume is proportional to the change in temperature

$$\delta Q = \rho C \delta T \tag{9.1}$$

where C is the specific heat capacity (the amount of energy in joules required to increase 1 kg of material by 1 K) and ρ is the density. If there are no sources or sinks of heat, conservation of energy requires that

$$\rho C \frac{\partial T}{\partial t} = \nabla \left(k \nabla T \right) \tag{9.2}$$

In natural materials, k, ρ and C vary with temperature and pressure. C is also path-dependent.

9.3.2 *Extending the heat equation*

In geological situations there are several potential sources and sinks of heat into a mass of rock. The variation in temperature with time is dependent on changes in pressure, advection (solid and fluid), diffusion, radiogenic heating A, shear heating H_{shear} and l discontinuous chemical reactions proceeding at a rate R_l^* with reaction enthalpy H_l. The Eulerian formulation of this problem (the

formulation in the reference frame of the trench) is:

$$\rho(P,T)C(P,T)\left(\frac{\partial T}{\partial t}+\left(u+\bar{v}_z\phi\Gamma\right)\nabla T\right) = \nabla\left(k(P,T)\nabla T\right)+A+H_{\text{shear}}-\sum_l \Delta H_l R_l^* \tag{9.3}$$

Within oceanic lithosphere, radiogenic heating is low and can be neglected. Redistribution of heat by fluid advection and heating by shear are also likely to be small. In this situation, and where there is no internal deformation, it is easier to reformulate the problem in the reference frame of the slab (a Lagrangian formulation). If metamorphic equilibrium is maintained, and that there are no discontinuous reactions, 9.3 again simplifies to Equation 9.2.

9.3.3 *Incorporating thermodynamic data*

The numerical scheme to solve Equation 9.2 must be chosen with care. Expressions involving the heat capacity C result in numerical instabilities along near-isentropic paths, where no heat is required to induce a change in temperature. Replacing $C\Delta T$ with $C_{\text{P,eff}}(\Delta T-\Delta T_S)$ avoids this problem by splitting the temperature increase due to diffusion (ΔT) from that due to reaction and increases in pressure (ΔT_S). The heat equation then becomes (Schubert et al., 2001)

$$\rho(P,T)C_{\text{P,eff}}(P,T)\left(\frac{\partial T}{\partial t}-\left(\frac{\partial T}{\partial P}\right)_S\frac{\partial P}{\partial t}\right)=\nabla\left(k(P,T)\nabla T\right) \tag{9.4}$$

This technique is suitable for advective-diffusive processes, but only captures the effect of reactions when pressure is not fixed. This is an improvement on models such as that of Marton et al. (2005)[1], but is unsuitable for convection simulations where heat exchange during horizontal flow is important.

9.3.4 *Assemblage properties*

To obtain the mineral parameters required for thermal modelling, the mafic and ultramafic bulk compositions given in Table 8.1 are input into the Gibb's Free Energy minimisation program Perple_X. The minimum energy assemblages are then interrogated to create P-T grids of density $\rho(P,T)$ and heat capacity at constant pressure $C_P(P,T)$ (Figures 9.1 and 9.2). ρ and $C_{\text{P,eff}}$ are calculated as the spatial average of their start and end point values.

Entropy ($S=-(dG/dT)_P$) is also required by Equation 9.4, to model the isentropic increase in temperature along the subduction path (Figure 9.3). During each time step, S is evaluated at (T_i,P_i), (T_f,P_i) and (T_f,P_f). $(\partial T/\partial P)_S$ is then calculated along piecewise linear P-T paths using a three point

[1]Marton et al. (2005) applied a constant gradient mantle geotherm with a gradient of 0.27 K/km, but apparently neglected the entropic term from their simulation.

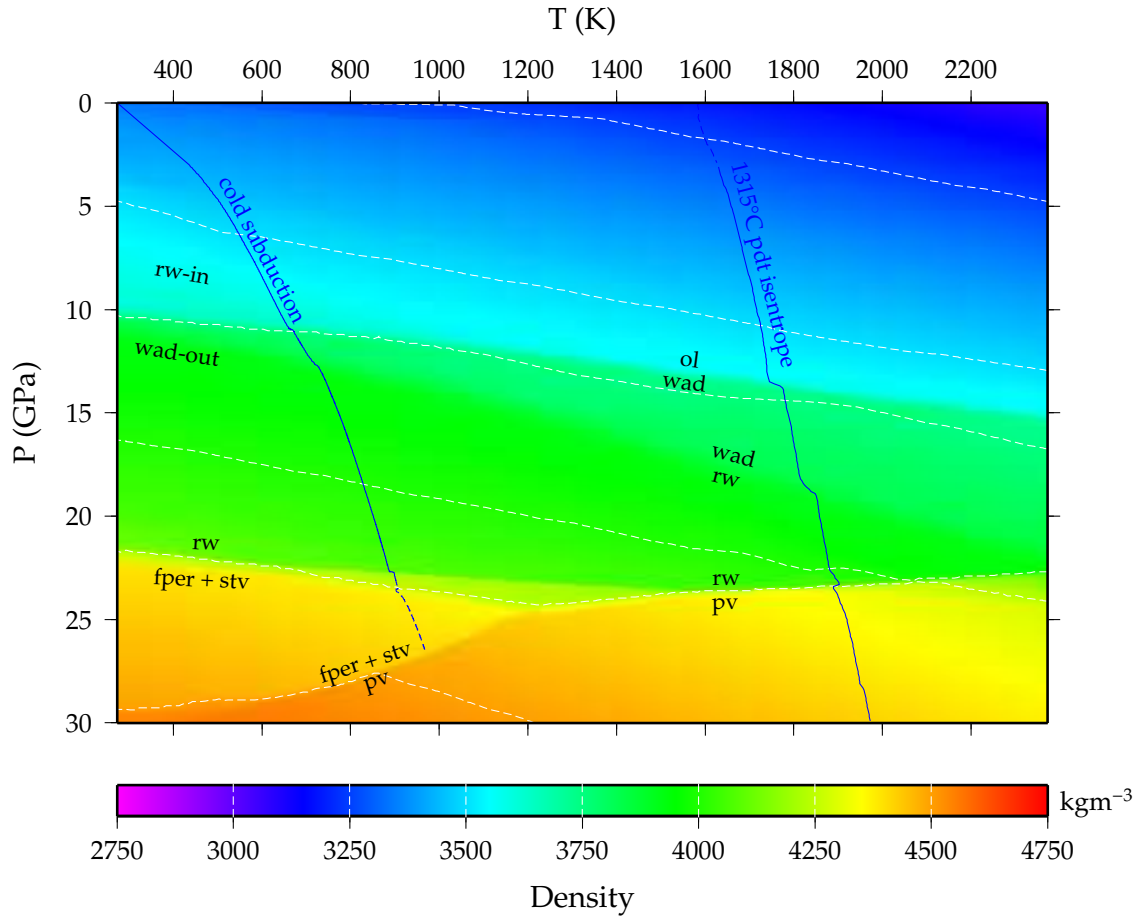

Figure 9.1: Density of the input harzburgite assemblage (Table 8.1; Figure 8.1) as a function of pressure and temperature. Blue lines correspond to the geotherms for convecting mantle (calculated from the pyrolitic composition in Table 8.1 with T_P=1315°C) and cold subducting slabs (minimum estimated temperature within the north Tonga slab). Annotations mark metamorphic reactions which have a major effect on slab density.

gradient method via the relation

$$\left(\frac{\partial P}{\partial S}\right)_T \left(\frac{\partial S}{\partial T}\right)_P \left(\frac{\partial T}{\partial P}\right)_S = -1 \tag{9.5}$$

The last parameter required by Equation 9.4 is thermal conductivity. From theoretical considerations, Hofmeister (1999) proposed a model for thermal conductivity which fits available laboratory data. She obtained pressure and absolute temperature dependences of transport properties from the Grüneisen parameter γ, bulk modulus K_T, and thermal expansivity α. Hofmeister expressed the lattice and radiative contributions as

$$\kappa_{\text{lat}} = \kappa_{\text{std}}(298/T)^a \cdot \exp\left[-(4\gamma + 1/3)\int_{298}^{T} \alpha(\theta)d\theta\right] \cdot (1 + K_0' P/K_0) \tag{9.6}$$

$$\kappa_{\text{rad}} = 1.75 \cdot 10^{-2} - 1.037 \cdot 10^{-4} T + 2.245 \cdot 10^{-7} T^2 - 3.407 \cdot 10^{11} T^3 \tag{9.7}$$

Values used to calculate conductivities are provided in Table 9.1.

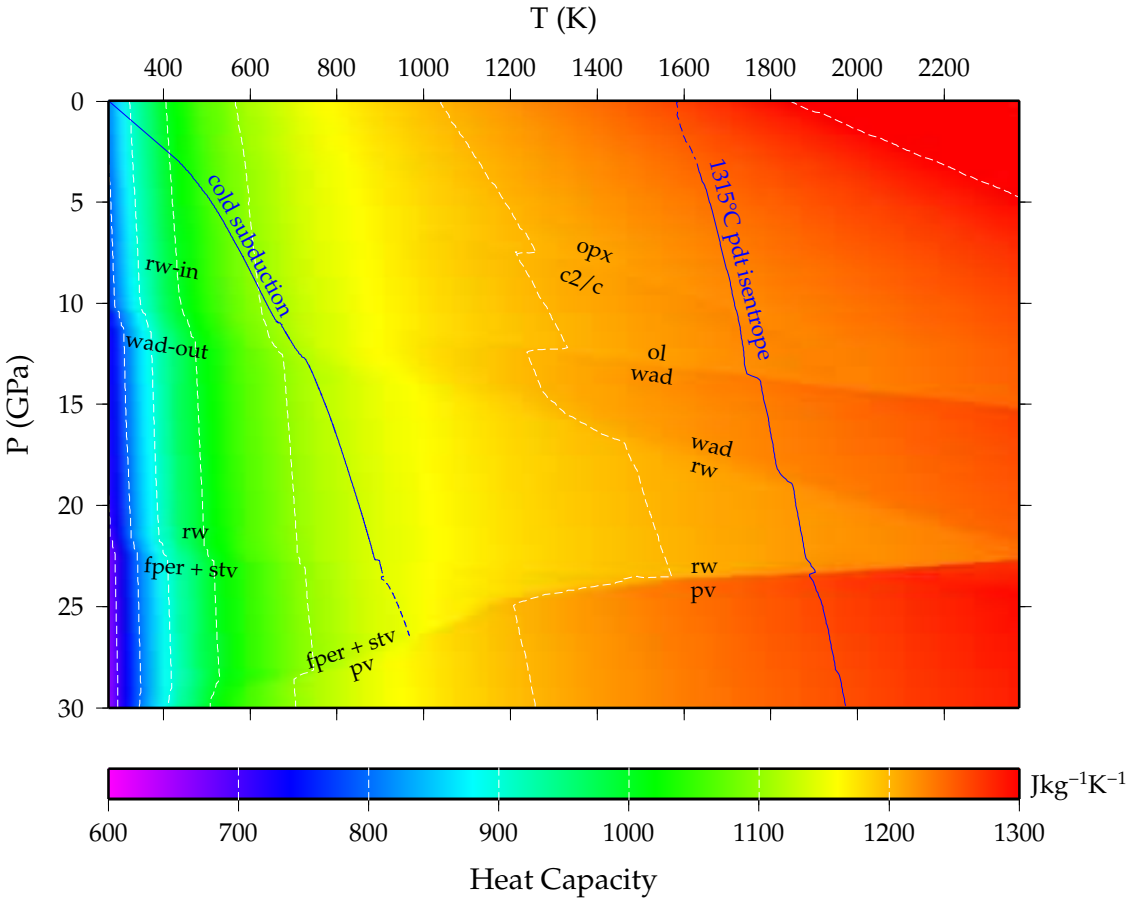

Figure 9.2: Heat capacity of the input harzburgite assemblage (Table 8.1; Figure 8.1) as a function of pressure and temperature. Blue lines correspond to the geotherms for convecting mantle (calculated from the pyrolitic composition in Table 8.1 with T_P=1315°C) and cold subducting slabs (minimum estimated temperature within the north Tonga slab). Annotations mark metamorphic reactions which have a major effect on heat capacity.

The polynomial describing the radiative contribution to thermal conductivity is a poor approximation to the analytical solution at high temperatures (H. Keppler, personal communication). At the low temperatures and iron contents corresponding to subduction zone conditions, the radiative contribution to total conductivity is small. The polynomial approximation is significantly more straightforward to implement than the analytical solution (e.g. Keppler et al., 2008) with existing data.

There is no unique solution for the effective thermal conductivity of multiphase substances based solely on the volume percentage and thermal conductivity of the constituent phases (Fuller Brown, 1955; Hashin and Shtrikman, 1962). Three averaging formulae have commonly been used: $f(\kappa) = \sum p_i f(\kappa_i)$, where $f(\kappa) = \kappa$, $1/\kappa$ or $\ln(\kappa)$. The arithmetic ($f(\kappa) = \kappa$, used by Hofmeister (1999)) and harmonic ($f(\kappa) = 1/\kappa$) means represent maximum and minimum estimates of conductivity, and correspond to uniform temperature gradient and heat flow. They apply only where the bulk rock is constructed from a set of parallel monomineralic plates parallel and perpendicular to the direction of heat flow. It is unknown to what extent shear causes alignment of minerals within cold subducting slabs, but a well-developed gneissic fabric is unlikely to be the dominant fabric.

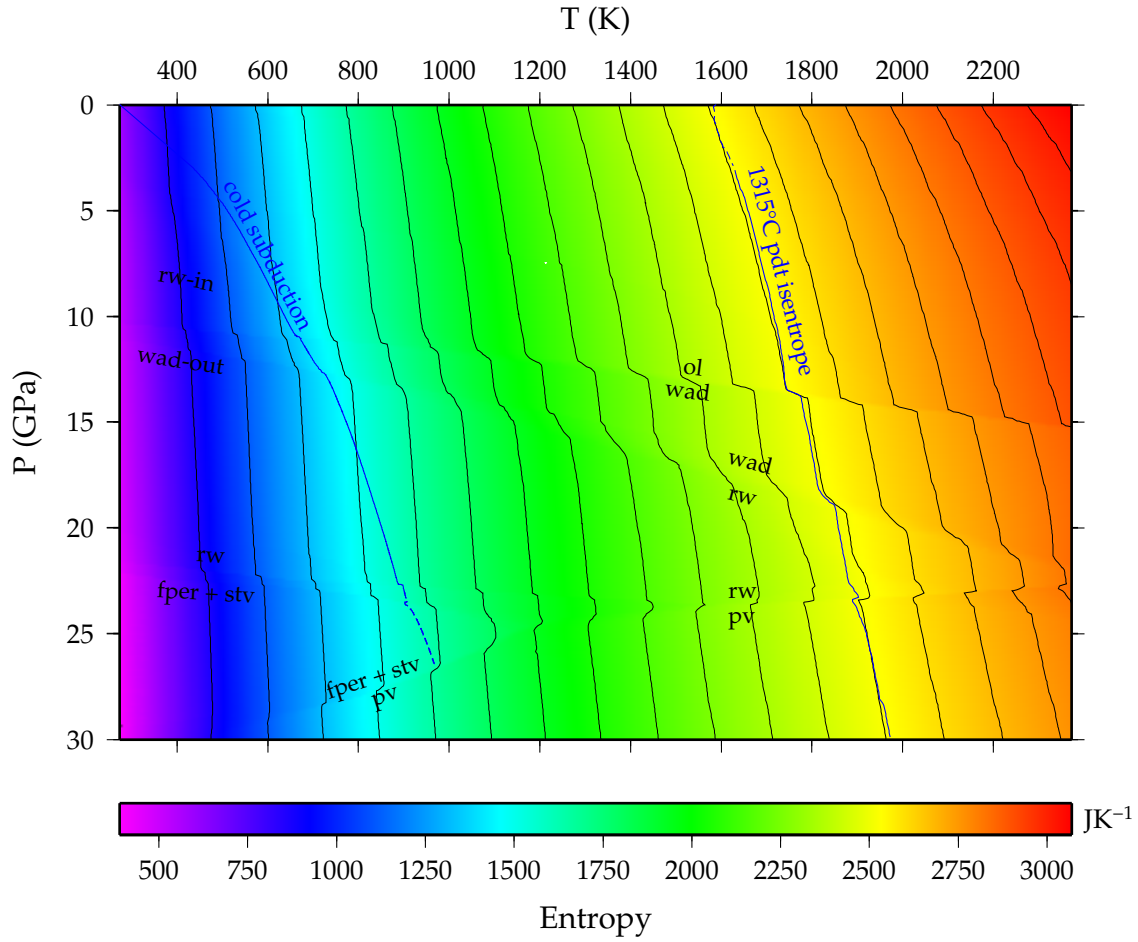

Figure 9.3: Entropy of the input harzburgite assemblage (Table 8.1; Figure 8.1) as a function of pressure and temperature. Isentropes are drawn at T_P intervals of 100 K. Blue lines correspond to the geotherms for convecting mantle (calculated from the pyrolitic composition in Table 8.1 with T_P=1315°C) and cold subducting slabs (minimum estimated temperature within the north Tonga slab). Annotations mark metamorphic reactions which have a major effect on entropy.

The conductivity of isotropic aggregates can be approximated by the addition of non-geometric terms to each of the potential averaging formulae (Fuller Brown, 1955), but the resulting equations rapidly become cumbersome. The third averaging formula ($f(\kappa) = \ln(\kappa)$) has been proposed as a good approximation to conductivity in isotropic media on semi-theoretical and empirical grounds (see references in Fuller Brown, 1955), and is the one adopted here.

Pyrolitic thermal conductivities calculated via Equation 9.7 are a complex function of pressure and temperature (Figure 9.4). The physical parameters (Table 9.1) of the various minerals in the equilibrium assemblages of the bulk composition in Table 8.1 produce gradients in conductivity greater than those expected for a single assemblage. The high conductivity wedge between 21 and 31 GPa below 1300 K in Figure 9.4 is a result of a large modal percentage of high conductivity MgO stable under these conditions. This assemblage is Mg-perovskite free, consisting of ferropericlase (magnesiowüstite; (Mg,Fe)O) and stishovite with minor akimotoite and Ca-perovskite.

The formulation of Hofmeister (1999) can be compared with data and other published expressions

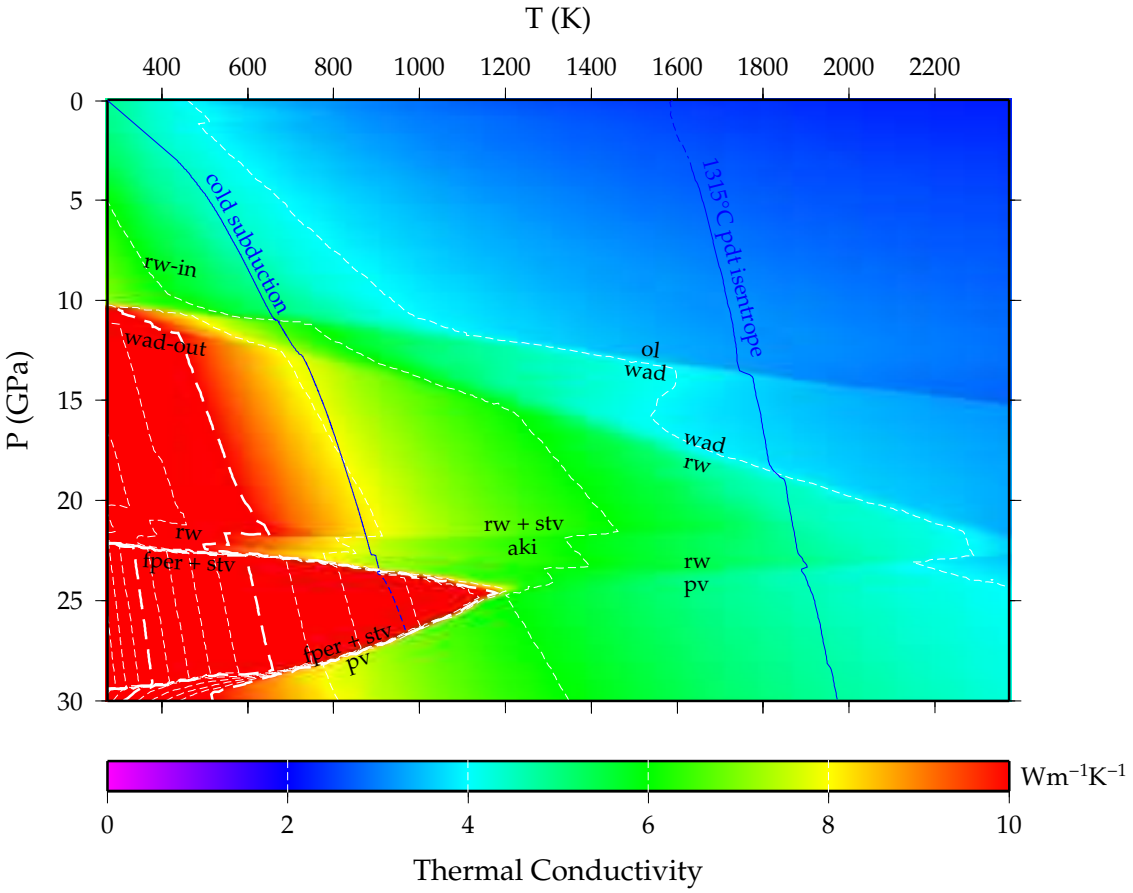

Figure 9.4: Conductivity of the input harzburgite assemblage (Table 8.1; Figure 8.1) as a function of pressure and temperature. Blue lines correspond to the geotherms for convecting mantle (calculated from the pyrolitic composition in Table 8.1 with T_P=1315°C) and cold subducting slabs (minimum estimated temperature within the north Tonga slab). Annotations mark metamorphic reactions which have a major effect on conductivity.

for conductivity in ultramafic compositions (Figure 9.5). The conductivities for wadsleyite and ringwoodite in the mantle transition zone are somewhat higher than those used by Marton et al. (2005), a discrepancy which arises mainly because Marton et al. (2005) assume that $K_0' \sim 4$; the values used here are 4.8 and 5.2 for wadsleyite and ringwoodite respectively (Knittle, 1995).

Only end-member compositions have been used to determine bulk conductivities. The uncertainties in both the thermodynamic and physical property datasets and errors resulting from the use of an approximate expression for conductivity are probably larger than those associated with not accounting for solid solutions in the thermodynamic database.

9.4 *Model setup*

9.4.1 *Initial thermal structure*

The initial thermal structure at the mid ocean ridge was calculated using expressions for isentropic upwelling and melting from McKenzie and Bickle (1988). The thermal evolution of the lithosphere prior to subduction was calculated as suggested by McKenzie et al. (2005) and Emmerson and McKen-

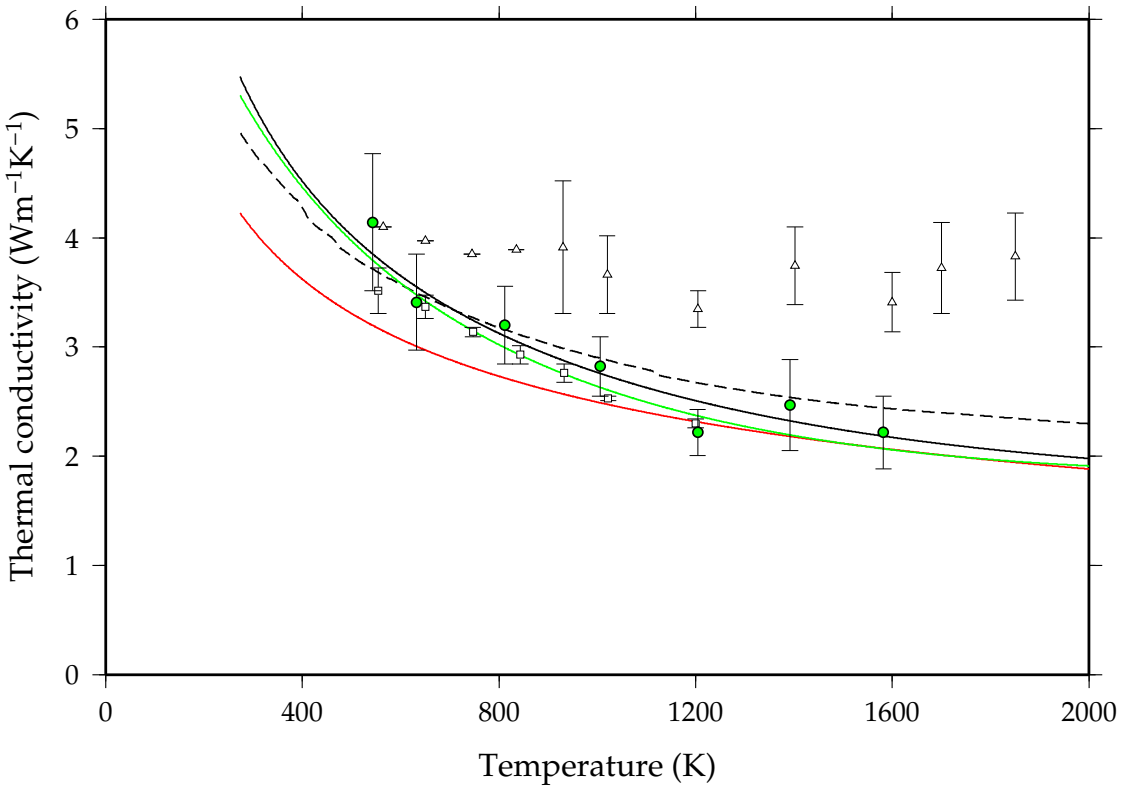

Figure 9.5: Estimates of the conductivity of olivines and peridotites at ambient pressure. The formulation of Hofmeister (1999) with forsterite is given by the solid black line, and the conductivity of the harzburgite assemblage (Table 8.1) output from Perple_X (using Fo90Fa10 and other mineral approximations in Table 9.1) is given by the dashed black line. The empirical equation of Xu et al. (2004) is shown by the red line, and Equation 4 of McKenzie et al. (2005) by the solid green line. Data points and their uncertainties are from Schatz and Simmons (1972): white triangles are measurements of conductivity from a single crystal of Fo86, white squares from the Twin Sisters Dunite (Fo94) and green circles from sintered Fo100. The latter dataset was used by McKenzie et al. (2005) to find the fitting parameters of their equation.

zie (2007), using temperature dependent conductivity, thermal expansivity, density and heat capacity assuming a slab composed of olivine. This monomineralic scheme is an adequate approximation to the real properties of the lithosphere at low pressure, especially given the considerable uncertainties in the data of Schatz and Simmons (1972). It is unlikely that the small percentage of kyanite (with its high conductivity) in the mineralogical model predicted using Perple_X will grow at the low temperatures of the uppermost mantle, providing a secondary reason to use a simplified scheme for the pre-subduction step.

9.4.2 *Model geometry and subduction parameters*

I use the same model geometry as that suggested by (Emmerson and McKenzie, 2007, Figure 9.6). The thermal evolution of subducting slabs is modelled in one dimension. Required variables are the dip of the subducting slab, the subduction velocity and the age of the subducted material when it was at the trench a_{sub}.

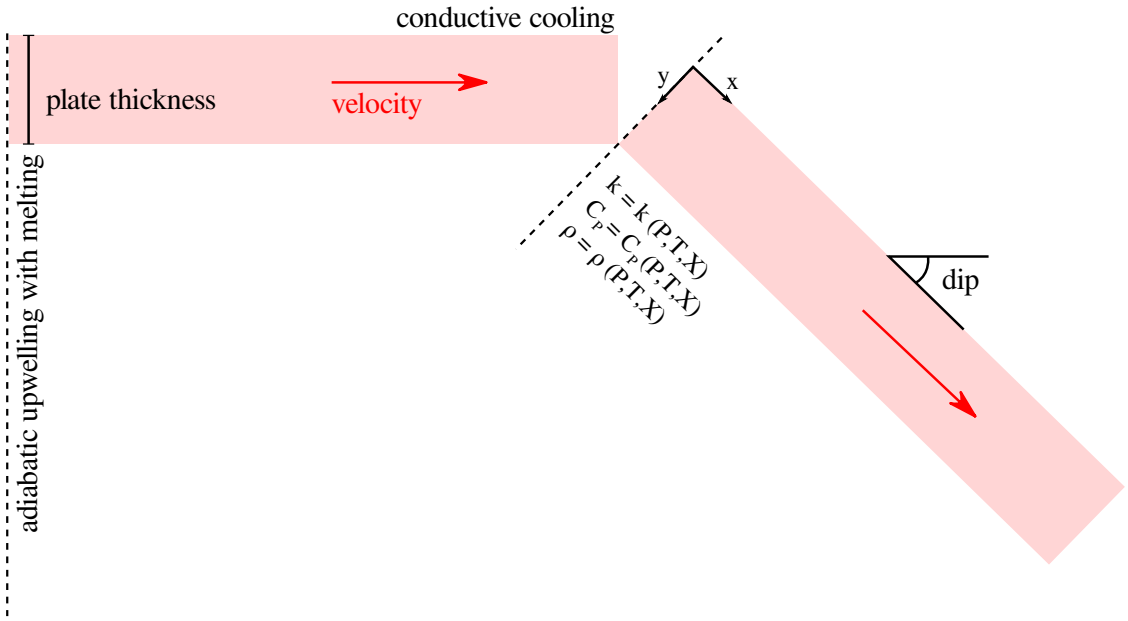

Figure 9.6: Model geometry as used by Emmerson and McKenzie (2007).

Dip

We follow Emmerson and McKenzie (2007) in estimating the average dip δ of the subducting slab by taking profiles through intermediate and deep focus seismicity from the catalogue of Engdahl et al. (1998). Arc-perpendicular profiles were constructed using the technique of England et al. (2004). Profiles were constructed every 50 km along the small circle best-fitting the volcanic arc. The dips of the Wadati-Benioff zones along chosen profiles were measured by fitting a linear trend to events deeper than 80 km by eye.

Average plate velocity

The average subduction velocity was obtained from the continuously closing plates model (Gurnis et al., 2010), by finding the time since the plate was subducted and the arc-perpendicular distance between the trench and the depth of interest. I estimate the length of lithosphere (l) subducted along selected arc perpendicular profiles ($l = z/cos(\delta)$) at intervals of 1 Ma, interpolating between these points using Akima Splines to find t_{sub} and the average velocity of the slab ($v = lt_{\text{sub}}$).

Plate age at the time of subduction

The age a_{sub} of the slab currently at a depth z when it was at the trench t_{sub} is estimated from the global plate-age dataset of Müller et al. (2008), by finding the age a_l and time before present t_l when it was at least 500 km from the trench. Since the time at subduction t_{sub} is already known, a_{sub} can be calculated ($a_{\text{sub}} = a_l + (t_l - t_{\text{sub}})$). This procedure is satisfactory for all but the youngest plates, where the picked age may be associated with the plate on the opposite side of the ridge.

This technique utilises much more data than that used by Emmerson and McKenzie (2007), and significantly reduces the uncertainties associated with a_{sub}, especially for profiles along the Japan Trench where plate ages decrease rapidly approaching the trench, but are thought to be relatively constant within the subducted slab. The results of the plate age and plate velocity calculations for a profile across the southern Bonin arc are shown in Figure 9.7.

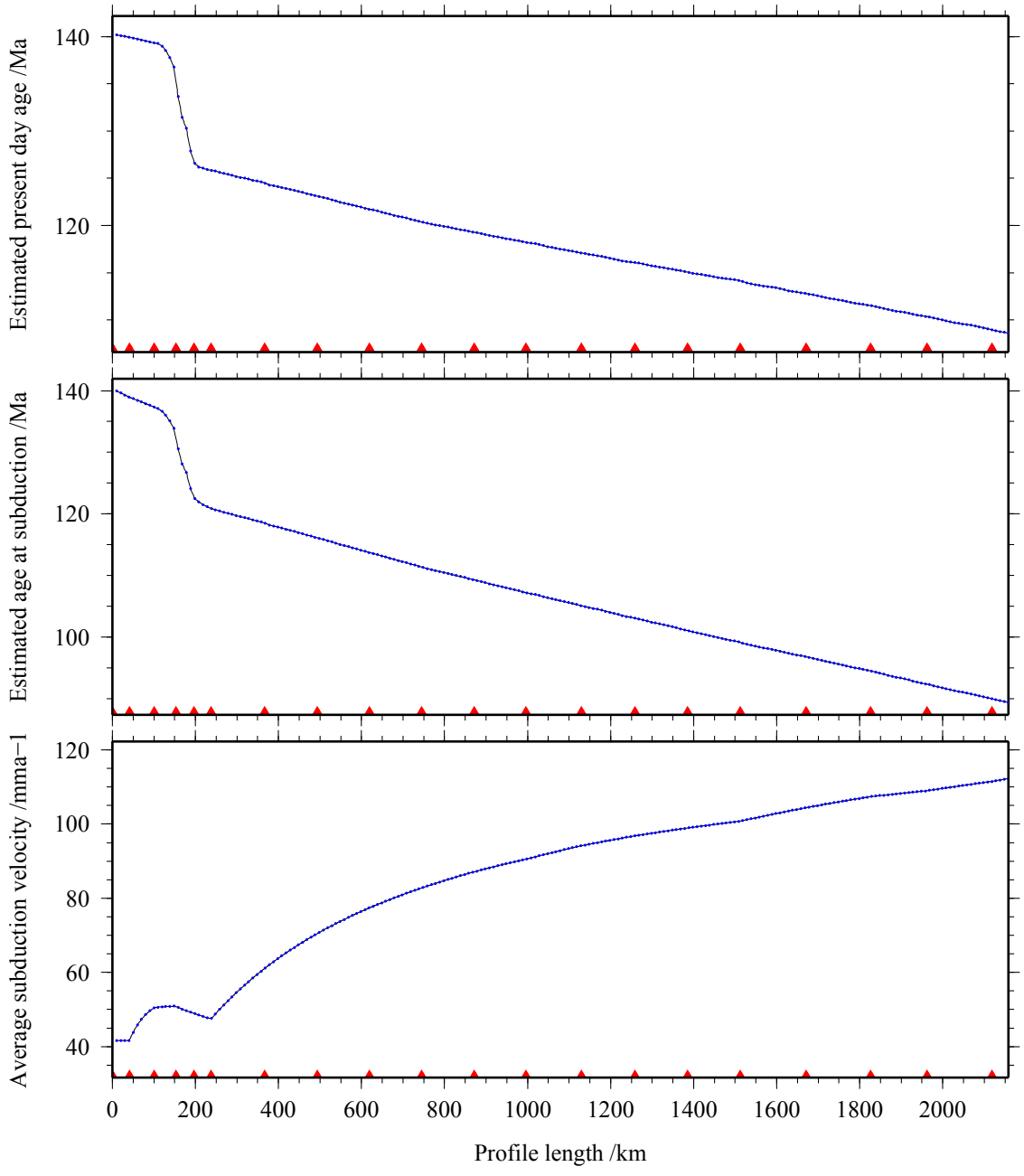

Figure 9.7: Estimated age of the subducting slab across the southern Bonin arc derived from the global plate-age and plate velocity models of Müller et al. (2008) and the continuously closing plate boundary model of Gurnis et al. (2010). Red triangles mark the amount of subduction at 1 Ma time intervals, which also corresponds to the original data points. Spline interpolation has yielded the blue data points.

Structure	Composition	κ_{std}	α_0 $(10^{-6})^1$	α_1 $(10^{-10})^1$	$\alpha_2{}^1$	$\gamma^{2,3,4}$	$K_0{}^{2,3,4}$	$K'_0{}^{2,3,4}$	a^{15}
Forsterite	Mg_2SiO_4	5.2[18]	28.54	100.80	-0.3842	1.25	127.9	4	0.45
Olivine	$Fo_{90}Fa_{10}$	4.7[8]	25.46[17]	77.41[17]	0.00126[17]	1.28	128.1	4.6	0.33
Wadsleyite	Mg_2SiO_4	8.06[5]	28.93	57.72	-0.8903	1	172	4.8	0.507[5]
Ringwoodite	Mg_2SiO_4	9.83[5]	24.97	36.39	-0.6531	1.25	183	5.2	0.494[5]
Garnet	$MgSiO_3$	3.2[9]	23.11	59.56	-0.4538	1.43	171.5	3.8	0.33
Ilmenite	$MgSiO_3$	4.7*	24.12[6]	–	–	1.7[15,16]	210	5.6	0.33
Perovskite	$MgSiO_3$	4.7[11]	22.00	–	–	1.5	261	5*	0.33
Orthopyroxene	$MgSiO_3$	4.5[13]	24.10	–	–	0.96	107	7.5	0.33
Clinopyroxene	$CaMgSi_2O_6$	4.9[9]	33.30	–	–	0.9	112	4.7	0.33
Periclase	MgO	55.2[10]	37.68	74.04	-0.7446	1.54	160	4.3	0.9
Quartz	SiO_2	7.7[12]	14.17	965.81	-1.6973	0.667	37.5	6.4	0.33
Stishovite	SiO_2	8.6[14]	15.74	78.86	-0.15	1.2	306	2.8	0.33
Coesite	SiO_2	1.45[12]	5.97	76.97	-0.1231	0.41	113	8.4	0.33
Spinel	$MgAl_2O_4$	9.5[9]	24.9	–	–	1.4	195.2	4.9	0.33
Plagioclase	$Ab_{77}An_{23}$	2.34[7]	16.12	76.83	-0.8603	0.57	60	4	0.33
Kyanite	Al_2SiO_5	7.15[7]	25.1	–	–	0.93	160	4	0.33

Table 9.1: Physical parameter values for minerals within metamorphic assemblages developed within upper mantle peridotite. $\alpha = \alpha_0 + \alpha_1 T + \alpha_2 T^{-2}$. *Data unavailable, 'reasonable' value picked. References are as follows: [1] Fei (1995), [2] Bass (1995), [3] Knittle (1995), [4] Sumino and Anderson (1984), [5] Xu et al. (2004), [6] Wang et al. (2004), [7] Clauser and Huenges (1995), [8] Chai et al. (1996), [9] Horai (1971), [10] Andersson and Bäckström (1986), [11] Osako and Ito (1991), [12] Beck et al. (1978), [13] Schloessin and Dvořák (1972), [14] Osako and Kobayashi (1979), [15] Hofmeister (1999), [16] Ashida et al. (1988), [17] computed from the Fo90.4 data of Singh and Simmons (1976), [18] Fujisawa et al. (1968).

9.5 Results

9.5.1 Comparing models

The effect of using different physical parameters in subduction zone thermal models is illustrated in Figure 9.8. In each model, temperature evolves within a 50 Ma old, 106 km thick slab subducting with a velocity 7.5 cm/a at an angle of 45°. The surrounding mantle has a potential temperature of 1315°C, and is allowed to cool by diffusion. Any advection of heat by the convecting mantle relative to the slab is ignored. The first two models have entrained mantle where the isentropic gradient is fixed at 0.3 K/km. The isentropic gradient in the other three models is calculated for a pyrolite bulk composition using Perple_X.

The first two models were presented by Emmerson and McKenzie (2007). The first uses constant values for conductivity (3.138 $Wm^{-1}K^{-1}$), thermal expansivity ($3.28{\cdot}10^{-5}$ K^{-1}), density at room temperature (3330 kgm^{-3}) and heat capacity (1200 $JK^{-1}kg^{-1}$) as used by Parsons and Sclater (1977). The second incorporates temperature-dependent material properties as calculated by McKenzie et al. (2005).

A consequence of the decrease in conductivity in the temperature-dependent parameter model of (Emmerson and McKenzie, 2007, Figure 9.8b) is the decrease in rates of heating within the subducting slab. Temperatures are reduced by ∼100 K when compared with the constant conductivity model. Incorporating *P-T-X*-dependent material properties (Figure 9.8c–e) increases temperatures within the subducting slab relative to the *T*-dependent case. The increased temperatures are predominantly the result of phase transformations at high pressure, which result in a much higher conductivity, as shown in Figure 9.9. Prominent jumps in conductivity are observed at the wadsleyite and ringwoodite-in reaction boundaries. A lens of very high (>10 $Wm^{-1}K^{-1}$) conductivity is observed at the base of the upper mantle where magnesiowüstite and stishovite are the dominant stable phases. A jump in crustal conductivities at the same depth is also due to the volumetric increase in high conductivity oxides.

The last three models in Figure 9.8 show variations in thermal structure resulting from different choices of oceanic pseudostratigraphy. Figure 9.8c is calculated assuming that the entire slab is composed of undepleted peridotite ('pyrolite') of the same composition as the entrained mantle. In Figure 9.8d, a 36 km thick layer of depleted peridotite (harzburgite) is added to the top of the slab. Finally, in Figure 9.8e a 7 km thick basaltic crust overlies a 29.1 km thick harzburgitic upper mantle.

Changes in pseudostratigraphy have only a minor influence on slab temperatures. A purely pyrolitic slab has slightly lower temperatures than one with a large harzburgitic surface, because of the larger proportion of relatively high conductivity olivine-wadsleyite-ringwoodite component in depleted lithospheric slab mantle. The addition of basaltic crust reduces temperatures slightly,

because basaltic compositions have low conductivities throughout the upper mantle.

Although the juxtaposition of low diffusivity crust on top of high diffusivity harzburgite results in very similar minimum temperatures to the pyrolitic case, the thermal gradient within the cold slab core is strongly reduced. This may have implications for interpretations of Wadati-Benioff zone thicknesses and the rupture dimensions of large deep-focus subduction zone earthquakes (see §9.6.2).

Considering the factor of two difference in conductivity between the present study and that of Emmerson and McKenzie (2007), the slab temperatures are perhaps surprisingly similar. At the base of the upper mantle, the temperature difference is $<$100 K. This muted difference is partially due to the limited time spent in the mantle transition zone where conductivity is high, and partially because increases in slab temperature require diffusion of heat from the overlying aesthenosphere, which has somewhat lower conductivities than the core of the slab.

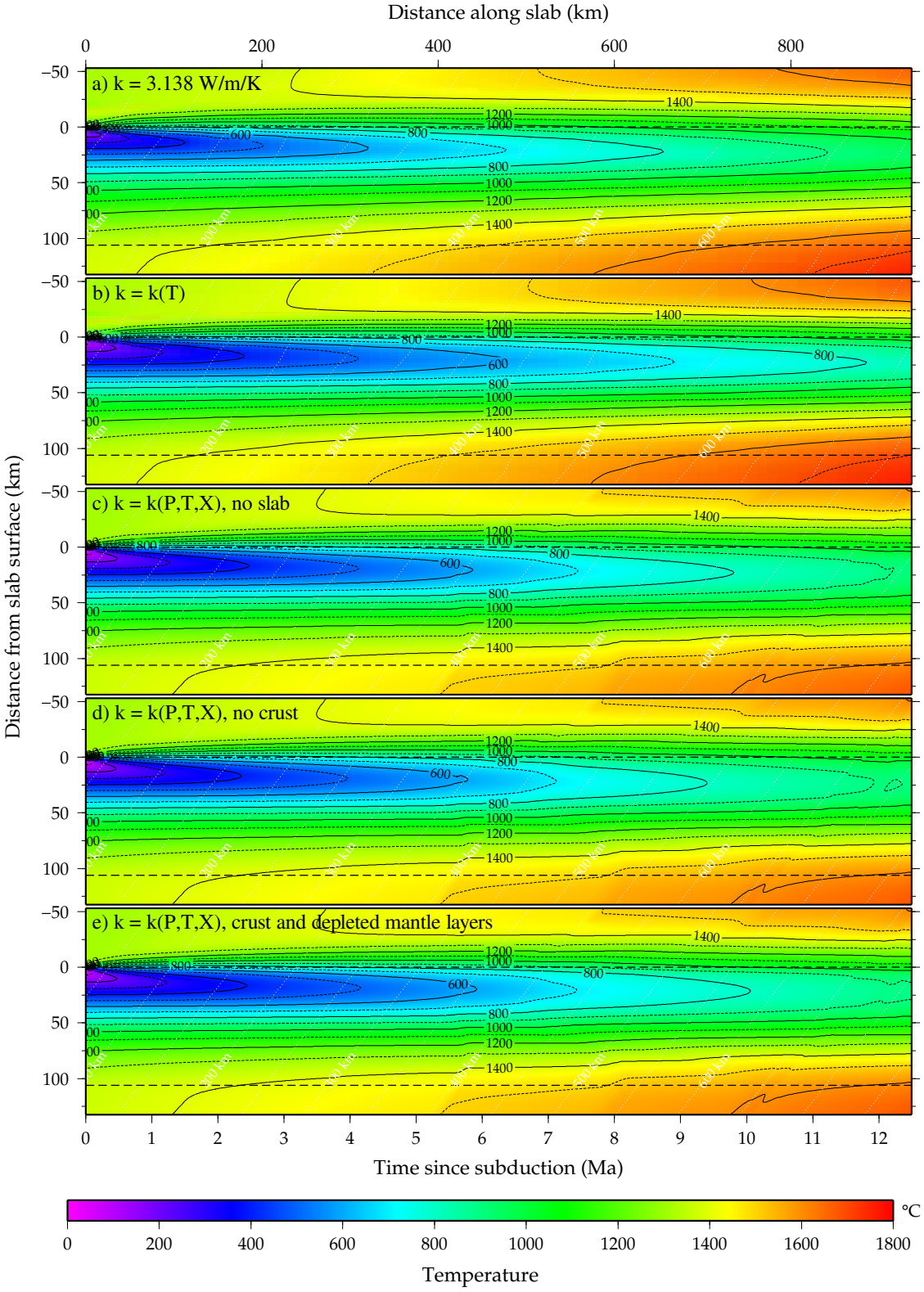

Figure 9.8: Comparisons between models with different input parameters. Each 106 km thick slab is 50 Myr old at subduction, subducting at 7.5 cm/a at an angle of 45°. a) Constant conductivity (3.138 $Wm^{-1}K^{-1}$), constant isentropic gradient. b) Temperature dependent conductivity and constant isentropic gradient as defined by Emmerson and McKenzie (2007). c) Pressure, temperature and mineralogy controlled physical parameters. Pyrolite only. d) No crust, with a 36 km thick harzburgitic lithosphere e) 7 km thick crust, 29.1 km thick harzburgitic upper mantle.

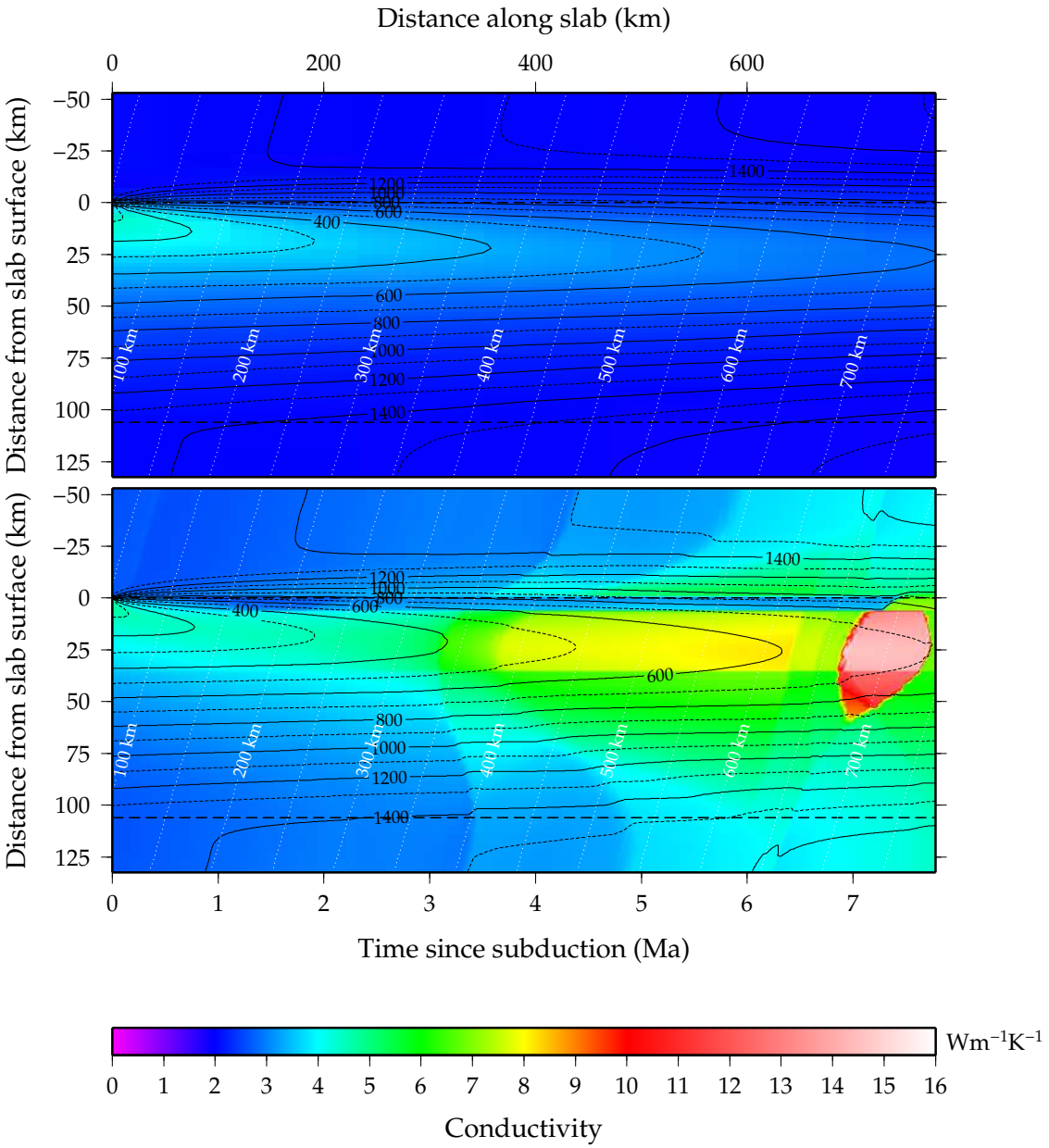

Figure 9.9: A comparison of conductivities and temperatures for temperature dependent conductivity (top), and mineral dependent conductivity (bottom). Slab model is for a 100 Myr old plate subducting at 10 cm/a with a dip of 60°.

9.5.2 Examples

Three examples of subduction zone models are shown in Figure 9.10. In Tonga, Marianas and Java, seismicity extends to ~ 660 km depth within slabs subducting at different velocities and dips. Tonga is particularly cold as a result of rapid subduction (vertical velocities are ~ 10 cm/a) of old oceanic lithosphere. Temperatures within the older, but more slowly subducting Marianas slab are similar. In both cases the 600°C isotherm just reaches 650 km depth. The modelled temperatures in the Java subducting slab along the profile in Figure 9.10 are 70–80°C warmer. The modelled temperatures along the Tonga and Java slabs vary with changing subduction parameters (see §9.5.3).

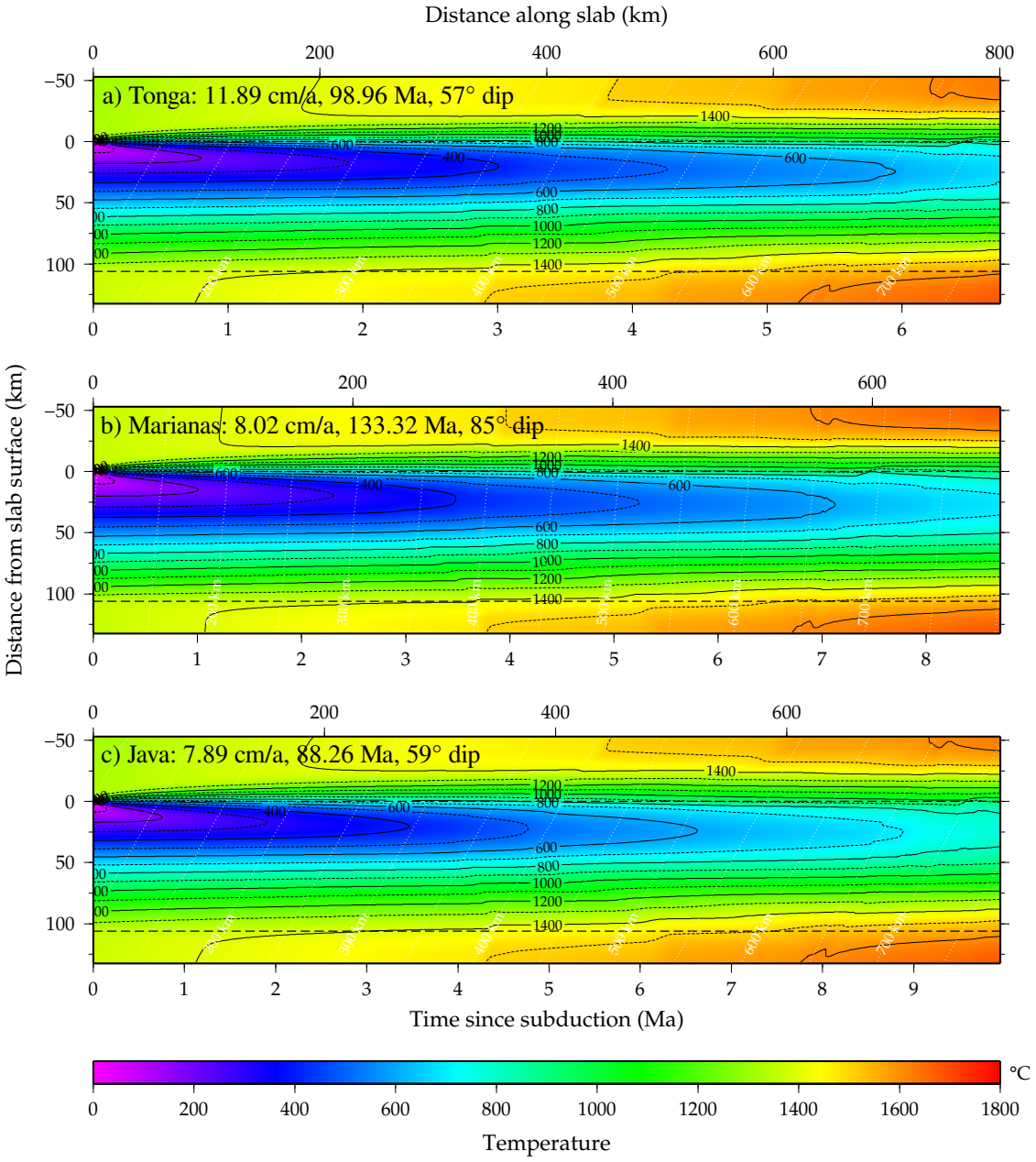

Figure 9.10: Example models for subduction zones where earthquakes occur at ~660 km depth. a) Tonga. b) Marianas. c) Java.

In all of the examples shown, the latent heat of reaction has a very small effect on temperatures within the slabs. Earlier models which applied fixed values of latent heat release to the olivine → wadsleyite phase transition overestimated the temperature increase within the slab (e.g. 135 K; Wortel, 1982). The effect can be seen in contours of entropy for the modelled bulk compositions (Figure 9.3); at temperatures relevant to the convecting mantle, temperature increases in harzburgite (which has a large proportion of olivine) are 50–70 K, but within cold slab interiors, latent heat release is negligible.

9.5.3 Seismogenic temperatures

Estimated temperatures at the maximum depth of seismicity for subducting slabs with seismic activity in the mantle transition zone are given in Table 9.2 and plotted in Figure 9.11. Uncertainties in past ocean ages and plate velocities are not reported by Müller et al. (2008) or Gurnis et al. (2010). Although using these datasets has removed the need to extrapolate present-day ocean floor ages and velocities back 5–20 Ma, it is not straightforward to estimate the potential errors in these values. The upper and lower bounds in Table 9.2 are calculated by assuming a 10% error in subduction velocity and by doubling the errors in present day age at the trench (as published in Müller et al., 2008). Minimum temperatures (blue) are 40–50 K hotter than those estimated by Emmerson and McKenzie (2007).

Table 9.2: Subduction zone profiles and parameters used to estimate temperature conditions where the deepest earthquakes are observed.

Region	Dip	a_{sub} (Ma)	v (cm/a)	z	T_{min} (°C)	$T_{7\,km}$ (°C)	$T_{47\,km}$ (°C)
Java	68	109.81 ± 5.20	8.92 ± 0.89	630	592^{+27}_{-24}	724^{+22}_{-20}	710^{+19}_{-17}
Java	60	99.50 ± 3.20	7.88 ± 0.79	640	660^{+26}_{-24}	788^{+21}_{-20}	759^{+19}_{-17}
Java	58	91.03 ± 6.40	7.61 ± 0.76	660	700^{+32}_{-41}	813^{+27}_{-23}	800^{+30}_{-27}
Java	59	88.25 ± 8.60	7.89 ± 0.79	670	710^{+33}_{-33}	813^{+30}_{-26}	807^{+39}_{-33}
Kamchatka	51	81.74 ± 12.80	8.34 ± 0.83	660	721^{+54}_{-44}	826^{+38}_{-32}	831^{+59}_{-48}
Kermadec	70	89.94 ± 6.60	5.99 ± 0.60	540	642^{+34}_{-29}	762^{+25}_{-21}	760^{+29}_{-25}
N. Kuriles	52	83.26 ± 12.80	8.42 ± 0.84	630	687^{+53}_{-43}	796^{+38}_{-31}	805^{+58}_{-46}
N. Kuriles	53	83.70 ± 12.20	8.64 ± 0.86	650	699^{+50}_{-48}	803^{+34}_{-26}	807^{+55}_{-41}
S. Kuriles	47	95.30 ± 7.80	10.55 ± 1.05	550	592^{+33}_{-29}	720^{+25}_{-22}	736^{+30}_{-25}
S. Kuriles	48	97.04 ± 6.60	10.32 ± 1.03	510	566^{+30}_{-26}	697^{+23}_{-21}	719^{+24}_{-21}
S. Kuriles	45	105.15 ± 4.40	10.88 ± 1.09	430	504^{+24}_{-21}	638^{+20}_{-17}	675^{+13}_{-12}
S. Sumatra	65	88.46 ± 10.40	7.54 ± 0.75	670	707^{+35}_{-33}	809^{+32}_{-28}	803^{+45}_{-37}
Izu	44	115.75 ± 5.40	9.15 ± 0.92	400	502^{+22}_{-21}	648^{+16}_{-17}	640^{+10}_{-11}
Izu	42	108.76 ± 8.80	8.96 ± 0.90	425	539^{+31}_{-26}	675^{+23}_{-20}	673^{+25}_{-20}
Izu	48	109.32 ± 9.80	8.54 ± 0.85	450	544^{+31}_{-28}	678^{+23}_{-20}	680^{+28}_{-23}
Izu	50	110.19 ± 9.00	8.52 ± 0.85	470	551^{+30}_{-27}	686^{+22}_{-21}	683^{+26}_{-22}
Izu	52	110.89 ± 9.00	8.42 ± 0.84	490	559^{+31}_{-27}	696^{+23}_{-21}	686^{+26}_{-22}
Izu	55	111.61 ± 7.00	8.19 ± 0.82	515	570^{+28}_{-25}	709^{+22}_{-20}	692^{+22}_{-19}
Izu	57	112.43 ± 7.20	8.06 ± 0.81	530	577^{+29}_{-25}	716^{+22}_{-20}	695^{+23}_{-20}
Izu	58	113.32 ± 6.00	7.85 ± 0.78	545	586^{+28}_{-24}	724^{+21}_{-19}	698^{+21}_{-18}
Marianas	85	133.38 ± 2.60	8.01 ± 0.80	650	583^{+22}_{-21}	721^{+19}_{-17}	682^{+12}_{-11}
Marianas	81	134.20 ± 1.80	8.20 ± 0.82	630	565^{+21}_{-17}	707^{+18}_{-17}	668^{+12}_{-10}
N. Tonga	57	98.97 ± 3.20	11.88 ± 1.19	670	623^{+10}_{-25}	738^{+20}_{-18}	749^{+14}_{-12}
N. Tonga	55	96.09 ± 2.60	10.69 ± 1.07	680	653^{+32}_{-20}	770^{+23}_{-21}	778^{+14}_{-12}
S. Tonga	53	84.55 ± 2.40	9.63 ± 0.96	620	650^{+25}_{-24}	762^{+21}_{-20}	786^{+16}_{-14}
S. Tonga	55	80.25 ± 1.80	8.84 ± 0.88	610	664^{+25}_{-22}	772^{+21}_{-19}	802^{+14}_{-12}
New Zealand	75	102.67 ± 12.00	4.70 ± 0.47	610	706^{+40}_{-36}	818^{+29}_{-27}	777^{+41}_{-35}

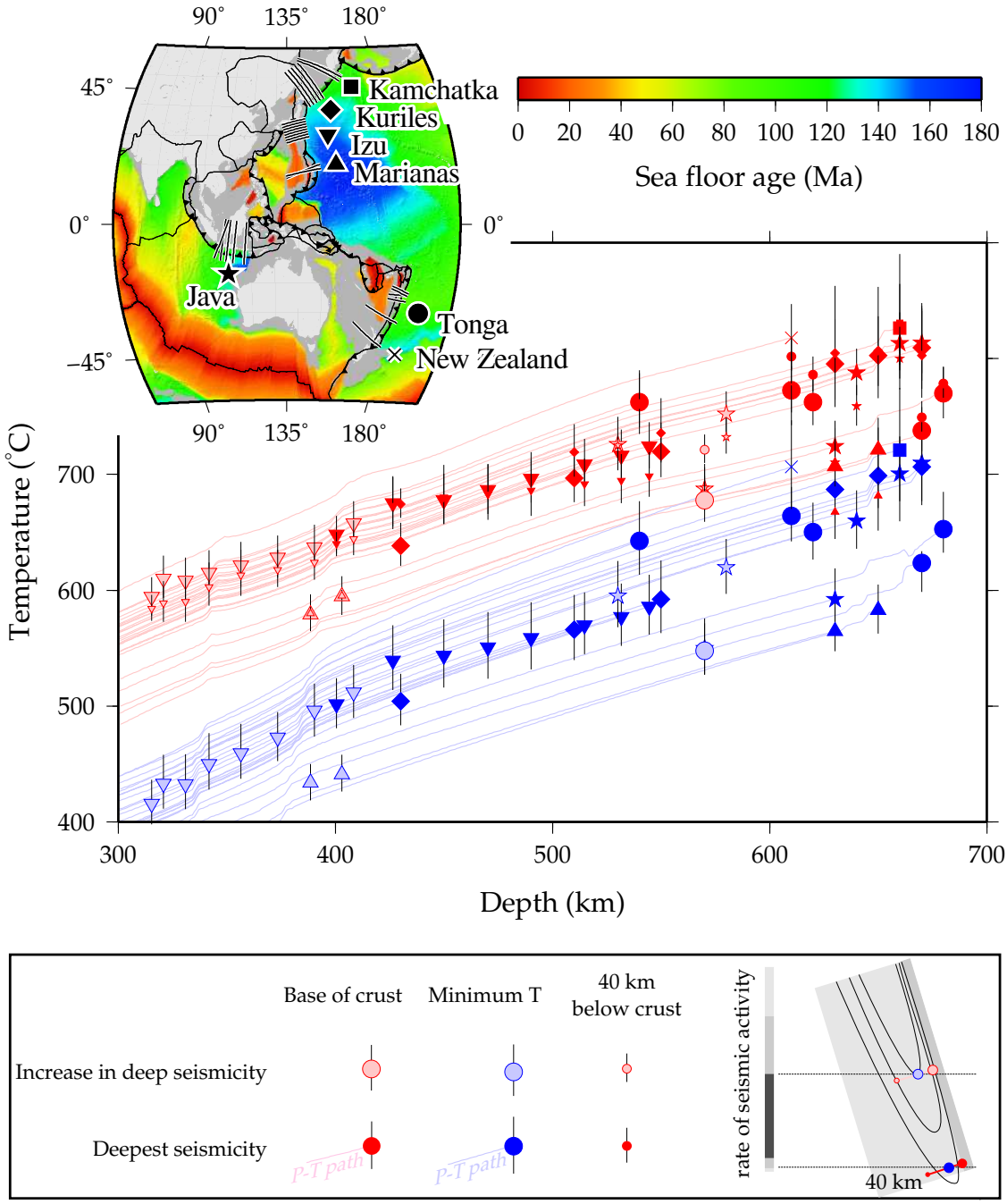

Figure 9.11: Temperature estimates and associated uncertainties within modelled subduction profiles listed in Table 9.2. Different symbols illustrate different subduction zones, and sizes and colours represent different locations within the slab (see figure legend). Blue symbols represent the minimum temperatures within the slab. Red symbols represent the temperature at the base of the 7 km thick slab crust (large symbols) and 40 km into the slab mantle (small symbols). Pastel symbols show estimated temperatures during increases in deep-focus seismicity. Brighter symbols show estimated temperatures at the depth of deepest seismicity. T_{min} and basal crustal estimates are accompanied by lines illustrating the *P-T* history of the slab.

9.6 Discussion

9.6.1 Uncertainties

Subduction parameters

Subduction velocities in some regions are poorly constrained, especially for the North Tonga and Marianas slabs where back-arc spreading rates are considerable. Lithosphere ages at subduction may also be associated with larger errors than those attributed in this study if fragments of older or younger lithosphere are incorporated into the plate, by rift jumps for example. This issue can probably be neglected, given the rarity of such fragments in ocean basins at the present day.

One-dimensional modelling of slab thermal evolution fails to incorporate several processes which may have an effect on temperatures. Although isotherms within the slab are sub-parallel to the slab surface, surfaces of constant conductivity cut across the slab, which will have a small effect on the temperature distribution through time.

Material properties

Material properties are also associated with uncertainties. The density and heat capacities of the mineral assemblages calculated by Perple_X have small associated uncertainties, but some of the reactions predicted by the thermodynamic dataset of Stixrude and Lithgow-Bertelloni (2011) may be associated with larger errors, particularly at lower temperatures, where fewer experiments have been conducted. Another source of error arises from the semi-empirical expression used to calculate conductivity. Additionally, the experimental data used derives only from end-member or fixed composition minerals, and with the exception of olivine contain no iron. Iron essentially removes the (already minor) radiative contribution to thermal conductivity, further reduced by small grain sizes (e.g. Hofmeister, 2005).

Metastability

Rates of reaction are important parameters in subduction models incorporating mineral-dependent conductivity and latent heat of reaction. Within subducting slabs, the most important reaction rates are those of the olivine and post-olivine phases. At low temperatures, sluggish reactions can lead to prolonged periods where the metamorphic assemblage is far from equilibrium. Below 600–700°C, metastable olivine may be maintained for millions of years within subducting slabs (e.g. Sung and Burns, 1976a,b; Kirby et al., 1996), although this is strongly dependent on the amount of hydration in olivine; just 300 p.p.m. is sufficient to suppress the formation of a metastable wedge (Diedrich et al., 2009). The rate of reaction of olivine will control the thermal evolution of subducting slabs through both the difference in diffusivity of olivine, wadsleyite and ringwoodite-bearing

assemblages (Figure 9.12), and the increasing latent heat of reaction as the olivine assemblage becomes increasingly metastable (Figure 9.13). The effect of incorporating sluggish reaction kinetics to the olivine-wadsleyite transition at low temperature is to increase the innermost slab temperatures, while decreasing the thermal gradient within the slab.

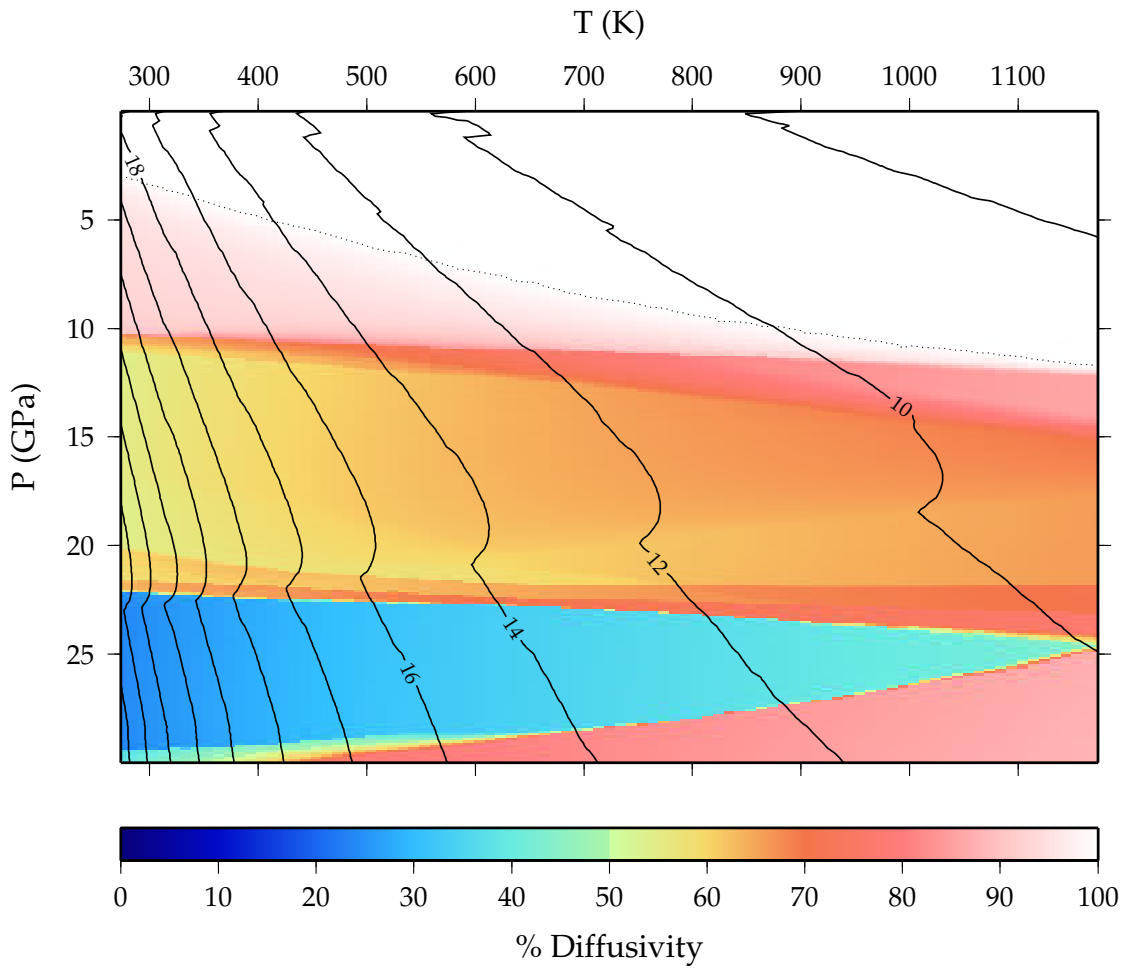

Figure 9.12: Diffusivity of harzburgite with metastable olivine. Solid black lines are in $10^{-6}m^2s^{-1}$. The dotted line represents the first appearance of the high pressure olivine polymorphs. Shading represents the diffusivity of the metastable assemblage as a percentage of the equilibrium assemblage.

Studies incorporating the presence of metastable olivine have disparate conclusions. Kirby et al. (1996) used the experimental data of Rubie and Ross (1994), and found that metastable olivine wedges along cold slab *P-T* paths could extend to the base of the upper mantle. Their incorporation of the latent heat of reaction had little effect on slab temperatures or phase relationships. The results of Kawakatsu and Yoshioka (2011) are broadly similar to that of Kirby et al. (1996). In contrast, Däßler and Yuen (1993, 1996) and Devaux et al. (1997) show that coupling of spinel growth rates with latent heats of reaction significantly reduce the maximum depth of metastable wedges, particularly in slabs with low subduction velocities. Models incorporating more recent kinetic data and intracrystalline transformation reveal that even in the case of the old, quickly subducting Tonga

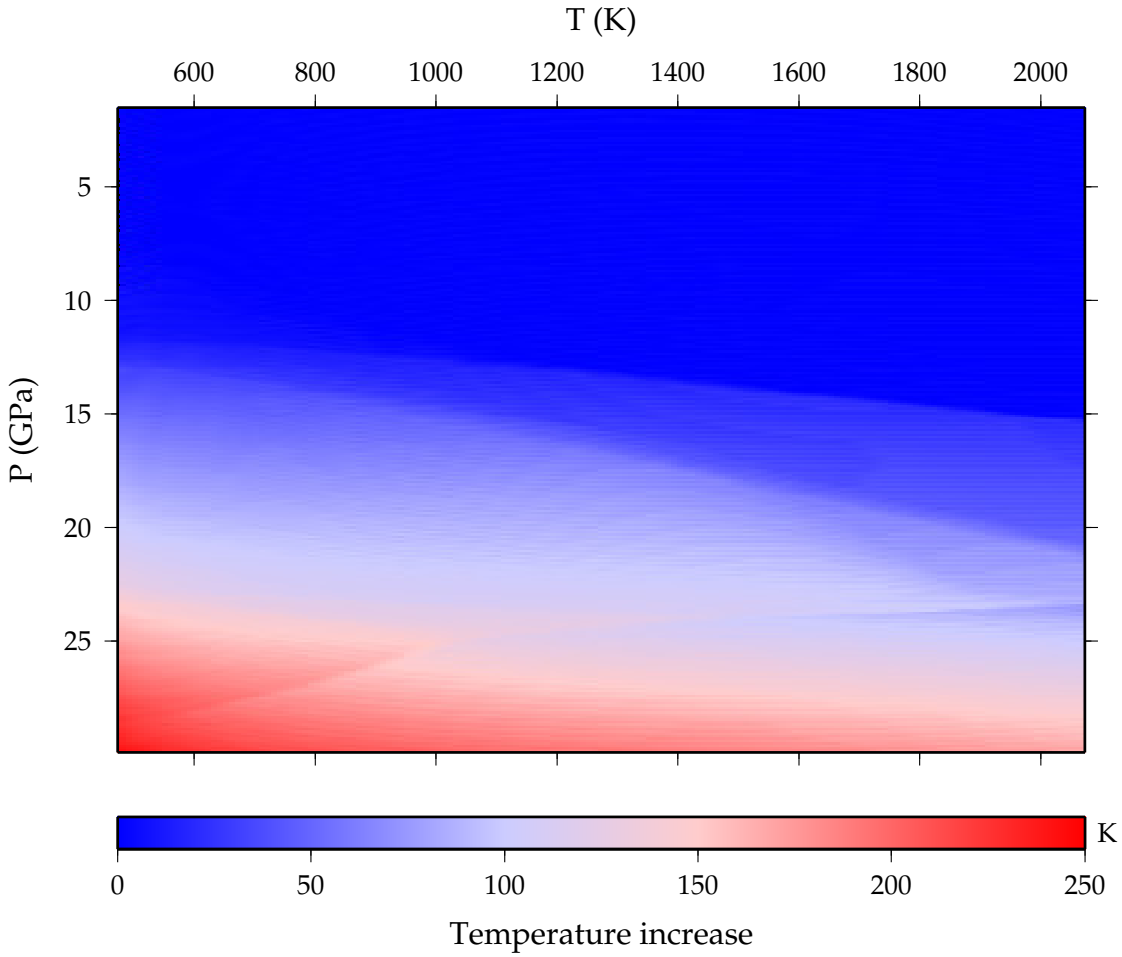

Figure 9.13: Change in temperature when a harzburgite assemblage with metastable olivine under given *P-T* conditions reacts to the equilibrium assemblage.

slab, the metastable wedge reaches only 500–550 km depth (Mosenfelder et al., 2001). Incorporating *P-T*-composition-dependent conductivity for the olivine phases has little effect on this conclusion (Marton et al., 2005).

The kinetics of the olivine-wadsleyite transition within subducting slabs remain poorly understood. Particularly important is the effect of strain, which enhances transformation rates (Wu et al., 1993; Liu et al., 1998). Wadsleyite first nucleates on grain boundaries, but growth rates decelerate markedly in low strain conditions, presumably because shear facilitates atomic rearrangement. In regions of subduction zones where strain rates are high, the reaction of olivine to wadsleyite may proceed more rapidly than predicted by (Mosenfelder et al., 2001).

Slab deformation

Deformation could also have a significant effect on slab temperatures. Applying kinematic boundary conditions to slab models may be appropriate above the transition zone (e.g. van Keken et al., 2002; Syracuse et al., 2010) where slab shape changes slowly. In the Tonga slab strain rates may exceed $10^{-15}s^{-1}$ in the mantle transition zone (Holt, 1995), resulting in down-dip shortening of several millimeters per year. Thickening could exceed 20% if this shortening is typical of the whole length of the slab. King (2001) suggests that some slabs might double in thickness during residence in the upper mantle. Since the time taken for diffusive heating scales as the square of the thickness of the body, thickening could result in much lower temperatures in the slab core. This would partially trade off against lower subduction velocities, especially where large down-dip gradients in thermal conductivity are observed.

In Chapter 5, it was revealed that the majority of earthquakes in the mantle transition zone are consistent with localised deformation within bends in the slab. If deformation remains within these bends, then most of the slab will experience temperatures similar to those modelled here. The parts of the slab which are most seismically active may be somewhat cooler, but because of the high thermal conductivity in the core of the slab, the difference in temperatures will be smaller than predicted using a constant conductivity model.

Mantle flow

The assumption that the aesthenosphere moves passively with the slab is an adequate approximation for purely conductive thermal modelling if there is negligible shear within the 20–50 km immediately above the subducting slab, where conductive cooling has a significant effect on mantle temperatures. Flow in the aesthenospheric mantle close to the slab is potentially promoted by strain weakening, fabric development, the presence of fluids and/or formation of hydrous minerals if the temperature in the wedge is sufficiently low to stabilise them (see §9.6.5). There is some evidence from receiver function studies that hydrous phases may be stable above the Japan slab (Tonegawa et al., 2008).

If the aesthenosphere overlying the subducting slab is allowed to shear, the temperature of the slab will depend on the history of subduction in the area, and the rate of replenishment of the mantle wedge with uncooled aesthenosphere. In the Marianas system, where subduction has been ongoing for 40–50 Ma (Richards and Lithgow-Bertelloni, 1996), inefficient entrainment and sluggish convection would lead to cooling of the mantle wedge and subducting slab.

9.6.2 Thermal evolution

The thickness of the Tonga Wadati-Benioff zone at 600–650 km depth is 30–50 km. Large earthquakes such as the 1994 Bolivia and Tonga earthquakes can also rupture up to ∼50 km of the slab (e.g. Wiens and McGuire, 1995), and aftershocks can extend outside the normally active seismogenic zone (e.g. Wiens et al., 1994). Thick seismogenic zones near the base of the upper mantle have traditionally been a problem for strongly temperature-dependent mechanisms for deep earthquake generation. Fluid embrittlement relies on the presence of fluids, which if generated in the source region of the earthquakes must rely on the *P-T* path passing through a dehydration reaction. Some models of shear heating exhibit thermal runaway only within a restricted range of temperatures (e.g. Kelemen and Hirth, 2007). Others do not show this dependence, requiring only that temperatures remain below a critical value to maintain a satisfactory rheology (Karato et al., 2001). Finally, transformational faulting requires the presence of metastable olivine throughout the seismically active region, which in turn requires low temperatures.

To reflect these seismogenic thicknesses, maximum temperatures between the base of the crustal sequence and 40 km further within the slab are also plotted in Figure 9.11. The ∼100 K difference between these estimates is much smaller than the 300–400 K estimate obtained using constant conductivity models (Wiens, 2001). This result means that if metamorphic equilibrium is maintained within subducting slabs, large earthquakes and their aftershock sequences do not necessarily experience large variations in temperature, relieving the restrictions on physical mechanism of earthquake generation.

It should be noted that the presence of metastable olivine wedges, with their lower conductivity, will result in higher thermal gradients within subducting slabs in the mantle transition zone than the equilibrium model. As suggested by Wiens (2001) and reviewed by Marton et al. (2005), current kinematic models of olivine → wadsleyite reaction are inconsistent with the depth range and widths of Wadati-Benioff zones in cold slabs. After transformation, very low thermal gradients (promoted by the strong temperature dependence on the reaction) might enable other thermally-controlled earthquake-generating mechanisms to act through significant thicknesses of subducting slabs.

In addition to reducing thermal gradients, the high conductivity of equilibrium assemblages within cold subducting slabs reduces the temperature variations between slabs. For the coldest slabs, the wedge of extremely high conductivity at 650–700 km depth results in a rapid decrease in thermal gradient within the cold slab core, as first hypothesised by Toksöz et al. (1973). The rate of heating also increases, but the effect on the temperature evolution of present day slabs will likely be <50 K, because they either stagnate above the region where the ferropericlase plus stishovite assemblage is stable, or penetrate directly into the lower mantle.

9.6.3 *Temperature dependence of seismicity*

The modelled slabs have minimum estimated temperatures that are $< 500°C$ at 300 km depth. Slabs which have few or no deep-focus earthquakes (e.g. those beneath the Aleutians, the Solomons, Middle and South America and the South Sandwich Islands) tend to be warmer at 300 km (e.g. Emmerson and McKenzie, 2007), suggesting that the increased temperature may enable strain to be taken up aseismically, except at very high strain rates.

There is a weak correlation between the maximum depth of deep-focus seismicity and estimated minimum temperatures in the slab. This correlation cannot be used as evidence for a *P*-*T*-dependence on where seismicity is possible, because the *P*-*T* trend is approximately coincident with the *P*-*T* paths taken by the slabs. This is particularly clear for the Izu-Bonin results; the deepest seismicity increases in depth to the south even though the estimated slab *P*-*T* paths are very similar.

9.6.4 *The lack of seismicity in the lower mantle*

Several slabs have seismicity that continues to the base of the upper mantle at 670–680 km (Stark and Frohlich, 1985; Rees and Okal, 1987; Okal and Bina, 1998), without large numbers of outboard earthquakes. Estimated minimum temperatures within these slabs lie between 560 and 720°C. Some of this variation may be due to errors in input parameters and the model assumptions. Nevertheless, the cessation of seismicity does not appear to be purely temperature controlled.

If slabs are unable to directly penetrate the lower mantle, then no earthquakes would be expected. However, given the lack of events outboard from the Marianas or north Kuriles slab, and tomographic studies that suggest that these slabs might penetrate the upper-lower mantle boundary without stagnating, alternative suggestions are required. Potential explanations include:

- Increased viscosity in the lower mantle, which might result in stress-strain conditions unsuitable for faulting.
- Mineral changes within the slab. These changes could be rheological, especially in the coldest slabs, where ferropericlase and stishovite are stable. Ferropericlase is about three orders of magnitude weaker than perovskite within the lower mantle (Ammann, 2011, and references therein). Assemblages with a rheology controlled by ferropericlase could potentially be weaker than the lower mantle. Conversion to weaker assemblages could be enhanced by feedback between reaction rates and deformation.
- The mechanism of faulting. Proponents of transformational faulting point out that the decomposition of olivine to perovskite and ferropericlase cannot cause brittle failure (Green and Zhou, 1996; Gleason and Green, 2009). Increased conductivity (as expected from the growth of ferropericlase) inhibits the development of adiabatic shear instabilities (Hobbs and Ord, 1988).

9.6.5 Hydrous minerals

If water is able to penetrate into the upper mantle prior to subduction, hydration will probably be localised along shear zones. If the ratio of hydrous to anhydrous material is low, the thermal structure of the slab can be modelled using anhydrous assemblages as determined in the current study. The stable phases and maximum water contents of subducting mantle assemblages can then be projected onto the *P-T* map of the slab (Figure 9.14). All subduction zones with deep-focus earthquakes have core temperatures low enough that hydrous minerals within the slab can carry water beyond 300 km depth.

In the mantle transition zone, temperatures in the mantle directly above the subducting slab are low enough to stabilise hydrous phases. Even if deep hydration of oceanic lithosphere is impossible, the transfer of water from dehydrating crust at ~300 km depth to dense hydrous magnesium silicates in the overlying mantle may provide a route for water to enter the lower mantle.

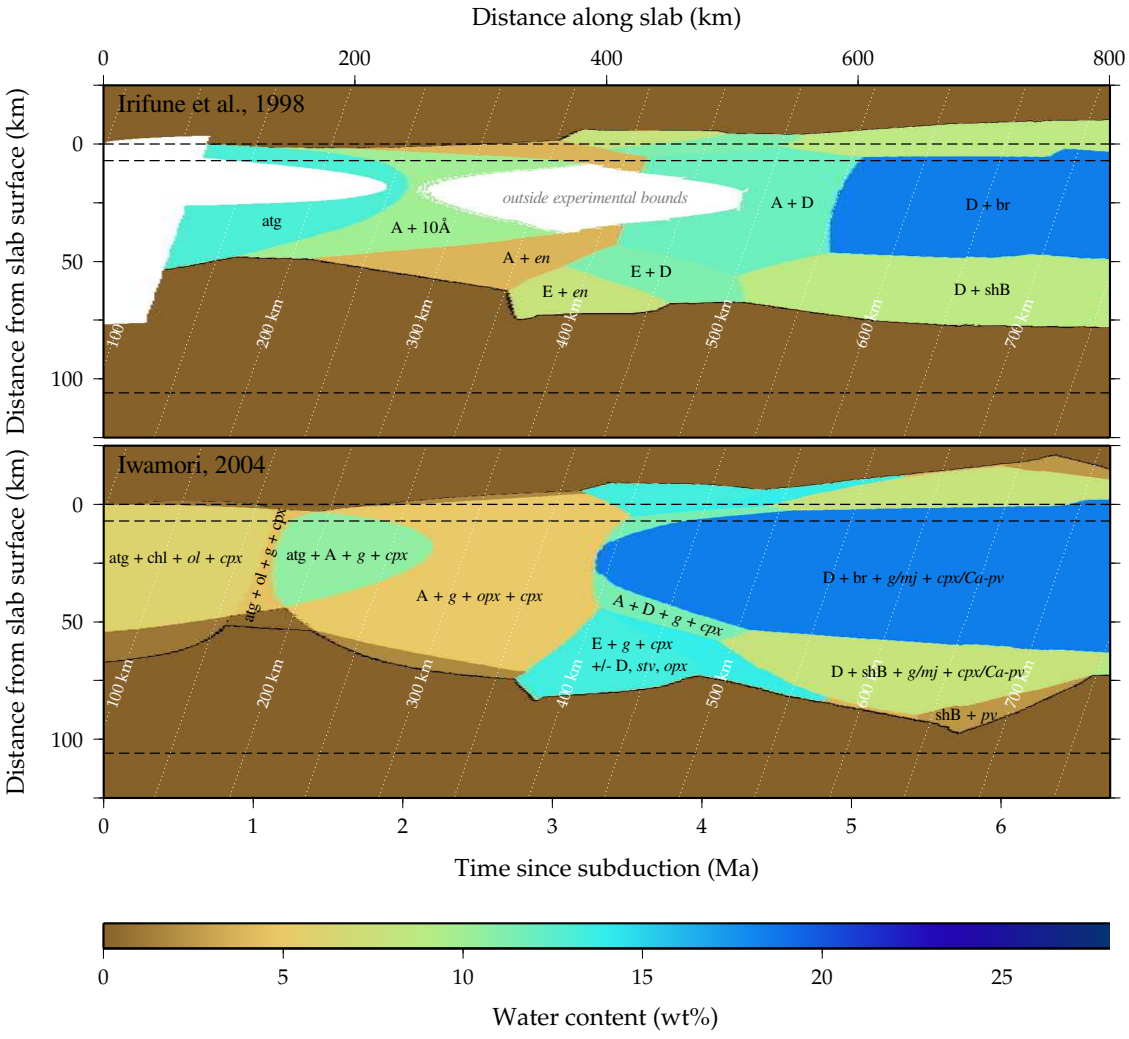

Figure 9.14: Estimated maximum water concentrations (in weight percent) in ultramafic sections of the Tonga slab, based on serpentine experimental data (top; Irifune et al., 1998) and interpolation and extrapolation of data from multiple studies on a variety of ultramafic bulk compositions (bottom; Iwamori, 2004). Phase fields are annotated with important mineral phases, with nominally anhydrous phases in italics.

It has been suggested that hydrous fluids may play a role in controlling the locations of deep focus seismicity (e.g. Omori et al., 2004). For this to be true, *P-T* paths in seismically active slabs must allow creation or maintenance of a free fluid phase.

The stable hydrous assemblages of Irifune et al. (1998) and Iwamori (2004) increase in water capacity with depth. This increase is the result of the stabilisation of brucite and phase D at the expense of less water-rich phases. Rather than releasing water, the phase maps suggest that hydrous assemblages in the mantle transition zone tend to absorb free fluids. This is an major issue for proponents of dehydration embrittlement causing deep-focus earthquakes (e.g. Omori et al., 2004), or any other process which requires the presence of free fluids in the mantle transition zone. There are four potential ways to resolve this issue if the modelled thermal structures are accurate. Firstly, shear within the slab could locally increase slab temperatures and cause decomposition of hydrous phases. Secondly, fluid-solid phase boundaries may be inaccurate, or poorly represented in the experimental bulk compositions. The brucite + phase D $\rightarrow$ superhydrous Phase B + H_2O reaction boundary, for example, spans 200 km at the base of the upper mantle at 600–900°C but is constrained by only four data points separated by 200 K and 5 GPa (Irifune et al., 1998). Thirdly, water contents are determined by mass balance assuming a pure H_2O fluid phase. This assumption may be correct at $<$ 300 km depth, but is almost certainly wrong in the mantle transition zone. The solubility of Mg, Fe and Si in hydrous fluids released by dehydration reactions increases significantly at high pressures (e.g. Kawamoto, 2004; Fukui et al., 2005; Melekhova et al., 2007; Dvir et al., 2011), raising the possibility of continuous fluid release as slabs subduct and heat up. Finally, carbon-rich melts may also be important in the mantle transition zone (Harte, 2010; Litasov et al., 2011). These possibilities should be addressed through careful experimental work.

9.7 Conclusions

This study has shown that the *P-T*-mineral-dependent physical properties of mafic and ultramafic rocks can have a significant effect on temperatures in subduction zones. Estimated temperatures within subducting slabs are lower than those reported in studies using constant physical properties, but ∼50 K higher than those in models where physical properties are assumed to depend only on temperature. The temperature variations between models are dominated by variations in conductivity rather than density or heat capacity. Including a high-conductivity depleted uppermost mantle crust raises temperatures slightly, but this effect is counteracted by low-conductivity basaltic crust. High conductivities in the cold depleted parts of the slab dramatically reduce thermal gradients.

The latent heat produced during olivine-wadsleyite-ringwoodite reactions produce temperature jumps of several tens of degrees in the convecting mantle, but much more muted jumps in cold slabs. The ferropericlase-in reaction is endothermic in the convecting mantle, but exothermic in cold slabs.

Fully self-consistent thermal modelling of subducting slabs raises some interesting geodynamical questions. If reactions are rapid compared with the change in *P-T* conditions, current mineralogical models (Stixrude and Lithgow-Bertelloni, 2011) suggest that a ferropericlase and stishovite lens should be present in the coldest mantle. The formation of such a weak, high conductivity assemblage could have implications for deformation of the coldest slabs at the base of the upper mantle.

The temperatures within subduction zones are easily cold enough to stabilise hydrous phases, but current data suggests that the slab mantle should become absorbent with respect to hydrogen along subduction *P-T* paths. If free fluids are present within the slab mantle, they must be of unusual composition, have different phase relationships to those estimated from experimental data, or be released by localised heating of the subducting slab.

10 Stress and strain

10.1 Introduction

Deep earthquake locations, focal mechanisms and rupture characteristics provide key constraints on the state of stress and strain within subduction slabs. In Chapter 5, it was shown that the distributions and focal mechanisms of deep-focus earthquakes are at least partially controlled by slab bending. The evolving shape of subducting slabs explains why models assuming slab motion under a rigid template are unable to recreate the patterns of strain in the Tonga slab (Nothard et al., 1996b).

An alternative to slab bending is homogeneous shortening, i.e., where strain rates close to the surface of the slab are matched by strain rates deep within the mantle section (e.g. Isacks and Molnar, 1971). Bending and homogeneous shortening are both promoted by negative slab buoyancy and resistance to flow by a viscosity increase in the lower mantle, and are both likely to be contributors to strain rates in subducting lithosphere.

Estimates of seismic strain rates within subducting slabs are invariably lower than the rates required to take up convergence between the subducting plate and the upper-lower mantle boundary. Holt (1995) and Nothard et al. (1996a) showed that seismic activity probably accounts for less than half of the convergence rate within the south Tonga slab. Holt (1995) suggested that the discrepancy between seismic strain rates and convergence rates implied penetration of the slab into the lower mantle at $\gtrsim 30$ mm/yr. However, tomographic studies fail to image a high velocity slab in the lower mantle beneath the Tonga slab (e.g. Kennett and Gorbatov, 2004).

Slab bending has traditionally not been considered when attempts have been made to explain estimated strain rates in subducting slabs. This oversight is notable, since models of bending and shortening produce different distributions and rates of strain. In this chapter, I calculate estimated rates of deformation due to slab bending, and compare these rates to estimates of seismic strain. I investigate the possibility that bending can account for the discrepancy between seismic strain rates and convergence rates without requiring aseismic deformation in Wadati-Benioff zones or slab penetration into the lower mantle. The results are discussed in the context of slab rheology, and the extent to which numerical models reflect the dynamics of subducting slabs.

10.2 Methodology

10.2.1 Analytical kinematic modelling

In this study, I investigate the scenario in which bending subducting slabs can be treated as incompressible beams. A simplified model of an initially planar beam undergoing bending is shown in Figure 10.1. The beam is bent with a radius of curvature r. Strain parallel to the beam between two points A and B is equal to

$$\epsilon = \frac{\overline{A'B'} - \overline{AB}}{\overline{AB}} \tag{10.1}$$

If the distance between the line and line of no length change within the beam is γ, then

$$\epsilon = -\frac{\gamma}{r} \tag{10.2}$$

The instantaneous strain rate $\dot{\epsilon}$ at any time t can be calculated from the rate of change of $-\gamma/r$. Information on the change in γ and r over time is not required to determine instantaneous strain rates. From Figure 10.1 and $a = r\phi$ (ϕ in radians)

$$x = a\left(1 - \frac{\sin\phi}{\phi}\right) + b\left(1 - \cos\phi\right) \tag{10.3}$$

$$\frac{\mathrm{d}x}{\mathrm{d}\phi} = \left(\frac{a}{\phi^2} + b\right)\sin\phi - \frac{a}{\phi}\cos\phi \tag{10.4}$$

Generalising to slabs dipping at an angle δ, Expressions 10.3 and 10.4 become

$$x = a\left(1 - \frac{\sin\phi}{\phi}\right) + b\left(1 - \cos\phi\right) + \frac{1}{\tan\delta}\left(\frac{a}{\phi}(1 - \cos\phi) + b\sin\phi\right) \tag{10.5}$$

$$\frac{\mathrm{d}x}{\mathrm{d}\phi} = \left(\frac{a}{\phi^2} + b\right)\sin\phi - \frac{a}{\phi}\cos\phi + \frac{1}{\tan\delta}\left(\left(\frac{a}{\phi^2} + b\right)\cos\phi + \frac{a}{\phi}\sin\phi - \frac{a}{\phi^2}\right) \tag{10.6}$$

Using Equation 10.2 we have

$$\dot{\epsilon} = -\frac{\gamma}{a}\frac{\mathrm{d}\phi}{\mathrm{d}t} = -\frac{\gamma}{a}\frac{\mathrm{d}\phi}{\mathrm{d}x}\frac{\mathrm{d}x}{\mathrm{d}t} \tag{10.7}$$

Combining Equations 10.6 and 10.7 yields an equation describing how bending strain rate varies with velocity v and with distance from the line of no length change γ for a slab with constrained a, b and ϕ

$$\dot{\epsilon} = \frac{\gamma v}{a\left(\frac{a}{\phi}\cos\phi - \left(\frac{a}{\phi^2} + b\right)\sin\phi + \frac{1}{\tan\delta}\left(\frac{a}{\phi^2} - \left(\frac{a}{\phi^2} + b\right)\cos\phi - \frac{a}{\phi}\sin\phi\right)\right)} \tag{10.8}$$

$$= \frac{\gamma v}{a^2\left(\frac{1}{\phi}\cos\phi - \left(\frac{b}{a} + \frac{1}{\phi^2}\right)\sin\phi + \frac{1}{\tan\delta}\left(\frac{1}{\phi^2} - \frac{1}{\phi}\sin\phi - \left(\frac{b}{a} + \frac{1}{\phi^2}\right)\cos\phi\right)\right)} \tag{10.9}$$

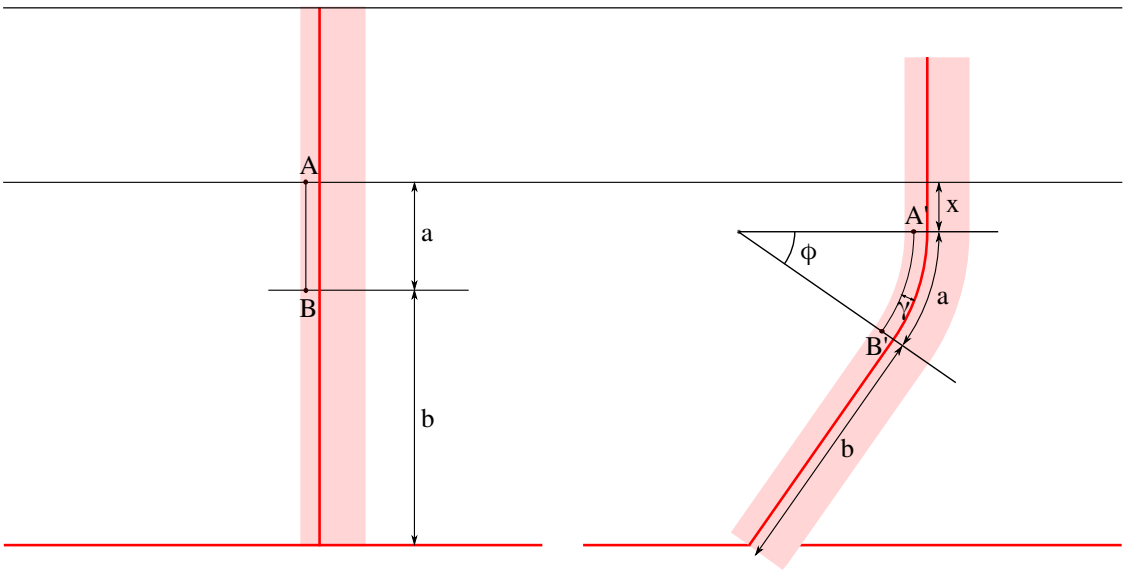

Figure 10.1: A simple beam model for bending slabs

Non-dimensionalised strain rate for a vertically dipping slab is plotted in Figure 10.2. To convert to strain rate, multiply by $\gamma v/a^2$. Bending within the Tonga and Bonin slabs occurs over arc lengths of >100–200 km (Karato et al., 2001; Buffett and Heuret, 2011), such that typical values of $\gamma v/a^2$ are on the order of 10^{-15} s^{-1} (for example, where $v = 10$ cm/a, $a = 150$ km and $\gamma = 7.1$ km).

10.2.2 Seismic strain rates

Model strain rates can be compared with estimates obtained from seismicity. For deformation occurring as discrete earthquakes over time Δt within a volume V having a shear modulus μ,

$$\bar{\dot{\epsilon}} = \frac{c \sum_i \mathbf{M}_i}{2\mu \Delta t V} \tag{10.10}$$

where c is a constant and $\sum_i \mathbf{M}_i$ is the sum over moment tensors during time duration Δt (Kostrov, 1974). Δt for the gCMT catalogue between January 1976 and January 2011 is 35 years. $\bar{\dot{\epsilon}}$ is the 'stress-free strain rate' (Backus and Mulcahy, 1976), which is assumed to dominate the seismic strain rate (e.g. Fischer and Jordan, 1991; Sandiford, 2008).

At shallow depths, crustal rocks have shear moduli μ typically estimated to be between $3 \cdot 10^{10}$ and $5 \cdot 10^{10}$ Nm^{-2}. However, μ is a function of pressure, temperature and the material being deformed. Shear modulus can be expressed in terms of density and shear velocity

$$\mu = \rho V_S^2 \tag{10.11}$$

The high density and wave velocity of peridotite mean that the shear modulus is about double that of crustal rocks at low pressure. Peridotite within cold slabs should undergo a ~2-fold increase in shear

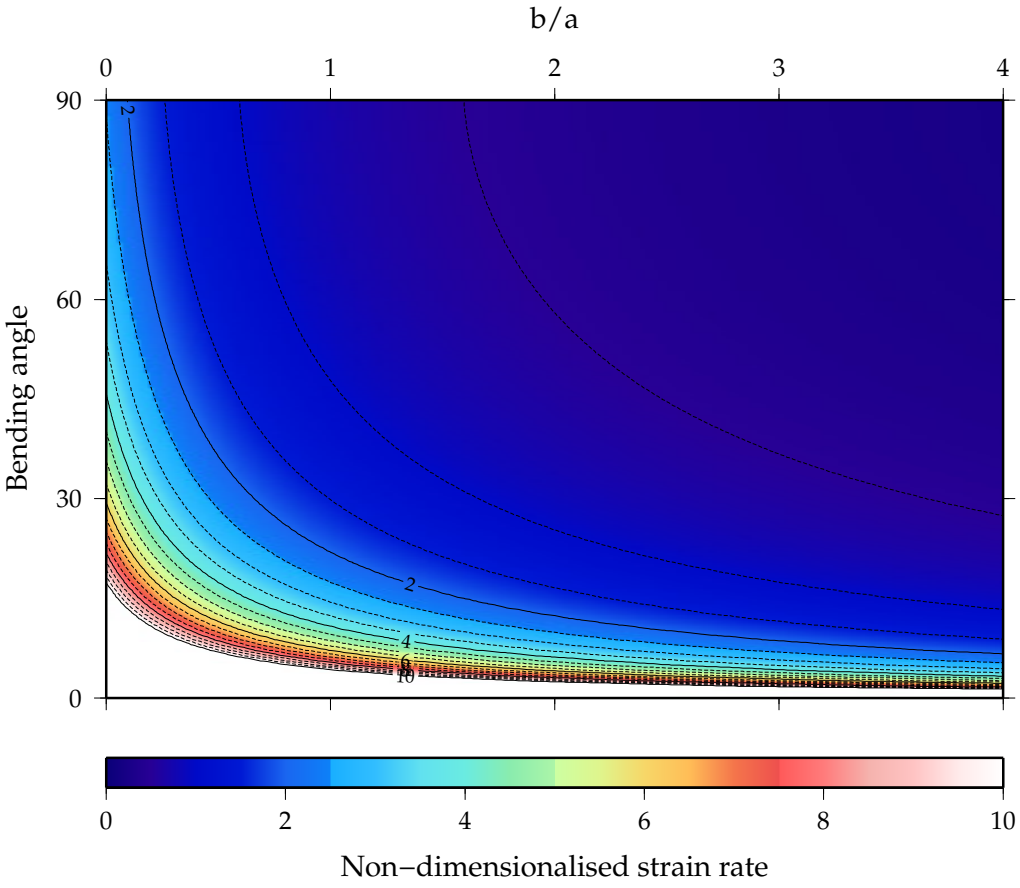

Figure 10.2: Non-dimensionalised strain rate for the bending beam model in Figure 10.1. To convert to strain rate as given in Equation 10.9, multiply by $\gamma v/a^2$.

modulus as they traverse the upper mantle. The expected value of μ for a equilibrium peridotite at 16 GPa (400–500 km depth) and 600°C is $\sim 1.3 \cdot 10^{11}$ Nm^{-2}, since $V_S = 5.8$ kms^{-1} and $\rho = 3957$ kgm^{-3} using the mineralogical model of Stixrude and Lithgow-Bertelloni (2011). Metastable persistence of olivine would reduce this to $\sim 1.0 \cdot 10^{11}$ Nm^{-2}. In the following analysis, $\mu = 1.3 \cdot 10^{11}$ Nm^{-2}. This high-end estimate may result in an underestimate of seismic strain rate.

The prefactor c in Equation 10.10 corrects the observed seismic strain rate such that the expression approximates the long term average strain rate. The two contributors to c are small, unobserved earthquakes and large, rare earthquakes. The value of c which accounts for small earthquakes when moment-frequency distributions obey the Gutenberg-Richter law is

$$c = \frac{M_{max}^{2-\beta}}{M_{max}^{2-\beta} - M_{min}^{2-\beta}} \tag{10.12}$$

where M_{min} and M_{max} are the scalar moments bounding consistently observed earthquakes. Because $\beta < 1$, small earthquakes contribute only a minor proportion of the total moment release, such that $c \sim 1$. Large, rare earthquakes are potentially a much more significant contributor to long term seismic moment release. In the 35 years covered by the gCMT catalogue, many areas may not have

experienced the largest earthquakes, such that estimates of seismic strain rate will be smaller than the long term average. Conversely, some regions may have experienced a larger earthquake than expected during a typical 35 year period, resulting in an overestimate of the long term seismic strain rate.

Even within the Wadati-Benioff zone, a proportion of the total strain may occur aseismically. The proportion is very difficult to assess without independent estimates of strain rate. From geometric considerations, Holt (1995) suggested that the aseismic contribution to strain within Wadati-Benioff zones is minor. The well-defined edge of most Wadati-Benioff zones suggests that the brittle-ductile transition is sharp, providing further evidence that most of the deformation within Wadati-Benioff zones occurs seismically.

Volumes V must be selected carefully to avoid underestimating strain rates. Wadati-Benioff zone thicknesses are often poorly constrained, so an alternative approach is to estimate volumetric strain rates per unit area, where the area is calculated on the surface of the slab. Rhombuses on the best fitting surface to seismicity are constructed using geodesic paths (Mitchell et al., 1987, see also Chapter 6), and their areas calculated from the lengths of the rhombus diagonals ($d_1 d_2/2$). Earthquakes are included in the analysis if they lie within the prism with rhomboid cross section.

10.3 Examples

10.3.1 Izu-Bonin

Cross sections perpendicular to the Izu-Bonin arc show a change in morphology along the length of the slab (Figure 10.3). In the south, the slab is almost vertical between 200 and 420 km, before bending in the mantle transition zone. The deepest earthquakes indicate that the slab becomes almost horizontal just above the 670 km discontinuity. Further north, the bend in the slab becomes shallower and less pronounced.

The densest seismicity is observed in parts of the slab undergoing bending. None of the earthquakes have in-plane T axes, which makes estimating the distance between the zone of seismicity and the zero-length-change surface (γ) difficult. Using a reasonable value of 20 km, an bending arc length $a = 100$ km and a subduction velocity of 8 cm/a, modelled strain rates due to bending at the southern end of the Bonin slab are $4 \cdot 10^{-15}$ s^{-1}. Further north, the decrease in bending angle largely counteracts the decrease in dip, keeping modelled strain rates at $\sim 3 - 4 \cdot 10^{-15}$ s^{-1}. These values are comparable to strain rates estimated from the distribution of seismicity, which, for a Wadati-Benioff zone width of 10 km are $10^{-16} - 10^{-14}$ s^{-1} (Figure 10.4). This order-of-magnitude variation in strain rates is likely to be due to the uncertainties described in §10.2.2. This hypothesis cannot easily be tested, and there appears to be little relationship between the estimated strain rate and proportion of the total moment release contributed by the largest earthquake in each subregion (Figure 10.4).

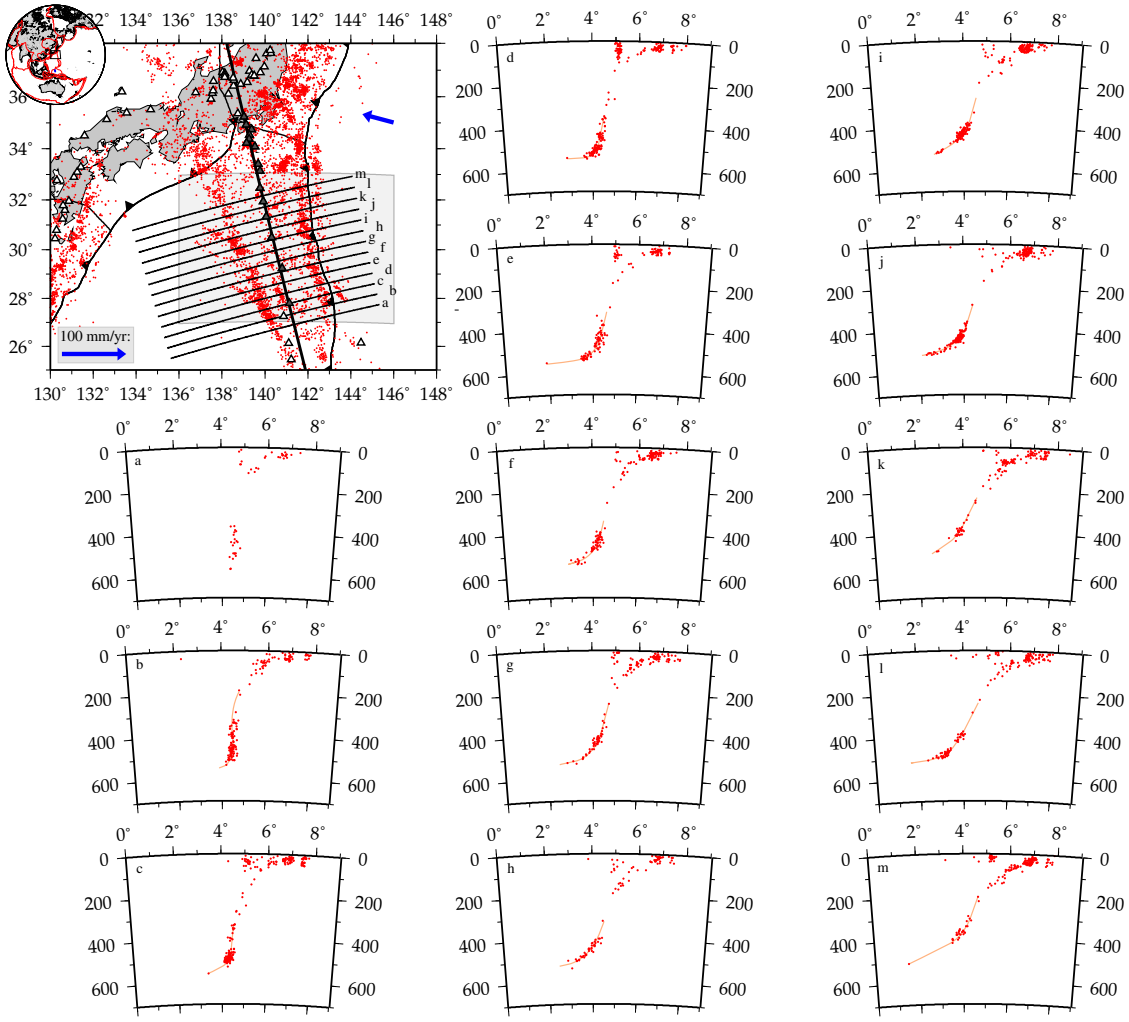

Figure 10.3: Cross sections through the Izu-Bonin subducting slab perpendicular to the arc. Distance between sections are 50 km, and section half-widths are 25 km. The map shows the plan view of the cross sections, the location of the trench and the best fit small circle to the Izu-Bonin arc. The shaded area corresponds to the region plotted in Figure 10.4.

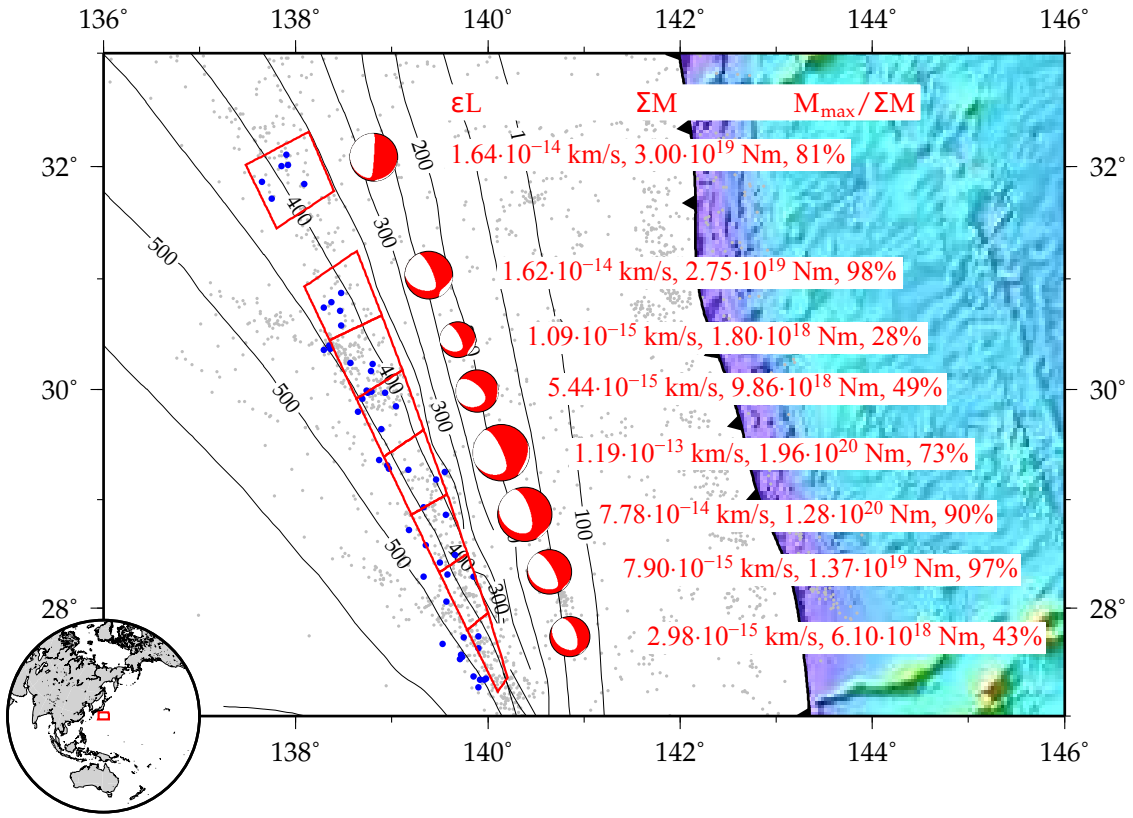

Figure 10.4: Estimates of seismic strain rate along the deep bend in the Izu-Bonin slab. Boxes show the individual areas on the slab surface selected for analysis. gCMT earthquakes that fall within the volume defined by each box are selected for analysis (blue events; as described in the text). Summed moment tensors are shown, and annotated with the estimated seismic strain rate multiplied by Wadati-Benioff zone thickness, the summed moment of all the selected earthquakes and the percentage of that sum contributed by the largest earthquake.

10.3.2 South Tonga

Like Izu-Bonin, the south Tonga slab is almost planar at 200-400 km depth. Unlike Izu-Bonin, there are two bends in the mantle transition zone, the first concave-up and the second convex-up. The bends become tighter and more angular to the north, until at about 23–24°S the Wadati-Benioff zone appears to split into two planes (Figure 10.5).

Making the assumption that the outboard slab fragment is almost stationary, the bending beam model can again be employed to estimate strain rates. Three down-dip extensional events some 30 km below the main plane of seismicity (Figure 5.9) suggest that the distance to the surface of zero-length change within the concave-up bend in the slab is on the order of 20 km. Since the bending parameters are similar to those chosen for the Izu-Bonin case study, the strain rates estimated from the kinematic model are also similar, at $2 - 5 \cdot 10^{-15}$ s^{-1}. Estimated seismic strain rates within the Wadati-Benioff zone are slightly lower than values from the kinematic model if the seismogenic layer is ∼10 km thick ($10^{-16} - 10^{-15}$ s^{-1}; Figure 10.6). The fraction of total moment released by the largest earthquake tends to be smaller than in the Izu-Bonin analysis, providing confidence in the seismic

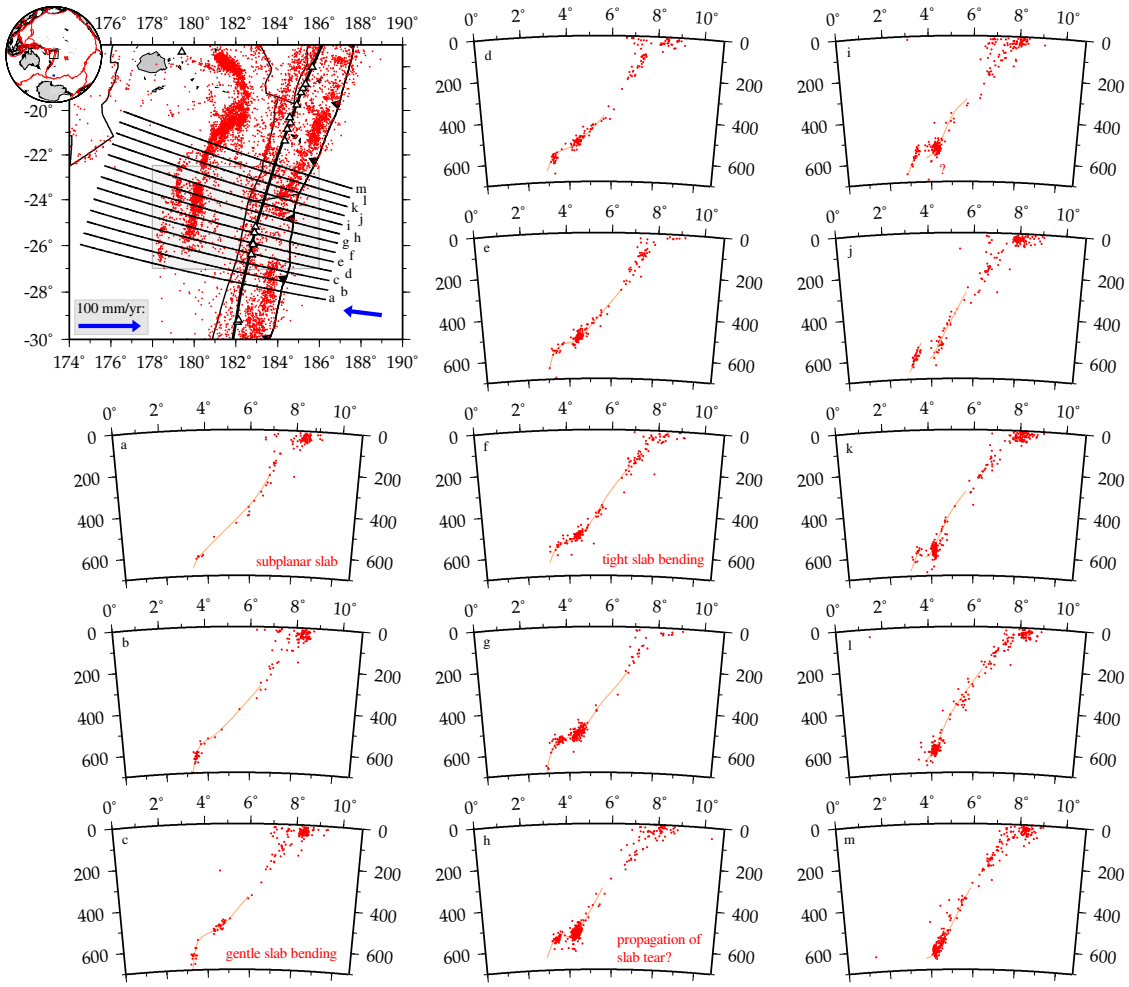

Figure 10.5: Cross sections through the southern end of the Tonga subducting slab perpendicular to the arc. Distance between sections are 50 km, and section half-widths are 25 km. The map shows the plan view of the cross sections, the location of the trench and the best fit small circle to the south Tonga arc. The shaded area corresponds to the region plotted in Figure 10.6.

estimates of strain rate within the south Tonga slab.

10.3.3 *North Tonga*

At the base of the Wadati-Benioff zone in north Tonga, different focal mechanisms appear at different depths within the slab (see §5.4.5). The majority of events indicate in-plane compression. The estimated seismic strain rate obtained from analysis of 46 events of this focal mechanism type is $\sim 6.5 \cdot 10^{-15}$ s^{-1}, assuming that the earthquakes occur in a zone 5 km thick as reported by Gesserman and Wiens (2010). The largest event accounted for 69% of the total $6.94 \cdot 10^{19}$ Nm moment release. Deeper within the slab, a diffuse cloud of down-dip P / slab-normal B events are observed. Seismic moments of 19 of these earthquakes sum to $3.29 \cdot 10^{20}$ Nm, corresponding to a strain rate of $\sim 10^{-14}$ s^{-1} for a zone 20 km thick. The largest event accounted for 93% of the total moment release, suggesting that large, rare earthquakes may be important contributors to total moment release in the deep north Tonga slab.

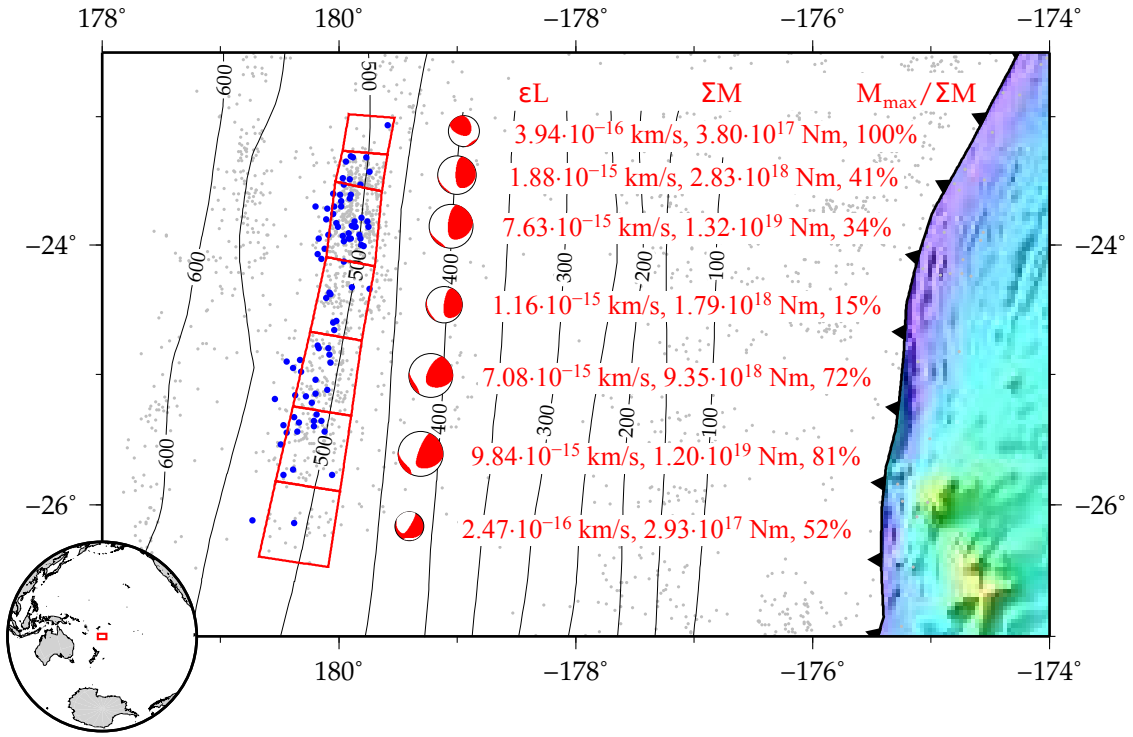

Figure 10.6: Estimates of seismic strain rate along the deep bend in the south Tonga slab. Boxes show the individual areas on the slab surface selected for analysis. gCMT earthquakes that fall within the volume defined by each box are selected for analysis (blue events; as described in the text). Summed moment tensors are shown, and annotated with the estimated seismic strain rate multiplied by Wadati-Benioff zone thickness, the summed moment of all the selected earthquakes and the percentage of that sum contributed by the largest earthquake.

Taken together, the seismic estimates of strain rate are slightly higher than the modelled values for a slab subducting at 10–12 cm/a and bending by an angle of 45° from the vertical where $\gamma = 15$ km, $a = 100$ km and $b = 50$ km ($\sim 10^{-14}$ s^{-1}). This difference is to some extent expected, since the focal mechanisms indicate that bending is not the only source of strain within the north Tonga slab. A proportion of strain from homogeneous in-plane compression comparable to that estimated from bending could explain both the discrepancies in strain rates and the distribution of focal mechanisms, as proposed in Chapter 5.

10.4 Discussion

10.4.1 Uncertainties

Seismic strain rates

The time period spanned by the gCMT and EHB catalogues may not be sufficiently long to provide a good estimate of long-term average strain rates within the deep Tonga and Izu-Bonin slabs. Large, rare earthquakes may account for a significant proportion of the total seismic strain rate. Two factors suggest that this problem is less severe for the regions chosen in this study than for subduction zones as a whole. Firstly, the areas chosen for seismic strain estimation are those with a high seismic

density. Whatever the physical mechanism of deep earthquakes, initiation of rupture appears not to be a problem in these areas. Secondly, the largest subduction zone earthquakes tend to occur in previously aseismic areas (Wiens and McGuire, 1995; Kirby et al., 1996, Figure 3.2). Perhaps more seismically active regions are incapable of producing earthquakes much larger than those observed over the last few decades. Nevertheless, it is possible that long term strain rates may be somewhat larger than those estimated here.

Errors in earthquake locations are a second source of uncertainty. Because slab areas are chosen to include all earthquakes within the high density areas, scatter will tend toward increases in volume and underestimates of seismic strain rate. However, this uncertainty is minor compared to that arising from poor constraints on Wadati-Benioff zone thickness. Within the Izu–Bonin slab, the 10 km estimate of seismogenic zone thickness is reasonable given the estimated rupture dimensions of some of the earthquakes (see Chapter 7). The 10 km estimated width of the south Tonga zone is more uncertain, but probably correct to within a factor of two.

The high pressure shear modulus used to calculate seismic strain rates may be too high, in which case estimated seismic strain rates are lower than true strain rates. Persistence of metastable phases, and shear heating or other mechanisms of weakening faulted material would both lower K_S. Nevertheless, the deviation from the used value is likely to be minor compared with other sources of error.

Model strain rates

The slab kinematics in this study are based on the assumption that the slab shape can be modelled as a flexible but inextensible membrane that was initially planar, i.e. a sheet that has zero gaussian curvature. Bevis (1986, 1988) suggested that the shapes of many slabs could not be approximated by modelling subducting plates in this way. Some slabs undergo significant along-strike membrane strains, such as the strongly curved Aleutian (Creager and Boyd, 1991) or Marianas (Bevis, 1986) slabs at intermediate depth, or the deep Tonga slab north of 21.5°S. Within the Izu-Bonin and Tonga slabs, gaussian curvature is almost zero, but this does not rule out homogeneous shortening. Indeed, the superposition of bending and compressional strains provides a simple explanation for some focal mechanisms in the deep Tonga slab (§5.4.5). Model strain rates should therefore be treated as minimum estimates.

The angle of the bend in the Izu-Bonin slab (Figure 10.3) is sometimes constrained by only a couple of earthquakes in each profile. This is not a significant source of uncertainty; the slab appears to be continuous, allowing adjacent profiles to be used to constrain slab shape. In addition, small changes in the angle of bending in the Izu-Bonin slab will have a relatively small effect on estimates of strain rate (Figure 10.2).

The uncertainties listed above suggest that the modelled and observed seismic strain rates in the current analysis should be treated as order-of-magnitude estimates. With this in mind, the results presented here provide good agreement between seismological and numerical models of strain rate within subducting slabs. In particular, they provide an important test for the idea that bending can reconcile seismic strain rates and subduction rates without requiring significant aseismic deformation or subduction into the lower mantle.

10.4.2 Strain in three dimensions

The summed moment tensors in Figures 10.4 and 10.6 reveal an apparent non-double-couple component. Beneath Bonin, the average P axes are associated with the extremal eigenvalues of the strain rate tensor. The relative magnitudes of the eigenvectors equate to a compensated linear vector dipole (CLVD) strain component of up to 36%. The same sign of CLVD component is observed in the majority of individual centroid moment tensors. Summed moment tensors in the south Tonga region reveal a similar apparent CLVD component (up to 35%), but here the T axes are associated with the extremal strain rate eigenvalue. CLVD components for individual earthquakes tend to be much smaller, with roughly equal numbers of positive and negative CLVD. The larger summed values largely reflect variation in individual focal mechanisms, rather than individual source properties.

CLVD components in summed moment tensors are less problematic than components in individual moment tensors. Variations in double-couple mechanism orientation can produce a strain field that could not be accomplished by faults in any single orientation. However, in individual moment tensors, a CLVD component implies data noise or error, that some aspect of waveform propagation has not been modelled satisfactorily (e.g. Tada and Shimazaki, 1994), or that the source cannot be adequately modelled by slip on a planar surface. Irregularity in fault zone orientation (Kuge and Lay, 1994), or the presence of more than one fault plane provide potential explanations for these observations. The consistent CLVD components in the Izu-Bonin slab rule out noise or data error, but without detailed synthetics incorporating realistic slab velocity structure and the same range of data types as used by the gCMT project, the relative importance of source geometry and local velocity cannot be determined.

10.4.3 Bending, strain rate and seismicity

The similarity between modelled and observed seismic strain rates in the Tonga and Izu-Bonin slabs suggest that bending is a significant source of strain in slabs within the upper mantle. More importantly, the results are consistent with seismic strain rates being of equal or greater importance than aseismic strain rates within deep seismogenic zones. A corollary of this suggestion is that after temperature, the factor most strongly governing whether a cold slab is seismic or not is the rate

of strain. Broad scale seismic distributions should not be used as evidence for any given physical mechanism of deep-focus earthquakes.

As discussed by Holt (1995) and Nothard et al. (1996a), the rate of down-dip shortening in the south Tonga slab is probably less than half of the total convergence rate. Without accounting for bending, this result suggests that either slabs penetrate into the lower mantle, or that deformation of the slab is largely aseismic. In contrast, bending of the slab can explain both the distribution of seismicity and the rate of seismic strain without requiring subduction into the lower mantle, consistent with tomographic studies that reveal normal or relatively low seismic velocities beneath the Tonga slab at 700–800 km depth (e.g. Kennett and Gorbatov, 2004).

10.4.4 Stress

If deep earthquakes allow subducting slabs to deform more quickly than would be possible via ductile mechanisms, then the strain rate at the transition between ductile and brittle deformation should correspond to the rate prescribed by the local stress, temperature and material flow laws governing the rheology of the slab.

Low stress dislocation and diffusion creep can be described by the following power-law formula:

$$\dot{\epsilon} = A\frac{\sigma^n}{d^m}C_{\mathrm{OH}}^r \exp\left(-\frac{H^*(C_{\mathrm{OH}},P)}{RT}\right) \tag{10.13}$$

where $\dot{\epsilon}$ is the strain rate, A, r, n and m are constants, σ is the deviatoric stress, d is grain size, C_{OH} is hydrogen content (1.0 if dry), $H^* = E^* + PV^*$ is the activation enthalpy for creep, P is pressure, R is the gas constant and T is the temperature. The values of n and m depend on the dominant mechanism of plastic flow. For diffusional creep, $n = 1$ and $m = 2 - 3$, and for dislocation creep, $n = 3 - 5$ and $m = 0$ (see Table 19.1 of Karato (2008) for flow laws of common Earth materials). At higher stresses ($\sigma/\mu > 10^{-3}s^{-1}$) the influence of stress on thermal activation becomes significant. At low temperatures, dislocation climb is inhibited and plastic deformation is governed by the dislocation glide 'Peierls' mechanism, which can be expressed in the form

$$\dot{\epsilon} = B(C_{\mathrm{OH}})\sigma^n \exp\left(-\frac{H^*(C_{\mathrm{OH}},P)}{RT}\left[1-\left(\frac{\sigma}{\hat{\sigma}(C_{\mathrm{OH}},P)}\right)^q\right]^s\right) \tag{10.14}$$

where $\hat{\sigma}$ is the Peierls stress. Two expressions for low temperature plasticity in dry olivine have been published. Raterron et al. (2004) parameterise Equation 10.14 with the values $B = 2.6 \cdot 10^{16}$ s^{-1}, $H^* = 564 \pm 89$ kJ mol^{-1}, $\hat{\sigma} = 15.4 \pm 1.0$ GPa, $n = 0$, $q = 0.667$, and $s = 2$.

In contrast, Mei et al. (2010) suggest that $B = 1.4 \cdot 10^{-7}$ $s^{-1}MPa^{-2}$, $H^* = 320 \pm 50$ kJ mol^{-1}, $\hat{\sigma}_{II} = 5.9 \pm 0.2$ GPa, $n = 2$, $q = 0.5$, and $s = 1$. The total strain rate is the sum of the strain rates due to each process

$$\dot{\epsilon} = \dot{\epsilon}_{diff} + \dot{\epsilon}_{dis} + \dot{\epsilon}_{Peierls} \tag{10.15}$$

Using the dry olivine flow laws for diffusion (Faul and Jackson, 2007), high temperature dislocation glide and climb (Kawazoe et al., 2009) and low temperature dislocation glide (Peierls mechanism) (Raterron et al., 2004; Mei et al., 2010), relationships between strain rate, stress and temperature can be derived (Figure 10.7). Deformation at high pressure and low temperature is mostly accommodated by dislocation creep.

For slabs in the mantle transition zone, where seismicity ceases at $\sim 800°C$ (Chapter 9) and deviatoric stresses are on the order of 100–200 MPa (Alisic et al., 2010, and references therein), the low-temperature high-pressure flow law of Raterron et al. (2004) predicts a slab that is too weak to be governed by brittle deformation at strain rates of $\sim 10^{-14}$ s^{-1}. In contrast, a mantle rheology just slightly weaker than that proposed by Mei et al. (2010) would adequately explain seismic strain rates and distributions in the mantle transition zone. The agreement between seismic and rheological estimates of strain rate provides tentative support for the hypothesis that the dynamics of subducting slabs are governed by their ability to deform seismically. Nevertheless, material flow laws and changes in rheology during subduction and accompanying metamorphism clearly need to be constrained more tightly before any definite statements can be made.

The uncertainty in rheological models and estimates of deviatoric slab stresses implies that comparisons of seismicity with results obtained from finite element modelling should be treated with caution. Even if suitable boundary conditions can be found, several other aspects of modelling present significant problems. Slab shapes must be modelled with care, preferably using earthquake focal mechanisms and moment release as a guide (and therefore in some ways prescribing the eventual results). The temperature dependence on rheology is extremely important, so accurate thermal models must be incorporated into any geodynamic simulations. Finally, the behaviour of the region undergoing brittle failure may not be satisfactorily approximated by either a constant viscosity or a constant stress rheology, both of which are commonly used in numerical modelling. This may explain why surprisingly weak viscous rheologies are required to match slab deformation in numerical models (e.g. Zhong and Gurnis, 1995); it is not the viscous rheology that controls the deformation of cold slabs, but the brittle behaviour of the strong slab core. Highly viscous slabs are not at odds with geoid highs above subduction zones such as Tonga (e.g. Moresi and Gurnis, 1996; Zhong and Davies, 1999), because brittle deformation of the cold slab core results in an apparently weaker slab.

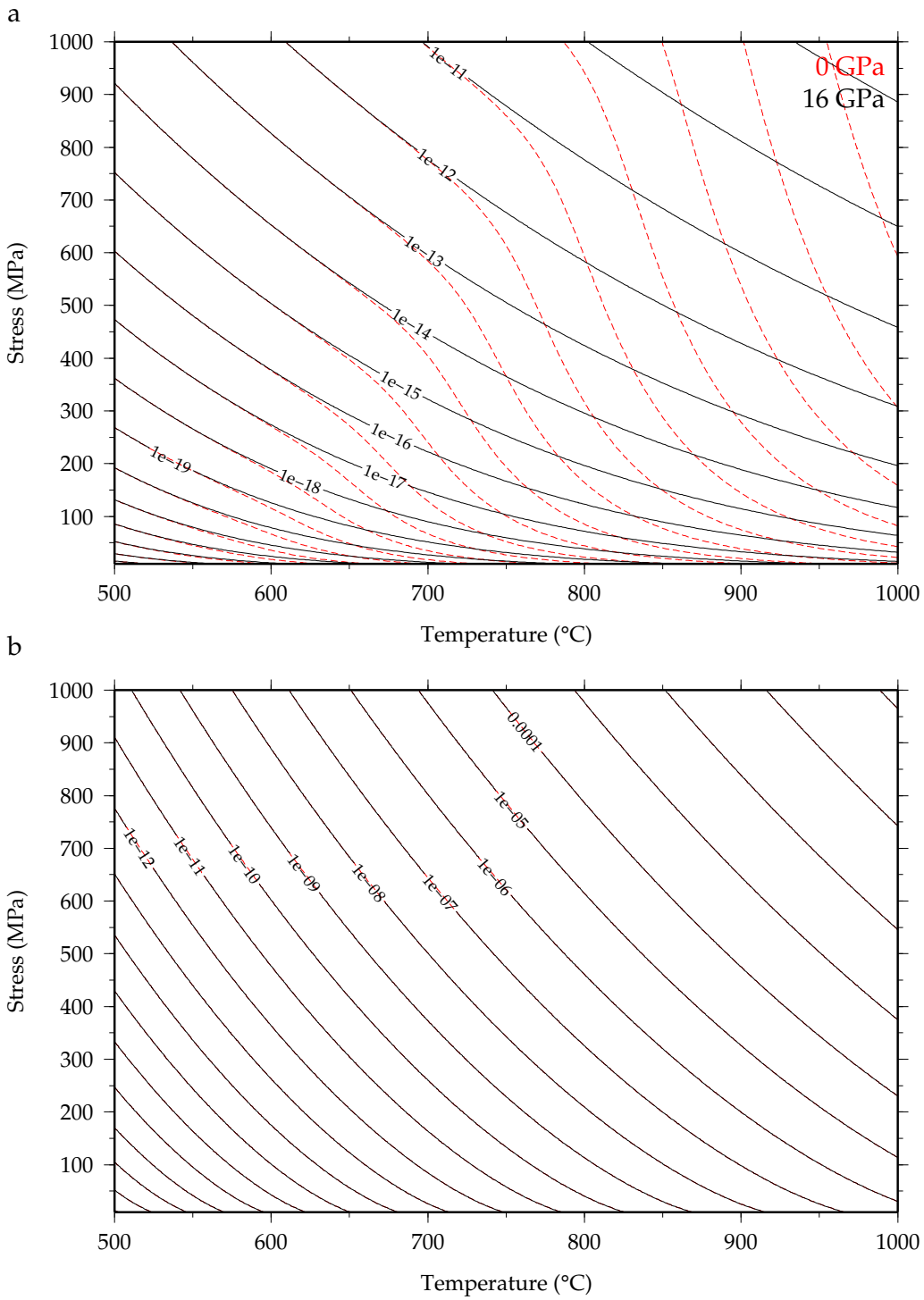

Figure 10.7: Dry olivine strain rates (in s^{-1}) at given stresses and temperatures. a) Using the diffusion flow law of Faul and Jackson (2007), high temperature dislocation glide and climb flow law of Kawazoe et al. (2009) and low temperature dislocation glide (Peierls) flow law of Mei et al. (2010) at 0 and 16 GPa. b) The same as a, but using the Peierls mechanism flow law of Raterron et al. (2004). The grain size is 0.03 m, but as grain-size-independent dislocation creep is the dominant mechanism of flow at high stress, changing the grain size has little effect on the calculated strain rates.

10.5 Conclusions

A simple kinematic model of bending within subducting slabs yields strain rates which are similar to estimates of seismic strain in the south Tonga and Izu-Bonin slabs. Bending may therefore have a considerable effect on seismic activity in the mantle transition zone.

Rates of slab shortening are often slow compared with convergence rates. The ability of slabs to change shape reconciles these two values, by allowing convergence to be taken up by rotation and translation in addition to thickening. Bending also explains the presence of double seismic zones (Wiens et al., 1993) and in-plane extensional deep-focus earthquakes in the Tonga and Solomons slabs.

Applying the kinematic model to the base of the north Tonga slab produces a strain rate estimate which is at the low end of seismic strain estimates. This is consistent with a mixture of bending and whole-slab compression accounting for the total strain in the slab. This interpretation is supported by the range of focal mechanisms, which include along-hinge extensional events (Chapter 5).

Estimated strain rates at the brittle-ductile transition are similar to the strain rates obtained by some experimentally-derived high pressure-low temperature flow laws. Much more work needs to be carried out to fully characterise the rheology of upper mantle rocks at low temperatures, but existing data suggests that stress and temperature play the dominant roles in determining the distribution of seismicity in subducting slabs.

Part IV

Discussion

11 Toward a physical mechanism of deep earthquakes

11.1 Introduction

The observations and analysis presented in the previous chapters integrate information from earthquake locations, mechanisms and rupture processes to provide a framework from which potential explanations can be tested. I have shown that the majority of deep-focus earthquake characteristics can be explained using only the concepts of negative buoyancy, resistance to flow and the resulting deformation of subducting slabs.

Since earthquake behaviour can largely be explained by deformation, two questions arise. Firstly, are there observations which cannot be explained through consideration of the simple kinematics of subducting slabs? Secondly, what else can the seismological observations tell us about the processes, mechanisms and conditions required for deep earthquakes to occur? In the following chapter, I will briefly address these two questions.

11.2 Existing constraints on the physical mechanism of deep earthquakes

Numerous studies have attempted to provide a link between seismic observations and the physical mechanism (or mechanisms) of deep earthquakes. The continuing support for transformational faulting, thermal runaway and dehydration embrittlement suggest that none of the links are conclusive, or even particularly convincing. A summary of key observations is presented in Table 11.1, along with potential mechanism-specific explanations for each. The last column is dedicated to mechanism-independent explanations. Observations of stress drop have not been included because of the large uncertainties inherent in determining the areal extent of the fault and the distribution of slip over the fault (Frohlich, 2006).

Many seismic observations can be explained without resorting to mechanism specific interpretations. The distribution of seismic activity, variation in focal mechanisms, presence of deep-focus double seismic zones, and potentially even the distinct patterns of fault plane orientations can be explained independently of the exact mechanism of deformation.

The relationship between the focal mechanism of the earthquake and the local stress field, rupture

Observation of deep seismicity	Mechanism-specific explanation for the observation			Mechanism-independent explanation
	Fluid embrittlement	Shear instability	Transformational faulting	
Size	Pervasive fluids	Scaling unknown	Scaling unknown	Dependent on rheology and the distribution of stress
Rupture velocity	Pervasive fluids	Large areas approaching conditions for instability concurrently	Closely spaced anticracks	
Uneven distribution of moment release	Location of fluids	Compositional dependence on rheology	Compositional dependence on transformation	Rheology / stress / strain control?
Double seismic zones	Thermally controlled (Hacker et al., 2003)	Thermally controlled (Karato et al., 2001)	Thermally controlled (Wiens et al., 1993)	Stress / strain control
Fault-like seismic structures (small scale, not reactivated)	Accumulation of fluids in fine-grained shear zones (Kiser et al., 2011)	Temporary weakening by thermal runaway (e.g. Wiens and Snider, 2001)	—	Grain size reduction, transient stress changes
Fault-like seismic structures (large scale, possible reactivation)	Surface formed faults prone to hydration (Nakajima and Hasegawa, 2006)	Composition or grain size promoting shear	Grain-size dependence on transformation?	Rheological variation due to compositional or grain size changes
Paucity (but presence) of aftershocks / swarm-like behaviour	Slow fluid migration (Frohlich, 2006, p279)	Decay of heat anomaly (Wiens and Snider, 2001)	Consumption of metastable olivine (Persh and Houston, 2004)	Stress, strain; increased rate of stress relaxation at high temperature
Delayed earthquake triggering	Near-critical faults (Tibi et al., 2003)	Complex nonlinear time dependent shear (Tibi et al., 2003)	Nonlinear rheology and development of microcracks (Green, 2003)	
Double couple source mechanisms	Slip on faults (e.g. Dobson et al., 2004)	Localisation of shear (Ogawa, 1987)	Fault-like slip on joined-up anticracks (Green and Burnley, 1989)	
Orientation of focal mechanisms at $\sim 45^\circ$ to maximum compressive stress	Dependent on friction coefficient along the fault (0.6 close to the surface; Byerlee, 1978) although possibly $\lesssim 0.1$ just 10–20 km down (Copley et al., 2011)	Shear develops along fine grained reaction zones	Anticracks form perpendicular to σ_1, and faults at $\sim 30^\circ$ to σ_1 in germanate (Green and Burnley, 1989) and silicate olivine (Green et al., 1990)	
Subhorizontal orientation of fault planes	Preferential fluid accumulation along shallowly-dipping fine-grained shear zones (Kiser et al., 2011)	—	—	Simple shear due to bending and other external forces, (e.g. Suzuki and Kasahara, 1996)
Global depth distribution and restriction of deep-focus earthquakes to cold slabs	*P-T* controlled via breakdown of hydrous phases (Omori et al., 2004)	Rheology controlled (Karato et al., 2001)	Olivine metastability (Kirby et al., 1996)	Rheology dependent
Cessation of seismic activity at ~ 700 km depth	—	High conductivity inhibits the initiation and propagation of a dynamic instability (Hobbs and Ord, 1988)	Olivine $\rightarrow$ perovskite + ferropericlase isn't accompanied by anticrack formation (Gleason and Green, 2009)	Change in rheology or stress in the more viscous lower mantle

Table 11.1: Deep-focus earthquake observations and some potential explanations, categorised according to the underlying physical mechanism of faulting. Many observations can be explained without appealing to a specific mechanism. The majority can be explained in a variety of different ways.

velocity and delayed earthquake triggering are identified as observations which are dependent on the mechanism of faulting (Table 11.1). Unfortunately, there are potential explanations explaining the observations for each of the proposed mechanisms. Assessing the viability of each mechanism is difficult because of the large differences in strain rates and scales between experimental studies and deep earthquakes, and the difficulties involved in invoking brittle deformation at high pressure. Multi-anvil and diamond-anvil presses commonly deform samples up to a few mm in diameter. Large thermal gradients are common across cm-scale samples in the larger presses. Careful experimental work may be successful in ruling out the presence of fluids in the seismically active parts of Wadati-Benioff zones if it can be demonstrated that water solubility increases with continuing subduction. Ruling out either of the other mechanisms may be significantly harder, since scaling up experimental reaction rates and flow laws to kilometer-scales is challenging.

11.3 Similarities and potential feedbacks between mechanisms

An attractive idea is that all earthquakes are somehow related. The presence of open cracks distinguishes the fluid-related embrittlement hypothesis from the other two mechanisms, but otherwise the three mechanisms are all closely related, relying on the existence and development of a weak 'fluid-like' material along narrow sub-planar features. The similarity of Griffiths cracks and the anticracks of transformational faulting provides an elegant explanation for similarities between deep and shallow earthquakes even for very different mechanisms. It has even been suggested that both shallow and deep earthquakes are explained by plastic shear, rather than elastic stick-slip behaviour (Roberts and Turcotte, 2000).

Since all three mechanisms share many similarities, it may be that more than one mechanism is responsible for the seismic activity observed at depth. Figure 11.1 shows potential relationships between the different hypotheses.

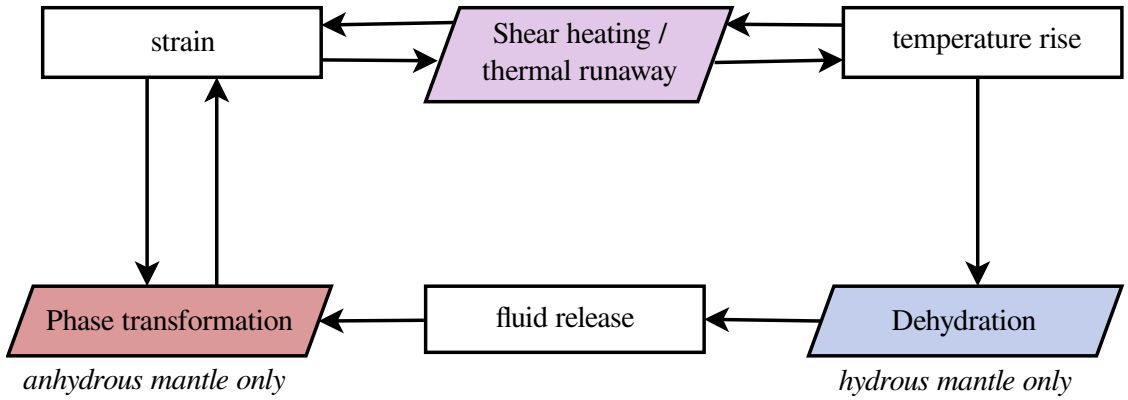

Figure 11.1: Flow chart describing the potential links between different mechanisms for deep-focus earthquakes. Anhydrous and hydrous mantle labels correspond to the local conditions within the slab, and do not imply homogeneity in slab chemistry. For example, rising temperatures could trigger dehydration and fluid release into previously anhydrous slab material, accelerating phase transformation.

11.4 Similarities between shallow and deep earthquakes

Even without a clear understanding of the physical mechanism of deep earthquakes, the observations presented throughout this dissertation provide important constraints on the mechanics of faulting. They add to many other observations of deep seismicity that fail to reveal significant differences between shallow and deep slabs. Deep earthquake activity is stress, strain and temperature controlled. Shallow earthquakes have a similar range in magnitudes and estimated stress drops (see discussion in Frohlich, 2006) and comparable non-double-couple components. Even commonly cited differences between shallow and deep seismic activity, such as rupture velocities and aftershock frequencies, are so variable within subducting slabs (and elsewhere) that the pressure dependence on these processes is almost entirely unconstrained.

Many of the problems traditionally reserved for discussions about deep earthquakes apply equally to some shallow earthquakes. A well-constrained example is the 2001 Bhuj earthquake (Copley et al., 2011). The mainshock rupture propagated from $\sim$ 25 km depth to the surface with up to 14 m of slip at $\sim$ 15 km depth. The estimated stress drop for this earthquake (35 MPa) corresponds to an apparent coefficient of friction ($\mu = \tau/\sigma_n$) of 0.08 ± 0.02. The stress drop reveals that deviatoric stress was high prior to the Bhuj earthquake, but apparently much lower than that required to accommodate failure by slip on strong faults (Byerlee, 1978). The problem is identical to that of deep earthquakes; is brittle failure governed by high pore fluid pressure, weak fault rocks, or is there something more fundamentally wrong with our present understanding of fault mechanics? As a result of the similarities between shallow and deep earthquakes, it is tempting to suggest that by constraining the behaviour of more directly observable earthquakes like the shallow Bhuj event, deeper seismicity will also become better understood.

12 *Concluding remarks*

Deep earthquakes have presented a problem for geologists, geophysicists and materials scientists since before the birth of plate tectonics. Although origin times and locations are well-constrained by geophysical techniques, why and how brittle failure occurs at high pressure remains unknown. This dissertation has sought to determine the environmental and geological conditions that govern where deep earthquakes do and do not occur, and the factors that control their source properties.

A major theme of this dissertation has been to produce a framework from which to understand seismic strain in subducting slabs. Location data, focal mechanism information and fault plane orientations all provide complementary information relating to deformation. Negative buoyancy and resistance to flow from a viscosity jump at the upper-lower mantle boundary appear to be the primary contributors to deep earthquake activity. The realisation that earthquakes cluster around parts of the slab that have become warped and are continuing to deform (Chapters 5 and 10) is a logical extension to the classic study by Isacks and Molnar (1971). The variation of focal mechanisms reported by Apperson and Frohlich (1987) is an expected result of the variation in slab morphologies. The dominance of subhorizontal and westward dipping faults beneath Izu-Bonin and the Marianas can also be explained by resistance to westward motion imposed by the lower mantle (Chapter 7). The insights gained from an integrated study of earthquake behaviour provide a coherent alternative to the multitude of other explanations proposed to explain the global depth distribution of seismicity.

The differences in seismic activity between slabs can largely be understood by combining the concept of slab bending with results from thermal modelling. Bending of cold slabs results in broad, dense zones of seismicity. As a result of the high conductivity of mantle minerals at low temperatures, the temperature variations in Wadati-Benioff zones in cold slabs are probably $\lesssim$100 K, despite often being 30–50 km wide (Chapter 9). In warmer slabs such as those beneath the Solomons, South America and New Zealand, ductile creep can account for higher strain rates, so slabs are generally aseismic. Areas of intense bending or buckling induce faulting along narrow bands. The continuity of these slabs is difficult to confirm, since both high quality, high resolution images of the 3D velocity and attenuation structure of the upper mantle and a detailed understanding of how different structures might affect these images are required. However, bending provides a much more coherent explanation for the lineations of seismicity than long, narrow slivers of lithosphere which

have somehow become detached from the shallower slab.

The preceding synthesis does not address the possibility that slabs in the mantle transition zone are materially weak enough to accommodate high strain rates without faulting, such that faulting is not a requirement of the kinematics, but rather a consequence of the conditions required by the physical mechanism allowing brittle rupture. There is evidence to suggest that this isn't the case. Folding of the Indian oceanic lithosphere at wavelengths of 100–300 km and amplitudes of $\lesssim$1 km (McAdoo and Sandwell, 1985; Krishna et al., 2001) indicates that oceanic lithosphere before subduction is strong (Beekman et al., 1996; Gerbault, 2000). Bevis (1986, 1988) showed that seismic strain rates accounted for a significant proportion of the strain expected from slab bending at 75–175 km depth. Significant material weakening might be expected across the equilibrium olivine $\rightarrow$ wadsleyite transition (Karato et al., 2001), but beneath Marianas and the north Kuriles, where transition-zone seismicity is divorced from changes in slab shape, there is only a minor and sporadic increase in seismic activity, an observation which doesn't support a drastic change in rheology. My opinion is that the cold parts of oceanic lithosphere are materially strong throughout the upper mantle.

A small proportion of deep-focus earthquakes may provide a unique insight into the physical mechanism allowing them to occur. The streaks of seismicity within the Izu-Bonin and stagnant Vitiaz slabs are apparently unrelated to bending or unbending, so their distributions imply some mineralogical, chemical or grain size control on the distribution of seismicity (Chapter 6). At intermediate depths, dehydration is commonly invoked to explain clustering of seismicity along subducted fracture zones or seamount chains, but phase relationships at mantle transition zone pressures remain too uncertain to make similar inferences at greater depths. The orientations of the streaks of seismicity may be consistent with subducted fracture zones, but these features are not seismically active at intermediate depths, making the link to pre-subduction structures difficult. These unusual events are worthy of further study.

The similarities between deep earthquakes and their shallow intraplate counterparts are remarkable. Apart from the obvious change in setting, from low pressure flat lying lithosphere to contorted dipping slabs, most observations can be explained as at shallow depths. Even rupture velocities and aftershock productivity, commonly cited as marking a difference between shallow and deep earthquakes are extremely variable, and may be related more closely to temperature than pressure or the physical mechanism of faulting.

Part V

Appendices

A Clustering

Let us define a matrix **M**, such that the elements of the matrix are the cross correlation coefficients between waveforms i and j. One example might be:

Table A.1: Example correlation matrix

	1	2	3	4
1	1.0	0.2	0.9	0.6
2	0.2	1.0	0.2	0.5
3	0.9	0.2	1.0	0.8
4	0.6	0.5	0.8	1.0

A dissimilarity matrix $\mathbf{K^0}$ is constructed from the cross correlation matrix **M** (Equation A.1).

$$K_{ij} = 1 - M_{ij} \tag{A.1}$$

The smallest element from this matrix K^0_{ij} (with $i \neq j$) is chosen (in this case K^0_{13}), and a fusing vector $\mathbf{k}^1$ constructed, effectively merging the two events into one cluster. For N events, and where $m = 1 : N$, Rowe et al. (2002) construct each element of the vector by using the equation

$$k^1_m = \alpha_1 K^0_{im} + \alpha_2 K^0_{jm} + \beta K^0_{ij} + \gamma \left| K^0_{im} - K^0_{jm} \right| \tag{A.2}$$

The coefficients of Equation A.2 are variable. The α coefficients determine the relative importance of the two fused events, whilst β governs the spatial relationships of the clustering hierarchy. When β approaches -1, the system is dilated, similar to complete linkage schemes. Conversely, when β approaches 0, the system is contracted, similar to single linkage schemes. An automated clustering scheme requires that successive minimum values of the dissimilarity matrix increase monotonically. This constraint is satisfied when $\alpha_1 + \alpha_2 + \beta = 1$. We have clustered events using the group mean hierarchical method, where $\alpha_1 = x(i)/x(i,j)$, $\alpha_2 = x(j)/x(i,j)$, $\beta = \gamma = 0$ and $x(i)$, $x(j)$ and $x(i,j)$ represent the number of events in the ith, jth and combined (i,j) groups respectively, to ensure that there is no preference for small or large clusters. The vector $\mathbf{k}^1$ is then added as an extra row and

column to $\mathbf{K^0}$ (Table A.2). In this first step, $\alpha_1 = \alpha_2 = 1/2$, as both groups have only one element.

Table A.2: Matrix during fusion of first two elements (1 and 3)

	1	**2**	**3**	**4**	$\mathbf{k}^1$
1	0.0	0.8	0.1	0.4	$0.0\alpha_1 + 0.1\alpha_2 + 0.1\beta = 0.05$
2	0.8	0.0	0.8	0.5	$0.8\alpha_1 + 0.8\alpha_2 + 0.1\beta = 0.8$
3	0.1	0.8	0.0	0.2	$0.1\alpha_1 + 0.0\alpha_2 + 0.1\beta = 0.05$
4	0.4	0.5	0.2	0.0	$0.4\alpha_1 + 0.2\alpha_2 + 0.1\beta = 0.3$
$\mathbf{k}^1$	0.05	0.8	0.05	0.3	0.0

After the new matrix has been created, the two rows and two columns i and j (**1** and **3** in our example) are removed, creating a new dissimilarity matrix $\mathbf{K}^1$. The same procedure is undertaken with this matrix, and each successive new matrix $\mathbf{K}^g$ at step g until all events have been fused. Table A.3 illustrates the second step of the fusion process for the example data and chosen coefficients. The ith group contains 1 element (event 4), whilst the jth contains 2 (events 1 and 3), so $\alpha_1 = 1/3$ and $\alpha_2 = 2/3$. Columns **4** and $\mathbf{k}^1$ are removed.

Table A.3: Matrix during the second fusion (event 4 to events 1 and 3)

	2	**4**	$\mathbf{k}^1$	$\mathbf{k}^2$
2	0.0	0.5	0.8	$0.5\alpha_1 + 0.8\alpha_2 + 0.3\beta = 0.7$
4	0.5	0.0	0.3	$0.0\alpha_1 + 0.3\alpha_2 + 0.3\beta = 0.2$
$\mathbf{k}^1$	0.8	0.3	0.0	$0.3\alpha_1 + 0.0\alpha_2 + 0.3\beta = 0.1$
$\mathbf{k}^2$	0.7	0.2	0.1	0.0

There are now two clusters (represented by row and column vectors **2** and $\mathbf{k}^2$), which are finally fused at a dissimilarity value of 0.7. In order to select clusters of similar waveforms we choose a minimum correlation value ϵ (0.85 for the bulk of analysis in this paper). Clustering stops when the minimum dissimilarity value within the matrix exceeds $1 - \epsilon$, yielding a collection of single and fused waveforms constituting the clusters to be compared.

B Directivity modelling results

B.1 Izu-Bonin

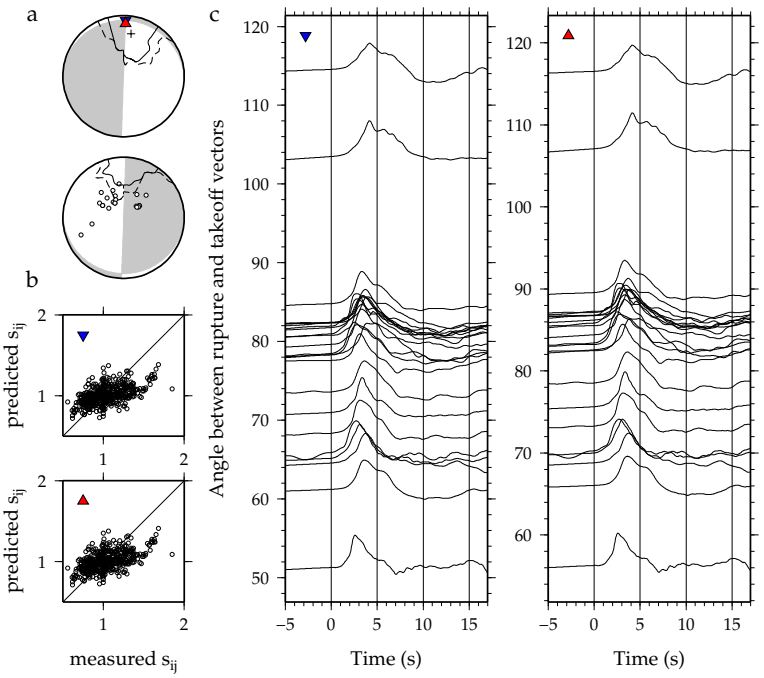

Figure B.1: Results for the 11 October 1993 (15:54:22.30) earthquake.

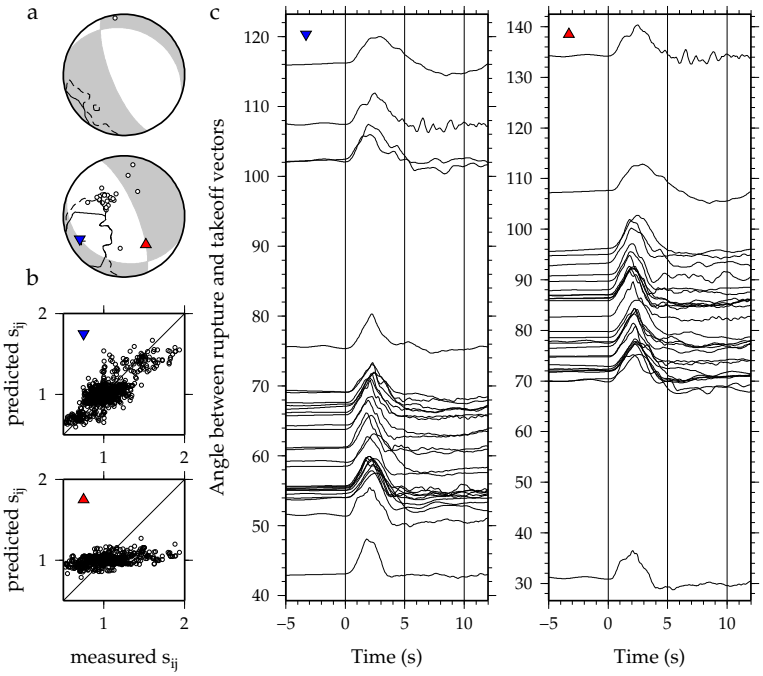

Figure B.2: Results for the 26 June 1996 (03:22:04.10) earthquake. Subplots are as described in Figure B.1.

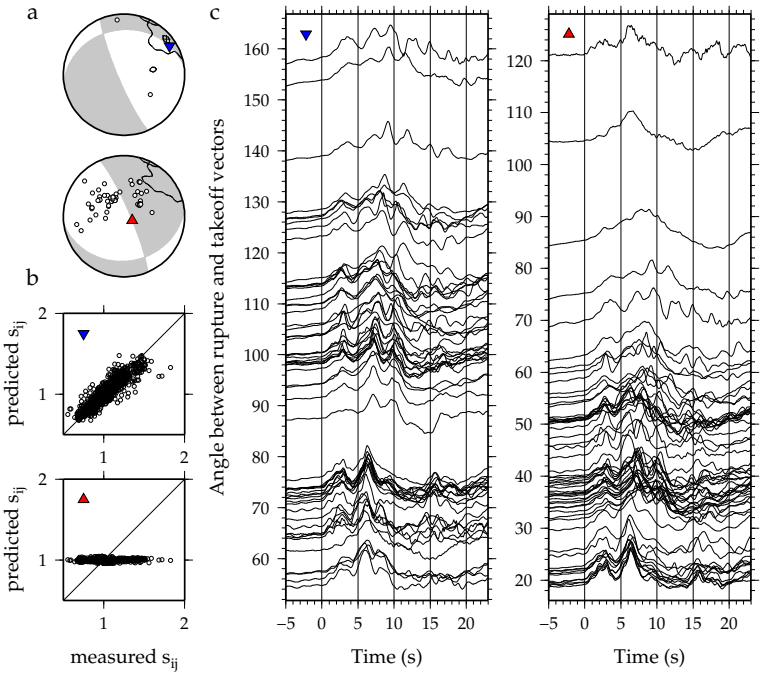

Figure B.3: Results for the 20 August 1998 (06:40:55.50) earthquake. Subplots are as described in Figure B.1.

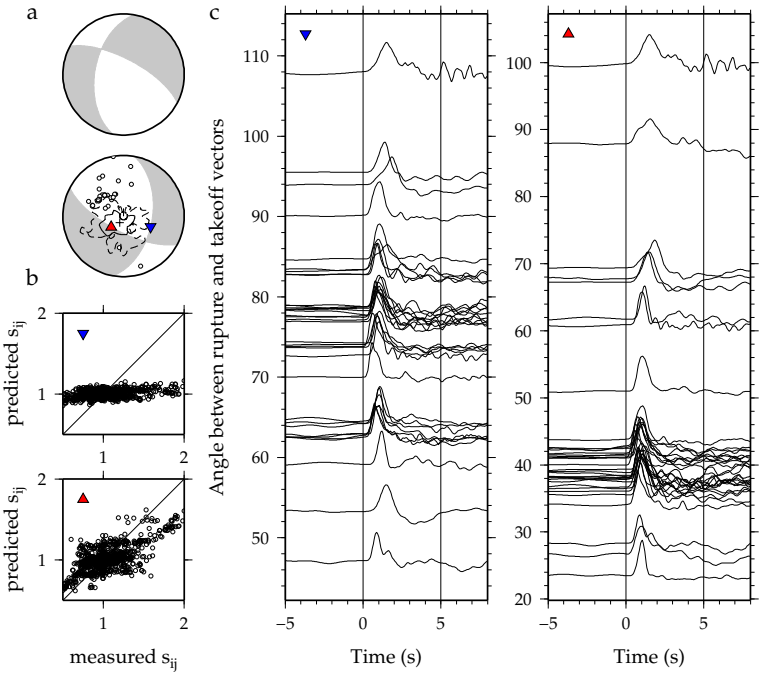

Figure B.4: Results for the 12 January 1999 (02:32:26.60) earthquake. Subplots are as described in Figure B.1.

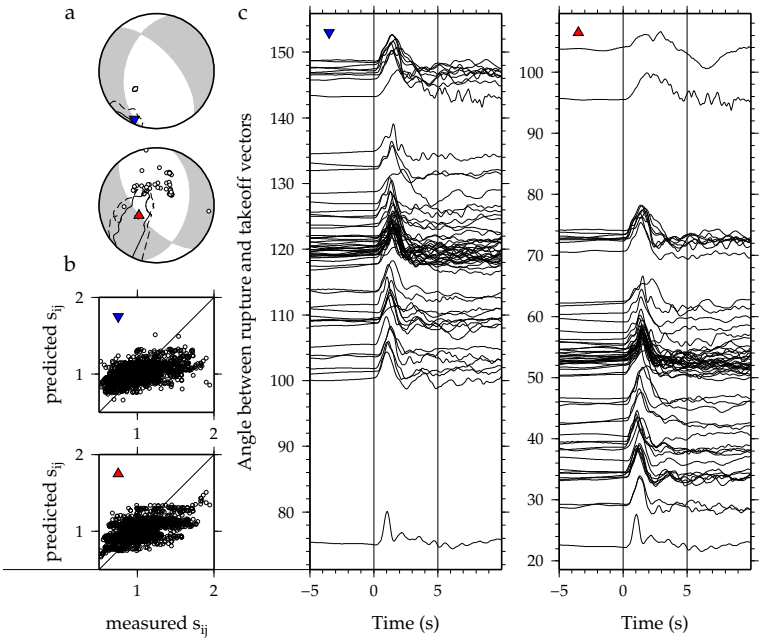

Figure B.5: Results for the 3 July 1999 (05:30:11.20) earthquake. Subplots are as described in Figure B.1.

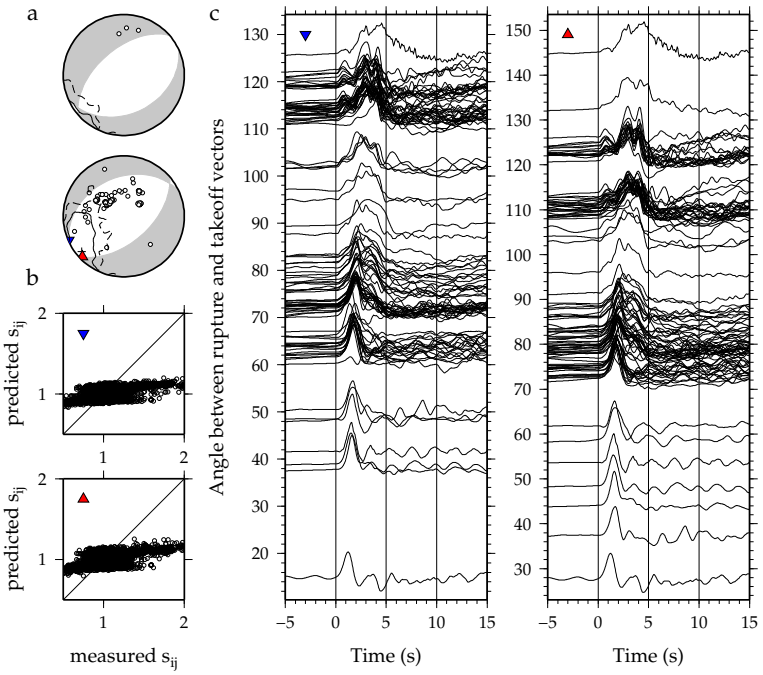

Figure B.6: Results for the 9 June 2000 (23:31:45.90) earthquake. Subplots are as described in Figure B.1.

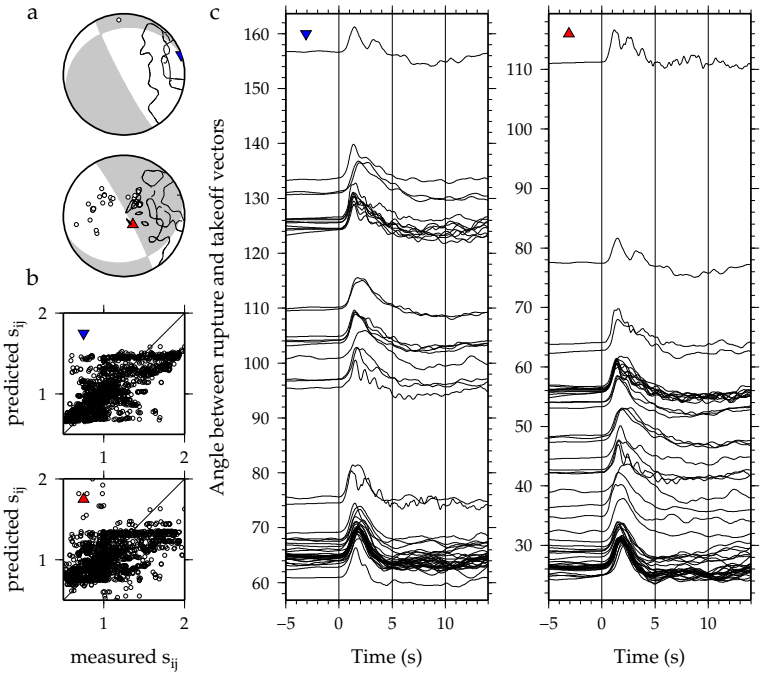

Figure B.7: Results for the 2 August 2002 (23:11:39.40) earthquake. Subplots are as described in Figure B.1.

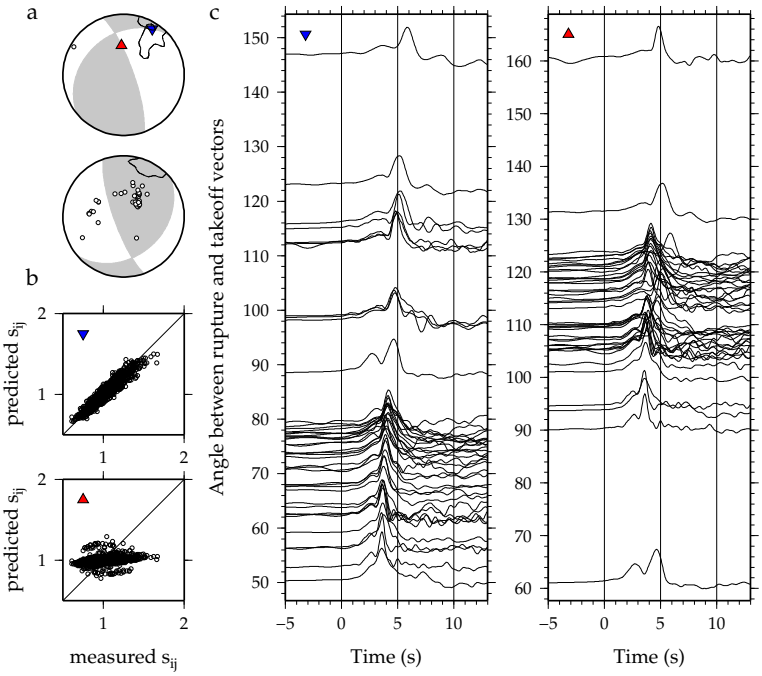

Figure B.8: Results for the 12 November 2003 (08:26:44.70) earthquake. Subplots are as described in Figure B.1.

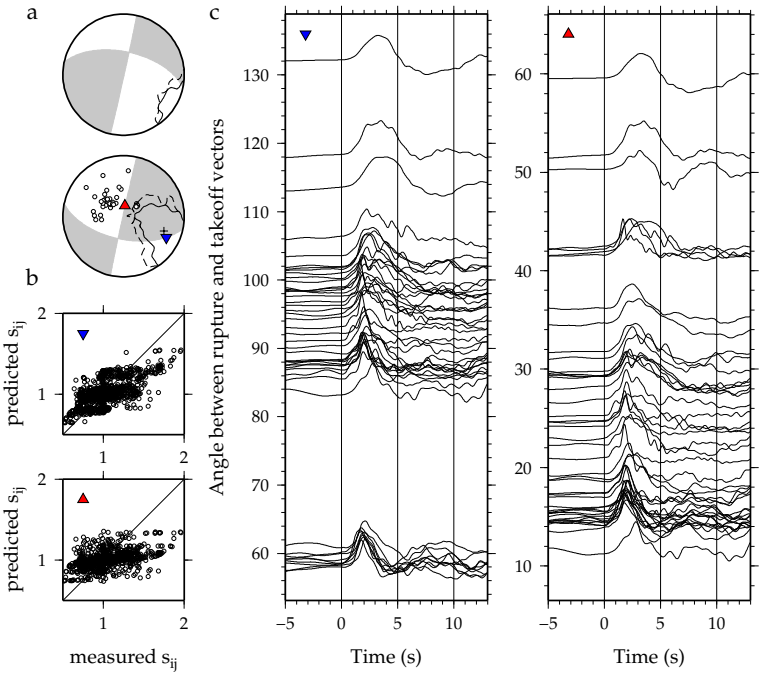

Figure B.9: Results for the 8 March 2007 (05:03:32.10) earthquake. Subplots are as described in Figure B.1.

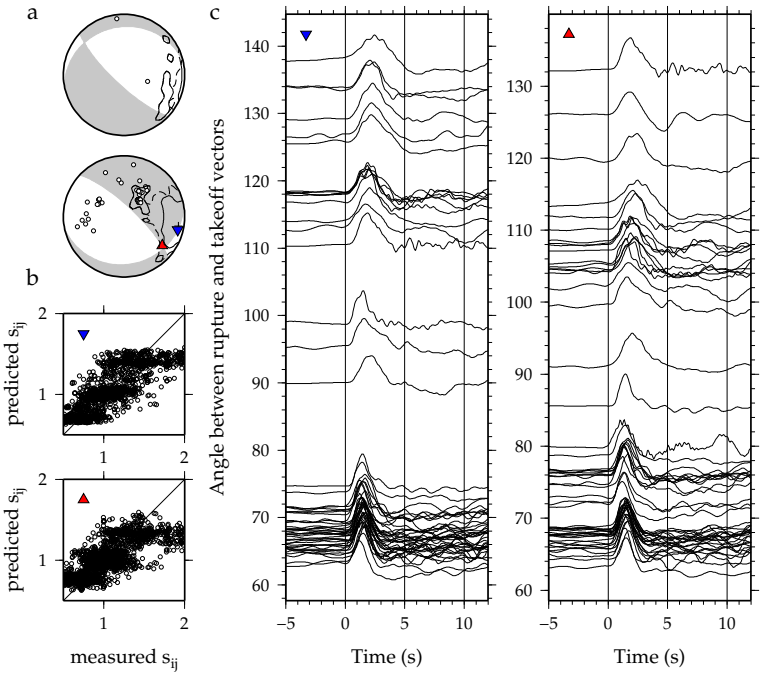

Figure B.10: Results for the 20 July 2008 (21:30:31.80) earthquake. Subplots are as described in Figure B.1.

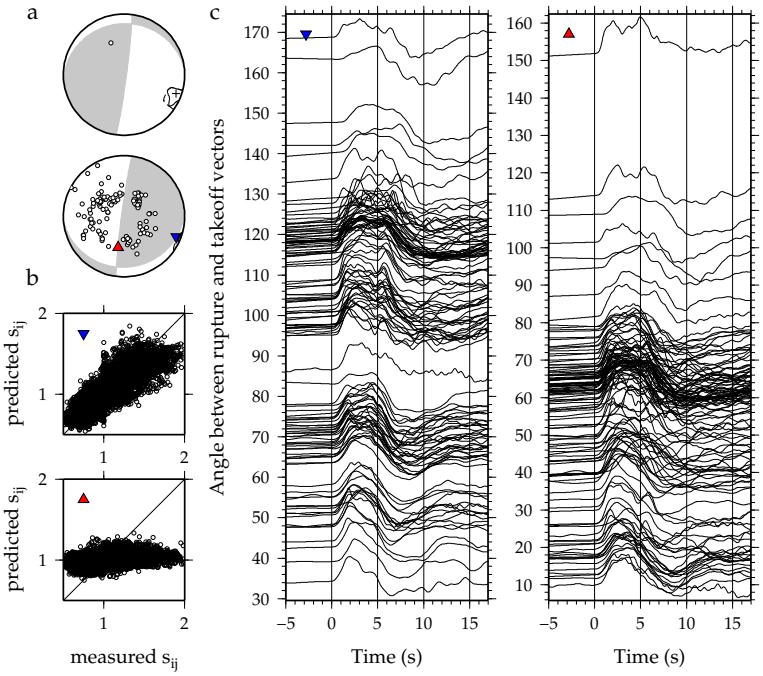

Figure B.11: Results for the 9 August 2009 (10:55:58.80) earthquake. Subplots are as described in Figure B.1.

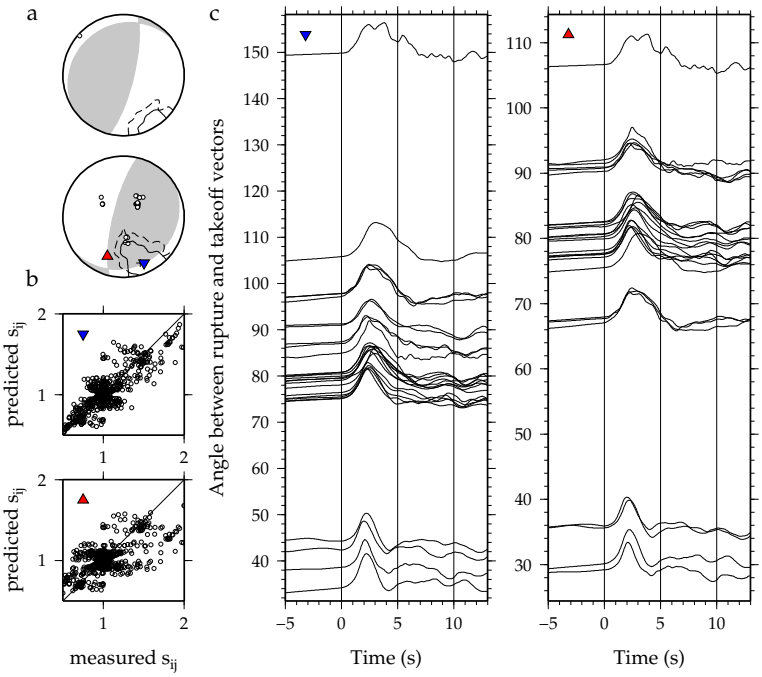

Figure B.12: Results for the 12 August 2009 (22:48:55.90) earthquake. Subplots are as described in Figure B.1.

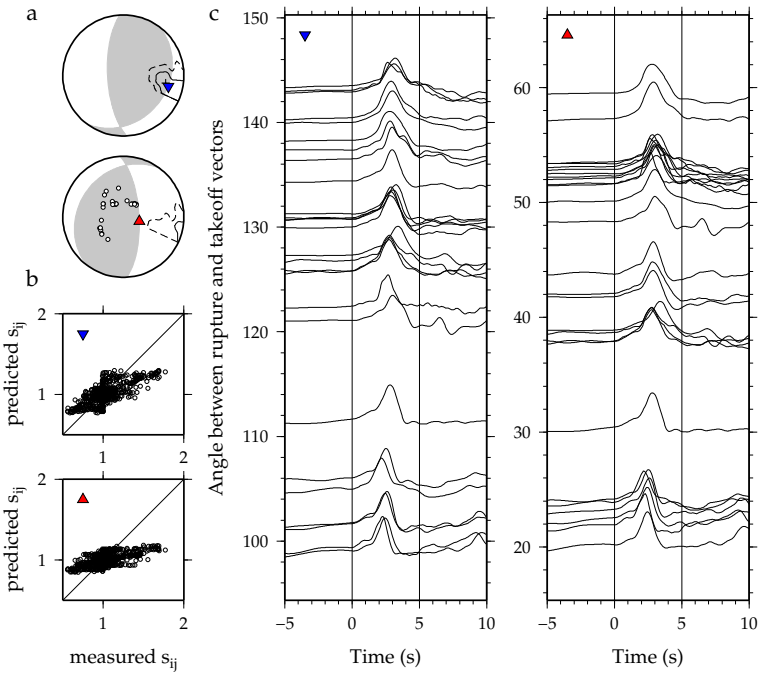

Figure B.13: Results for the 3 May 2010 (10:27:47.80) earthquake. Subplots are as described in Figure B.1.

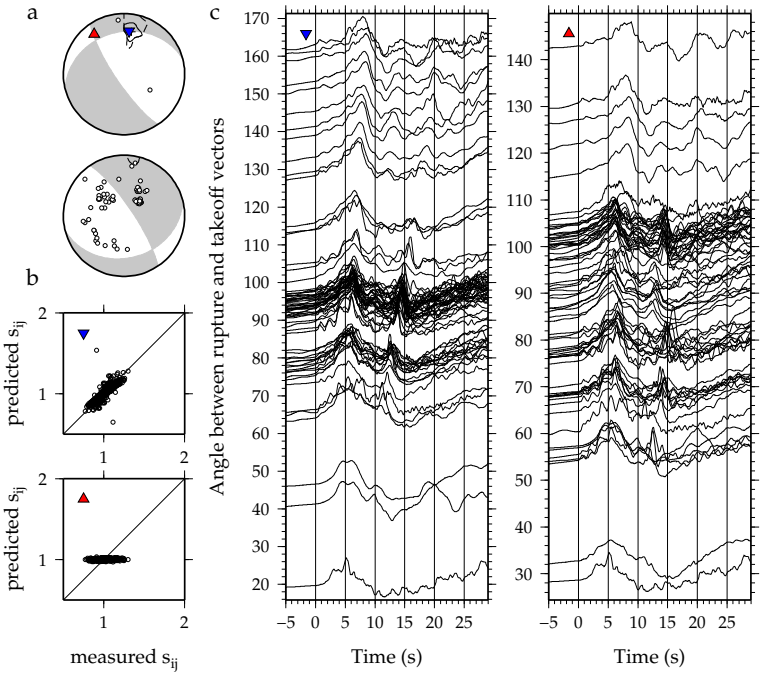

Figure B.14: Results for the 30 November 2010 (03:24:49.10) earthquake. Subplots are as described in Figure B.1.

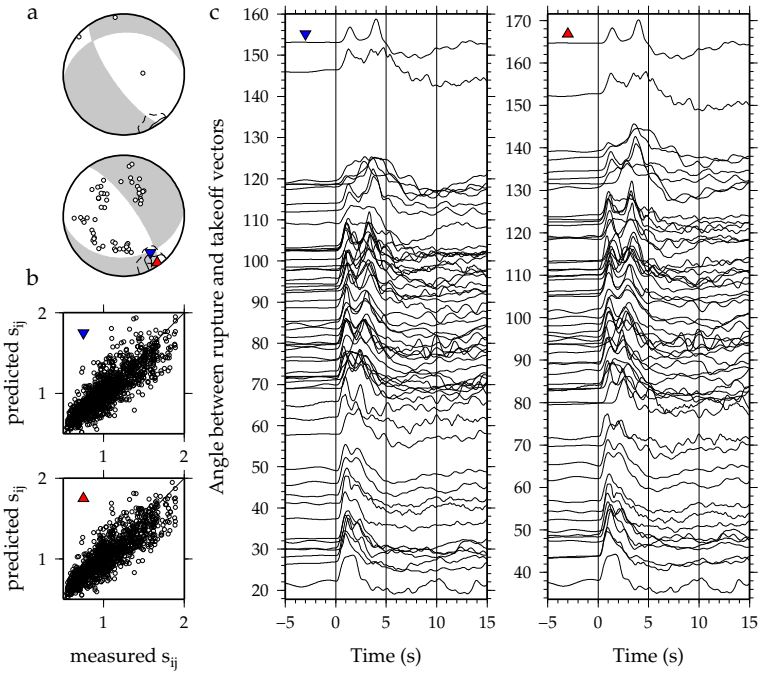

Figure B.15: Results for the 12 January 2011 (21:32:58.20) earthquake. Subplots are as described in Figure B.1.

B.2 Volcano Islands

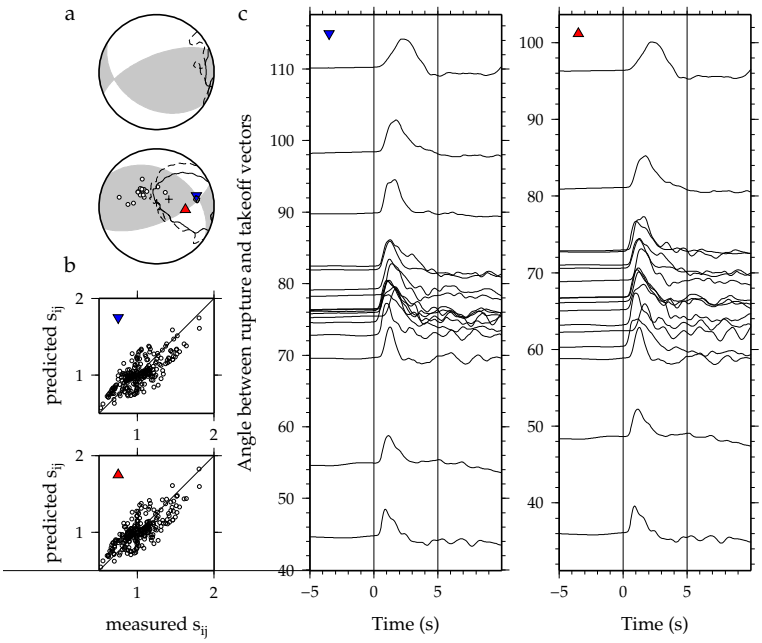

Figure B.16: Results for the 8 April 1995 (17:45:14.00) earthquake. Subplots are as described in Figure B.1.

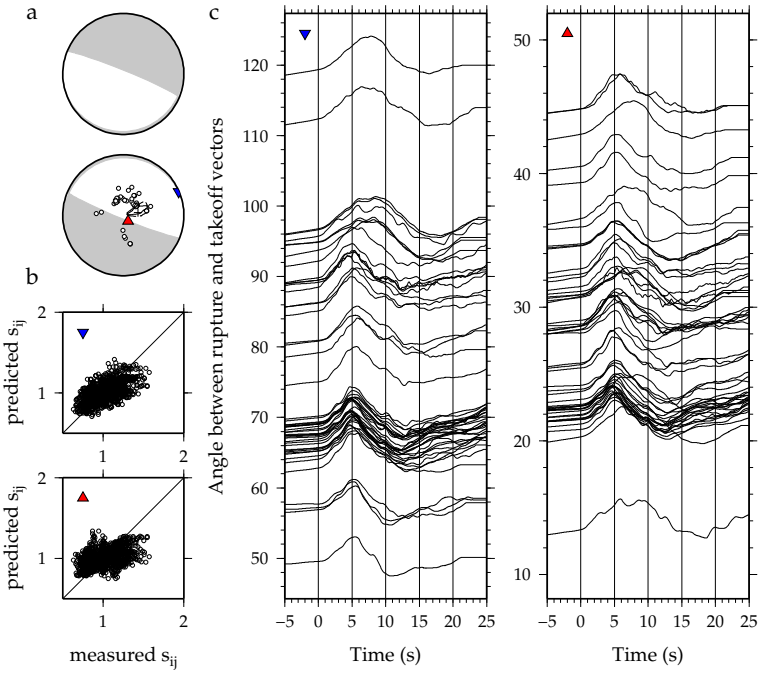

Figure B.17: Results for the 28 March 2000 (11:00:20.40) earthquake. Subplots are as described in Figure B.1.

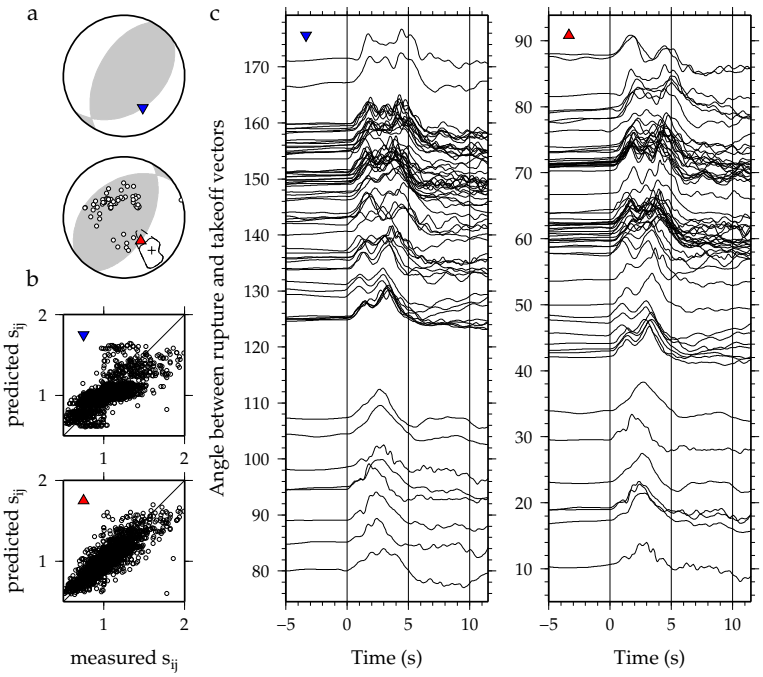

Figure B.18: Results for the 3 July 2001 (13:10:43.90) earthquake. Subplots are as described in Figure B.1.

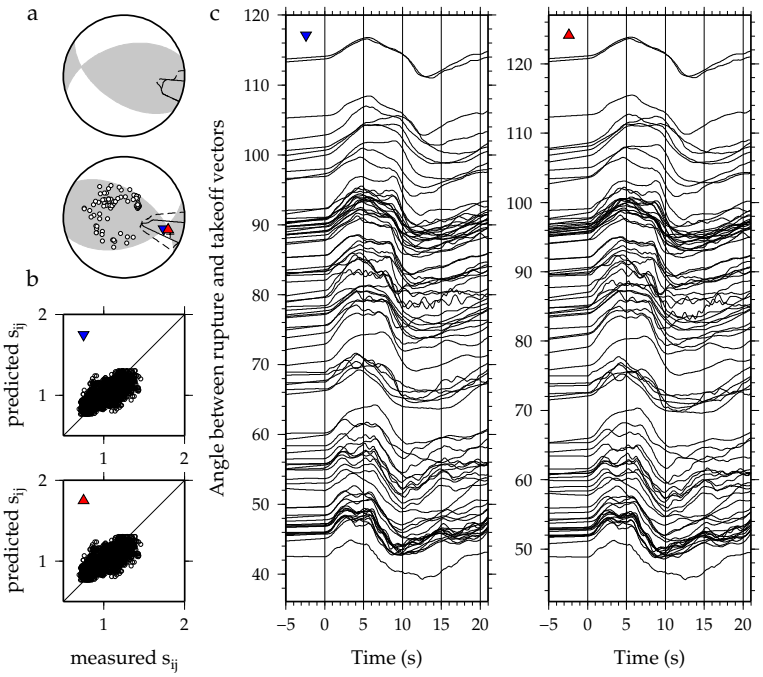

Figure B.19: Results for the 28 September 2007 (13:39:03.90) earthquake. Subplots are as described in Figure B.1.

B.3 Marianas

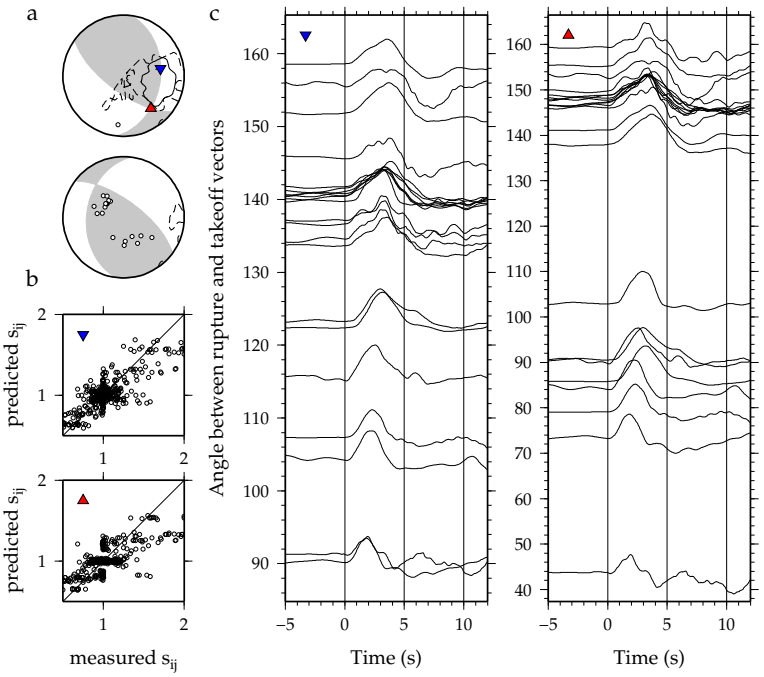

Figure B.20: Results for the 30 December 1994 (15:12:33.20) earthquake. Subplots are as described in Figure B.1.

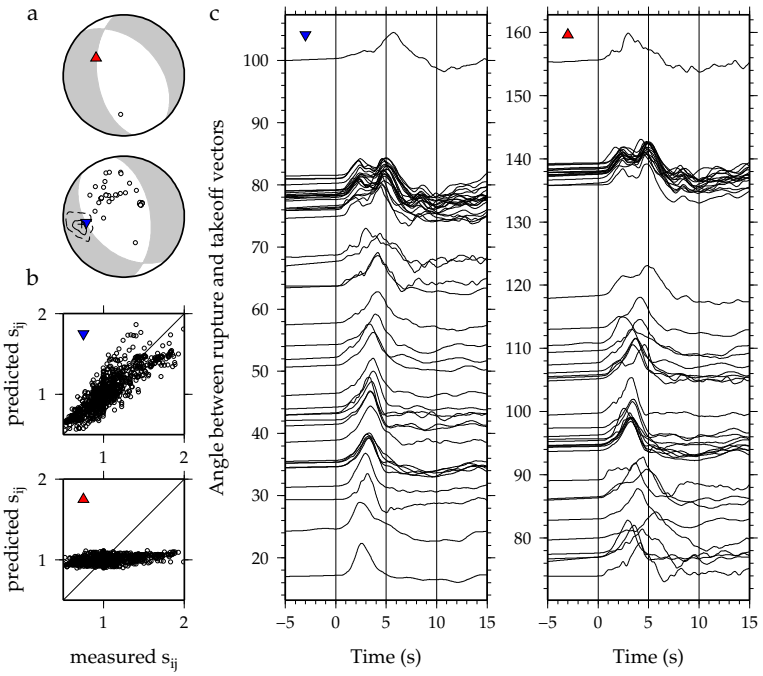

Figure B.21: Results for the 23 August 1995 earthquake. Subplots are as described in Figure B.1.

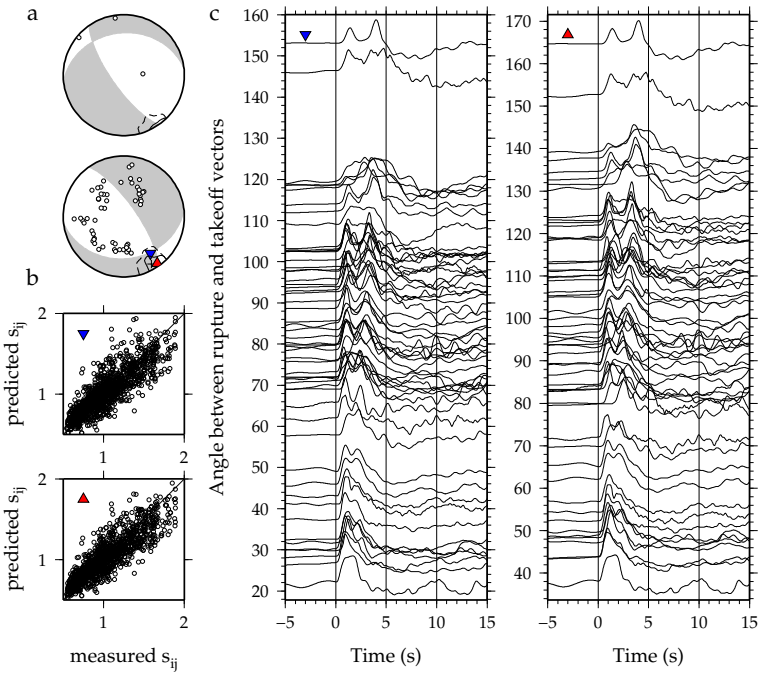

Figure B.22: Results for the 15 July 1996 (16:51:23.00) earthquake. Subplots are as described in Figure B.1.

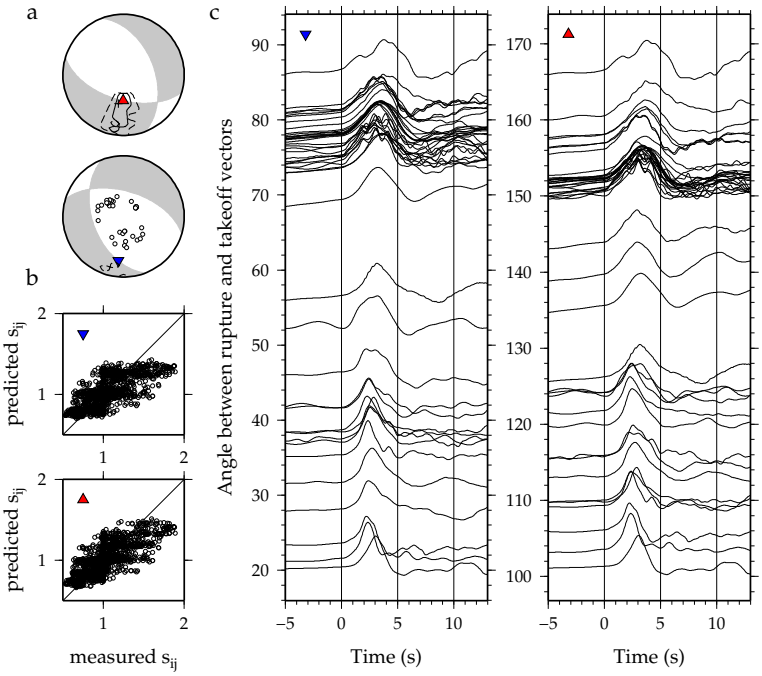

Figure B.23: Results for the 23 April 1997 (19:44:29.80) earthquake. Subplots are as described in Figure B.1.

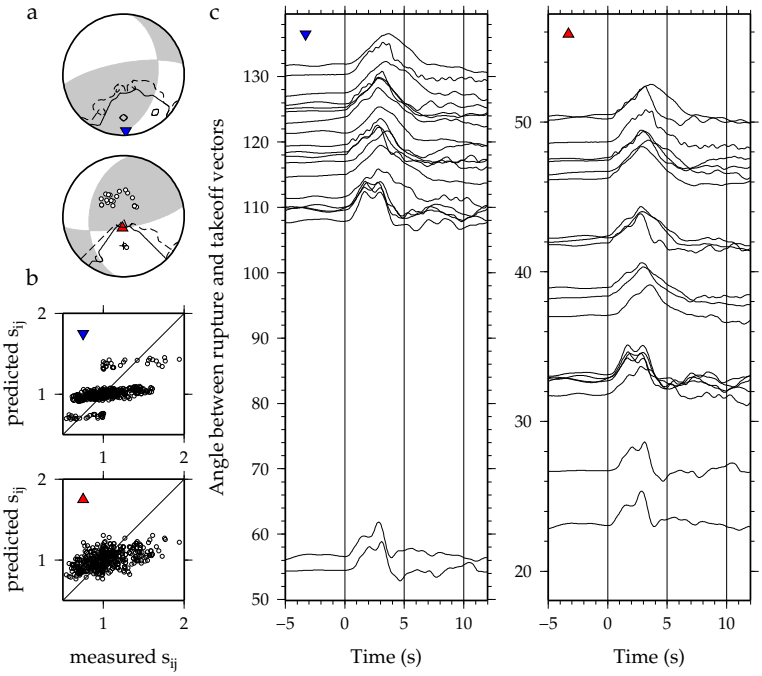

Figure B.24: Results for the 15 May 1998 (05:58:07.90) earthquake. Subplots are as described in Figure B.1.

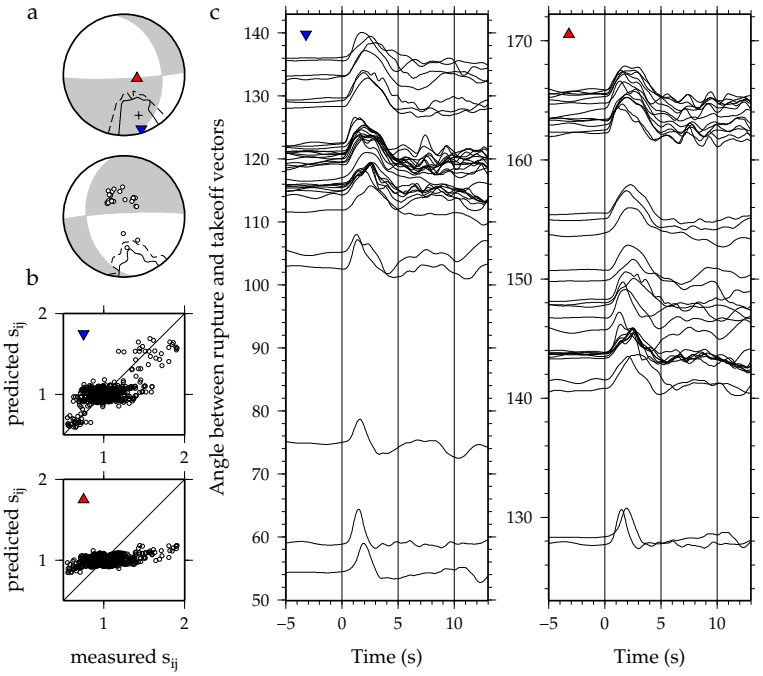

Figure B.25: Results for the 21 June 2000 (16:25:08.00) earthquake. Subplots are as described in Figure B.1.

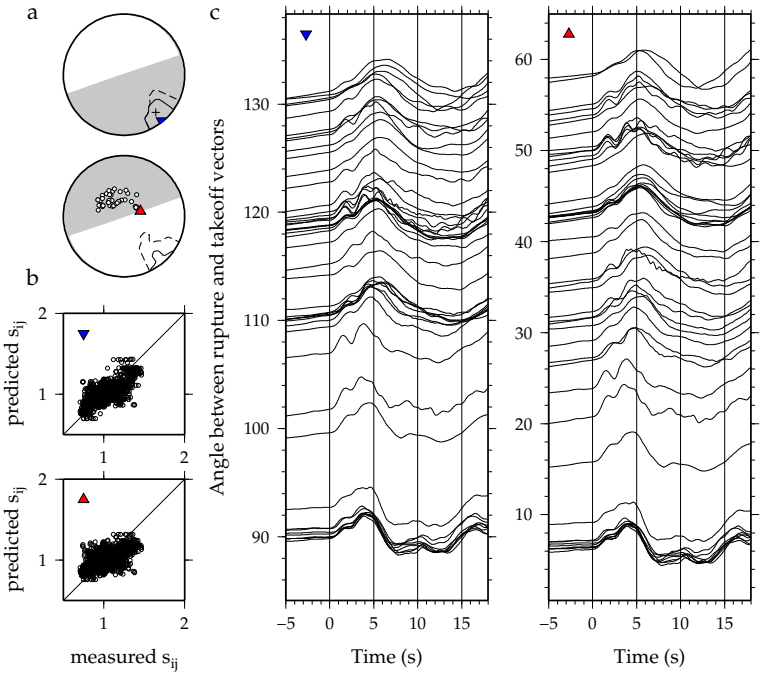

Figure B.26: Results for the 26 April 2002 (16:06:05.13) earthquake. Subplots are as described in Figure B.1.

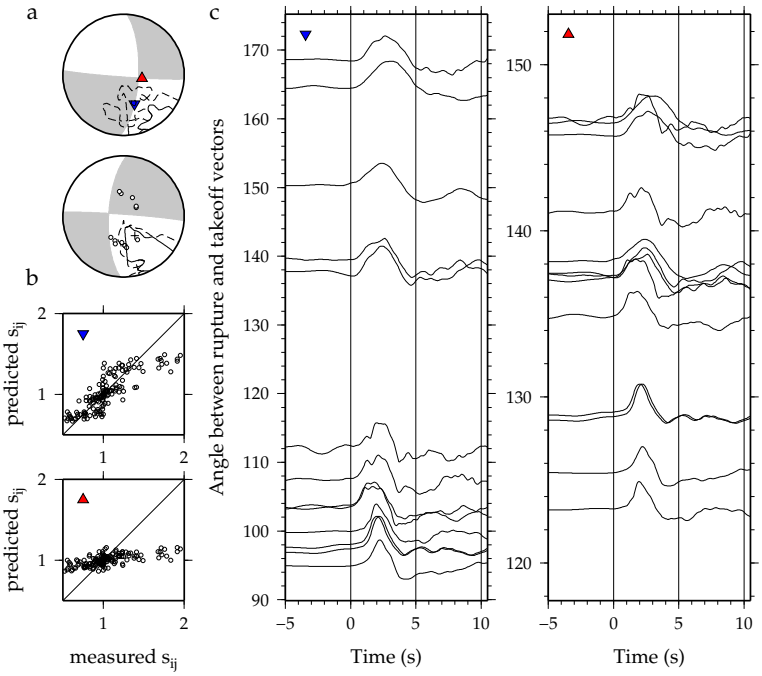

Figure B.27: Results for the 2 February 2005 (02:30:25.90) earthquake. Subplots are as described in Figure B.1.

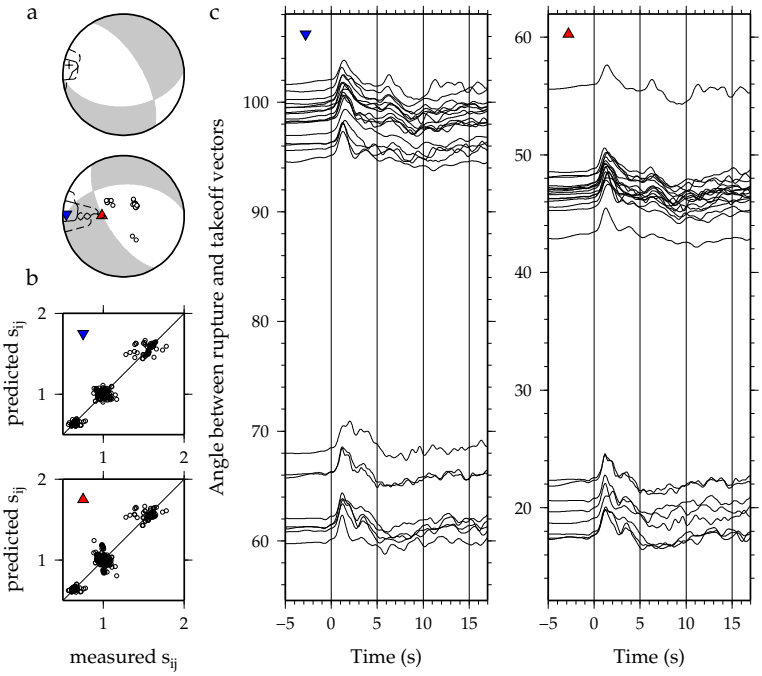

Figure B.28: Results for the 5 February 2005 (03:34:26.00) earthquake. Subplots are as described in Figure B.1.

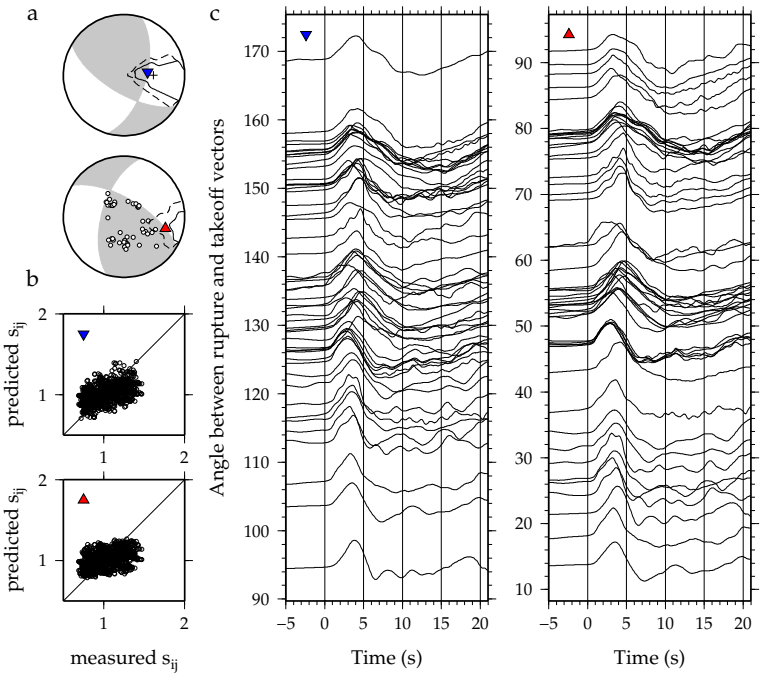

Figure B.29: Results for the 31 October 2007 (03:30:25.50) earthquake. Subplots are as described in Figure B.1.

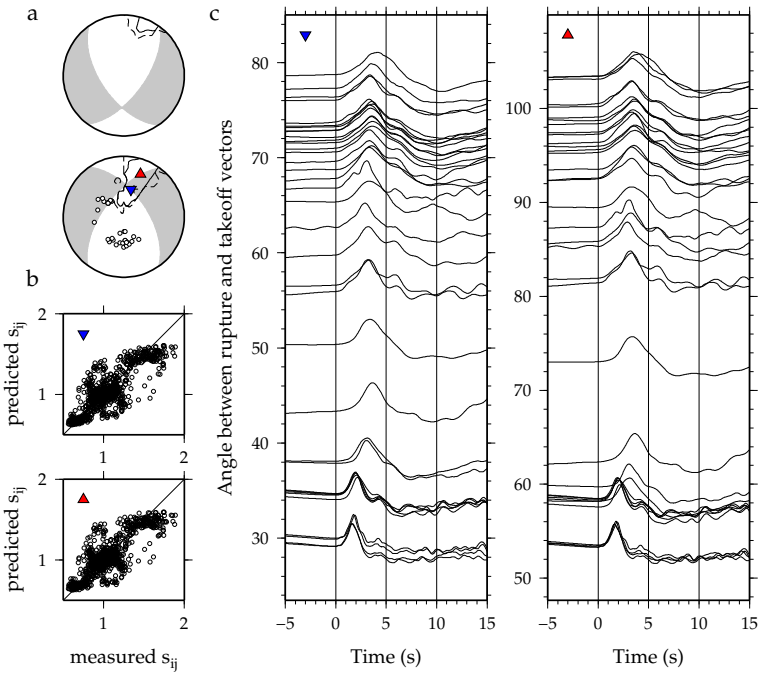

Figure B.30: Results for the 09 May 2008 (21:51:35.90) earthquake. Subplots are as described in Figure B.1.

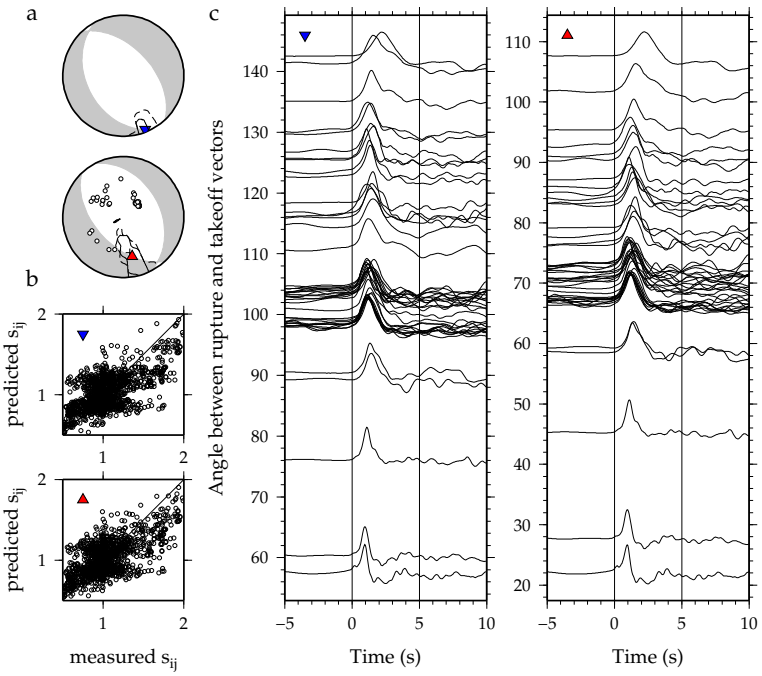

Figure B.31: Results for the 8 March 2010 (09:47:11.40) earthquake. Subplots are as described in Figure B.1.

References

R. D. Adams. Source characteristics of some deep New Zealand earthquakes. *N.Z. J. Geol. Geophys.*, 6:209–220, 1963. 13

K. Aki. A probabilistic synthesis of precursory phenomena. *Maurice Ewing Series*, 4:566–574, 1981. 16

L. Alisic, M. Gurnis, G. Stadler, C. Burstedde, L. C. Wilcox, and O. Ghattas. Slab stress and strain rate as constraints on global mantle flow. *Geophysical Research Letters*, 37:L22308, 2010. doi:10.1029/2010GL045312. 23, 44, 48, 66, 164

C. J. Allègre and D. L. Turcotte. Implications of a two-component marble-cake mantle. *Nature*, 323:123–127, 1986. doi:10.1038/323123a0. 117

L. A. Alpert, T. W. Becker, and I. W. Bailey. Global slab deformation and centroid moment tensor constraints on viscosity. *Geochemistry, Geophysics, Geosystems*, 11:Q12006, 2010. doi:10.1029/2010GC003301. 7, 48

M. Ammann. *Diffusion in minerals of the Earth's Lower Mantle: Constraining rheology from First Principles*. PhD thesis, University College London, UK, 2011. 148

T. B. Andersen, K. Mair, H. Austrheim, Y. Y. Podladchikov, and J. C. Vrijmoed. Stress release in exhumed intermediate and deep earthquakes determined from ultramafic pseudotachylyte. *Geology*, 36(12):995–998, 2008. doi:10.1130/G25230A.1. 9, 11

D. L. Anderson. Thermally induced phase changes, lateral heterogeneity of the mantle, continental roots, and deep slab anomalies. *Journal of Geophysical Research (Solid Earth)*, 92:13968–13980, 1987. doi:10.1029/JB092iB13p13968. 6

H. Anderson and T. Webb. New Zealand seismicity: Patterns revealed by the upgraded National Seismograph Network. *New Zealand Journal of Geology and Geophysics*, 37(4):477–493, 1994. doi:10.1080/00288306.1994.9514633. 13

J. G. Anderson, M. Savage, and R. Quaas. "Strong" ground motions in North America from the Bolivia earthquake of June 9, 1994 (M_w=8.3). *Geophysical Research Letters*, 22:2293–2296, 1995. doi:10.1029/95GL01808. 1

R. N. Anderson, S. Uyeda, and A. Miyashiro. Geophysical and geochemical constraints at converging plate boundaries? Part I: Dehydration in the downgoing slab. *Geophysical Journal International*, 44:333–357, 1976. doi:10.1111/j.1365-246X.1976.tb03660.x. 124

R. N. Anderson, S. E. Delong, and W. M. Schwarz. Thermal model for subduction with dehydration in the downgoing slab. *Journal of Geology*, 86:731–739, 1978. doi:10.1086/649739. 124

R. N. Anderson, S. E. Delong, and W. M. Schwarz. Dehydration, Asthenospheric Convection and Seismicity in Subduction Zones. *Journal of Geology*, 88:445–451, 1980. doi:10.1086/628527. 124

S. Andersson and G. Bäckström. Techniques for determining thermal conductivity and heat capacity under hydrostatic pressure. *Review of Scientific Instruments*, 57:1633–1639, 1986. doi:10.1063/1.1138542. 134

S. Angiboust, P. Agard, H. Raimbourg, P. Yamato, and B. Huet. Subduction interface processes recorded by eclogite-facies shear zones (Monviso, W. Alps). *Lithos*, 127(1-2):222 – 238, 2011. doi:10.1016/j.lithos.2011.09.004. 11

J. H. Ansell and D. Gubbins. Anomalous high-frequency wave propagation from the Tonga–Kermadec seismic zone to New Zealand. *Geophysical Journal International*, 85:93–106, 1986. doi:10.1111/j.1365-246X.1986.tb05173.x. 22

M. Antolik, D. Dreger, and B. Romanowicz. Rupture processes of large deep-focus earthquakes from inversion of moment rate functions. *Journal of Geophysical Research (Solid Earth)*, 104:863–894, 1999. doi:10.1029/1998JB900042. 20, 23, 85, 93, 107

K. D. Apperson and C. Frohlich. The relationship between Wadati-Benioff zone geometry and P, T and B axes of intermediate and deep focus earthquakes. *Journal of Geophysical Research (Solid Earth)*, 921:13821–13831, 1987. doi:10.1029/JB092iB13p13821. 6, 19, 43, 44, 46, 65, 85, 172

J. Arkwright, E. Rutter, K. Brodie, and S. Llana-Funez. Role of porosity and dehydration reaction on the deformation of hot-pressed serpentinite aggregates. *Journal of the Geological Society*, 165(3):639–649, 2008. doi:10.1144/0016-76492007-119.8

T. Ashida, S. Kume, E. Ito, and A. Navrotsky. $MgSiO_3$ ilmenite: Heat capacity, thermal expansivity, and enthalpy of transformation. *Physics and Chemistry of Minerals*, 16:239–245, 1988. doi:10.1007/BF00220691. 134

H. Austrheim and T. B. Andersen. Pseudotachylytes from Corsica: fossil earthquakes from a subduction complex. *Terra Nova*, 16(4):193–197, 2004. doi:10.1111/j.1365-3121.2004.00551.x. 11

H. Austrheim and T. M. Boundy. Pseudotachylytes generated during seismic faulting and eclogitization of the deep crust. *Science*, 265:82–83, 1994. doi:10.1126/science.265.5168.82. 11

W. Bach and G. L. Früh-Green. Alteration of the oceanic lithosphere and implications for seafloor processes. *Elements*, 6(3):173–178, 2010. doi:10.2113/gselements.6.3.173. 114

F. Bachmann, R. Hielscher, and H. Schaeben. Texture Analysis with MTEX–Free and Open Source Software Toolbox. *Solid State Phenomena*, 160:63–68, 2010. doi:10.4028/www.scientific.net/SSP.160.63. 121

G. Backus and M. Mulcahy. Moment tensors and other phenomenological descriptions of seismic sources? I. Continuous displacements. *Geophysical Journal International*, 46:341–361, 1976. doi:10.1111/j.1365-246X.1976.tb04162.x. 154

I. Bailey, L. Alpert, T. Becker, and M. Miller. Co-seismic deformation of deep slabs based on summed CMT data. *Journal of Geophysical Research (Solid Earth)*, 117:B04404, 2012. doi:10.1029/2011JB008943. 7, 44, 47, 48, 65, 66

S. Baisch, L. Ceranna, and H.-P. Harjes. Earthquake cluster: what can we learn from waveform similarity? *Bulletin of the Seismological Society of America*, 98:2806–2814, 2008. doi:10.1785/0120080018. 41

M. B. Baker and J. R. Beckett. The origin of abyssal peridotites: a reinterpretation of constraints based on primary bulk compositions. *Earth and Planetary Science Letters*, 171:49–61, 1999. doi:10.1016/S0012-821X(99)00130-2. 112

M. Barazangi and B. L. Isacks. Spatial distribution of earthquakes and subduction of the Nazca plate beneath South America. *Geology*, 4:686, 1976. doi:10.1130/0091-7613(1976)4<686:SDOEAS>2.0.CO;2. 66

J. D. Bass. Elasticity of minerals, glasses and melts. In T. J. Ahrens, editor, *AGU Reference Shelf 2: Mineral Physics and Crystallography; A handbook of physical constants*, pages 45–63. American Geophysical Union, 1995. 134

A. E. Beck, D. M. Darbha, and H. H. Schloessin. Lattice conductivities of single-crystal and polycrystalline materials at mantle pressures and temperatures. *Physics of the Earth and Planetary Interiors*, 17(1):35–53, 1978. doi:10.1016/0031-9201(78)90008-0. 134

K. Becker and E. E. Davis. *In situ* determinations of the permeability of the igneous oceanic crust. In E. E. Davis and H. Elderfield, editors, *Hydrogeology of the Oceanic Lithosphere*, pages 189–224. Cambridge University Press, Cambridge, UK, 2004. 114, 115

F. Beekman, J. Bull, S. Cloetingh, and R. Scrutton. Crustal fault reactivation facilitating lithospheric folding/buckling in the central Indian Ocean. *Geological Society, London, Special Publications*, 99(1):251–263, 1996. doi:10.1144/âĂŃGSL.SP.1996.099.01.19. 173

H. Benioff. Seismic evidence for the fault origin of seismic deeps. *Geological Society of America Bulletin*, 60(12):1837–1856, 1949. doi:10.1130/0016-7606(1949)60[1837:SEFTFO]2.0.CO;2. 1, 5

M. Bevis. The curvature of Wadati-Benioff zones and the torsional rigidity of subducting plates. *Nature*, 323:52–53, 1986. doi:10.1038/323052a0. 161, 173

M. Bevis. Seismic slip and down-dip strain rates in Wadati-Benioff zones. *Science*, 240:1317–1319, 1988. doi:10.1126/science.240.4857.1317. 161, 173

L. Bezacier, B. Reynard, J. D. Bass, C. Sanchez-Valle, and B. van de Moortèle. Elasticity of antigorite, seismic detection of serpentinites, and anisotropy in subduction zones. *Earth and Planetary Science Letters*, 289:198–208, 2010. doi:10.1016/j.epsl.2009.11.009. 121

M. I. Billen, M. Gurnis, and M. Simons. Multiscale dynamics of the Tonga-Kermadec subduction zone. *Geophysical Journal International*, 153:359–388, 2003. doi:10.1046/j.1365-246X.2003.01915.x. 106

S. Billington and B. L. Isacks. Identification of fault planes associated with deep earthquakes. *Geophysical Research Letters*, 2:63–66, 1975. doi:10.1029/GL002i002p00063. 71

C. R. Bina. Patterns of deep seismicity reflect buoyancy stresses due to phase transitions. *Geophysical Research Letters*, 24: 3301–3304, 1997. doi:10.1029/97GL53189. 44, 65

C. R. Bina, S. Stein, F. C. Marton, and E. M. Van Ark. Implications of slab mineralogy for subduction dynamics. *Physics of the Earth and Planetary Interiors*, 127:51–66, 2001. doi:10.1016/S0031-9201(01)00221-7. 44

S. H. Bloomer, B. Taylor, C. J. MacLeod, R. J. Stern, P. Fryer, J. W. Hawkins, and L. Johnson. Early arc volcanism and the ophiolite problem: A perspective from drilling in the Western Pacific. In B. Taylor and J. P. Natland, editors, *Active Margins and Marginal Basins of the Western Pacific: American Geophysical Union Geophysical Monograph 88*, pages 67–96. American Geophysical Union, Washington D.C., 1995. 85

T. Boddington, C. J. Parkin, and D. Gubbins. Isolated deep earthquakes beneath the North Island of New Zealand. *Geophysical Journal International*, 158:972–982, 2004. doi:10.1111/j.1365-246X.2004.02340.x. 13, 66

T. Boffa Ballaran, D. J. Frost, M. Pamato, and N. Miyajima. A super-aluminous phase D stable within subducting oceanic crust in the Earth's lower mantle. In *EGU General Assembly Conference Abstracts*, volume 12 of *EGU General Assembly Conference Abstracts*, page 10077, 2010. 116

G. A. Bollinger. Determination of earthquake fault parameters from long-period P waves. *Journal of Geophysical Research (Solid Earth)*, 73:785–807, 1968. doi:10.1029/JB073i002p00785. 86

M. Bouchon and P. Ihmlé. Stress drop and frictional heating during the 1994 deep Bolivia earthquake. *Geophysical Research Letters*, 26:3521–3524, 1999. doi:10.1029/1999GL005410. 9

P. W. Bridgman. Shearing phenomena at high pressure of possible importance for geology. *Journal of Geology*, 44:653–669, 1936. doi:10.1086/624468. 8

M. R. Brudzinski and W.-P. Chen. Variations in P wave speeds and outboard earthquakes: Evidence for a petrologic anomaly in the mantle transition zone. *Journal of Geophysical Research (Solid Earth)*, 105:21661–21682, 2000. doi:10.1029/2000JB900160. 13, 22, 79

M. R. Brudzinski and W.-P. Chen. A petrologic anomaly accompanying outboard earthquakes beneath Fiji-Tonga: Corresponding evidence from broadband P and S waveforms. *Journal of Geophysical Research (Solid Earth)*, 108(B6), 2003. doi:10.1029/2002JB002012. 13, 22, 23, 79

M. R. Brudzinski and W.-P. Chen. Earthquakes and strain in subhorizontal slabs. *Journal of Geophysical Research (Solid Earth)*, 110(B9):8303–8314, 2005. doi:10.1029/2004JB003470. 79

M. R. Brudzinski, C. H. Thurber, B. R. Hacker, and E. R. Engdahl. Global prevalence of double Benioff zones. *Science*, 316 (5830):1472–1474, 2007. doi:10.1126/science.1139204. 7, 9, 14, 43

B. A. Buffett and A. Heuret. Curvature of subducted lithosphere from earthquake locations in the Wadati-Benioff zone. *Geochemistry, Geophysics, Geosystems*, 12:Q06010, 2011. doi:10.1029/2011GC003570. 154

E. Buforn, A. Udías, and R. Madariaga. Intermediate and deep earthquakes in Spain. *Pure and Applied Geophysics*, 136: 375–393, 1991. doi:10.1007/BF00878576. 13

E. Buforn, C. Pro, S. Cesca, A. Udias, and C. Del Fresno. The 2010 Granada, Spain, deep earthquake. *The Bulletin of the Seismological Society of America*, 101:2418–2430, 2011. doi:10.1785/0120110022. 13

P. C. Burnley, H. W. Green, II, and D. J. Prior. Faulting associated with the olivine to spinel transformation in Mg_2GeO_4 and its implications for deep-focus earthquakes. *Journal of Geophysical Research (Solid Earth)*, 96:425–443, 1991. doi:10.1029/90JB01937. 10

J. Byerlee. Friction of rocks. *Pure and Applied Geophysics*, 116:615–626, 1978. doi:10.1007/BF00876528. 169, 171

R. L. Carlson and D. J. Miller. Mantle wedge water contents estimated from seismic velocities in partially serpentinized peridotites. *Geophysical Research Letters*, 30(5):050000–1, 2003. doi:10.1029/2002GL016600. 117

M. Chai, J. M. Brown, and L. J. Slutsky. Thermal diffusivity of mantle minerals. *Physics and Chemistry of Minerals*, 23: 470–475, 1996. doi:10.1007/BF00202033. 134

P.-F. Chen, C. R. Bina, and E. A. Okal. A global survey of stress orientations in subducting slabs as revealed by intermediate-depth earthquakes. *Geophysical Journal International*, 159:721–733, 2004. doi:10.1111/j.1365-246X.2004.02450.x. 6, 43, 44, 46, 47, 83, 106

W.-P. Chen and M. R. Brudzinski. Evidence for a large-scale remnant of subducted lithosphere beneath Fiji. *Science*, 292: 2475–2479, 2001. doi:10.1126/science.292.5526.2475. 13, 22, 34, 40, 79

W.-P. Chen and M. R. Brudzinski. Seismic anisotropy in the mantle transition zone beneath Fiji-Tonga. *Geophysical Research Letters*, 30(13):130000–1, 2003. doi:10.1029/2002GL016330. 13, 22

W.-P. Chen and P. Molnar. Focal depths of intracontinental and intraplate earthquakes and their implications for the thermal and mechanical properties of the lithosphere. *Journal of Geophysical Research (Solid Earth)*, 88:4183–4214, 1983. doi:10.1029/JB088iB05p04183. 123

W.-P. Chen, L.-R. Wu, and M. A. Glennon. Thermo-mechanical evolution of oceanic lithosphere : Implications for the subduction process and deep earthquakes. In G. E. Bebout, D. W. Scholl, S. H. Kirby, and J. P. Platt, editors, *Subduction: Top to bottom: American Geophysical Union Geophysical Monograph 96*, pages 1–17. American Geophysical Union, Washington D.C., 1996. 19, 85

L. J. Chernak and G. Hirth. Deformation of antigorite serpentinite at high temperature and pressure. *Earth and Planetary Science Letters*, 296:23–33, 2010. doi:10.1016/j.epsl.2010.04.035. 8, 106, 122

L. J. Chernak and G. Hirth. Syndeformational antigorite dehydration produces stable fault slip. *Geology*, 39(9):847–850, 2011. doi:10.1130/G31919.1. 8, 122

C. Christova and C. H. Scholz. Stresses in the Vanuatu subducting slab: A test of two hypotheses. *Geophysical Research Letters*, 30(15):1790, 2003. doi:10.1029/2003GL017701. 106

W.-Y. Chung and H. Kanamori. Source process and tectonic implications of the Spanish deep-focus earthquake of March 29, 1954. *Physics of the Earth and Planetary Interiors*, 13:85–96, 1976. doi:10.1016/0031-9201(76)90073-X. 13

C. Clauser and E. Huenges. Thermal conductivity of rocks and minerals. In T. J. Ahrens, editor, *AGU Reference Shelf 3: Rock physics and phase relations; A handbook of physical constants*, pages 105–126. American Geophysical Union, 1995. 134

D. Comte, L. Dorbath, M. Pardo, T. Monfret, H. Haessler, L. Rivera, M. Frogneux, B. Glass, and C. Meneses. A double-layered seismic zone in Arica, northern Chile. *Geophysical Research Letters*, 26:1965–1968, 1999. doi:10.1029/1999GL900447. 14

J. A. D. Connolly. Computation of phase equilibria by linear programming: A tool for geodynamic modeling and its application to subduction zone decarbonation. *Earth and Planetary Science Letters*, 236:524–541, 2005. doi:10.1016/j.epsl.2005.04.033. 113, 125

J. A. D. Connolly. The geodynamic equation of state: What and how. *Geochemistry, Geophysics, Geosystems*, 10:Q10014, 2009. doi:10.1029/2009GC002540. 113, 125

E. Contreras-Reyes, I. Grevemeyer, E. R. Flueh, M. Scherwath, and J. Bialas. Effect of trench-outer rise bending-related faulting on seismic Poisson's ratio and mantle anisotropy: a case study offshore of Southern Central Chile. *Geophysical Journal International*, 173:142–156, 2008. doi:10.1111/j.1365-246X.2008.03716.x. 117

A. Copley, J.-P. Avouac, J. Hollingsworth, and S. Leprince. The 2001 M_w 7.6 Bhuj earthquake, low fault friction, and the crustal support of plate driving forces in India. *Journal of Geophysical Research (Solid Earth)*, 116:B08405, 2011. doi:10.1029/2010JB008137. 169, 171

S. J. D. Cox and C. H. Scholz. Rupture initiation in shear fracture of rocks: An experimental study. *Journal of Geophysical Research (Solid Earth)*, 93:3307–3320, 1988a. doi:10.1029/JB093iB04p03307. 68

S. J. D. Cox and C. H. Scholz. On the formation and growth of faults: an experimental study. *Journal of Structural Geology*, 10:413–430, 1988b. doi:10.1016/0191-8141(88)90019-3. 68

K. C. Creager and T. M. Boyd. The geometry of Aleutian subduction: Three-dimensional kinematic flow model. *Journal of Geophysical Research (Solid Earth)*, 96:2293–2307, 1991. doi:10.1029/90JB01918. 44, 161

R. Däßler and D. A. Yuen. The effects of phase transition kinetics on subducting slabs. *Geophysical Research Letters*, 20: 2603–2606, 1993. doi:10.1029/93GL02811. 144

R. Däßler and D. A. Yuen. The metastable olivine wedge in fast subducting slabs: Constraints from thermo-kinetic coupling. *Earth and Planetary Science Letters*, 137(1-4):109–118, 1996. doi:10.1016/0012-821X(95)00219-3. 125, 144

G. F. Davies. Mechanics of subducted lithosphere. *Journal of Geophysical Research (Solid Earth)*, 85:6304–6318, 1980. doi:10.1029/JB085iB11p06304. 66

R. P. Denlinger. A revised estimate for the temperature structure of the oceanic lithosphere. *Journal of Geophysical Research (Solid Earth)*, 97:7219–7222, 1992. doi:10.1029/91JB02998. 124

J. P. Devaux, G. Schubert, and C. Anderson. Formation of a metastable olivine wedge in a descending slab. *Journal of Geophysical Research (Solid Earth)*, 102:24627–24638, 1997. doi:10.1029/97JB02334. 144

G. DeVore. Relations between subduction, slab heating, slab dehydration and continental growth. *Lithos*, 16:255–263, 1983. doi:10.1016/0024-4937(83)90014-2. 124

H. J. B. Dick, J. Lin, and H. Schouten. An ultraslow-spreading class of ocean ridge. *Nature*, 426:405–412, 2003. 115

D. Diedrich, T. G. Sharp, K. Leinenweber, and J. R. Holloway. The effect of small amounts of H_2O on olivine to ringwoodite transformation growth rates and implications for subduction of metastable olivine. *Chemical Geology*, 262(1-2):87–99, 2009. doi:10.1016/j.chemgeo.2009.01.011. 143

D. P. Dobson, P. G. Meredith, and S. A. Boon. Detection and analysis of microseismicity in multi anvil experiments. *Physics of the Earth and Planetary Interiors*, 143:337–346, 2004. doi:10.1016/j.pepi.2003.09.023. 10, 169

H. Douma and R. Snieder. Correcting for bias due to noise in coda wave interferometry. *Geophysical Journal International*, 164:99–108, 2006. doi:10.1111/j.1365-246X.2005.02807.x. 28

C. Dupas-Bruzek, T. G. Sharp, D. C. Rubie, and W. B. Durham. Mechanisms of transformation and deformation in $Mg_{1.8}Fe_{0.2}SiO_4$ olivine and wadsleyite under non-hydrostatic stress. *Physics of the Earth and Planetary Interiors*, 108:33–48, 1998. doi:10.1016/S0031-9201(98)00086-7. 10

O. Dvir, T. Pettke, P. Fumagalli, and R. Kessel. Fluids in the peridotite-water system up to 6 GPa and 800°C: new experimental constraints on dehydration reactions. *Contributions to Mineralogy and Petrology*, 161:829–844, 2011. doi:10.1007/s00410-010-0567-2. 150

A. M. Dziewonski, T. A.-. Chou, and J. H. Woodhouse. Determination of earthquake source parameters from waveform data for studies of global and regional seismicity. *Journal of Geophysical Research (Solid Earth)*, 86:2825–2852, 1981. doi:10.1029/JB086iB04p02825. 15, 16, 38, 47, 68, 69, 88, 90

G. Ekström, M. Nettles, and A. Dziewoński. The global CMT project 2004–2010: Centroid-moment tensors for 13,017 earthquakes. *Physics of the Earth and Planetary Interiors*, 200-201(0):1–9, 2012. doi:10.1016/j.pepi.2012.04.002. 47

B. Emmerson and D. McKenzie. Thermal structure and seismicity of subducting lithosphere. *Physics of the Earth and Planetary Interiors*, 163:191–208, 2007. doi:10.1016/j.pepi.2007.05.007. 57, 130, 131, 132, 133, 135, 136, 137, 140, 148

E. R. Engdahl and C. H. Scholz. A double Benioff zone beneath the central Aleutians - An unbending of the lithosphere. *Geophysical Research Letters*, 4:473–476, 1977. doi:10.1029/GL004i010p00473. 43, 44

E. R. Engdahl, R. D. van der Hilst, and J. Berrocal. Imaging of subducted lithosphere beneath South America. *Geophysical Research Letters*, 22:2317–2320, 1995. doi:10.1029/95GL02013. 13

E. R. Engdahl, R. van der Hilst, and R. Buland. Global teleseismic earthquake relocation with improved travel times and procedures for depth determination. *Bulletin of the Seismological Society of America*, 88(3):722–743, 1998. 1, 12, 26, 38, 46, 68, 69, 83, 84, 90, 132

P. England, R. Engdahl, and W. Thatcher. Systematic variation in the depths of slabs beneath arc volcanoes. *Geophysical Journal International*, 156:377–408, 2004. doi:10.1111/j.1365-246X.2003.02132.x. 132

J. Escartín, G. Hirth, and B. Evans. Effects of serpentinization on the lithospheric strength and the style of normal faulting at slow-spreading ridges. *Earth and Planetary Science Letters*, 151:181–189, 1997. doi:10.1016/S0012-821X(97)81847-X. 115

C. H. Estabrook. Seismic constraints on mechanisms of deep earthquake rupture. *Journal of Geophysical Research (Solid Earth)*, 109:B02306, 2004. doi:10.1029/2003JB002449. 45

M. Faccenda, T. V. Gerya, and L. Burlini. Deep slab hydration induced by bending-related variations in tectonic pressure. *Nature Geoscience*, 2:790–793, 2009. doi:10.1038/ngeo656. 115

M. Faccenda, T. V. Gerya, N. S. Mancktelow, and L. Moresi. Fluid flow during slab unbending and dehydration: Implications for intermediate-depth seismicity, slab weakening and deep water recycling. *Geochem. Geophys. Geosyst.*, 13: Q01010, 2012. doi:10.1029/2011GC003860. 115

U. H. Faul and I. Jackson. Diffusion creep of dry, melt-free olivine. *Journal of Geophysical Research (Solid Earth)*, 112:B04204, 2007. doi:10.1029/2006JB004586. 164, 165

Y. Fei. Thermal expansion. In T. J. Ahrens, editor, *AGU Reference Shelf 2: Mineral Physics and Crystallography; A handbook of physical constants*, pages 29–44. American Geophysical Union, 1995. 134

K. M. Fischer and T. H. Jordan. Seismic strain rate and deep slab deformation in Tonga. *Journal of Geophysical Research (Solid Earth)*, 96:14429–14444, 1991. doi:10.1029/91JB00153. 58, 65, 154

K. M. Fischer, K. C. Creager, and T. H. Jordan. Mapping the Tonga slab. *Journal of Geophysical Research (Solid Earth)*, 96: 14403–14427, 1991. doi:10.1029/90JB02703. 58

J. Frechet. Sismogenèse et doublets sismiques. *These d'Etat, Univ. Sci. Technol. Medic., Grenoble*, page 207, 1985. 37

C. Frohlich. The nature of deep-focus earthquakes. *Annual Review of Earth and Planetary Sciences*, 17:227, 1989. doi:10.1146/annurev.ea.17.050189.001303. 82

C. Frohlich. Triangle diagrams: ternary graphs to display similarity and diversity of earthquake focal mechanisms. *Physics of the Earth and Planetary Interiors*, 75:193–198, 1992. doi:10.1016/0031-9201(92)90130-N. 47

C. Frohlich. Earthquakes with non-double-couple mechanisms. *Science*, 264:804–809, 1994. doi:10.1126/science.264.5160.804. 19

C. Frohlich. Does maximum earthquake size depend on focal depth? *Bulletin of the Seismological Society of America*, 88(2): 329–336, 1998. 15

C. Frohlich. *Deep Earthquakes*. Cambridge University Press, 2006. 9, 11, 13, 14, 17, 168, 169, 171

C. Frohlich and S. D. Davis. Teleseismic b values - Or, much ado about 1.0. *Journal of Geophysical Research (Solid Earth)*, 98: 631–644, 1993. doi:10.1029/92JB01891. 17

C. Frohlich, K. Kadinsky-Cade, and S. D. Davis. A reexamination of the Bucaramanga, Colombia, earthquake nest. *Bulletin of the Seismological Society of America*, 85(6):1622–1634, 1995. 14, 17

G. L. Früh-Green, D. S. Kelley, S. M. Bernasconi, J. A. Karson, K. A. Ludwig, D. A. Butterfield, C. Boschi, and G. Proskurowski. 30,000 Years of Hydrothermal Activity at the Lost City Vent Field. *Science*, 301:495–498, 2003. doi:10.1126/science.1085582. 114

H. Fujisawa, N. Fujii, H. Mizutani, H. Kanamori, and S.-I. Akimoto. Thermal Diffusivity of Mg_2SiO_4, Fe_2SiO_4, and NaCl at High Pressures and Temperatures. *Journal of Geophysical Research (Solid Earth)*, 73:4727–4733, 1968. doi:10.1029/JB073i014p04727. 124, 134

K. Fujita and H. Kanamori. Double seismic zones and stresses of intermediate depth earthquakes. *Geophysical Journal International*, 66:131–156, 1981. doi:10.1111/j.1365-246X.1981.tb05950.x. 44

Y. Fukao, M. Obayashi, H. Inoue, and M. Nenbai. Subducting slabs stagnant in the mantle transition zone. *Journal of Geophysical Research (Solid Earth)*, 97:4809–4822, 1992. doi:10.1029/91JB02749. 83

H. Fukui, T. Inoue, T. Yasui, T. Katsura, K. Funakoshi, and O. Ohtaka. Decomposition of brucite up to 20 GPa: evidence for high MgO-solubility in the liquid phase. *Eur J Mineral*, 17(2):261–267, 2005. doi:10.1127/0935-1221/2005/0017-0261. 150

W. Fuller Brown, Jr. Solid mixture permittivities. *Journal of Chemical Physics*, 23:1514–1517, 1955. 128, 129

Y. Furukawa. Two types of deep seismicity in subducting slabs. *Geophysical Research Letters*, 21:1181–1184, 1994. doi:10.1029/94GL01083. 45

J. B. Gaherty and B. H. Hager. Compositional vs. thermal buoyancy and the evolution of subducted lithosphere. *Geophysical Research Letters*, 21:141–144, 1994. doi:10.1029/93GL03466. 7

R. J. Geller and C. S. Mueller. Four similar earthquakes in Central California. *Geophysical Research Letters*, 7:821–824, 1980. doi:10.1029/GL007i010p00821. 25, 41

M. Gerbault. At what stress level is the central Indian Ocean lithosphere buckling? *Earth and Planetary Science Letters*, 178: 165–181, 2000. doi:10.1016/S0012-821X(00)00054-6. 173

R. Gesserman and D. A. Wiens. A dominant shear zone and other modes of deformation in the deep Tonga slab. *AGU Fall Meeting Abstracts*, page A1946, 2010. 38, 159

D. Giardini and J. H. Woodhouse. Deep seismicity and modes of deformation in Tonga subduction zone. *Nature*, 307: 505–509, 1984. doi:10.1038/307505a0. 13, 17, 19, 57, 58, 61, 65, 66, 68, 69, 71, 72, 73, 75, 79, 81

D. Giardini and J. H. Woodhouse. Horizontal shear flow in the mantle beneath the Tonga arc. *Nature*, 319:551–555, 1986. doi:10.1038/319551a0. 65

G. C. Gleason and H. W. Green. A general test of the hypothesis that transformation-induced faulting cannot occur in the lower mantle. *Physics of the Earth and Planetary Interiors*, 172:91–103, 2009. doi:10.1016/j.pepi.2008.06.019. 148, 169

S. Goes and J. Ritsema. A broadband P wave analysis of the large deep Fiji Island and Bolivia earthquakes of 1994. *Geophysical Research Letters*, 22:2249–2252, 1995. doi:10.1029/95GL02011. 9

S. Goes, F. A. Capitanio, and G. Morra. Evidence of lower-mantle slab penetration phases in plate motions. *Nature*, 451: 981–984, 2008. doi:10.1038/nature06691. 66

A. Gorbatov and V. Kostoglodov. Maximum depth of seismicity and thermal parameter of the subducting slab: general empirical relation and its application. *Tectonophysics*, 277:165–187, 1997. doi:10.1016/S0040-1951(97)00084-X. 123, 124

J.-L. Got, J. Frechet, and F. W. Klein. Deep fault plane geometry inferred from multiplet relative relocation beneath the south flank of Kilauea. *Journal of Geophysical Research (Solid Earth)*, 99(B8):15375–15386, 1994. doi:10.1029/94JB00577. 25, 37

S. P. Grand. Mantle shear structure beneath the Americas and surrounding oceans. *Journal of Geophysical Research (Solid Earth)*, 991:11591–11622, 1994. doi:10.1029/94JB00042. 6

S. P. Grand, R. D. van der Hilst, and S. Widiyantoro. Global seismic tomography: A snapshot of convection in the Earth. *GSA Today*, 7(4):1–7, 1997. doi:10.1130/GSAT01707GW.1. 6

H. Green and Y. Zhou. Transformation-induced faulting requires an exothermic reaction and explains the cessation of earthquakes at the base of the mantle transition zone. *Tectonophysics*, 256:39–56, 1996. doi:10.1016/0040-1951(95)00164-6. 148

H. W. Green, T. E. Young, D. Walker, and C. H. Scholz. Anticrack-associated faulting at very high pressure in natural olivine. *Nature*, 348:720–722, 1990. doi:10.1038/348720a0. 10, 169

H. W. Green, W. Chen, and M. R. Brudzinski. Seismic evidence of negligible water carried below 400-km depth in subducting lithosphere. *Nature*, 467:828–831, 2010. doi:10.1038/nature09401. 23, 64, 106

H. W. Green, II and H. Houston. The Mechanics of Deep Earthquakes. *Annual Review of Earth and Planetary Sciences*, 23: 169–214, 1995. doi:10.1146/annurev.ea.23.050195.001125. 9

I. H. W. Green. Tiny triggers deep down. *Nature*, 424:893–894, 2003. doi:10.1038/424893a. 15, 169

I. H. W. Green. Shearing instabilities accompanying high-pressure phase transformations and the mechanics of deep earthquakes. *Proceedings of the National Academy of Sciences*, 104(22):9133–9138, 2007. doi:10.1073/pnas.0608045104. 45

I. H. W. Green and P. C. Burnley. A new self-organizing mechanism for deep-focus earthquakes. *Nature*, 341:733–737, 1989. doi:10.1038/341733a0. 10, 122, 169

P. Green, E. J. Kelly, and M. Levin. A comparison of seismic array processing methods. *Geophysical Journal of the Royal Astronomical Society*, 11(1):67–84, 1966. doi:10.1111/j.1365-246X.1966.tb03493.x. 31, 32

I. Grevemeyer, C. R. Ranero, E. R. Flueh, D. Kläschen, and J. Bialas. Passive and active seismological study of bending-related faulting and mantle serpentinization at the Middle America trench. *Earth and Planetary Science Letters*, 258: 528–542, 2007. doi:10.1016/j.epsl.2007.04.013. 117

D. Griggs. Hydrolytic weakening of quartz and other silicates*. *Geophysical Journal of the Royal Astronomical Society*, 14(1-4): 19–31, 1967. 8

D. Griggs and J. Handin. Observations on fracture and hypothesis of earthquakes. *Geological Society of America Memoir*, 79: 347–364, 1960. 7

D. T. Griggs and D. W. Baker. The origin of deep-focus earthquakes. In H. Mark and S. Fernbach, editors, *The Properties of Matter under Unusual Conditions*, pages 23–42. Interscience, New York, NY, 1969. 8, 9

D. Gubbins and R. Snieder. Dispersion of P waves in subducted lithosphere: Evidence for an eclogite layer. *Journal of Geophysical Research (Solid Earth)*, 96:6321–6333, 1991. doi:10.1029/90JB02741. 22

Ó. Gudmundsson and M. Sambridge. A regionalized upper mantle (RUM) seismic model. *Journal of Geophysical Research (Solid Earth)*, 103:7121–7136, 1998. doi:10.1029/97JB02488. 46

A. Guest, G. Schubert, and C. W. Gable. Stress field in the subducting lithosphere and comparison with deep earthquakes in Tonga. *Journal of Geophysical Research (Solid Earth)*, 108:2288, 2003. doi:10.1029/2002JB002161. 45

A. Guest, G. Schubert, and C. W. Gable. Stresses along the metastable wedge of olivine in a subducting slab: possible explanation for the Tonga double seismic layer. *Physics of the Earth and Planetary Interiors*, 141:253–267, 2004. doi:10.1016/j.pepi.2003.11.012. 45

M. Gurnis, J. Ritsema, H.-J. van Heijst, and S. Zhong. Tonga slab deformation: The influence of a lower mantle upwelling on a slab in a young subduction zone. *Geophysical Research Letters*, 27:2373–2376, 2000. doi:10.1029/2000GL011420. 44

M. Gurnis, M. Turner, L. DiCaprio, S. Spasojevic, R. Müller, J. Boyden, M. Seton, V. Manea, and D. Bower. Global plate reconstructions with continuously closing plates. *Geochemistry, Geophysics, Geosystems in review*, 2010. 132, 133, 140

B. R. Hacker, S. M. Peacock, G. A. Abers, and S. D. Holloway. Subduction factory 2. Are intermediate-depth earthquakes in subducting slabs linked to metamorphic dehydration reactions? *Journal of Geophysical Research (Solid Earth)*, 108:2030, 2003. doi:10.1029/2001JB001129. 169

T. Hara, K. Kuge, and H. Kawakatsu. Determination of the isotropic component of deep focus earthquakes by inversion of normal-mode data. *Geophysical Journal International*, 127(2):515–528, 1996. doi:10.1111/j.1365-246X.1996.tb04737.x. 19

B. Harte. Diamond formation in the deep mantle: the record of mineral inclusions and their distribution in relation to mantle dehydration zones. *Mineral Mag*, 74(2):189–215, 2010. doi:10.1180/minmag.2010.074.2.189. 150

A. Hasegawa, N. Umino, and A. Takagi. Double-planed structure of the deep seismic zone in the northeastern Japan arc. *Tectonophysics*, 47:43–58, 1978. doi:10.1016/0040-1951(78)90150-6. 7, 14

A. Hasegawa, J. Nakajima, S. Kita, T. Okada, T. Matsuzawa, and S. H. Kirby. Anomalous deepening of a belt of intraslab earthquakes in the Pacific slab crust under Kanto, central Japan: Possible anomalous thermal shielding, dehydration reactions, and seismicity caused by shallower cold slab material. *Geophysical Research Letters*, 34:L09305, 2007. doi:10.1029/2007GL029616. 76

Z. Hashin and S. Shtrikman. A variational approach to the theory of the effective magnetic permeability of multiphase materials. *Journal of Applied Physics*, 33:3125–3131, 1962. doi:10.1063/1.1728579. 128

N. A. Haskell. Total energy and energy spectral density of elastic wave radiation from propagating faults. *Bulletin of the Seismological Society of America*, 54(6A):1811–1841, 1964. 85

G. R. Helffrich, S. Stein, and B. J. Wood. Subduction zone thermal structure and mineralogy and their relationship to seismic wave reflections and conversions at the slab/mantle interface. *Journal of Geophysical Research (Solid Earth)*, 94: 753–763, 1989. doi:10.1029/JB094iB01p00753. 22

H. H. Hess. History of the ocean basins, preprint. page 38, 1960. 5

H. H. Hess. History of the ocean basins. In A. E. J. Engel, H. L. James, and B. F. Leonard, editors, *Petrologic Studies: A Volume in Honor of A. F. Buddington*, pages 599–620. Geological Society of America, New York, 1962. 5

G. Hirth and D. L. Kohlstedt. Water in the oceanic upper mantle: implications for rheology, melt extraction and the evolution of the lithosphere. *Earth and Planetary Science Letters*, 144:93–108, 1996. doi:10.1016/0012-821X(96)00154-9. 114

B. E. Hobbs and A. Ord. Plastic instabilities: Implications for the origin of intermediate and deep focus earthquakes. *Journal of Geophysical Research (Solid Earth)*, 93:10521–10540, 1988. doi:10.1029/JB093iB09p10521. 9, 122, 148, 169

A. M. Hofmeister. Mantle values of thermal conductivity and the geotherm from phonon lifetimes. *Science*, 283:1699–1706, 1999. doi:10.1126/science.283.5408.1699. 127, 128, 129, 131, 134

A. M. Hofmeister. Dependence of diffusive radiative transfer on grain-size, temperature, and Fe-content: Implications for mantle processes. *Journal of Geodynamics*, 40:51–72, 2005. doi:10.1016/j.jog.2005.06.001. 143

T. J. B. Holland and R. Powell. An internally consistent thermodynamic data set for phases of petrological interest. *Journal of Metamorphic Geology*, 16(3):309–343, 1998. doi:10.1111/j.1525-1314.1998.00140.x. 125

T. J. B. Holland and R. Powell. An improved and extended internally consistent thermodynamic dataset for phases of petrological interest, involving a new equation of state for solids. *Journal of Metamorphic Geology*, 29(3):333–383, 2011. doi:10.1111/j.1525-1314.2010.00923.x. 125

A. Holmes. The thermal history of the Earth. *Journal of the Washington Academy of Sciences*, 23:169–195, 1933. 5

W. E. Holt. Flow fields within the Tonga slab determined from the moment tensors of deep earthquakes. *Geophysical Research Letters*, 22:989–992, 1995. doi:10.1029/95GL00786. 65, 67, 146, 152, 156, 163

H. Honda. On the types of the seismograms and the mechanism of deep earthquakes. *Geophysical Magazine*, 5:301–324, 1932. 82

E. Honza, H. L. Davies, J. B. Keene, and D. L. Tiffin. Plate boundaries and evolution of the Solomon Sea region. *Geo-Marine Letters*, 7:161–168, 1987. doi:10.1007/BF02238046. 55

K.-I. Horai. Thermal conductivity of rock-forming minerals. *Journal of Geophysical Research (Solid Earth)*, 76:1278–1308, 1971. doi:10.1029/JB076i005p01278. 134

M. K. Hubbert and W. W. Rubey. Role of fluid pressure in overthrust faulting. *Bulletin of the Seismological Society of America*, 70:115–206, 1959. 8, 122

K. W. Hudnut and J. J. Taber. Transition from double to single Wadati-Benioff seismic zone in the Shumagin Islands, Alaska. *Geophysical Research Letters*, 14:143–146, 1987. doi:10.1029/GL014i002p00143. 14

T. Igarashi, T. Matsuzawa, and A. Hasegawa. Repeating earthquakes and interplate aseismic slip in the northeastern Japan subduction zone. *Journal of Geophysical Research (Solid Earth)*, 108(B5):2249–2257, 2003. doi:10.1029/2002JB001920. 25

T. Iidaka and Y. Furukawa. Double seismic zone for deep earthquakes in the Izu-Bonin subduction zone. *Science*, 263: 1116–1118, 1994. doi:10.1126/science.263.5150.1116. 14

T. Iidaka and K. Obara. Seismological evidence for the existence of anisotropic zone in the metastable wedge inside the subducting Izu-Bonin slab. *Geophysical Research Letters*, 24:3305–3308, 1997. doi:10.1029/97GL03277. 22

T. Iidaka and D. Suetsugu. Seismological evidence for metastable olivine inside a subducting slab. *Nature*, 356:593–595, 1992. doi:10.1038/356593a0. 21

B. Ildefonse, D. K. Blackman, B. E. John, Y. Ohara, D. J. Miller, C. J. MacLeod, and Ocean Drilling Program Expeditions 304/305 Science Party. Oceanic core complexes and crustal accretion at slow-spreading ridges. *Geology*, 35:623, 2007. doi:10.1130/G23531A.1. 115

T. Irifune, N. Kubo, M. Isshiki, and Y. Yamasaki. Phase transformations in serpentine and transportation of water into the lower mantle. *Geophysical Research Letters*, 25(2):203–206, 1998. doi:10.1029/97GL03572. 8, 119, 149, 150

B. Isacks and P. Molnar. Mantle earthquake mechanisms and the sinking of the lithosphere. *Nature*, 223:1121–1124, 1969. doi:10.1038/2231121a0. 19

B. Isacks and P. Molnar. Distribution of stresses in the descending lithosphere from a global survey of focal-mechanism solutions of mantle earthquakes. *Reviews of Geophysics and Space Physics*, 9:103–174, 1971. doi:10.1029/RG009i001p00103. 6, 13, 19, 43, 58, 67, 74, 82, 106, 152, 172

B. Isacks, J. Oliver, and L. R. Sykes. Seismology and the new global tectonics. *Journal of Geophysical Research (Solid Earth)*, 73:5855–5899, 1968. doi:10.1029/JB073i018p05855. 5, 8, 12, 43, 45, 82

B. L. Isacks, L. R. Sykes, and J. Oliver. Spatial and temporal clustering of deep and shallow earthquakes in the Fiji-Tonga-Kermadec region. *Bulletin of the Seismological Society of America*, 57(5):935–958, 1967. 25

M. Ivandic, I. Grevemeyer, A. Berhorst, E. R. Flueh, and K. McIntosh. Impact of bending related faulting on the seismic properties of the incoming oceanic plate offshore of Nicaragua. *Journal of Geophysical Research (Solid Earth)*, 113(B12): B05410, 2008. doi:10.1029/2007JB005291. 117

M. Ivandic, I. Grevemeyer, J. Bialas, and C. J. Petersen. Serpentinization in the trench-outer rise region offshore of Nicaragua: constraints from seismic refraction and wide-angle data. *Geophysical Journal International*, 180:1253–1264, 2010. doi:10.1111/j.1365-246X.2009.04474.x. 117

H. Iwamori. Transportation of H_2O and melting in subduction zones. *Earth and Planetary Science Letters*, 160:65–80, 1998. doi:10.1016/S0012-821X(98)00080-6. 124

H. Iwamori. Phase relations of peridotites under H_2O-saturated conditions and ability of subducting plates for transportation of H_2O. *Earth and Planetary Science Letters*, 227:57–71, 2004. doi:10.1016/j.epsl.2004.08.013. 118, 149, 150

H. Jeffreys. The times of transmission and focal depths of large earthquakes. *Geophysical Journal International*, 1:500–521, 1928. doi:10.1111/j.1365-246X.1928.tb05356.x. 7

G. Jiang and D. Zhao. Metastable olivine wedge in the subducting Pacific slab and its relation to deep earthquakes. *Journal of Asian Earth Sciences*, 42(6):1411–1423, 2011. doi:10.1016/j.jseaes.2011.08.005. 21

G. Jiang, D. Zhao, and G. Zhang. Seismic evidence for a metastable olivine wedge in the subducting Pacific slab under Japan Sea. *Earth and Planetary Science Letters*, 270:300–307, 2008. doi:10.1016/j.epsl.2008.03.037. 21

W. Jiao, P. G. Silver, Y. Fei, and C. T. Prewitt. Do intermediate- and deep-focus earthquakes occur on preexisting weak zones? An examination of the Tonga subduction zone. *Journal of Geophysical Research (Solid Earth)*, 105:28125–28138, 2000. doi:10.1029/2000JB900314. 7, 82, 105

T. John and V. Schenk. Interrelations between intermediate-depth earthquakes and fluid flow within subducting oceanic plates: Constraints from eclogite facies pseudotachylytes. *Geology*, 34:557–560, 2006. doi:10.1130/G22411.1. 11

T. John, S. Medvedev, L. H. Rüpke, T. B. Andersen, Y. Y. Podladchikov, and H. Austrheim. Generation of intermediate-depth earthquakes by self-localizing thermal runaway. *Nature Geoscience*, 2:137–140, 2009. doi:10.1038/ngeo419. 9

T. H. Jordan and K. A. Sverdrup. Teleseismic location techniques and their application to earthquake clusters in the south-central Pacific. *Bulletin of the Seismological Society of America*, 71:1105–1130, 1981. 25, 99

H. Jung, I. H. W. Green, and L. F. Dobrzhinetskaya. Intermediate-depth earthquake faulting by dehydration embrittlement with negative volume change. *Nature*, 428:545–549, 2004. doi:10.1038/nature02412. 8

Y. Y. Kagan. 3-D rotation of double-couple earthquake sources. *Geophysical Journal International*, 106:709–716, 1991. doi:10.1111/j.1365-246X.1991.tb06343.x. 48

Y. Y. Kagan. Universality of the seismic moment-frequency relation. *Pure and Applied Geophysics*, 155:537–573, 1999. doi:10.1007/s000240050277. 16, 17

H. Kanamori and D. L. Anderson. Theoretical basis of some empirical relations in seismology. *Bulletin of the Seismological Society of America*, 65(5):1073–1095, 1975. 16

H. Kanamori, N. Fujii, and H. Mizutani. Thermal diffusivity measurement of rock-forming minerals from 300° to 1100°K. *Journal of Geophysical Research (Solid Earth)*, 73:595–605, 1968. doi:10.1029/JB073i002p00595. 124

H. Kanamori, D. L. Anderson, and T. H. Heaton. Frictional melting during the rupture of the 1994 Bolivian earthquake. *Science*, 279:839, 1998. doi:10.1126/science.279.5352.839. 15

S. Kaneshima, T. Okamoto, and H. Takenaka. Evidence for a metastable olivine wedge inside the subducted Mariana slab. *Earth and Planetary Science Letters*, 258:219–227, 2007. doi:10.1016/j.epsl.2007.03.035. 21

H. Kao and W.-P. Chen. The double seismic zone in Kuril-Kamchatka: The tale of two overlapping single zones. *Journal of Geophysical Research (Solid Earth)*, 99:6913–6930, 1994. doi:10.1029/93JB03409. 14, 51

S.-I. Karato. *Deformation of Earth Materials: An Introduction to the Rheology of the Solid Earth*. Cambridge University Press, 2008. 163

S.-I. Karato, M. R. Riedel, and D. A. Yuen. Rheological structure and deformation of subducted slabs in the mantle transition zone: implications for mantle circulation and deep earthquakes. *Physics of the Earth and Planetary Interiors*, 127: 83–108, 2001. doi:10.1016/S0031-9201(01)00223-0. 9, 45, 66, 67, 147, 154, 169, 173

H. Kawakatsu. Observability of the isotropic component of a moment tensor. *Geophysical Journal International*, 126:525–544, 1996. doi:10.1111/j.1365-246X.1996.tb05308.x. 19

H. Kawakatsu and T. Seno. Triple seismic zone and the regional variation of seismicity along the northern Honshu arc. *Journal of Geophysical Research (Solid Earth)*, 88:4215–4230, 1983. doi:10.1029/JB088iB05p04215. 14

H. Kawakatsu and S. Yoshioka. Metastable olivine wedge and deep dry cold slab beneath southwest Japan. *Earth and Planetary Science Letters*, 303(1-2):1–10, 2011. doi:10.1016/j.epsl.2011.01.008. 21, 144

T. Kawamoto. Hydrous phase stability and partial melt chemistry in H_2O-saturated KLB-1 peridotite up to the uppermost lower mantle conditions. *Physics of the Earth and Planetary Interiors*, 143:387–395, 2004. doi:10.1016/j.pepi.2003.06.003. 150

T. Kawazoe, S.-I. Karato, K. Otsuka, Z. Jing, and M. Mookherjee. Shear deformation of dry polycrystalline olivine under deep upper mantle conditions using a rotational Drickamer apparatus (RDA). *Physics of the Earth and Planetary Interiors*, 174:128–137, 2009. doi:10.1016/j.pepi.2008.06.027. 164, 165

P. B. Kelemen and G. Hirth. A periodic shear-heating mechanism for intermediate-depth earthquakes in the mantle. *Nature*, 446:787–790, 2007. doi:10.1038/nature05717. 9, 14, 106, 147

D. S. Kelley, J. A. Karson, D. K. Blackman, G. L. Früh-Green, D. A. Butterfield, M. D. Lilley, E. J. Olson, M. O. Schrenk, K. K. Roe, G. T. Lebon, P. Rivizzigno, and a. AT3-60 Shipboard Party. An off-axis hydrothermal vent field near the Mid-Atlantic Ridge at 30° N. *Nature*, 412:145–149, 2001. doi:10.1038/35084000. 115

B. L. N. Kennett and E. R. Engdahl. Traveltimes for global earthquake location and phase identification. *Geophysical Journal International*, 105(2):429–465, 1991. doi:10.1111/j.1365-246X.1991.tb06724.x. 26

B. L. N. Kennett and A. Gorbatov. Seismic heterogeneity in the mantle-strong shear wave signature of slabs from joint tomography. *Physics of the Earth and Planetary Interiors*, 146:87–100, 2004. doi:10.1016/j.pepi.2003.07.033. 152, 163

H. Keppler, L. S. Dubrovinsky, O. Narygina, and I. Kantor. Optical absorption and radiative thermal conductivity of silicate perovskite to 125 gigapascals. *Science*, 322:1529–, 2008. doi:10.1126/science.1164609. 128

S. D. King. Subduction zones: observations and geodynamic models. *Physics of the Earth and Planetary Interiors*, 127:9–24, 2001. doi:10.1016/S0031-9201(01)00218-7. 7, 65, 146

S. Kirby, E. Engdahl, and R. Denlinger. Intermediate-depth intraslab earthquakes and arc volcanism as physical expressions of crustal and uppermost mantle metamorphism in subducting slabs. In G. E. Bebout, D. W. Scholl, S. H. Kirby, and J. P. Platt, editors, *Subduction: Top to bottom: American Geophysical Union Geophysical Monograph 96*, pages 195–214. American Geophysical Union, Washington D.C., 1996. 13, 76, 115, 123

S. H. Kirby and E. R. Engdahl. Curvilinear belts of intermediate-depth earthquakes in the Nazca slab: An expression of the thermomechanical effects of deeply subducted volcanic island-and-seamount chains? *Eos Trans. AGU*, 74:92, 1993. 13, 76

S. H. Kirby, W. B. Durham, and L. A. Stern. Mantle phase changes and deep-earthquake faulting in subducting lithosphere. *Science*, 252:216–225, 1991. doi:10.1126/science.252.5003.216. 12, 45, 123

S. H. Kirby, S. Stein, E. A. Okal, and D. C. Rubie. Metastable mantle phase transformations and deep earthquakes in subducting oceanic lithosphere. *Reviews of Geophysics*, 34:261–306, 1996. doi:10.1029/96RG01050. 10, 45, 124, 143, 144, 161, 169

S. H. Kirby, E. A. Okal, J. Laursen, and E. R. Engdahl. The volcanic Juan Fernandez Island-and-Seamount Chain and associated intraslab earthquake belt: Evidence for reactivation of faults in the Nazca Slab produced by subduction of the volcanic chain. *Eos Trans. AGU*, 82(47):S42D–07, 2001. 13

E. Kiser, M. Ishii, C. H. Langmuir, P. M. Shearer, and H. Hirose. Insights into the mechanism of intermediate-depth earthquakes from source properties as imaged by back projection of multiple seismic phases. *Journal of Geophysical Research (Solid Earth)*, 116(B15):B06310, 2011. doi:10.1029/2010JB007831. 23, 82, 106, 169

S. Klemme. The influence of Cr on the garnet-spinel transition in the Earth's mantle: experiments in the system MgO-Cr_2O_3-SiO_2 and thermodynamic modelling. *Lithos*, 77:639–646, 2004. doi:10.1016/j.lithos.2004.03.017. 112

E. Knittle. Static compression measurements of equations of state. In T. J. Ahrens, editor, *AGU Reference Shelf 2: Mineral Physics and Crystallography; A handbook of physical constants*, pages 98–142. American Geophysical Union, 1995. 130, 134

Y. Kobayashi. Anisotropy of thermal diffusivity in olivine, pyroxene, and dunite. *Journal of Physics of the Earth*, 22:359–373, 1974. 124

T. Komabayashi and S. Omori. Internally consistent thermodynamic data set for dense hydrous magnesium silicates up to 35 GPa, 1600°C: Implications for water circulation in the Earth's deep mantle. *Physics of the Earth and Planetary Interiors*, 156:89–107, 2006. doi:10.1016/j.pepi.2006.02.002. 106

L. P. G. Koning. Preliminary note on the frequency-depth relation of earthquakes. *K. Nederland. Akad. Wetensk. Proc.*, 56: 301–302, 1953. 12

K. D. Koper and D. A. Wiens. The waveguide effect of metastable olivine in slabs. *Geophysical Research Letters*, 27:581–+, 2000. doi:10.1029/1999GL011007. 22

K. D. Koper, D. A. Wiens, L. M. Dorman, J. A. Hildebrand, and S. C. Webb. Modeling the Tonga slab: Can travel time data resolve a metastable olivine wedge? *Journal of Geophysical Research (Solid Earth)*, 103:30079–30100, 1998. doi:10.1029/98JB01517. 21, 22

J. Korenaga. Thermal cracking and the deep hydration of oceanic lithosphere: A key to the generation of plate tectonics? *Journal of Geophysical Research (Solid Earth)*, 112:B05408, 2007. doi:10.1029/2006JB004502. 115

V. Kostrov. Seismic moment and energy of earthquakes, and seismic flow of rock. *Physics of the Solid Earth*, 1:13–21, 1974. 154

I. Y. Koulakov, N. L. Dobretsov, N. A. Bushenkova, and A. V. Yakovlev. Slab shape in subduction zones beneath the Kurile-Kamchatka and Aleutian arcs based on regional tomography results. *Russian Geology and Geophysics*, 52:650–667, 2011. doi:10.1016/j.rgg.2011.05.008. 66

K. S. Krishna, J. M. Bull, and R. A. Scrutton. Evidence for multiphase folding of the central Indian Ocean lithosphere. *Geology*, 29:715, 2001. doi:10.1130/0091-7613(2001)029<0715:EFMFOT>2.0.CO;2. 173

K. Kuge and H. Kawakatsu. Significance of non-double couple components of deep and intermediate-depth earthquakes: implications from moment tensor inversions of long-period seismic waves. *Physics of the Earth and Planetary Interiors*, 75: 243–266, 1993. doi:10.1016/0031-9201(93)90004-S. 19

K. Kuge and T. Lay. Systematic non-double-couple components of earthquake mechanisms: The role of fault zone irregularity. *Journal of Geophysical Research (Solid Earth)*, 99:15457, 1994. doi:10.1029/94JB00140. 162

T. Kummer and G. A. Spinelli. Hydrothermal circulation in subducting crust reduces subduction zone temperatures. *Geology*, 36:91–94, 2008. doi:10.1130/G24128A.1. 124

G. N. Lance and W. T. Williams. A general theory of classificatory sorting strategies: 1. Hierarchical systems. *The Computer Journal*, 9(4):373–380, 1967. doi:10.1093/comjnl/9.4.373. 28

D. Lange, F. Tilmann, A. Rietbrock, R. Collings, D. Natawidjaja, B. Suwargadi, P. Barton, T. Henstock, and T. Ryberg. The fine structure of the subducted Investigator Fracture Zone in western Sumatra as seen by local seismicity. *Earth and Planetary Science Letters*, 298(1-2):47–56, 2010. doi:10.1016/j.epsl.2010.07.020. 13, 76

T. Lay. Seismological constraints on the velocity structure and fate of subducting lithospheric slabs: 25 years of progress. In R. Dmowska and B. Saltzman, editors, *Seismological Structure of Slabs*, volume 35, pages 1–180. Elsevier, 1994. doi:10.1016/S0065-2687(08)60014-X. 6

M. Lefeldt and I. Grevemeyer. Centroid depth and mechanism of trench-outer rise earthquakes. *Geophysical Journal International*, 172:240–251, 2008. doi:10.1111/j.1365-246X.2007.03616.x. 115

M. Lefeldt, I. Grevemeyer, J. Goßler, and J. Bialas. Intraplate seismicity and related mantle hydration at the Nicaraguan trench outer rise. *Geophysical Journal International*, 178:742–752, 2009. doi:10.1111/j.1365-246X.2009.04167.x. 118

A. Leith and J. A. Sharpe. Deep-focus earthquakes and their geological significance. *Journal of Geology*, 44:877–917, 1936. doi:10.1086/624495. 9

C. Li and R. D. van der Hilst. Structure of the upper mantle and transition zone beneath southeast Asia from traveltime tomography. *Journal of Geophysical Research (Solid Earth)*, 115(B14):B07308, 2010. doi:10.1029/2009JB006882. 83

C. Li, R. D. van der Hilst, E. R. Engdahl, and S. Burdick. A new global model for P wave speed variations in Earth's mantle. *Geochemistry, Geophysics, Geosystems*, 90:Q05018, 2008. doi:10.1029/2007GC001806. 13, 66

K. Litasov, A. Shatskiy, and N. Pokhilenko. Phase relations and melting in the systems of peridotite-H_2O-CO_2 and eclogite-H_2O-CO_2 at pressures up to 27 GPa. *Doklady Earth Sciences*, 437:498–502, 2011. doi:10.1134/S1028334X11040143. 150

M. Liu, L. Kerschhofer, J. L. Mosenfelder, and D. C. Rubie. The effect of strain energy on growth rates during the olivine-spinel transformation and implications for olivine metastability in subducting slabs. *Journal of Geophysical Research (Solid Earth)*, 103:23897–23910, 1998. doi:10.1029/98JB00794. 145

J. A. Ludwig and J. F. Reynolds. *Statistical Ecology; A Primer on Methods and Computing*. John Wiley and Sons, New York, 1988. 28

M. G. Lund and H. Austrheim. High-pressure metamorphism and deep-crustal seismicity: evidence from contemporaneous formation of pseudotachylytes and eclogite facies coronas. *Tectonophysics*, 372:59–83, 2003. doi:10.1016/S0040-1951(03)00232-4. 11

P. Lundgren and D. Giardini. Isolated deep earthquakes and the fate of subduction in the mantle. *Journal of Geophysical Research (Solid Earth)*, 99:15833–15842, 1994. doi:10.1029/94JB00038. 15

P. Lundgren and D. Giardini. The June 9 Bolivia and March 9 Fiji deep earthquakes of 1994: I. Source processes. *Geophysical Research Letters*, 22:2241–2244, 1995. doi:10.1029/95GL02233. 20

P. R. Lundgren and D. Giardini. Seismicity, shear failure and modes of deformation in deep subduction zones. *Physics of the Earth and Planetary Interiors*, 74:63–74, 1992. doi:10.1016/0031-9201(92)90068-7. 13, 19, 50, 68, 79, 81, 100, 102, 108

C. S. Lynnes and T. Lay. Source process of the great 1977 Sumba earthquake. *Journal of Geophysical Research (Solid Earth)*, 93: 13407–13420, 1988. doi:10.1029/JB093iB11p13407. 115

A. MacDonald and W. Fyfe. Rate of serpentinization in seafloor environments. *Tectonophysics*, 116:123–135, 1985. doi:10.1016/0040-1951(85)90225-2. 114

D. Mainprice, Y. Le Page, J. Rodgers, and P. Jouanna. Predicted elastic properties of the hydrous D phase at mantle pressures: Implications for the anisotropy of subducted slabs near 670-km discontinuity and in the lower mantle. *Earth and Planetary Science Letters*, 259:283–296, 2007. doi:10.1016/j.epsl.2007.04.053. 23

F. C. Marton, T. J. Shankland, D. C. Rubie, and Y. Xu. Effects of variable thermal conductivity on the mineralogy of subducting slabs and implications for mechanisms of deep earthquakes. *Physics of the Earth and Planetary Interiors*, 149: 53–64, 2005. doi:10.1016/j.pepi.2004.08.026. 10, 125, 126, 130, 145, 147

D. G. Masson. Fault patterns at outer trench walls. *Marine Geophysical Researches*, 13:209–225, 1991. doi:10.1007/BF00369150. 78, 105

D. C. McAdoo and D. T. Sandwell. Folding of oceanic lithosphere. *Journal of Geophysical Research (Solid Earth)*, 90:8563–8569, 1985. doi:10.1029/JB090iB10p08563. 173

J. J. McGuire, L. Zhao, and T. H. Jordan. Teleseismic inversion for the second-degree moments of earthquake space-time distributions. *Geophysical Journal International*, 145:661–678, 2001. doi:10.1046/j.1365-246X.2001.01414.x. 85

D. McKenzie. Temperature and potential temperature beneath island arcs. *Tectonophysics*, 10:357–366, 1970. doi:10.1016/0040-1951(70)90115-0. 5, 8, 124

D. McKenzie and M. J. Bickle. The volume and composition of melt generated by extension of the lithosphere. *Journal of Petrology*, 29:625–679, 1988. doi:10.1093/petrology/29.3.625. 130

D. McKenzie, J. Jackson, and K. Priestley. Thermal structure of oceanic and continental lithosphere. *Earth and Planetary Science Letters*, 233:337–349, 2005. doi:10.1016/j.epsl.2005.02.005. 80, 123, 124, 130, 131, 135

D. P. McKenzie. Speculations on the consequences and causes of plate motions. *Geophysical Journal International*, 18:1–32, 1969a. doi:10.1111/j.1365-246X.1969.tb00259.x. 5, 8, 124

D. P. McKenzie. The relation between fault plane solutions for earthquakes and the directions of the principal stresses. *Bulletin of the Seismological Society of America*, 59(2):591–601, 1969b. 43

C. Meade and R. Jeanloz. Deep-focus earthquakes and recycling of water into the Earth's mantle. *Science*, 252:68–72, 1991. doi:10.1126/science.252.5002.68. 8

S. Mei, A. M. Suzuki, D. L. Kohlstedt, N. A. Dixon, and W. B. Durham. Experimental constraints on the strength of the lithospheric mantle. *Journal of Geophysical Research (Solid Earth)*, 115(B14):B08204, 2010. doi:10.1029/2009JB006873. 66, 164, 165

E. Melekhova, M. W. Schmidt, P. Ulmer, and T. Pettke. The composition of liquids coexisting with dense hydrous magnesium silicates at 11-13.5 GPa and the endpoints of the solidi in the MgO-SiO_2-H_2O system. *Geochimica et Cosmochimica Acta*, 71:3348–3360, 2007. doi:10.1016/j.gca.2007.03.034. 150

A. J. Michael. Spatial patterns of aftershocks of shallow focus earthquakes in California and implications for deep focus earthquakes. *Journal of Geophysical Research (Solid Earth)*, 94:5615–5626, 1989. doi:10.1029/JB094iB05p05615. 14

J. W. Minear and M. N. Toksöz. Thermal regime of a downgoing slab and New Global Tectonics. *Journal of Geophysical Research (Solid Earth)*, 75:1397–1419, 1970. doi:10.1029/JB075i008p01397. 124

J. S. B. Mitchell, D. M. Mount, and C. H. Papadimitriou. The discrete geodesic problem. *SIAM J. Comput.*, 16(4):647–668, 1987. doi:10.1137/0216045. 77, 156

L. Moresi and M. Gurnis. Constraints on the lateral strength of slabs from three-dimensional dynamic flow models. *Earth and Planetary Science Letters*, 138:15–28, 1996. doi:10.1016/0012-821X(95)00221-W. 66, 164

H. Moriya, H. Niitsuma, and R. Baria. Multiplet-clustering analysis reveals structural details within the seismic cloud at the Soultz geothermal field, France. *Bulletin of the Seismological Society of America*, 93(4):1606–1620, 2003. doi:10.1785/0120020072. 25

J. L. Mosenfelder, F. C. Marton, C. R. Ross, L. Kerschhofer, and D. C. Rubie. Experimental constraints on the depth of olivine metastability in subducting lithosphere. *Physics of the Earth and Planetary Interiors*, 127:165–180, 2001. doi:10.1016/S0031-9201(01)00226-6. 10, 125, 145

R. D. Müller, M. Sdrolias, C. Gaina, and W. R. Roest. Age, spreading rates, and spreading asymmetry of the world's ocean crust. *Geochemistry, Geophysics, Geosystems*, 9:4006–4025, 2008. doi:10.1029/2007GC001743. 57, 83, 132, 133, 140

S. C. Myers, T. C. Wallace, S. L. Beck, P. G. Silver, G. Zandt, J. Vandecar, and E. Minaya. Implications of spatial and temporal development of the aftershock sequence for the M_W 8.3 June 9, 1994 deep Bolivia earthquake. *Geophysical Research Letters*, 22:2269–2272, 1995. doi:10.1029/95GL01600. 1, 14

R. Myhill. Slab bending and its effect on the distributions and focal mechanisms of deep-focus earthquakes. *Geophysical Journal International, submitted*, 2012. 43

R. Myhill and L. M. Warren. Fault plane orientations of deep earthquakes in the Izu-Bonin-Marianas subduction zone. *Journal of Geophysical Research (Solid Earth)*, 117:B06307, 2012. doi:10.1029/2011JB009047. 82, 86, 96, 99, 103, 104

R. Myhill, D. McKenzie, and K. Priestley. The distribution of earthquake multiplets beneath the southwest Pacific. *Earth and Planetary Science Letters*, 301:87–97, 2011. doi:10.1016/j.epsl.2010.10.023. 25, 29

J. Nakajima and A. Hasegawa. Anomalous low-velocity zone and linear alignment of seismicity along it in the subducted Pacific slab beneath Kanto, Japan: Reactivation of subducted fracture zone? *Geophysical Research Letters*, 33:L16309, 2006. doi:10.1029/2006GL026773. 13, 76, 169

J. Nakajima, Y. Tsuji, A. Hasegawa, S. Kita, T. Okada, and T. Matsuzawa. Tomographic imaging of hydrated crust and mantle in the subducting Pacific slab beneath Hokkaido, Japan: Evidence for dehydration embrittlement as a cause of intraslab earthquakes. *Gondwana Research*, 16(3-4):470–481, 2009. doi:10.1016/j.gr.2008.12.010. 22, 76, 119

J. Nakajima, A. Hasegawa, and S. Kita. Seismic evidence for reactivation of a buried hydrated fault in the Pacific slab by the 2011 M9.0 Tohoku earthquake. *Geophysical Research Letters*, 38:L00G06, 2011. doi:10.1029/2011GL048432. 23, 68, 105, 119

M. Nakanishi. Bending-related topographic structure of the subducting plate in the northwestern Pacific Ocean. In Y. Ogawa, R. Anma, and Y. Dilek, editors, *Accretionary Prisms and Convergent Margin Tectonics in the northwest Pacific Basin, modern approaches in solid Earth sciences 8*, pages 1–38. Springer Science+Business Media B.V., Berlin, 2011. doi:10.1007/978-90-481-8885-7.1. 83

M. Nakanishi, K. Tamaki, and K. Kobayashi. Magnetic anomaly lineations from Late Jurassic to Early Cretaceous in the west-central Pacific Ocean. *Geophysical Journal International*, 109:701–719, 1992. doi:10.1111/j.1365-246X.1992.tb00126.x. 78, 83

S. H. Nawab, F. U. Dowla, and R. T. Lacoss. Direction determination of wideband signals. *IEEE Transactions on Acoustics Speech and Signal Processing*, 33(5):1114–1122, 1985. doi:10.1109/TASSP.1985.1164705. 32

M. R. Nedimović, D. R. Bohnenstiehl, S. M. Carbotte, J. Pablo Canales, and R. P. Dziak. Faulting and hydration of the Juan de Fuca plate system. *Earth and Planetary Science Letters*, 284:94–102, 2009. doi:10.1016/j.epsl.2009.04.013. 118

S. Nothard, J. Haines, J. Jackson, and B. Holt. Distributed deformation in the subducting lithosphere at Tonga. *Geophysical Journal International*, 127:328–338, 1996a. doi:10.1111/j.1365-246X.1996.tb04723.x. 65, 152, 163

S. Nothard, D. McKenzie, J. Haines, and J. Jackson. Gaussian curvature and the relationship between the shape and the deformation of the Tonga slab. *Geophysical Journal International*, 127:311–327, 1996b. doi:10.1111/j.1365-246X.1996.tb04722.x. 44, 152

A. J. Oakley, B. Taylor, and G. F. Moore. Pacific Plate subduction beneath the central Mariana and Izu-Bonin fore arcs: New insights from an old margin. *Geochemistry, Geophysics, Geosystems*, 90:Q06003, 2008. doi:10.1029/2007GC001820. 83, 105

M. Ogawa. Shear instability in a viscoelastic material as the cause of deep focus earthquakes. *Journal of Geophysical Research (Solid Earth)*, 92:13801–13810, 1987. doi:10.1029/JB092iB13p13801. 9, 169

E. A. Okal. "Detached" deep earthquakes: are they really? *Physics of the Earth and Planetary Interiors*, 127:109–143, 2001. doi:10.1016/S0031-9201(01)00224-2. 13

E. A. Okal and C. R. Bina. On the cessation of seismicity at the base of the transition zone. *Journal of Seismology*, 2:65–86, 1998. doi:10.1023/A:1009789222914. 12, 148

E. A. Okal and S. H. Kirby. Frequency-moment distribution of deep earthquakes; implications for the seismogenic zone at the bottom of slabs. *Physics of the Earth and Planetary Interiors*, 92:169–187, 1995. doi:10.1016/0031-9201(95)03037-8. 17

E. A. Okal and S. H. Kirby. Deep earthquakes beneath the Fiji Basin, SW Pacific: Earth's most intense deep seismicity in stagnant slabs. *Physics of the Earth and Planetary Interiors*, 109(1-2):25–63, 1998. doi:10.1016/S0031-9201(98)00116-2. 13, 40, 79

E. A. Okal and J. Talandier. T waves from the great 1994 Bolivian deep earthquake in relation to channeling of S wave energy up the slab. *Journal of Geophysical Research (Solid Earth)*, 102:27421–27438, 1997. doi:10.1029/97JB02718. 13

R. Oldham. The geological interpretation of the Earth-movements associated with the Californian earthquake of April 18th, 1906. *Quarterly Journal of the Geological Society*, 65(1-4):1–20, 1909. 5

D. A. Oleskevich, R. D. Hyndman, and K. Wang. The updip and downdip limits to great subduction earthquakes: Thermal and structural models of Cascadia, south Alaska, SW Japan, and Chile. *Journal of Geophysical Research (Solid Earth)*, 104: 14965–14992, 1999. doi:10.1029/1999JB900060. 1

J. Oliver and B. Isacks. Deep earthquake zones, anomalous structures in the upper mantle and the lithosphere. *Journal of Geophysical Research (Solid Earth)*, 72:4259–4275, 1967. doi:10.1029/JZ072i016p04259. 5

S. Omori, T. Komabayashi, and S. Maruyama. Dehydration and earthquakes in the subducting slab: empirical link in intermediate and deep seismic zones. *Physics of the Earth and Planetary Interiors*, 146:297–311, 2004. doi:10.1016/j.pepi.2003.08.014. 8, 23, 45, 64, 106, 150, 169

E. Orowon. Mechanism of seismic faulting. *Geol. Soc. Amer. Mem.*, 79:323–345, 1960. 9

M. Osako and E. Ito. Thermal diffusivity of MgSiO3 perovskite. *Geophysical Research Letters*, 18:239–242, 1991. doi:10.1029/91GL00212. 134

M. Osako and Y. Kobayashi. Thermal diffusivity of stishovite. *Physics of the Earth and Planetary Interiors*, 18:P1–P4, 1979. doi:10.1016/0031-9201(79)90128-6. 134

E. R. Oxburgh and D. L. Turcotte. The physico-chemical behaviour of the descending lithosphere. *Tectonophysics*, 32: 107–128, 1976. doi:10.1016/0040-1951(76)90088-3. 115, 124

J. A. Padrón-Navarta, A. Tommasi, C. J. Garrido, V. L. Sánchez-Vizcaíno, M. T. Gómez-Pugnaire, A. Jabaloy, and A. Vauchez. Fluid transfer into the wedge controlled by high-pressure hydrofracturing in the cold top-slab mantle. *Earth and Planetary Science Letters*, 297(1-2):271–286, 2010. doi:10.1016/j.epsl.2010.06.029. 121

S.-C. Park and J. Mori. Rupture velocity estimation of large deep-focus earthquakes surrounding Japan. *Journal of Geophysical Research (Solid Earth)*, 113:B08303, 2008. doi:10.1029/2007JB005434. 20, 85, 99

B. Parsons and J. G. Sclater. An analysis of the variation of ocean floor bathymetry and heat flow with age. *Journal of Geophysical Research (Solid Earth)*, 82:802–827, 1977. doi:10.1029/JB082i005p00803. 135

S. Peacock. Are the lower planes of double seismic zones caused by serpentine dehydration in subducting oceanic mantle? *Geology*, 29(4):299–302, 2001. doi:10.1130/0091-7613(2001)029<0299:ATLPOD>2.0.CO;2. 14, 115

S. Peacock. Insight into the hydrogeology and alteration of oceanic lithosphere based on subduction zones and arc volcanism. In E. E. Davis and H. Elderfield, editors, *Hydrogeology of the Oceanic Lithosphere*, pages 659–676. Cambridge University Press, Cambridge, UK, 2004. 118

S. M. Peacock. Numerical simulation of metamorphic pressure-temperature-time paths and fluid production in subducting slabs. *Tectonics*, 9:1197–1211, 1990. doi:10.1029/TC009i005p01197. 124

S. M. Peacock. The importance of blueschist → eclogite dehydration reactions in subducting oceanic crust. *Geological Society of America Bulletin*, 105(5):684–694, 1993. doi:10.1130/0016-7606(1993)105<0684:TIOBED>2.3.CO;2. 124

S. M. Peacock and R. D. Hyndman. Hydrous minerals in the mantle wedge and the maximum depth of subduction thrust earthquakes. *Geophysical Research Letters*, 26:2517–2520, 1999. doi:10.1029/1999GL900558. 1

S. M. Peacock and K. Wang. Seismic consequences of warm versus cool subduction metamorphism: Examples from southwest and northeast Japan. *Science*, 286(5441):937–939, 1999. doi:10.1126/science.286.5441.937. 124

S. E. Persh and H. Houston. Strongly depth-dependent aftershock production in deep earthquakes. *The Bulletin of the Seismological Society of America*, 94:1808–1816, 2004. doi:10.1785/012003191. 169

L. Pilgrim. Die berechnung der laufzeiten eines erdstosses mit berücksichtigung der herdtiefen, getstützt auf neurere beobachtungen. *Gerlands Beiträge zur Geophysik*, 12:363–483, 1913. 5

S. Poli and M. W. Schmidt. Petrology of subducted slabs. *Annual Review of Earth and Planetary Sciences*, 30:207–235, 2002. doi:10.1146/annurev.earth.30.091201.140550. 116, 117

D. D. Pollard, P. Segall, and P. T. Delaney. Formation and interpretation of dilatant echelon cracks. *GSA Bulletin*, 93(12): 1291–1303, 1982. doi:10.1130/âĂŃ0016-7606(1982)âĂŃ93<1291:FAIODE>âĂŃ2.0.CO;2. 68

G. Poupinet, W. L. Ellsworth, and J. Frechet. Monitoring velocity variations in the crust using earthquake doublets - an application to the Calaveras Fault, California. *Journal of Geophysical Research (Solid Earth)*, 89(NB7):5719–5731, 1984. doi:10.1029/JB089iB07p05719. 25, 26, 41

G. Poupinet, J. Got, and F. Brenguier. Chapter 14: Monitoring temporal variations of physical properties in the crust by cross-correlating the waveforms of seismic doublets. *Advances in Geophysics*, 50:373–399, 2008. doi:10.1016/S0065-2687(08)00014-9. 26

C. B. Raleigh. Tectonic implications of serpentinite weakening. *Geophysical Journal of the Royal Astronomical Society*, 14(1-4): 113–118, 1967. doi:10.1111/j.1365-246X.1967.tb06229.x. 8

C. B. Raleigh and M. S. Paterson. Experimental deformation of serpentinite and its tectonic implications. *Journal of Geophysical Research (Solid Earth)*, 70:3965–3985, 1965. doi:10.1029/JZ070i016p03965. 8

G. E. Randall and T. J. Owens. Array analysis of the large-aperture array of the 1988-89 PASSCAL Basin and Range Passive-Source Seismic Experiment. *Geophysical Journal International*, 116(3):618–636, 1994. doi:10.1111/j.1365-246X.1994.tb03285.x. 31

C. R. Ranero and V. Sallarès. Geophysical evidence for hydration of the crust and mantle of the Nazca plate during bending at the north Chile trench. *Geology*, 32:549–552, 2004. doi:10.1130/G20379.1. 117

C. R. Ranero, J. Phipps Morgan, K. McIntosh, and C. Reichert. Bending-related faulting and mantle serpentinization at the Middle America trench. *Nature*, 425:367–373, 2003. doi:10.1038/nature01961. 105, 115, 118

C. R. Ranero, A. Villaseñor, J. Phipps Morgan, and W. Weinrebe. Relationship between bend-faulting at trenches and intermediate-depth seismicity. *Geochemistry, Geophysics, Geosystems*, 6:Q12002, 2005. doi:10.1029/2005GC000997. 82, 105

P. Raterron, Y. Wu, D. J. Weidner, and J. Chen. Low-temperature olivine rheology at high pressure. *Physics of the Earth and Planetary Interiors*, 145:149–159, 2004. doi:10.1016/j.pepi.2004.03.007. 163, 164, 165

P. Raterron, J. Chen, T. Geenan, and J. Girard. Pressure effect on forsterite dislocation slip systems: Implications for upper mantle LPO and low viscosity zone. *Physics of the Earth and Planetary Interiors*, pages 26–36, 2011. doi:10.1016/j.pepi.2011.06.009. 106

B. A. Rees and E. A. Okal. The depth of the deepest historical earthquakes. *Pure and Applied Geophysics*, 125:699–715, 1987. doi:10.1007/BF00878029. 1, 148

H. Reid. *The California Earthquake of April 18, 1906: The Mechanics of the Earthquake*. Carnegie Inst., 1910. 5

B. Reynard, J. Nakajima, and H. Kawakatsu. Earthquakes and plastic deformation of anhydrous slab mantle in double Wadati-Benioff zones. *Geophysical Research Letters*, 37:L24309, 2010. doi:10.1029/2010GL045494. 22, 68, 119, 120, 121

M. Reyners, D. Eberhart-Phillips, G. Stuart, and Y. Nishimura. Imaging subduction from the trench to 300 km depth beneath the central North Island, New Zealand, with V_P and V_P/V_S. *Geophysical Journal International*, 165:565–583, 2006. doi:10.1111/j.1365-246X.2006.02897.x. 13

M. A. Richards and C. Lithgow-Bertelloni. Plate motion changes, the Hawaiian-Emperor bend, and the apparent success and failure of geodynamic models. *Earth and Planetary Science Letters*, 137:19–27, 1996. doi:10.1016/0012-821X(95)00209-U. 85, 146

A. Rietbrock and F. Waldhauser. A narrowly spaced double-seismic zone in the subducting Nazca plate. *Geophysical Research Letters*, 31:L10608, 2004. doi:10.1029/2004GL019610. 7, 14

D. C. Roberts and D. L. Turcotte. Earthquakes: Friction or a plastic instability? In J. B. Rundle, D. L. Turcotte, and W. Klein, editors, *GeoComplexity and the physics of earthquakes: American Geophysical Union Geophysical Monograph 120*, pages 97–103. American Geophysical Union, Washington D.C., 2000. 170

S. W. Roecker. Velocity structure of the Pamir-Hindu Kush region: Possible evidence of subducted crust. *Journal of Geophysical Research (Solid Earth)*, 87(B2):945–959, 1982. doi:10.1029/JB087iB02p00945. 111

E. Roland, M. D. Behn, and G. Hirth. Thermal-mechanical behavior of oceanic transform faults: Implications for the spatial distribution of seismicity. *Geochemistry, Geophysics, Geosystems*, 11:Q07001, 2010. doi:10.1029/2010GC003034. 80, 114

A. D. Rosa, C. Sanchez-Valle, S. Ghosh, and S. Merkel. Elasticity and rheology of Phase D and implications for seismic anisotropy in deep subducted slabs. *AGU Fall Meeting Abstracts*, pages –, 2011. 23

C. Rowe, R. Aster, B. Borchers, and C. Young. An automatic, adaptive algorithm for refining phase picks in large seismic data sets. *Bulletin of the Seismological Society of America*, 92(5):1660–1674, 2002. doi:10.1785/0120010224. 28, 29, 48, 175

D. C. Rubie and C. R. Ross, II. Kinetics of the olivine-spinel transformation in subducting lithosphere: experimental constraints and implications for deep slab processes. *Physics of the Earth and Planetary Interiors*, 86:223–241, 1994. doi:10.1016/0031-9201(94)05070-8. 144

A. M. Rubin, D. Gillard, and J. Got. Streaks of microearthquakes along creeping faults. *Nature*, 400:635–641, 1999. doi:10.1038/23196. 25

J. L. Rubinstein and G. C. Beroza. Full waveform earthquake location: Application to seismic streaks on the Calaveras Fault, California. *Journal of Geophysical Research (Solid Earth)*, 112(B11):5303–5316, 2007. doi:10.1029/2006JB004463. 25

J. F. Rudge, P. B. Kelemen, and M. Spiegelman. A simple model of reaction-induced cracking applied to serpentinization and carbonation of peridotite. *Earth and Planetary Science Letters*, 291(1-4):215–227, 2010. doi:10.1016/j.epsl.2010.01.016. 114

E. H. Rutter, S. Llana-Fúnez, and K. H. Brodie. Dehydration and deformation of intact cylinders of serpentinite. *Journal of Structural Geology*, 31:29–43, 2009. doi:10.1016/j.jsg.2008.09.008. 8

M. Sandiford. Seismic moment release during slab rupture beneath the Banda Sea. *Geophysical Journal International*, 174: 659–671, 2008. doi:10.1111/j.1365-246X.2008.03838.x. 154

D. T. Sandwell and W. H. F. Smith. Global marine gravity from retracked Geosat and ERS-1 altimetry: Ridge segmentation versus spreading rate. *Journal of Geophysical Research (Solid Earth)*, 114(B13):1411–1428, 2009. doi:10.1029/2008JB006008. 78

B. Savage. Seismic constraints on the water flux delivered to the deep earth by subduction. *Geology*, 40(3):235–238, 2012. doi:10.1130/G32499.1. 119

J. Savage. The mechanics of deep-focus faulting. *Tectonophysics*, 8:115–127, 1969. doi:10.1016/0040-1951(69)90085-7. 7, 82, 105, 106

D. P. Schaff and P. G. Richards. Repeating seismic events in China. *Science*, 303(5661):1176–1178, 2004. doi:10.1126/science.1093422. 25

J. F. Schatz and G. Simmons. Thermal conductivity of Earth materials at high temperatures. *Journal of Geophysical Research (Solid Earth)*, 77:6966–6983, 1972. doi:10.1029/JB077i035p06966. 124, 131

H. H. Schloessin and Z. Dvořák. Anisotropic lattice thermal conductivity in enstatite as a function of pressure and temperature. *Geophysical Journal International*, 27:499–516, 1972. doi:10.1111/j.1365-246X.1972.tb06105.x. 134

N. Schmerr and C. Thomas. Subducted lithosphere beneath the Kuriles from migration of PP precursors. *Earth and Planetary Science Letters*, 311(1-2):101–111, 2011. doi:10.1016/j.epsl.2011.09.002. 21

D. Schorlemmer, S. Wiemer, and M. Wyss. Variations in earthquake-size distribution across different stress regimes. *Nature*, 437:539–542, 2005. doi:10.1038/nature04094. 17

G. Schubert, D. L. Turcotte, and P. Olson. *Mantle convection in the Earth and planets*. Cambridge University Press, Cambridge, UK, 2001. ISBN 052135367X. 126

M. Sdrolias and R. D. Müller. Controls on back-arc basin formation. *Geochemistry, Geophysics, Geosystems*, 7:Q04016, 2006. doi:10.1029/2005GC001090. 79

M. Searle, B. R. Hacker, and R. Bilham. The Hindu Kush Seismic Zone as a Paradigm for the Creation of Ultrahigh-Pressure Diamond- and Coesite-Bearing Continental Rocks. *Journal of Geology*, 109:143–153, 2001. doi:10.1086/319244. 111

G. F. Sella, T. H. Dixon, and A. Mao. REVEL: A model for Recent plate velocities from space geodesy. *Journal of Geophysical Research (Solid Earth)*, 107:2081, 2002. doi:10.1029/2000JB000033. 85

P. Shearer, E. Hauksson, and G. Q. Lin. Southern California hypocenter relocation with waveform cross-correlation, Part 2: Results using source-specific station terms and cluster analysis. *Bulletin of the Seismological Society of America*, 95(3): 904–915, 2005. doi:10.1785/0120040168. 25

H. Shiobara, H. Sugioka, K. Mochizuki, S. Oki, T. Kanazawa, Y. Fukao, and K. Suyehiro. Double seismic zone in the north Mariana region revealed by long-term ocean bottom array observation. *Geophysical Journal International*, 183:1455–1469, 2010. doi:10.1111/j.1365-246X.2010.04799.x. 14

P. Silver. Retrieval of source-extent parameters and the interpretation of corner frequency. *Bulletin of the Seismological Society of America*, 73(6A):1499–1511, 1983. 85

P. G. Silver, S. L. Beck, T. C. Wallace, C. Meade, S. C. Myers, D. E. James, and R. Kuehnel. Rupture characteristics of the deep Bolivian earthquake of 9 June 1994 and the mechanism of deep-focus earthquakes. *Science*, 268:69–73, 1995. doi:10.1126/science.268.5207.69. 105

H. P. Singh and G. Simmons. X-ray determination of thermal expansion of olivines. *Acta Crystallographica Section A*, 32: 771–773, 1976. doi:10.1107/S0567739476001575. 134

R. Slunga, S. T. Rognvaldsson, and R. Bodvarsson. Absolute and relative locations of similar events with application to microearthquakes in southern Iceland. *Geophysical Journal International*, 123:409–419, 1995. doi:10.1111/j.1365-246X.1995.tb06862.x. 25

W. H. F. Smith and P. Wessel. Gridding with continuous curvature splines in tension. *Geophysics*, 55:293–305, 1990. doi:10.1190/1.1442837. 46, 76

P. H. A. Sneath and R. R. Sokal. *Numerical taxonomy: the principles and practice of numerical classification*. WH Freeman. San Francisco. US, 1973. 28

R. Snieder. Coda wave interferometry and the equilibration of energy in elastic media. *Physical Review E*, 66(4):046615–046622, 2002. doi:10.1103/PhysRevE.66.046615. 41

R. Snieder and M. Vrijlandt. Constraining the source separation with coda wave interferometry: Theory and application to earthquake doublets in the Hayward fault, California. *Journal of Geophysical Research (Solid Earth)*, 110(B9):4301–4315, 2005. doi:10.1029/2004JB003317. 28

A. V. Sobolev, A. W. Hofmann, D. V. Kuzmin, G. M. Yaxley, N. T. Arndt, S.-L. Chung, L. V. Danyushevsky, T. Elliott, F. A. Frey, M. O. Garcia, A. A. Gurenko, V. S. Kamenetsky, A. C. Kerr, N. A. Krivolutskaya, V. V. Matvienkov, I. K. Nikogosian, A. Rocholl, I. A. Sigurdsson, N. M. Sushchevskaya, and M. Teklay. The amount of recycled crust in sources of mantle-derived melts. *Science*, 316:412–417, 2007. doi:10.1126/science.1138113. 117

H. Soosalu, J. Key, R. S. White, C. Knox, P. Einarsson, and S. S. Jakobsdóttir. Lower-crustal earthquakes caused by magma movement beneath Askja volcano on the north Iceland rift. *Bulletin of Volcanology*, page 40, 2009. doi:10.1007/s00445-009-0306-6. 123

P. B. Stark and C. Frohlich. The depths of the deepest deep earthquakes. *Journal of Geophysical Research (Solid Earth)*, 90: 1859–1870, 1985. doi:10.1029/JB090iB02p01859. 1, 12, 148

S. Stein and C. Stein. Thermo-mechanical evolution of oceanic lithosphere : Implications for the subduction process and deep earthquakes. In G. E. Bebout, D. W. Scholl, S. H. Kirby, and J. P. Platt, editors, *Subduction: Top to bottom: American Geophysical Union Geophysical Monograph 96*, pages 1–17. American Geophysical Union, Washington D.C., 1996. 124

M. G. Steltenpohl, G. Kassos, and A. Andresen. Retrograded eclogite-facies pseudotachylytes as deep-crustal paleoseismic faults within continental basement of Lofoten, north Norway. *Geosphere*, 2(1):61–72, 2006. doi:10.1130/GES00035.1. 11

R. J. Stern and S. H. Bloomer. Subduction zone infancy: Examples from the Eocene Izu-Bonin-Mariana and Jurassic California arcs. *Geological Society of America Bulletin*, 104(12):1621–1636, 1992. doi:10.1130/0016-7606(1992)104<1621:SZIEFT>2.3.CO;2. 85

R. J. Stern, M. J. Fouch, and S. L. Klemperer. An overview of the Izu-Bonin-Mariana subduction factory. In J. Eiler, editor, *Inside the Subduction Factory: American Geophysical Union Geophysical Monograph 138*, pages 175–222. American Geophysical Union, Washington D.C., 2003. doi:10.1029/138GM10. 83

L. Stixrude and C. Lithgow-Bertelloni. Thermodynamics of mantle minerals - II. Phase equilibria. *Geophysical Journal International*, 184:1180–1213, 2011. doi:10.1111/j.1365-246X.2010.04890.x. 113, 125, 143, 151, 155

A. Sugimura and S. Uyeda. A possible anisotropy of the upper mantle accounting for deep earthquake faulting. *Tectonophysics*, 5:25–33, 1967. doi:10.1016/0040-1951(67)90042-X. 106

Y. Sumino and O. Anderson. Elastic constants of minerals. In R. S. Carmichael, editor, *Handbook of physcial properties of rocks III*, pages 39–138. CRC, Boca Raton, 1984. 134

C. Sung and R. Burns. Kinetics of the olivine $\rightarrow$ spinel transition: Implications to deep-focus earthquake genesis. *Earth and Planetary Science Letters*, 32(2):165–170, 1976a. doi:10.1016/0012-821X(76)90055-8. 143

C. Sung and R. Burns. Kinetics of high-pressure phase-transformations - implications to evolution of olivine-spinel transition in the downgoing lithosphere and its consequences on the dynamics of the mantle. *Tectonophysics*, 31(1-2): 1–32, 1976b. doi:10.1016/0040-1951(76)90165-7. 143

S. Suzuki and M. Kasahara. Unbending and horizontal fracture of the subducting Pacific plate, as evidenced by the 1993 Kushiro-oki and the 1981 and 1987 intermediate-depth earthquakes in Hokkaido. *Physics of the Earth and Planetary Interiors*, 93:91–104, 1996. doi:10.1016/0031-9201(95)03090-5. 23, 107, 119, 169

L. R. Sykes. Deep-focus earthquakes in the New Hebrides region. *Journal of Geophysical Research (Solid Earth)*, 69:5353–5355, 1964. doi:10.1029/JZ069i024p05353. 13

L. R. Sykes. The seismicity and deep structure of island arcs. *Journal of Geophysical Research (Solid Earth)*, 71:2981–3006, 1966. doi:10.1029/JZ071i012p02981. 5, 12, 43, 45

E. M. Syracuse and G. A. Abers. Systematic biases in subduction zone hypocenters. *Geophysical Research Letters*, 361:L10303, 2009. doi:10.1029/2009GL037487. 21, 79

E. M. Syracuse, P. E. van Keken, and G. A. Abers. The global range of subduction zone thermal models. *Physics of the Earth and Planetary Interiors*, 183:73–90, 2010. doi:10.1016/j.pepi.2010.02.004. 124, 146

T. Tada and K. Shimazaki. How much does a high-velocity slab contribute to the apparent non-double-couple components in deep-focus earthquakes? *Bulletin of the Seismological Society of America*, 84(4):1272–1278, 1994. 19, 162

W. C. Tao and R. J. O'Connell. Deformation of a weak subducted slab and variation of seismicity with depth. *Nature*, 361: 626–628, 1993. doi:10.1038/361626a0. 23, 44

R. Tibi, C. H. Estabrook, and G. Bock. The 1996 June 17 Flores Sea and 1994 March 9 Fiji-Tonga earthquakes: source processes and deep earthquake mechanisms. *Geophysical Journal International*, 138:625–642, 1999. doi:10.1046/j.1365-246x.1999.00879.x. 20, 85

R. Tibi, D. A. Wiens, and J. A. Hildebrand. Aftershock locations and rupture characteristics of the 1995 Mariana deep earthquake. *Geophysical Research Letters*, 28:4311–4314, 2001. doi:10.1029/2001GL013059. 93

R. Tibi, G. Bock, and C. H. Estabrook. Seismic body wave constraint on mechanisms of intermediate-depth earthquakes. *Journal of Geophysical Research (Solid Earth)*, 107:2047, 2002. doi:10.1029/2001JB000361. 20, 85, 89

R. Tibi, G. Bock, and D. A. Wiens. Source characteristics of large deep earthquakes: Constraint on the faulting mechanism at great depths. *Journal of Geophysical Research (Solid Earth)*, 108:2091, 2003. doi:10.1029/2002JB001948. 20, 85, 96, 99

R. Tibi, D. A. Wiens, and H. Inoue. Remote triggering of deep earthquakes in the 2002 Tonga sequences. *Nature*, 424(6951): 921–925, 2003. doi:10.1038/nature01903. 14, 15, 20, 23, 40, 169

F. J. Tilmann, I. Grevemeyer, E. R. Flueh, T. Dahm, and J. Goßler. Seismicity in the outer rise offshore southern Chile: Indication of fluid effects in crust and mantle. *Earth and Planetary Science Letters*, 269:41–55, 2008. doi:10.1016/j.epsl.2008.01.044. 80, 117, 123

T. Tingle, H. W. Green, C. H. Scholz, and T. A. Koczynski. The rheology of faults triggered by the olivine-spinel transformation in Mg_2GeO_4 and its implications for the mechanism of deep-focus earthquakes. *Journal of Structural Geology*, 15:1249–1256, 1993. doi:10.1016/0191-8141(93)90167-9. 10

M. A. Tinker, T. C. Wallace, S. L. Beck, P. G. Silver, and G. Zandt. Aftershock source mechanisms from the June 9, 1994, deep Bolivian earthquake. *Geophysical Research Letters*, 22:2273–2276, 1995. doi:10.1029/95GL01090. 14

M. N. Toksöz, J. W. Minear, and B. R. Julian. Temperature field and geophysical effects of a downgoing slab. *Journal of Geophysical Research (Solid Earth)*, 76:1113–1138, 1971. doi:10.1029/JB076i005p01113. 124

M. N. Toksöz, N. H. Sleep, and A. T. Smith. Evolution of the downgoing lithosphere and the mechanisms of deep focus earthquakes. *Geophysical Journal of the Royal Astronomical Society*, 35(1-3):285–310, 1973. doi:10.1111/j.1365-246X.1973.tb02429.x. 124, 147

T. Tonegawa, K. Hirahara, T. Shibutani, H. Iwamori, H. Kanamori, and K. Shiomi. Water flow to the mantle transition zone inferred from a receiver function image of the Pacific slab. *Earth and Planetary Science Letters*, 274:346–354, 2008. doi:10.1016/j.epsl.2008.07.046. 21, 146

E. Tryggvason and J. E. Lawson. The intermediate earthquake source near Bucaramanga, Colombia. *Bulletin of the Seismological Society of America*, 60(1):269–276, 1970. 13

K. Tsumura. Microearthquake activity in the Kanto district. *Special Publication of the Earthquake Research Institute: Publications for the 50th Anniversary of the Great Kanto Earthquake (in Japanese)*, pages 67–87, 1973. 14

H. H. Turner. On the arrival of earthquake waves at the antipodes, and on the measurement of the focal depth of an earthquake. *Geophysical Journal International*, 1:1–13, 1922. doi:10.1111/j.1365-246X.1922.tb05354.x. 5

S. Uyeda. *The new view of the Earth*. San Francisco, CA., W. H. Freeman, 1971. 5

H. J. A. Van Avendonk, W. S. Holbrook, D. Lizarralde, and P. Denyer. Structure and serpentinization of the subducting Cocos plate offshore Nicaragua and Costa Rica. *Geochemistry, Geophysics, Geosystems*, 120:Q06009, 2011. doi:10.1029/2011GC003592. 117

R. van der Hilst and R. Snieder. High-frequency precursors to P wave arrivals in New Zealand: Implications for slab structure. *Journal of Geophysical Research (Solid Earth)*, 101:8473–8488, 1996. doi:10.1029/95JB03113. 22

R. van der Hilst, R. Engdahl, W. Spakman, and G. Nolet. Tomographic imaging of subducted lithosphere below northwest Pacific island arcs. *Nature*, 353:37–43, 1991. doi:10.1038/353037a0. 66

P. E. van Keken, B. Kiefer, and S. M. Peacock. High-resolution models of subduction zones: Implications for mineral dehydration reactions and the transport of water into the deep mantle. *Geochemistry, Geophysics, Geosystems*, page 1056, 2002. doi:10.1029/2001GC000256. 124, 146

M. S. Vassiliou. The state of stress in subducting slabs as revealed by earthquakes analysed by moment tensor inversion. *Earth and Planetary Science Letters*, 69:195–202, 1984. doi:10.1016/0012-821X(84)90083-9. 43, 47

M. S. Vassiliou and B. H. Hager. Subduction zone earthquakes and stress in slabs. *Pure and Applied Geophysics*, 128:547–624, 1988. doi:10.1007/BF00874550. 44

M. S. Vassiliou, B. H. Hager, and A. Raefsky. The distribution of earthquakes with depth and stress in subducting slabs. *Journal of Geodynamics*, 1:11–28, 1984. doi:10.1016/0264-3707(84)90004-8. 44

J. E. Vidale. Waveform effects of a high-velocity, subducted slab. *Geophysical Research Letters*, 14:542–545, 1987. doi:10.1029/GL014i005p00542. 22

K. Wadati. Existence and study of deep earthquakes (in Japanese). *Journal of the Meteorological Society of Japan, Series 2*, 5: 119–145, 1927. 5

K. Wadati. Shallow and deep earthquakes. *Geophysical Magazine*, 1:161–202, 1928. 5

K. Wadati. Shallow and deep earthquakes. *Geophysical Magazine*, 2:1–36, 1929. 5, 11, 12

K. Wadati. On the activity of deep-focus earthquakes in the Japan Islands and neighbourhoods. *Geophysical Magazine*, 8: 305–325, 1935. 1, 5

F. Waldhauser and W. L. Ellsworth. A double-difference earthquake location algorithm: Method and application to the northern Hayward Fault, California. *Bulletin of the Seismological Society of America*, 90(6):1353–1368, 2000. doi:10.1785/0120000006. 37

F. Waldhauser and W. L. Ellsworth. Fault structure and mechanics of the Hayward Fault, California, from double-difference earthquake locations. *Journal of Geophysical Research (Solid Earth)*, 107:2054–2070, 2002. doi:10.1029/2000JB000084. 25

F. Waldhauser and D. P. Schaff. Large-scale relocation of two decades of Northern California seismicity using cross-correlation and double-difference methods. *Journal of Geophysical Research (Solid Earth)*, 113(B12):8311–8325, 2008. doi:10.1029/2007JB005479. 25

F. Waldhauser, W. L. Ellsworth, D. P. Schaff, and A. Cole. Streaks, multiplets, and holes: High-resolution spatio-temporal behavior of Parkfield seismicity. *Geophysical Research Letters*, 31:18608–18611, 2004. doi:10.1029/2004GL020649. 25

G. W. Walker. The problem of finite focal depth revealed by seismometers. *Philosophical Transactions of the Royal Society of London*, A122:45–51, 1921. 5

L. M. Wallace, C. Stevens, E. Silver, R. McCaffrey, W. Loratung, S. Hasiata, R. Stanaway, R. Curley, R. Rosa, and J. Taugaloidi. GPS and seismological constraints on active tectonics and arc-continent collision in Papua New Guinea: Implications for mechanics of microplate rotations in a plate boundary zone. *Journal of Geophysical Research (Solid Earth)*, 109:B05404, 2004. doi:10.1029/2003JB002481. 55

K. Wang. Unbending combined with dehydration embrittlement as a cause for double and triple seismic zones. *Geophysical Research Letters*, 29(18):1889, 2002. doi:10.1029/2002GL015441. 14

Y. Wang, T. Uchida, J. Zhang, M. L. Rivers, and S. R. Sutton. Thermal equation of state of akimotoite $MgSiO_3$ and effects of the akimotoite-garnet transformation on seismic structure near the 660 km discontinuity. *Physics of the Earth and Planetary Interiors*, 143:57–80, 2004. doi:10.1016/j.pepi.2003.08.007. 134

D. A. Wark and E. B. Watson. Effect of grain size on the distribution and transport of deep-seated fluids and melts. *Geophysical Research Letters*, 27:2029–2032, 2000. doi:10.1029/2000GL011503. 106

L. M. Warren. Measurement of differential rupture duration as constraints on the source finiteness of deep-focus earthquakes: 2. Synthetic tests to estimate errors in rupture vectors and their effect on fault plane identification. *Journal of Geophysical Research (Solid Earth)*, 115(B14):B09307, 2010. doi:10.1029/2009JB007071. 85, 103

L. M. Warren and P. M. Shearer. Mapping lateral variations in upper mantle attenuation by stacking P and PP spectra. *Journal of Geophysical Research (Solid Earth)*, 107:2342, 2002. doi:10.1029/2001JB001195. 88

L. M. Warren and P. G. Silver. Measurement of differential rupture durations as constraints on the source finiteness of deep-focus earthquakes. *Journal of Geophysical Research (Solid Earth)*, 111(B10):B06304, 2006. doi:10.1029/2005JB004001. 20, 85, 86, 99, 103, 104, 108

L. M. Warren, A. N. Hughes, and P. G. Silver. Earthquake mechanics and deformation in the Tonga-Kermadec subduction zone from fault plane orientations of intermediate- and deep-focus earthquakes. *Journal of Geophysical Research (Solid Earth)*, 112(B11):B05314, 2007. doi:10.1029/2006JB004677. 7, 20, 82, 86, 89, 92, 105, 107, 108, 109

L. M. Warren, M. A. Langstaff, and P. G. Silver. Fault plane orientations of intermediate-depth earthquakes in the Middle America Trench. *Journal of Geophysical Research (Solid Earth)*, 113(B12):B01304, 2008. doi:10.1029/2007JB005028. 7, 20, 86, 89, 92, 103, 107

A. Wegener. *Die entstehung der kontinente und ozeane*. Brunswick, Sammlung Vieweg, 1915. 5

P. Wessel and W. H. F. Smith. New, improved version of generic mapping tools released. *EOS Transactions*, 79:579–579, 1998. doi:10.1029/98EO00426. 12

S. Wiemer and J. P. Benoit. Mapping the b-value anomaly at 100 km depth in the Alaska and New Zealand subduction zones. *Geophysical Research Letters*, 23:1557–1560, 1996. doi:10.1029/96GL01233. 17

D. A. Wiens. Seismological constraints on the mechanism of deep earthquakes: temperature dependence of deep earthquake source properties. *Physics of the Earth and Planetary Interiors*, 127:145–163, 2001. doi:10.1016/S0031-9201(01)00225-4. 17, 147

D. A. Wiens and H. J. Gilbert. Effect of slab temperature on deep-earthquake aftershock productivity and magnitude-frequency relations. *Nature*, 384:153–156, 1996. doi:10.1038/384153a0. 17, 18

D. A. Wiens and J. J. McGuire. The 1994 Bolivia and Tonga events: Fundamentally different types of deep earthquakes? *Geophysical Research Letters*, 22:2245–2248, 1995. doi:10.1029/95GL01598. 147, 161

D. A. Wiens and J. J. McGuire. Aftershocks of the March 9, 1994, Tonga earthquake: The strongest known deep aftershock sequence. *Journal of Geophysical Research (Solid Earth)*, 105:19067–19084, 2000. doi:10.1029/2000JB900097. 14

D. A. Wiens and N. O. Snider. Repeating deep earthquakes: Evidence for fault reactivation at great depth. *Science*, 293: 1463–1467, 2001. doi:10.1126/science.1063042. 25, 26, 31, 39, 40, 42, 61, 68, 169

D. A. Wiens and S. Stein. Age dependence of oceanic intraplate seismicity and implications for lithospheric evolution. *Journal of Geophysical Research (Solid Earth)*, 88:6455–6468, 1983. doi:10.1029/JB088iB08p06455. 23, 123

D. A. Wiens, J. J. McGuire, and P. J. Shore. Evidence for transformational faulting from a deep double seismic zone in Tonga. *Nature*, 364:790–793, 1993. doi:10.1038/364790a0. 7, 14, 45, 60, 65, 166, 169

D. A. Wiens, J. J. McGuire, P. J. Shore, M. G. Bevis, K. Draunidalo, G. Prasad, and S. P. Helu. A deep earthquake aftershock sequence and implications for the rupture mechanism of deep earthquakes. *Nature*, 372:540–543, 1994. doi:10.1038/372540a0. 14, 61, 85, 147

D. A. Wiens, H. J. Gilbert, B. Hicks, M. E. Wysession, and P. J. Shore. Aftershock sequences of moderate-sized intermediate and deep earthquakes in the Tonga subduction zone. *Geophysical Research Letters*, 24:2059–2062, 1997. doi:10.1029/97GL01957. 14

R. J. Willemann. A simple explanation for the depth distribution of deep earthquakes. *Geophysical Research Letters*, 18: 1123–1126, 1991. doi:10.1029/91GL01081. 44

R. J. Willemann and G. F. Davies. Bending stresses in subducted lithosphere. *Geophysical Journal International*, 71:215–224, 1982. doi:10.1111/j.1365-246X.1982.tb04994.x. 67

R. J. Willemann and C. Frohlich. Spatial patterns of aftershocks of deep focus earthquakes. *Journal of Geophysical Research (Solid Earth)*, 92:13927–13943, 1987. doi:10.1029/JB092iB13p13927. 14

C. J. Wolfe, B. A. Brooks, J. H. Foster, and P. G. Okubo. Microearthquake streaks and seismicity triggered by slow earthquakes on the mobile south flank of Kilauea Volcano, Hawai'i. *Geophysical Research Letters*, 34:23306–23310, 2007. doi:10.1029/2007GL031625. 25

R. K. Workman and S. R. Hart. Major and trace element composition of the depleted MORB mantle (DMM). *Earth and Planetary Science Letters*, 231:53–72, 2005. doi:10.1016/j.epsl.2004.12.005. 112

M. J. R. Wortel and N. J. Vlaar. Subduction zone seismicity and the thermo-mechanical evolution of downgoing lithosphere. *Pure and Applied Geophysics*, 128:625–659, 1988. doi:10.1007/BF00874551. 44

R. Wortel. Seismicity and rheology of subducted slabs. *Nature*, 296:553–556, 1982. doi:10.1038/296553a0. 124, 140

D. J. Wright, S. H. Bloomer, C. J. MacLeod, B. Taylor, and A. M. Goodlife. Bathymetry of the Tonga Trench and forearc: a map series. *Marine Geophysical Research*, 21:489–512, 2000. doi:10.1023/A:1026514914220. 105

L.-R. Wu and W.-P. Chen. Anomalous aftershocks of deep earthquakes in Mariana. *Geophysical Research Letters*, 26:1977–1980, 1999. doi:10.1029/1999GL900389. 14, 20, 93

T. C. Wu, W. A. Bassett, P. C. Burnley, and M. S. Weathers. Shear-promoted phase transitions in Fe_2SiO_4 and Mg_2SiO_4 and the mechanism of deep earthquakes. *Journal of Geophysical Research (Solid Earth)*, 98(B11):19767–19, 1993. doi:10.1029/93JB01614. 145

M. Wyss, F. Klein, K. Nagamine, and S. Wiemer. Anomalously high b-values in the South Flank of Kilauea volcano, Hawaii: evidence for the distribution of magma below Kilauea's East rift zone. *Journal of Volcanology and Geothermal Research*, 106: 23–37, 2001. doi:10.1016/S0377-0273(00)00263-8. 17

M. Wyss, C. Sammis, R. Nadeau, and S. Wiemer. Fractal dimension and b-value on creeping and locked patches of the San Andreas Fault near Parkfield, California. *The Bulletin of the Seismological Society of America*, 94:410–421, 2004. doi:10.1785/0120030054. 17

S. Wyss and M. Wiemer. Mapping spatial variability of the frequency-magnitude distribution of earthquakes. *Advances in Geophysics*, 45(C):259–302, 2002. doi:10.1016/S0065-2687(02)80007-3. 17

W. Xu, C. Lithgow-Bertelloni, L. Stixrude, and J. Ritsema. The effect of bulk composition and temperature on mantle seismic structure. *Earth and Planetary Science Letters*, 275(1-2):70–79, 2008. doi:10.1016/j.epsl.2008.08.012. 112

Y. Xu, T. J. Shankland, S. Linhardt, D. C. Rubie, F. Langenhorst, and K. Klasinski. Thermal diffusivity and conductivity of olivine, wadsleyite and ringwoodite to 20 GPa and 1373 K. *Physics of the Earth and Planetary Interiors*, 143:321–336, 2004. doi:10.1016/j.pepi.2004.03.005. 131, 134

T. Yamashita. Pore creation due to fault slip in a fluid-permeated fault zone and its effect on seismicity: generation mechanism of earthquake swarm. *Pure and Applied Geophysics*, 155:625–647, 1999. doi:10.1007/s000240050280. 17

J. J. Yang and R. Powell. Ultrahigh-pressure garnet peridotites from the devolatilization of sea-floor hydrated ultramafic rocks. *Journal of Metamorphic Geology*, 26:695–716(22), 2008. doi:10.1111/j.1525-1314.2008.00780.x. 114

S. Yoshida. Waveform inversion for rupture processes of two deep earthquakes in the Izu-Bonin region. *Physics of the Earth and Planetary Interiors*, 52:85–101, 1988. doi:10.1016/0031-9201(88)90058-1. 103

Y. Yoshida, K. Abe, and K. Satake. The large normal-faulting Mariana earthquake of April 5, 1990 in uncoupled subduction zone. *Geophysical Research Letters*, 19:297–300, 1992. doi:10.1029/92GL00165. 83

H. Zhang and C. Thurber. Development and applications of double-difference seismic tomography. *Pure and Applied Geophysics*, 163:373–403, 2006. doi:10.1007/s00024-005-0021-y. 120

J. Zhang, H. W. Green, K. Bozhilov, and Z. Jin. Faulting induced by precipitation of water at grain boundaries in hot subducting oceanic crust. *Nature*, 428:633–636, 2004. doi:10.1038/nature02475. 8, 82

J. Zhang, P. G. Richards, and D. P. Schaff. Wide-scale detection of earthquake waveform doublets and further evidence for inner core super-rotation. *Geophysical Journal International*, 174:993–1006, 2008. doi:10.1111/j.1365-246X.2008.03856.x. 25, 26

S. Zhong and G. F. Davies. Effects of plate and slab viscosities on the geoid. *Earth and Planetary Science Letters*, 170:487–496, 1999. doi:10.1016/S0012-821X(99)00124-7. 66, 164

S. Zhong and M. Gurnis. Mantle convection with plates and mobile, faulted plate margins. *Science*, 267:838–843, 1995. doi:10.1126/science.267.5199.838. 66, 164